University of Minnesota
ST. ANTHONY FALLS HYDRAULIC LABORATORY

Project Report No. 170

ON AN ACOUSTIC FIELD GENERATED BY SUBSONIC JETS AT LOW REYNOLDS NUMBERS

by

Kingo Yamamoto

and

Roger E. A. Arndt

Prepared for

NATIONAL AERONAUTICS & SPACE ADMINISTRATION
NASA-Lewis Research Center

March 1978
Minneapolis, Minnesota

ABSTRACT

This thesis deals with the experimental investigation of an acoustic field generated by subsonic jets at low Reynolds numbers. This work is motivated by the need to increase the fundamental understanding of the jet noise generation mechanism which is essential to the development of further advanced techniques of noise suppression.

The scope of this study consists of two major investigations. One is a study of large scale coherent structure in the jet turbulence, and the other is a study of the Reynolds number dependence of jet noise. With this in mind, extensive flow and acoustic measurements in low Reynolds number turbulent jets ($8.93 \times 10^3 \leq R_e \leq 2.20 \times 10^5$) were undertaken using miniature nozzles of the same configuration but different diameters at various exit Mach numbers ($0.2 \leq M \leq 0.9$).

All the experimental works reported herein were conducted in an anechoic-chamber with a 300 Hz cut-off frequency located at the NASA LEWIS RESEARCH CENTER, Cleveland, Ohio.

The validity of the Michalke's spectral theory was verified for the first time in this study utilizing only experimental data. The procedure involved the use of Chan's prediction method for the intensity of a single-azimuthal component of the jet noise. This method was found to be adequate for the prediction of the detail of the acoustic field.

The results of circumferential cross-correlation measurements in the far field show that only the axisymmetric and the first helical modes have any practical importance in jet noise for Strouhal numbers between 0.1 and 1.0. It also has been established each azimuthal mode has a corresponding dominant emission angle. Coherency of jet noise is observed

over a rather broad range of frequency at emission angle close to the jet axis. One may reasonably conclude from measured directivity patterns that stronger coherency can be observed in the downstream direction rather than the lateral direction.

A careful study of the narrow-band spectrum of the radiated sound has revealed the existence of a critical Reynolds number associated with the peak frequency of jet noise. That is to say, the spectral characteristics of the jet noise were a function of Reynolds number at values below about 10^5. This suggests that proper simulation of the proptotype acoustic field can be achieved only with model jets operating at Reynolds numbers in excess of 10^5.

TABLE OF CONTENTS

Page

LIST OF TABLES

LIST OF FIGURES

LIST OF SYMBOLS

a	Location of jet's virtual origin
a_n	Real part of Fourier spectrum
a_o	Ambient speed of sound
b_n	Imaginary part of Fourier spectrum
$b_{\omega m}$	Fourier coefficient of coherence function
B	Cyclical frequency bandwidth
c_α	Numerical constant
c_{ph}	Phase velocity
c_ω	Co-spectrum
$c_{\omega m}$	Fourier coefficient of c_ω
COP	Coherent output power
CSD	Cross spectral density
D	Jet diameter
$\overline{e^2}$	Mean value of square of fluctuating voltage
e_{ij}	Strain rate
$E(k)$	Energy spectrum
f	Frequency
f_c	Anti-aliasing filter cutoff frequency
f_p	Peak frequency
f_s	Sampling rate
$f(M,R_e)$	Arbitrary function of M and R_e
F	Analysis frequency range
$\hat{F}_m$	Longitudinal source distribution function (m-component)
$F(R_e)$	Arbitrary function of R_e

$F(\bar{x}), \hat{F}(\bar{x})$	Longitudinal source distribution function and its normalized form
$F_{max}(\bar{x})$	Maximum value of $F(\bar{x})$
$\Delta F, \Delta f$	Weighting frequency and filter spacing, respectively
FFT	Fast Fourier transform
$\hat{G}$	Power spectral density estimate
$G(f), G(\omega), G_x(f), G_y(f)$	Power spectral density
$G_{xy}(f)$	Cross spectral density
$\hat{G}_{xy}(f)$	Cross spectral density estimate
$G(\bar{r}), \hat{G}(\bar{r})$	Lateral source distribution function and its normalized form
$G_{max}(\bar{r})$	Maximum velocity of $G(\bar{r})$
$G(M, R_e, \hat{\theta})$	Arbitrary function of M, R_e and $\hat{\theta}$
$\hat{G}_m$	Lateral source distribution function (m-component)
$H(f)$	Function of f defined by Eq. (A.4)
$\lvert I_x \rvert$	Longitudinal source integral
$\lvert I_r \rvert_o, \lvert I_r \rvert_1, \lvert I_r \rvert_2$	Lateral source integral for m = 0, 1 and 2
$I_{m\omega}$	Product of $\lvert I_x \rvert$ and $\lvert I_r \rvert$
$I(\hat{X}, \omega)$	Power spectrum measured at $\hat{X}$
j	Pure imaginary
J_m	Bessel function of first kind and mth order
k	Wave number
K	Numerical constant
ℓ	Longitudinal extent of source distribution in terms of normalized distance and wire length
L	Longitudinal extent of source distribution and length of wall boundary layer
m	Mode number and mass flow rate
M	Mach number

MAG^2	Square value of amplitude
M_c	Convection Mach number
$N(\hat{\theta})$	Power index
N,n	Number of samples and mode number, respectively
OASPL	Overall sound pressure level
p	Fluctuating pressure and static pressure
p_o	Ambient static pressure
$p^{(0)}$	Pseudosound pressure
p_m, p_m^*	Fourier coefficient of p and its complex conjugate
P_m	Fourier transform of p_m
$P_m^{(0)}$	Fourier transform of $p^{(0)}$
$P(\omega)$	Power spectral density
P_T	Total pressure
P_f^2	Mean square of pressure fluctuation
$\hat{p}_\omega^2$	Power spectral density
PSD	Power spectral density
q	Source function
q_m, q_m^*	Fourier coefficient of q and its complex conjugate
Q_m	Fourier transform of q_m
$\hat{Q}_m$	Amplitude of Q_m
$Q_{ij'k\ell}$	Fourth order correlation function
r	Radial coordinate of source
r'	Radial coordinate of observer
$\hat{r}$	Distance from jet exit to observer
$\bar{r}$	Normalized coordinate of r
r_o	Distance between source and observer
R	Microphone location from jet exit

$\hat{R}$	Lateral extent of source distribution
R_e	Reynolds number
S	Non-dimensionalized frequency parameter
Sh	Strouhal number
SPL	Sound pressure level
S_n, S_x^*	Fourier spectrum and its complex conjugate
t	Time
T	Memory period and period in general
T_a	Ambient air temperature
T_j	Total jet temperature
T_{ij}	Lighthill stress tensor.
T_T	Flow temperature
u, u_i	Fluctuating velocity (x-component)
u_m	Maximum value of u (or u_i)
$\overline{u}$	RMS value of u (or u_i)
U	Mean flow velocity
U_c	Convection velocity
U_j	Jet exit velocity
U_m	Center velocity of mean flow
$\overline{V}$	Effective volume of turbulence
W	Total acoustic power and ratio of maximum shear noise to self noise
X	Axial coordinate of source
X'	Axial coordinate of observer
$X_i, X_j, \hat{X}$	Free space coordinate
$\overline{X}$	Normalized axial coordinate of source
x(t), y(t)	Time dependent variables
y, y	Source field coordinate

y_o	Source field coordinate (of reference point)
Z	Source field coordinate
Z_α	100α% point of the standardized normal distribution
$Z_{0.5}$	Radial location where $U = 0.5\ U_m$
α	Axial wave number
γ	Coherence function
Γ	Gamma function
δ_{ij}	Kronecker delta
ε	Energy dissipation rate
η	Degree of freedom and reduced radial coordinate
$\hat{\theta}$	Sound emission angle
$\hat{\theta}_c$	Mach angle
λ	Sound wavelength
λ_G	Spacial length scale
κ	Correction factor
μ	Viscosity
ν	Kinematic viscosity
ξ	Normalized radial coordinate
ξ	Separation vector between two sources
ρ	Gas density
ρ'	Fluctuating density
ρ_o	Ambient density
$\rho^{(0)}$	Pseudosound density
$\overline{\rho}$	Local mean density
ρ_m	Air density in mixing region
σ_h	Standard deviation
$\tau, \Delta\tau$	Correlation delay time

ϕ	Azimuthal coordinate of source
$\hat{\phi}$	Azimuthal coordinate of observe
χ_η	Chi-square distribution
ψ_m	Source phase function
$\psi(\hat{\theta})$	Directivity factor
ω	Angular frequency

ACKNOWLEDGEMENTS

This work was carried out at the Pennsylvania State University and at the NASA-Lewis Research Center under Grant NGR-39-009-270.

The authors would like to thank Dr. Yamamoto's thesis committee for many helpful suggestions and stimulating discussions which led to the successful completion of this project. The members of the committee are Professor J. Eisenbuth, Professor B. Lakshminarayana and Professor G. Reethof. In addition, a special word of thanks should go to Professor B. Lakshminarayana who acted as graduate student advisor to Mr. Yamamoto while the junior author was on sabbatical leave.

Special acknowledgement should be given to Mr. Jeffrey Essary who was instrumental in overcoming the many problems which cropped up during the experimental program at the NASA-Lewis Research Center.

Chapter I

INTRODUCTION

1.1 General Statement of the Problem

The introduction of the turbofan jet engines into commercial aircraft service some fifteen years ago resulted in a significant reduction of jet noise. This engine differs from the conventional turbojet engine in that some of the air entering the inlet bypasses the engine combustion system and merges with the burned gases at the exhaust outlet pipe. Thrust power from the engine is directly related to the exhaust velocity as $\rho U^3 D^2$ in contrast to the acoustic power which varies like $\rho U^8 D^2$. The turbofan engine achieves its thrust with high mass flow at low velocity (large diameter D and small velocity U) compared to the turbojet engine which has high exhaust velocities (small D and large U). Thus, at a specified thrust, the turbofan engine is inherently quieter, as far as jet noise is concerned. The new generation of commercial aircrafts represented by the Lockheed L1011 and Douglas DC-10 provides tangible evidence of the progress in noise reduction achieved with the development of the high-bypass-ratio turbofan engines. However, further noise reduction of jets at lower jet velocities is not foreseen at this point since current noise suppressor technology is ineffective at such low velocities. This fact may indicate that an even more basic understanding of the jet noise generation mechanism will be required for further effective noise suppression. Over the past two decades, the search for a better understanding of the nature of the acoustic sources generated by turbulent shear layers has focused on the determination of the dominant noise producing structure in jets.

1.2 Previous Related Studies

There have been two major hypotheses concerning the structure of jet turbulence as a dominant source of jet noise. They are the eddy-model of jet turbulence and the large scale coherent structure model. Ribner (1962) remarked, "A turbulent jet may be regarded as an assemblage of 'eddies' (correlation volumes) which radiate sound independently or incoherently: the total pressure fluctuations can be represented by summing mean square fluctuations due to each eddy." However, this assumption of a spatially random jet turbulence is not self-evident, as pointed out by Michalke (1972a). Many experimental studies which have been undertaken up to this point imply that the components with high space correlation may exist in jet turbulence. Mollo-Christensen (1967) suggested, "Turbulence may be more regular than we think it is." His experimental results of the pressure fluctuations measured outside of a turbulent jet revealed that the jet turbulence appears to be composed of well defined, more or less identical, wave packets containing components of all frequencies. Furthermore, different frequency components preserve their phase relationship over a few jet diameters. The possibility of a wave-like coherent structure in jet turbulence is particularly appealing to those responsible for advances in noise suppression technology. This wave-like coherent structure in the jet is more probably "a manifestation of free shear flow instabilities" (Liu, 1974) and could probably be the most significant noise source in the jet flow.

Combining visual and hot-wire techniques Crow and Champagne (1971) conducted turbulence measurements with the aim of demonstrating the existence of orderly structure in a turbulent jet by artificially introducing disturbances of specified frequency. These disturbances were

observed to interact strongly with the jet. The fundamental wave generated by acoustic excitation grows in amplitude downstream until nonlinear effects result in a harmonic wave which retards the growth of the fundamental wave. Both the fundamental and the harmonic attain saturation at an intensity which is independent of forcing amplitude. The final growth rate was found to be a maximum at a Strouhal number fD/U of 0.3.

From the measurements made in the non-turbulent regions (namely, the potential core and the entrainment region), Lau, Fisher and Fuchs (1972) concluded that their observations are consistent with their postulated model, namely a series of equally spaced toroidal vortices buried in the jet mixing region and convected at a 0.6U, where U is the jet exit velocity.

A wave-like structure in jet turbulence was also found by Fuchs (1972). He pointed out, after having measured the space-correlation of axisymmetric spectral components of the fluctuating pressure in jet turbulence, that for certain frequencies a wave-like coherency can be observed up to eight diameters downstream of the jet orifice and that a strong spatial correlation exists in the lateral direction also.

As pointed out by Michalke (1970a), an infinite train of propagating waves with amplitude which is time dependent but uniform in the direction of propagation does not produce sound because of cancellation. However, if this wave train were cut off, then it would give rise to sound. Hydrodynamic instability waves of finite length are postulated to be representative of the coherent structures in turbulence. On this point, Mollo-Christensen (1967) described that these instability waves in real growing shear flow could grow in amplitude but subsequently decay. Thus, the concept of a radiated sound field due to the spatial growth and decay

of hydrodynamic instabilities is plausible from a physical point of view. The concept of instability waves in a laminar free shear flow where the unstable waves decay due to mean flow spreading and viscous dissipation is generally accepted. However, it has been observed by many researchers that such instability wave or coherent structure is found even in the turbulent wakes and in the mixing region of jet turbulence. To put it in another way, such instability waves possibly exist in turbulent free shear flows as well.

Michalke (1970b), using linear stability theory, predicted the most amplified frequency for periodic forcing. He found that this frequency depended upon the ratio of mixing-layer momentum thickness to the effective jet diameter.

Ffowcs-Williams (1974) and Chan (1974b) also conjectured that there is a close relationship between coherent structure and the instability mechanism in the turbulent shear flow. Recent advances have been made in stability theory, and it is now possible to take into account the steadily growing shear layer width and the wall effect at the flow origin.

It should also be noted that Meecham (1969) made the following remarks, ". . . thus we can expect that the large-scale characteristics (energy range) of the turbulence depend upon details of the jet generation process. Because most of the acoustic radiation comes from the large-scale eddies, we can say at the outset that the total acoustic power produced by a given turbulent motion will depend upon the manner in which the turbulence is generated."

Michalke's success (1974) in introducing the shape of the mean velocity profile of the jet into the stability calculations is somewhat encouraging to those who work on the jet noise problem. His theory

reveals the large-scale coherent structure buried in jet turbulence with aid of instability analysis. Keeping in mind previous experimental results which seem to confirm the existence of the wave-like structure in jet turbulence, Michalke (1972a) proposed a spectral theory based on an expansion scheme for the noise from round jets. This would permit the direct correlation of the radiated sound field of jet with the Lighthill stress tensor, expressed in terms of the "properly described" coherent eddies-waves (Liu, 1975). Three years before the appearance of Michalke's theory, Pao and Lowson (1969) disclosed their concept about the spectral theory of jet noise based upon an eddy-model of jet turbulence. Unfortunately, the predicted directivities based on their spectral theory were not consistent with observations particularly for high frequency sound. Michalke commented upon this inconsistency by suggesting that some assumptions made by using the eddy-model are doubtful or, at least, very limited.

Taking into account the geometrical configuration of a circular jet, Michalke (1972a) adopted the cylindrical coordinate system to describe the source term in the integral solution of the Lighthill equation. He then expanded the source term in terms of a Fourier series with respect to the azimuthal angle. Furthermore, he made a Fourier transform of the expanded source function to produce the cross spectral density of the source term components. Then he introduced the wave-like model of jet turbulence into his formulation. After several manipulations he finally obtained an expression for the intensity of radiated sound due to a single azimuth-frequency component of the noise source. This result shows that the sound emitters distributed in the turbulent flow of a circular jet can be classified according to the azimuthal wave number and

frequency. The expression for the intensity of the sound includes two important functions, i.e., the Bessel function of the first kind and the mth order and an exponential function. These terms are decreasing functions of increasing argument. From a physical point of view, this indicates the effect of cancellation and interference between various sound sources. As a result, jet turbulence may be regarded as a noticeably ineffective sound emitter.

In the spectral theory of Michalke, two parameters play a decisive role in the determination of the directivity of jet noise. The jet thickness parameter defined by $k\hat{R}\sin\hat{\theta}$ appears as an argument of the Bessel function in Michalke's formula, where k and $\hat{R}$ are the wave number of the radiated sound and lateral extent of source distribution in jet, respectively. As will be discussed in Chapter III, $k\hat{R}$, often referred to as the Helmholtz number, is a ratio of lateral source extent to sound wavelength. Since for small argument, the Bessel function of the $m = 0$ order is dominant, we can say that the sound whose wavelength is significantly larger than the lateral source extent $\hat{R}$ is exclusively a result of axisymmetric emitters ($m = 0$) in the jet turbulence. Another important parameter is the convection parameter $\alpha L(1 - M_c \cos\hat{\theta})$ which is responsible for the intensified sound radiation in the direction of the jet axis ($\hat{\theta} = 0°$) for $0 \leq M_c \leq 1$, where M_c is the convection Mach number defined as an axial phase velocity divided by local sound speed, c_{ph}/a_o. Since the azimuthal wave number m determines the order of the Bessel function, we note that the axisymmetric emitters ($m = 0$) and the non-axisymmetric emitters ($m \neq 0$) have entirely different directivity patterns.

One of the most surprising features of Michalke's spectral theory may be the fact that without specifying the source term of the Lighthill equation, one can draw some useful conclusions about the noise generation mechanism.

The Pao and Lowson's theory, however, is based on the eddy-model characterized by the assumption that the turbulent eddies can be described by overall-correlation functions of the convected Gaussian form. Michalke (1972a) pointed out that this leads to a very limited type of turbulence. Therefore, some results derived under these assumptions may be used only with caution. It should be pointed out here that Michalke's spectral theory includes the Pao and Lowson's theory as a special case (see Michalke (1972a)).

Fuchs (1974) conducted circumferential cross-correlation measurements in round jets employing static pressure probes, and obtained power spectra of the lower-order azimuthal components of the fluctuating pressure field as a result of a Fourier decomposition of narrow band cross spectral density. He found that only the lower azimuthal components of the turbulent pressure have any practical importance in generating sound for moderate Strouhal frequencies. Furthermore, he observed, by an experimental analysis of the structure of jet turbulence at low Mach numbers, the presence of lower azimuthal pressure components which play a dominant role in sound generation. In summarizing he described, "It would be feasible that all the coherent phenomena together with their acting as efficient sound emitters took place in an entirely irrelevant range of frequencies. In this context, it is worth mentioning that the orderly structures occur at Strouhal number between 0.1 and 1.0 where

jets at high Mach numbers are known to radiate most of the acoustic power" (Fuchs, 1974).

It was Chan (1974) at the National Aeronautical Establishment, Canada who first proposed an evaluation method of the axisymmetric component of the intensity of the radiated sound based upon Michalke's spectral theory using the experimental results of his direct measurements of the pressure waves in an acoustically excited jet shear flow.

He expressed the source term in Michalke's prediction formula in terms of the pressure fluctuations according to Ribner's dilation theory (1962). After taking a Fourier transform of the source function, he obtained the longitudinal and lateral amplitude distributions of the pressure waves in a jet, assuming that the pressure source function which is nothing more than a Fourier transform of pseudo-sound $p^{(0)}$ can be expressed as a product of two mutually independent functions of x and r. These two amplitude distributions were determined by the measurements of the spatial development of a pressure disturbance in a turbulent free jet for the first three azimuthal modes (Chan, 1974b, 1976). He observed in his measurements that the wave number of the disturbances for any of the three modes was a monotonically increasing function of Strouhal frequency and that the wave front was slightly inclined to the jet axis. Furthermore, he noted that the pressure disturbance grew first to a maximum, progressed downstream and then decayed away. He showed that the pressure amplitude distributions in the shear layer could be scaled by a normalized distance $(Sh \cdot x)/D$. He concluded his analysis of the pressure wave measurements by saying that the pressure disturbances of all modes are well modelled by a wave theory in which the local properties

of the wave propagation is described by a linear instability theory of an inviscid shear flow.

It is well-known that the aerodynamic properties of a jet can be a function of Reynolds number, UD/ν. However, the acoustic field of a jet is primarily a function of Mach number, U/a_o and variations in Reynolds number are normally disregarded. In general, the sound power of jet noise satisfies the following relationship

$$W/(\tfrac{1}{2}\rho U^3 D^2) = f(M,R_e) \quad .$$

Thus, at high Reynolds number, the acoustic power satisfies the approximate relationship

$$W/(\tfrac{1}{2}\rho U^3 D^2) \simeq KM^5$$

where K is a constant.

All experiments which have been conducted up to this point at moderate to high Reynolds numbers confirm this. However, there is some evidence that even at Reynolds numbers of the order of 10^5, the spectral characteristics of jet noise are dependent on Reynolds number, although such evidence has been largely ignored. Mollo-Christensen et al. (1964) studied the Reynolds number dependence of the far field noise, partly quantitatively but mostly qualitatively and found that the rms value of the far field sound pressure is proportional to $(Re)^m$ where m has values of $1 \leq m \leq 3$. Furthermore, they observed that the non-dimensionalized narrow band spectra of the noise also varied with Reynolds number. This was confirmed by using two jets of different diameters and various exit Mach numbers, corresponding to Reynolds numbers of approximately $3Mx10^5$ and $6Mx10^5$, respectively, where M represents the Mach number. Mollo-Christensen (1967) conjectured that the wall boundary layer of a jet

nozzle must be fully turbulent at $R_e = U\ell/\nu = 10^6$ or larger, where ℓ represents the boundary layer length. This corresponds to the Reynolds number of 2×10^5 based on jet diameter. Above this value of Reynolds number all the spectra have similar profiles because Reynolds number ceases to be an important parameter. Other evidence confirming this fact can be found in the experimental data provided by Ahuja and Bushall (1973). Although they did not give any discussion on it, they noted that at lower Reynolds numbers there is less variation of peak frequency with observation angle. This may have the same physical basis with the observations by McLaughlin et al. (1976) in which the low Reynolds number spectrum was dominated by a few discrete modes.

1.3 Specific Statement of the Problem

There is considerable evidence that a wavelike coherent structure exists in a jet, and that it can play an important role in noise generation. However, as has been reviewed, we still lack a definite one-to-one correlation between the coherent structure and the radiated sound.

Although some information about the dependence of jet noise on Reynolds number has been reported, a more systematic and quantitative investigation is necessary for a complete understanding of the role of Reynolds number in jet noise production. An important reason for the interest in low Reynolds number flows is the fact that much of our knowledge about coherent structure in jets has been obtained through flow visualization studies carried out with jets operating at low Reynolds numbers. Therefore, it seems logical to consider the acoustic radiation at the same low Reynolds numbers in order to obtain a 1:1 correlation between coherent structure and the properties of jet noise.

The aim of this study was to determine, in a more quantitative way, the role of coherent structure in the noise radiation mechanism. It was expected that coherent structure would be more dominant in the jet flow at low Reynolds numbers.

The scope of this study consists of two major parts. One is a study of large scale coherent structure in the jet turbulence, and the other is a study of the Reynolds number dependence of jet noise.

The research work was basically experimental, and it was carried out in five steps as shown below:

1. First, the flow characteristics of jets emanating from five different nozzles were studied using a hot-wire probe.

2. Acoustical measurements in the radiated field were conducted using a B&K 6.35 mm microphones.

3. The cross correlation between hot-wire signals in the flow and microphone signals in the far field were determined.

4. Phase velocity of instability waves in the jet flow was measured in an acoustically excited jet.

5. Finally, the coherence function of the circumferentially cross correlated signals of jet noise were measured.

Throughout the entire experimental work, emphasis was placed on the measurement of narrow band spectra of the fluctuating velocity in the flow, as well as, of the radiated sound.

In the second chapter a detailed description of the experimental apparatus and procedure is given. The third chapter introduces Michalke's spectral theory followed by Chan's prediction method of jet noise. The fourth chapter is concerned with the description and discussion of the experimental results, and it also includes a comparison of the

observations with theory. Finally, in Chapter V a summary and conclusions are presented. Error estimates of the measured power spectral density and coherence function are given in Appendix A. Appendix B deals with the detail of phase velocity measurements.

Chapter II

EXPERIMENTAL APPARATUS AND PROCEDURE

In this chapter, the experimental apparatus and procedure will be discussed in some detail. The jet facility and measuring apparatus are first described. Then, various aspects of the electronic instrumentation used in the present study will be discussed with emphasis on the signal processing utilizing a Fast Fourier Transform (FFT) digital signal processor. Finally, the experimental procedure will be explained.

2.1 Test Facility

The experiments were conducted in an anechoic chamber at the NASA Lewis Research Center, Cleveland, Ohio, with dimensions 20mx16mx5m measured from the tip of the wedges with a lower cutoff frequency of about 300 Hz. The general floor plan and elevation of the anechoic chamber are shown in Figures 1 and 2, respectively. The entire inside surface of the room is lined with fiberglass wedge blocks which were designed for a low-frequency cutoff of 150 Hz. Figure 3 is an isometric view of one of the acoustic wedges.

2.1.1 Air supply, settling chamber and jet nozzles

Air is supplied to the jet by a continuosuly running compressor. Three pressure reducing valves, 20, 10 and 3.8 cm, in the supply lines control the settling chamber pressure which is monitored by a total pressure transducer and a D.C. millivoltmeter. The schematic diagram of the flow control system is shown in Figure 4. Air is fed to the settling chamber through an acoustic muffler. Figure 5 illustrates the settling

chamber and jet nozzle. Honeycomb steel wool pads and a set of screens to ensure an uniform velocity distribution at the nozzle entry were placed upstream of the nozzle. The nozzles were designed such that a uniform velocity distribution would result at the nozzle exit plane (Smith and Wang, 1944). The nozzles were made of steel and were carefully finished to obtain a smooth inside surface. Figure 6 displays the cross-section of the nozzle.

In the present investigation, five nozzles of different sizes but of similar configuration were employed. The nozzle sizes utilized are listed in Table 1. The contraction ratio of the nozzle is 36:1. The jets used in the present study were practically cold subsonic jets and no attempt to heat the jets was undertaken.

2.1.2 Hot-wire traversing mechanism and microphone rotating mechanism

In Figure 7, a remote control xyz-traversing mechanism is displayed pictorially. It was located underneath the settling pipe and was used for precision incremental positioning of the hot-wire probe. It had a positioning accuracy of $\pm$ 0.0254 mm over its entire span of 914 mm in each of the three dimensions. An actuator control (Model PSI-AP-SM, L. C. Smith Co.) and a digital indicator (L. C. Smith Co.) were setup in the control room for remote positioning of the hot-wire.

A rotating mechanism was employed to rotate a microphone horizontally in the range 0° to 180° relative to the downstream jet axis. The microphone boom position was indicated by a digitial indicator (L. C. Smith Co.).

2.2 Instrumentation

An overall view of the electronic instrumentation used in this study is illustrated in Figures 8, 9 and 10.

2.2.1 Flow measurement system

The hot-wire anemometer used in this study was a constant temperature anemometer (DISA 55M). A DISA 55D10 linearizer was employed to obtain constant resolution across the entire velocity range encountered. The linearizer's D.C. output was determined with a B&K integrating digital voltmeter. The same voltmeter was used for the determination of the rms levels of components of turbulence. In each case the output from the meter was recorded by a precisely calibrated XY-plotter. Both DISA 55P11 miniature hot-wire probe and Thermo Systems A718 hot-film probes were used for velocity measurements. The probes were carefully calibrated before and after each running with a TSI Model 1125 calibrator. Raw velocity data were recorded on a thirteen channel SABRE III FM taperecorder. The power spectral density, the probability density function and the cross spectral density of the fluctuating velocity signals were determined with a Spectral Dynamics SD-360 FFT Spectrum Analyzer. The flow temperature and total pressure were monitored with a thermocouple and a pitot tube probe, respectively, which were inserted in the settling pipe.

2.2.2 Acoustical measurement system

Eight Brüel and Kjaer 6.35 mm microphones were used as the field microphones. These were located more than 50 jet diameters from the center of the jet exit plane. The acoustical signals from the pressure sensor were preamplified by B&K Type 2618 preamplifer, further amplified

with the B&K Type 2108 amplifier, filtered by the active filter Model AF-120 and finally fed into the FM taperecorder, the FFT spectrum analyzer and the 1/3 octave analyzer (General Radio Type 1921 Real-Time 1/3 Octave Analyzer) simultaneously. A Tektronix type RM502A dual-beam oscilloscope, a MDS 1200 printer and an Easterline Co. XYY'-plotter (Model XXY'540) were used for data display. Photographs of noise spectra were taken with the Tektronix C-53 oscilloscope camera together with a C-50 pack film back. B&K 6.35 mm microphones were regularly calibrated by a B&K pistonephone, type 4220.

2.3 Experimental Procedure

As mentioned in the introduction, the Reynolds number dependence of jet noise was one of the major areas of this study. Throughout this investigation, Reynolds number has been treated as one of the important parameters for both the flow and acoustical characteristics of jets.

Reynolds number is defined by $R_e = U_j D/\nu$, where U_j, D and ν are jet exit velocity, effective jet diameter and kinematic viscosity, respectively. Practically speaking, we may change either jet exit velocity or jet diameter to obtain a broad range of Reynolds number. An alternative procedure was used by MacLaughlin et al. (1976) whereby low Reynolds numbers were obtained by operating at reduced exhaust pressures. Since the intensity of jet noise is strongly dependent on Mach number, it is necessary to utilize jet diameter as a variable in order to achieve similitude of both Mach number and Reynolds number. For this reason five nozzles of the same configuration but of different sizes were designed and extensively used during the present study giving a Reynolds number

range shown in Table 1. At the same time, a rather broad range of jet exit Mach number was used in present investigation.

It has been well established that the compressibility effect can be neglected in hot-wire measurements at Mach numbers less than about M = 0.3. However, in the present study, practical considerations made it necessary to collect velocity data at higher Mach numbers. It was found that the same calibration procedure proposed by Norman (1967) could be used. The deviation from King's law at M = 0.58, for example, was found to be less than 5%.

2.3.1 Mean velocity and turbulence intensity measurements

As previously stated, both TSI hot-film probe (A718) and DISA hot-wire probe (55P11) were extensively used. The former is made of nickel film deposited on 70 μm diameter quartz fiber with overall length 3 mm. The sensitive film length is 1.25 mm, and the sensor is copper and gold plated at each end. The film is protected by a quartz coating approximately 2 μm in thickness. The sensor material of the DISA 55P11 hot-wire probe is platinum plated tungsten. The sensor has a diameter of 5 μm and a length of 1.25 mm. The probe units were placed in a mounting tube which was held in a guide tube by a chuck. The guide tube system was used in conjunction with a three-dimensional traversing mechanism.

This custom built traversing mechanism can travel up to 0.9 m in any of the three directions and is operated by electrical pulses. The minimum travelling speed of the traversing mechanism is 0.0254 mm/sec. Throughout the present study the traversing speed was selected to be 0.254 mm/sec for flow measurements. It was confirmed that the selected

traversing speed of 0.254 mm/sec could achieve the desired resolution in velocity measurements.

This system permits automatic and continuous plotting of velocity profiles on the xy-recorder. The traversing mechanism is driven from a stepper motor which in turn is remotely controlled from a sweep drive unit. The output level corresponding to any given probe position is displayed with high accuracy on a five-digit electronic counter on the sweep drive unit (L. C. Smith Co.). This signal also controls the X-deflection of the recorder. The anemometer signal is fed to the Y-axis of the recorder. In this way, the movement of the anemometry probes can be accurately supervised and controlled. Flow data were collected with three of the jet nozzles; 12.7 mm, 6.35 mm and 3.18 mm in diameter. The experimental setup for the mean velocity measurements and the schematic diagram of the instrumentation are shown in Figure 11.

Before actual flow measurements could be taken, the true jet axis had to be determined. The true jet axis is defined by the locus of points of minimum turbulence intensity at various axial positions within the jet. These points were determined by an extensive series of intensity measurements carried out over the entire plane normal to the geometrical jet axis at each of ten axial positions. In this manner the true jet axis is not artificially limited to lying in a plane bisecting the jet and containing the geometrical jet axis. Thus, if the true jet axis is helical in shape this characteristic will be detected by this procedure.

Mean velocity measurements were made across the entire jet in the radial direction in order to establish the symmetry of the flow about its center plane (Figure 12). The D.C. output voltage of the linearlizer was calibrated in terms of Mach number rather than velocity.

The traversing speed of the probe was selected to be 0.254 mm/sec and the averaging time of the autoranging digital voltmeter was set to three seconds. At equally spaced stations ranging from one diameter to ten diameters downstream, the probe was traversed in the lateral direction up to ± 5 diameters about the true jet axis. A mean velocity profile was directly depicted on a XY-recorder. In order to obtain the variation of the peak mean velocity along the true jet axis, the probe was continuously moved along the true jet axis between X = D and X = 10D.

The u-component of the fluctuating velocities were also measured with the same single hot-wire or hot-film probe for three different nozzles and varying jet exit velocities. The fluctuating velocities were determined at the same time that the mean velocity profile was being plotted on the XY-recorder. As shown in Figure 11, the AC output voltage of the DISA 55D10 linearlizer was fed to a B&K 2427 autoranging digital voltmeter where the signals were averaged over three seconds. Fluctuating velocity data can be continuously plotted as a function of Z/D for a fixed value of X/D.

2.3.2 Power spectral density measurements in flow field

Presumably, the most important single description characteristic of stationary random data is the power spectral density function. For constant parameter linear physical systems, the output power spectrum can be expressed as the input power spectrum multiplied by the square of the gain factor of the system. Therefore, power spectrum measurements can yield information concerning the dynamic characteristics of the system. In the present survey a substantial amount of power spectral density data was collected in order to analyze the flow and acoustical properties of

the jets in the frequency domain. In addition, throughout the entire period of the experimental works the power spectral density of either fluctuating velocity signals or acoustical signals was always displayed and monitored on the wide screen of the Spectral Dynamics 13116-2A XY-Display Oscilloscope to check any anomalous signals involved.

Instead of the conventional time-consuming analog spectrum analyzer, the Spectral Dynamics SD-360 Digital Signal Processor was used. This is a hardwired Fast Fourier Transform (FFT) analyzer that combines the capability of two real time analyzers, a transfer function analyzer, two analog signal conditioners and a computer in one package. This device provides a complete signal analysis capability from 0.01 Hz to 150,000 Hz. The mutli-directional cursor control on the front panel of this instrument acts as a direct interface between operator and processor during data entry, display and recording. It provides maximum operational flexibility and complete editing capabilities on input waveforms in addition to continuous control of the various modes of processed data readout. This FFT analyzer has several unsurpassed features not found in other wave analyzers. It performs a dozen different data functions, providing 57 frequency analysis ranges up to 150 KHz. This unit can provide precomputation delay of up to 7 1/2 memory periods for cross correlation and cross spectrum analysis and complete editing capabilities on both input channels using a cursor stick and selectable weighting functions (Kaiser-Bessel or rectangular time domain weighting). It has anti-aliasing filters built-in for all 57 frequency ranges which were automatically set for proper range or independently located at any 57 cut-off frequencies. It also has simultaneous high-speed oscilloscope display

and low-speed XY-recording, six-digit readout of analysis parameters and analysis results, and a coherent output power display.

If the Fourier spectrum of an input signal is defined as $S_x(j\omega) = a_n + jb_n$, then the power spectrum $G_{xx}(\omega)$ at that frequency is given by

$$G_{xx}(\omega) = S_x(j\omega)S_x^*(j\omega) = (a_n + jb_n)(a_n - jb_n)$$

$$= a_n^2 + b_n^2$$

An estimate of the true power spectral density is given by averaging the results of several ensembles because the signal is random in nature.

The basic method of implementing the power spectral density formula $G_{xx}(\omega) = S_x(j\omega)S_x^*(j\omega)$ digitally is as follows: 1) Take N samples of data, 2) Do a Fourier transform of the signals, 3) Multiply the Fourier transform of the signal by its complex conjugate (*), 4) Add this power spectrum, $(a_n^2 + b_n^2)$ to the previous sum of power spectra stored in a memory location, 5) Repeat desired number of times (N), 6) Divide sum of power spectra by the total number (N) and display results by selecting MAG^2 display control (Spectral Dynamics Corporation, 1975).

With this device, the signal processing for the power spectrum analysis of the hot-wire fluctuating signals is performed as follows. AC signals either directly from the DISA 55M anemometer or from the DISA 55D10 Linearlizer are entered and conditioned on Channel A through buffer amplifiers to phase-matched anti-aliasing lowpass filters. The signals are then sampled at 2.048 times the upper frequency of the range selected, using two synchronous analog-to-digital converters and then stored in two input buffer memories. The contents of these memories are transfered to the processor memory at intervals determined by the analysis rate selected. The data are then given Kaiser-Bessel weighting and processed according

to the Function 2(Forward Transform A(1024)). The results of the signal processing for the power spectrum analysis are stored in the output memory and then simultaneously displayed on the high speed oscilloscope and the low-speed XY-recorder through the output conditioner and control.

In any spectrum analysis where noise-like and narrow-band signals are present there is always a tradeoff between resolution and stability. Resolution is obviously desirable for an accurate measurement of line frequencies. This dictates small values of filter spacing and large values of sampling point which results in accurate frequency measurement of spectral lines but relatively inaccurate measurement of broadband spectral levels because the measurement variance of each frequency sample is large. On the other hand, stability is desirable for accurately measuring broadband spectral shapes. This dictates larger values of filter spacing, smaller sampling and more averaging over time or frequency for each frequency sample. Most spectrum analysis problems involve trading off between these two considerations to try to obtain the most information from a given set of data samples (Ackerman, 1974).

As mentioned previously, the square of the magnitude of a sampled signal is used as a basic power spectrum estimate. Since this spectral estimate has a large variance, some smoothing should be done. The Spectral Dynamics SD-360 FFT Digital Signal Processor has two built-in time domain window functions, i.e., multiplication of the time function by either a Kaiser-Bessel or a rectangular weighting function before taking the FFT. Throughout the present study the Kaiser-Bessel was exclusively employed. In Figure 13, two weightings are illustrated. It can be noted in Figure 13a that the rectangular window has a narrow main lob. The side lobes, however, are very large and roll off slowly. The

top of the main lob is quite rounded and can introduce large measurement errors. This window is only useful when an integer number of periods of the time waveform are included in the window. Otherwise, leakage is very severe. Figure 13b shows the Kaiser-Bessel window. This window uses a modified Bessel function of the zeroth order of the first kind. The Kaiser-Bessel window, while optimizing main-lob energy and reducing the energy in the side lobes, produces no side lobe greater than -72 dB from full scale.

There are five important parameters associated with data processing with the 3D-360. They are sampling rate (f_s), memory period (T), filter spacing (Δf), anti-aliasing filter cutoff frequency (f_c) and averaging. This device samples at a rate of f_s = 2.048 F samples/sec, where F denotes the analysis frequency range of the processor expressed as a convenient decimal value. The sampling rate and the analysis range are specified independently from the anti-aliasing filter cutoff frequency f_c. The memory period is the time it will take to fill the input buffer memory sampling at a rate equal to f_s. For a single length transform (1024 points) the memory period is given by T = 500/F sec. For spectrum analysis, the filter spacing is equal to the frequency range covered divided by the number of equally spaced frequency resolution points. For single length analysis (1024 points), the resolution is given by Δf = F/500 Hz. Anti-aliasing low pass filter which are dual and phase matched can either be automatically set to 80% of the selected frequency range or manually preset to 80% of any of the available 57 built-in frequency ranges. For a single-channel transform, these anti-aliasing filters can be cascaded to double the rolloff in dB/octave. The cutoff frequency is given by f_c = 0.80 F. For many applications, the processing results are

averaged to obtain signal-to-noise enhancement or to improve the statistical confidence in the results. The SD-360 performs a frequency analysis on any given sample of data with two degrees of freedom, $\eta = 2BT = 2(F/500)(500/F) = 2$. By averaging the spectral ensembles, the statistical degrees of freedom figure is increased by the number of independent samples averaged. The SD-360 allows the averaging of non-redundant data to be performed (one ensemble per memory period). Redundant data can also be averaged (2, 4 or maximum transform per memory period) to assure that all data is analyzed in the center portion of weighting function.

Throughout the present investigation, two modes of averaging were extensively used. One is the linear ensemble averaging. In this mode, up to 4096 (2^{12}) ensembles of frequency (time) data are linearly summed and displayed as the average of the sum. The display is always within 6 dB of the final, properly normalized value. The other mode of averaging is exponential. This is a form of digital filtering that produces a time-running average of the data. The effective time constant of the filter is given by NT, where N is the number of ensembles selected and T is the time between the start of two successive ensembles. As is known, the distribution of the power spectral density estimate about the true value follows a Chi-square distribution with the statistical confidence of the data estimate increasing as the number of ensembles increases. However, the improvement in the power spectral density estimate is a converging function of the number of ensembles included. A value of N between 2^7 (128) and 2^9 (512) is adequate (c.f., Instruction Manual of SD-360, Spectral Dynamics Corporation, 1975). The statistical errors associated with the spectrum analysis will be discussed in detail in Appendix A.

The XY-plotter calibration for spectrum analysis was made as follows. The plotter's Y-axis zero control was adjusted for a -80 dB point which corresponds to the calibration level of four on the p-switch setting provided on the front panel of the SD-360. For turbulence measurements 0.14 volt^2/Hz corresponds to 0 dB with 25 dB attenuation. Therefore, with the same attenuation 0.014 volt^2/Hz corresponds to -20 dB.

2.3.3 Overall sound pressure level and spectrum measurements in far field

The experimental setup and the schematic diagram of instrumentation for overall sound pressure level (OASPL) and 1/3 octave band spectrum measurements are illustrated in Figure 14. Most of the acoustical data were obtained using a horizontal array of eight microphones located on a semi-circle of radius 100 D, where D denotes the effective jet diameter.

Measurements of the 1/3 octave SPL spectrum in the frequency range 0.5 to 80 KHz were conducted at all angles to the jet axis equally spaced between 15° and 120°.

For each angular position jet velocity was varied in five steps from 136 to 309 m/sec. These measurements were undertaken for five nozzles of 12.7, 6.35, 3.18, 1.59 and 0.79 mm in diameter. The stagnation temperature in the settling chamber was assumed to be equal to the room temperature for these measurements. Throughout the entire acoustical measurements of the present survey the B&K 6.35 mm microphone (Type 4135) was exclusively used without a protecting grid because of its interference with high frequency sound generated by the smaller nozzles. During the preliminary testing, the B&K 3.18 mm microphone (Type 4138) was used to measure 1/3 octave spectra. However, its poor stability of response for long running periods precluded its further use in the present study. Before and after

each run, the eight microphones and amplifiers were carefully calibrated using a B&K pistonphone (Type 4220).

Because of significant background noise below 300 Hz, the incoming signals to the General Radio Multifilter (Type 1925) were attenuated, up to 12 dB in the frequency range less than 500 Hz.

During the preliminary testing, contamination of the incoming signal by reflection was carefully investigated and elminated by removing part of the supporting structure and covering the non-removable part of structure with acoustic foam. Due to the nonlinear frequency response of the 6.35 mm microphone (Type 4135) at frequencies above about 10 KHz, a proper correction must be made on the data. This correction can be easily made by selecting the appropriate value of attenuation for each frequency band on the General Radio Multifilter (Type 1925). An atmospheric absorption correction was also applied to the raw data. A Type 1921 Real-Time Analyzer (General Radio) was used to determine sound pressure level (SPL) spectra referenced to 2×10^{-5} N/m^2. The resulting SPL spectra were then corrected for the atmospheric attenuation and background noise in addition to the microphone correction. These corrected SPL spectra were then used to compute the overall sound pressure level.

The same analysis system was used for both turbulence and acoustic measurements and also for measurement of the correlation between turbulent velocity fluctuations and acoustic pressure. Figure 15 is a block diagram of the instrumentation and analysis setup for this measurement. Appropriate portions of the system were used for independent analysis of either the acoustic pressure field or the flow field.

2.3.4 Coherent output power measurements

Coherent output power (COP) is defined by

$$COP = \frac{|G_{xy}(f)|^2}{G_x(f)G_y(f)} \cdot G_y(f)$$

$$= \gamma^2 G_y(f)$$

Coherent output power is nothing more than the portion of the output power produced by a given input. In the definition of COP, $G_x(f)$ represents the power spectral density of the input signal, $G_y(f)$ denotes the power spectral density of the output signal and $G_{xy}(f)$ corresponds to the cross spectral density of the input and output signals. The coherence function between the input and output is represented by γ^2. Here we are concerned with what portion of the sound energy observed at a specified microphone location in the far field is contributed by the pressure (or velocity) fluctuations at a specified hot-wire location. In these correlation measurements, a B&K 6.35 mm microphone was located at R = 317.5 mm, $\hat{\theta} = 30°$ as shown in Figure 12. One may argue that the microphone is not positioned in the complete far-field because of its rather close location to the jet axis. Therefore, the results of these correlation measurements should be interpreted with caution. It also should be pointed out here that the hot-wire probe should be inclined to the jet axis so that the microphone and the hot-wire sensor are aligned. Seiner (1974), however, showed that in the mixing layer of a jet the measured values of shear noise coherency was almost independent of the orientation of the wire probe and that in the potential core the situation is similar except for Strouhal frequencies lower than 0.2. With this in mind, the hot-wire sensor portion was always oriented

vertically to the jet flow. The block diagram of the hot-wire and microphone cross-correlation measuring system is shown in Figure 15. Table 2 is a list of the experimental conditions under which COP measurements were undertaken. The coherent output power is expressed in terms of dB, with 0.1 volt peak voltage of a sinusoidal signal at 1000 Hz being taken as reference. This reference power was designated to be 0 dB.

2.3.5 Circumferential cross correlation measurements

In his paper, Fuchs (1973) reported the results of his circumferential space correlation measurements of the fluctuating pressures in turbulent jets. He first obtained the cross spectral density of the circumferentially cross correlated signals sampled in the mixing layer at three diameters downstream. He then expanded the real part of the cross spectral density (co-spectrum) in terms of a Fourier series with respect to the circumferential separation angle. Thus, he found that only a first few modes have any practical importance in Strouhal number range between 0.1 and 1.0. From this result he conjectured that a considerable amount of turbulent energy is contained in the lower order azimuthal components and, in particular, in the large scale coherent axisymmetric type of fluctuation. He pointed out that ". . . this confirms earlier experimental results by Crow and Champagne (1971), who showed how orderly structures develop in the turbulent region of an externally excited jet." With the motivation of Fuchs' experiments, it was decided to perform similar space correlation measurements in the sound field using two microphones one of which is circumferentially moved about the jet axis.

Figure 16 illustrates the experimental setup for the circumferential cross correlation measurements in the radiated field. Two B&K 6.35 mm microphones were located at 60 jet diameters away from the center of the jet exit plane with a 30° inclination from the jet axis. A microphone was rotated from 0° to 360° along a circle of radius 30 jet diameters which is vertical to the jet axis. At each 15° increment of azimuthal angle, the signals from the two microphones were cross correlated.

Every system, mechanical, electrical, etc. and every system component responds to an input forcing stimulus in a special way. The frequency response characteristics of the system is a unique repeatable parameter and is often referred to as a transfer function of the system. Ideally, a transfer function measurement is performed on two signals, one representing a unique system forcing function, the other representing the measured system's response. In the absence of any extraneous noise with no other responses, and if the system being analyzed is linear, the transfer function measurement should be excellent. However, since the basic cross spectrum measurement does not give a casuality relationship, it has been found useful to define a measurement qualifier. This parameter called the coherence function tries to identify how much of the measured cross spectrum is related to the measured input and output power spectra (Bendat and Piersol, 1971; Spectral Dynamics Corporation, 1975).

The coherence function is defined by

$$\gamma^2(f) = \frac{|G_{xy}(f)|^2}{G_x(f)G_y(f)} \quad , \; 0 \leq \gamma^2 \leq 1$$

and has a real value, where $G_x(f)$, $G_y(f)$ and $G_{xy}(f)$ are the power spectral density of input, the power spectral density of output and the cross spectral density between input and output, respectively.

Evidently, if and only if, the input x(t) and the output y(t) are completely correlated, the coherency is perfect, namely $\gamma^2(f) = 1$. The other extremity is the case when x(f) and y(t) are not correlated at all. Then $\gamma^2(f)$ should be zero. As is known $\gamma^2(f)$ represents the fractional portion of the output energy of a linear system which is contributed by the input signal at a specified frequency.

The numerator of the $\gamma^2(f)$ represents the square value of the cross spectral density which is generally a complex quantity. However, if there is no phase shift between x(f) and y(f), then $G_{xy}(f)$ now reduces to the co-spectrum (real part) of the cross spectral density. A block diagram of the instrumentation for the coherence function analysis is shown in Figure 17. Table 3 contains the experimental conditions for the determination of coherence function. The error estimate for the measured coherence functions will be discussed in Appendix A.

Before any correlation measurements can be made, it is first necessary to determine whether or not there is any phase lag between the two microphones. This was achieved with the aid of the SD-360 FFT analyzer. With the Function 5 (cross spectrum) setting on SD-360 and introducing a white noise signal in the frequency range 800 Hz $\leq f \leq$ 40 KHz, a plot of the phase lag versus frequency could be made. The maximum phase lag was found to be 3° in the frequency range of interest and could be ignored for all practical purposes.

Chapter III

REVIEW OF THEORIES

In this chapter, the spectral theory of Michalke (1970a) is first reviewed. This is followed by discussion of a method for single azimuth-frequency components of jet noise developed by Chan (1974b).

It is known that the intensity of jet noise observed in the far field can be computed if we are given the correlation function of the Lighthill stress tensor. This correlation function is determined by introducing a suitable model of jet turbulence based on certain assumptions into the formulation of the stress tensor. This method has been successful in predicting the overall characteristics of jet noise, i.e., the overall sound pressure level dependence on Mach number and the overall directivity. However, the method based on overall correlation does not provide enough information to reveal the spectral characteristics of the sound generation mechanism. It has been pointed out that different jets have different directivity patterns for the same frequency bands. To fully understand this fact, we have to deal with the physical quantities involved in the frequency domain. Stated another way, the spectral method based on Fourier transformation with respect to time should be introduced to the study of radiation of single frequency components.

One of the well-known spectral theories is that of Pao and Lowson (1969). They partly succeeded in predicting the directivities of the radiated sound based on the assumption of isotropic turbulence. However, to predict the characteristics of single azimuth-frequency components of jet noise, Pao and Lownson's theory is not adequate. Thus, the spectral

theory of Michalke which was formulated on an entirely different basis will be discussed with its application to this study in mind.

3.1 The Spectral Theory of Michalke

Consider first the acoustic analogy approach introduced by Lighthill (1952). We consider a fluid in which only a finite region contains a unsteady flow. Far away from that region, the fluid is assumed to be uniform with density ρ_o and sound speed a_o and to be at rest apart from the small motions induced by the passage of sound waves generated by the unsteady flow.

Assuming no external sources of mass and no external forces acting on the fluid, the continuity and momentum equations can be written as

$$\frac{\partial \rho}{\partial t} + \frac{\partial}{\partial x_j} \rho u_j = 0 \tag{3.1.1}$$

$$\rho\left(\frac{\partial u_i}{\partial t} + u_j \frac{\partial}{\partial x_j} u_i\right) = - \frac{\partial p}{\partial x_i} + \frac{\partial e_{ij}}{\partial x_j} \tag{3.1.2}$$

where e_{ij} is the viscous stress tensor. For a Newtonian fluid,

$$e_{ij} = \mu\left(\frac{\partial u_i}{\partial x_j} + \frac{\partial u_j}{\partial x_i} - \frac{2}{3} \frac{\partial u_k}{\partial x_k} \delta_{ij}\right) \tag{3.1.3}$$

where μ is the coefficient of viscosity.

Combining Eq. 3.1.1 and Eq. 3.1.2, after Eq. 3.1.1 being multiplied by u_i, we obtain

$$\frac{\partial}{\partial t} \rho u_i + \frac{\partial}{\partial x_j}(\rho u_i u_j + \delta_{ij} p - e_{ij}) = 0$$

which upon adding and substracting $a_o^2(\partial \rho / \partial x_i)$ yields

$$\frac{\partial}{\partial t} \rho u_i + a_o^2 \frac{\partial \rho}{\partial x_i} = - \frac{\partial}{\partial x_i} T_{ij} \tag{3.1.4}$$

where

$$T_{ij} = \rho u_i u_j + \{(p - p_o) - a_o^2(\rho - \rho_o)\}\delta_{ij} - e_{ij} \qquad (3.1.5)$$

Eliminating ρu_i between Eq. 3.1.1 and Eq. 3.1.4, we finally have Lighthill's equation

$$\{\frac{\partial^2}{\partial t^2} - a_o^2\nabla^2\}\rho' = \frac{\partial^2}{\partial x_i \partial x_j} T_{ij} \qquad (3.1.6)$$

where $\rho' = \rho - \rho_o$.

By the same procedure, we can obtain the Lighthill equation in terms of the fluctuating pressure p, given as

$$\{\frac{1}{a_o^2}\frac{\partial}{\partial t^2} - \nabla^2\}p = q(x_i,t) \qquad (3.1.7)$$

where

$$q(x_i,t) = \frac{\partial}{\partial x_i \partial x_j}(\rho u_i u_j - e_{ij}) + \frac{1}{a_o^2}\frac{\partial^2}{\partial t^2}(p - a_o^2\rho) \quad . \qquad (3.1.8)$$

In the following derivation, the fluctuating pressure p is exclusively considered.

Throughout this section we strictly limit our discussion to the circular subsonic cold jet.

To locate source points in the circular jet the cylindrical coordinate system is adopted and the far field observation point where the fluctuating pressure is measured is denoted by spherical coordinates. The coordinate systems are shown in Figure 18.

The integral solution of Eq. 3.1.7 is given by

$$p(\hat{r},\hat{\theta},\hat{\phi},t) = \frac{1}{4\pi}\iiint_V q(x,r,\phi,t - \frac{r_o}{a_o})\frac{r}{r_o}\, d\phi dr dx \qquad (3.1.9)$$

where r_o is the distance between the source point in the jet and the observation point in the far field and is given by

$$r_o^2 = \hat{r}^2 - 2x\hat{r}\cos\hat{\theta} - 2r\hat{r}\sin\hat{\theta}\cos(\phi - \hat{\phi}) + x^2 + r^2 \quad (3.1.10)$$

Here a_o is the sound speed of the undisturbed medium.

As is known, the extent of the jet noise source region is very limited both in downstream and cross-stream directions. Then, the limits of the integral of Eq. 3.1.9 are

$$\text{downstream direction:} \quad 0 \leq x \leq L$$

$$\text{cross-stream direction:} \quad 0 \leq r \leq \hat{R}$$

$$\text{circumferential direction:} \quad 0 \leq \phi \leq 2\pi \ .$$

Outside of this region $q(x,r,\phi,t - (r_o/a_o))$ is assumed to be zero.

In axisymmetric jets, the noise source or the instantaneous pressure fluctuations have periodicity with respect to the circumferential angle ϕ. Hence, the source term in Eq. 3.1.9 can be properly expanded in a Fourier series of ϕ with the period 2π.

For convenience the complex form of Fourier series is chosen;

$$q(x,r,\phi,t) = \sum_{m=o}^{\infty}\{q_m(x,r,t)e^{jm\phi} + q_m^*(x,r,t)\overline{e^{jm\phi}}\} \quad (3.1.11)$$

The complex conjugate of q_m is denoted by q_m^* and m can take any integer value from zero to infinity.

Since the rms value of $q(x,r,\phi,t)$ has to be independent of ϕ, the following assumptions can be made.

$$\overline{q_m} \equiv \lim_{T\to\infty} \frac{1}{T}\int_{t_o}^{t_o+T} q_m(x,r,t)dt = 0$$

for any azimuthal wave number m and

$$\overline{q_m q_n} \equiv \lim_{T\to\infty} \frac{1}{T}\int_{t_o}^{t_o+T} q_m(x,r,t)q_n(x,r,t)dt = 0 \text{ for } m \neq n \ .$$

The source term q is a function of r. When r approaches to zero, q has to be finite. Then, the order of q_m in Eq. 3.1.10 with respect to r

can be shown to be $O[r^m]$. The next step is to expand the pressure fluctuation of Eq. 3.1.9 in a Fourier series with respect to ϕ. The feasibility of this expansion is evident. Using the same notation as those found in Eq. 3.1.10, we obtain

$$p(\hat{r},\hat{\theta},\hat{\phi},t) = \sum_{m=o}^{\infty}\{p_m(\hat{r},\hat{\theta},t)e^{jm\hat{\phi}} + p_m^*(\hat{r},\hat{\theta},t)e^{-jm\hat{\phi}}\} \qquad (3.1.12)$$

Substitution of Eq. 3.1.10 and Eq. 3.1.11 into Eq. 3.1.9 yields

$$p_m(\hat{r},\hat{\theta},t) = \frac{1}{4\pi}\iiint_V \frac{r}{r_o} q_m(x,r,t - \frac{r_o}{a_o})e^{jm(\phi-\hat{\phi})}dxdrd(\phi - \hat{\phi}) \qquad (3.1.13)$$

where $p_m(\hat{r}.\hat{\theta}.t)$ is the mth azimuthal component of the instantaneous pressure observed in the far field.

Next, it is necessary to transfer from the time domain to the frequency domain in order to consider single azimuth-frequency components. This can be achieved by taking a Fourier transform of p_m and q_m in Eq. 3.1.12 with respect to time t:

$$P_m(\hat{r},\hat{\theta},\omega) = \int_{-\infty}^{\infty} p_m(\hat{r},\hat{\theta},t)e^{j\omega t}dt \qquad (3.1.14)$$

$$Q_m(x,r,\omega) = \int_{-\infty}^{\infty} q_m(x,r,t - \frac{r_o}{a_o})e^{j(\omega t - kr_o)}dt \qquad (3.1.15)$$

where k is the wave number of sound defined by ω/a_o. Eliminating p_m and q_m from Eq. 3.1.12, Eq. 3.1.13 and Eq. 3.1.14, we have

$$P_m(\hat{r},\hat{\theta},\omega) = \frac{1}{4\pi}\int_o^L\int_o^R\int_o^{2\pi} \frac{r}{r_o} e^{j\{kr_o + m(\phi-\hat{\phi})\}} Q_m(x,r,\omega)dxdrd(\phi - \hat{\phi}) \qquad (3.1.16)$$

where r_o is given by Eq. 3.1.10.

At this point the far field approximation is introduced. Eq. 3.1.10 can be written as

$$r_o^2 = \hat{r}^2\{1 - \frac{x}{\hat{r}}(2\cos\hat{\theta}) - \frac{r}{\hat{r}}(2\sin\hat{\theta}\cos(\phi - \hat{\phi})) + \frac{x^2 + r^2}{\hat{r}^2}\} .$$

Expanding r_o in a Taylor series with respect to r yields

$$r_o = \hat{r}\{1 - \frac{x}{\hat{r}}\cos\hat{\theta} - \frac{r}{\hat{r}}\sin\hat{\theta}\cos(\phi - \hat{\phi}) + O(\frac{1}{\hat{r}^2}) + \ldots\}$$

where $O(1/\hat{r}^2)$ represents terms of order of $1/\hat{r}^2$. If we assume $L << \hat{r}$ and $\hat{R} << \hat{r}$, then we have an approximation for r_o as

$$r_o = \hat{r} - x\cos\hat{\theta} - r\sin\theta\cos(\phi - \hat{\phi}) \qquad (3.1.17)$$

Substituting Eq. 3.1.17 into Eq. 3.1.16, we have the following result with respect to the integral of $(\phi - \hat{\phi})$ as

$$\int_o^{2\pi} \frac{1}{r_o} e^{j\{kr_o + m(\phi - \hat{\phi})\}} d(\phi - \hat{\phi}) =$$

$$= \int_o^{2\pi} \frac{e^{jk(\hat{r} - x\cos\hat{\theta})} e^{-j\{kr\sin\hat{\theta}\cos(\phi - \hat{\phi}) - m(\phi - \hat{\phi})\}}}{\hat{r} - x\cos\hat{\theta} - r\sin\hat{\theta}\cos(\phi - \hat{\phi})} d(\phi - \hat{\phi})$$

$$= \frac{1}{\hat{r}} e^{jk(\hat{r} - x\cos\hat{\theta})} \int_o^{2\pi} e^{-j\{kr\sin\hat{\theta}\cos(\phi - \hat{\phi}) - m(\phi - \hat{\phi})\}} d(\phi - \hat{\phi}) \qquad (3.1.18)$$

where we evaluate $\hat{r}$ to $O(1/\hat{r})$.

The integral of the right-hand side of Eq. 3.1.18 can be expressed in terms of Bessel function of the first kind and mth order. From formula 8.411.1 of Gradshteyn and Ryzhik (1965), we have

$$J_n(Z) = \frac{1}{2\pi}\int_{-\pi}^{\pi} e^{-j(n\theta - z\sin\theta)} d\theta$$

where n is natural number. The right-hand side of Eq. 3.1.18 can then be simplified to

$$\int_o^{2\pi} \frac{1}{r_o} e^{j\{kr_o + m(\phi - \hat{\phi})\}} d(\phi - \hat{\phi}) = \frac{2\pi}{j^m \hat{r}} e^{jk(\hat{r} - x\cos\hat{\theta})} J_m(kr\sin\hat{\theta}) \qquad (3.1.19)$$

By substituting Eq. 3.1.19 into Eq. 3.1.16, a single azimuth-frequency component of the sound pressure observed in the far field is obtained.

$$P_m(\hat{r},\hat{\theta},\omega) = \frac{e^{jkr}}{2j^m\hat{r}} \int_o^L \int_o^R rJ_m(kr\sin\hat{\theta}) \left| Q_m(x,r,\omega) \right| e^{j\{\psi_m(x,r,\omega) - kx\cos\hat{\theta}\}} dx dr \qquad (3.1.20)$$

where we have adopted an alternative form for $Q_m(x,r,\omega)$ of Eq. 3.1.15 as

$$Q_m(x,r,\omega) = |Q_m(x,r,\omega)|e^{j\psi_m(x,r,\omega)} \tag{3.1.21}$$

If the power spectral density of sound observed at $\hat{r} >> k^{-1}$ is denoted by $P(\omega)$, then we have

$$|P(\omega)|^2 = \sum_{m=o}^{\infty} |P_m(\hat{r},\hat{\theta},\omega)|^2$$
$$= \sum_{m=o}^{\infty} \frac{1}{4\hat{r}^2} \left| \int_o^L \int_o^R r J_m(kr\sin\hat{\theta}) |Q_m(x,r,\omega)| e^{j\{\psi_m(x,r,\omega) - kx\cos\hat{\theta}\}} dr dx \right|^2 \tag{3.1.22}$$

Practically, $|P(\omega)|^2$ can be approximated by the measured narrow band power spectral density of sound pressure.

In the derivation of Eq. 3.1.20 no specification has been made with respect to the structure of the source region except for axisymmetry. Nevertheless, we can derive some useful characteristics of jet noise generated by an axisymmetric turbulent jet from Eq. 3.1.20.

A single azimuth-frequency components of sound power spectral density given by Eq. 3.1.20 is characterized by two essential functions, i.e., $J_m(kr\sin\hat{\theta})$ and $\exp\{j\psi_m(x,r,\omega) - jkx\cos\hat{\theta}\}$.

The Bessel function of the first kind and the mth order is mainly responsible for the directivity of radiated sound. The magnitude of this function is determined by wave number m and jet thickness parameter which is defined by

$$\text{jet thickness parameter} \equiv k\hat{R}\sin\hat{\theta} \quad . \tag{3.1.23}$$

It is known that for $m >> 1$ and $x << m$ the Bessel function of the first kind can be expressed as

$$J_m(x) = \frac{1}{m!}\left(\frac{x}{2}\right)^m \left\{1 - \frac{1}{m+1}\left(\frac{x}{2}\right)^2 + \ldots\right\} ,$$

and for $m = 0$ and $x << 1$ we have

$$J_o(x) = 1 - (\frac{x}{2})^2 + \ldots$$

Hence, for small arguments $kr \sin\hat{\theta}$

$$J_m(kr \sin\hat{\theta}) = \frac{1}{m!}(\frac{kr \sin\hat{\theta}}{2})^m\{1 - \frac{1}{m+1}(\frac{kr \sin\hat{\theta}}{2})^2 + \ldots\}$$

$$= \frac{1}{m!}(k\hat{R} \sin\hat{\theta})^m(\frac{r}{2\hat{R}})^m\{1 - \frac{1}{m+1}(k\hat{R} \sin\hat{\theta})^2(\frac{r}{2\hat{R}})^2 + \ldots\}$$

where

$$k\hat{R} = \frac{2\pi\hat{R}}{\lambda} = \frac{2\pi\hat{R}}{(a_o/f)} = (\frac{f\hat{R}}{U})(\frac{U}{a_o}) = (Sh)(M) \quad . \qquad (3.1.24)$$

$k\hat{R}$ is nothing more than the product of Strouhal number (based on jet exit velocity U_j and lateral source extent $\hat{R}$) and flow Mach number.

As shown in Figure 19, $m = 0$ is dominant where the argument of $J_m(x)$ is small. Hence, for $k\hat{R} \sin\hat{\theta} << 1$ the power spectral density $|P(\omega)|^2$ is mainly a function of the axisymmetric component. At increasing values $k\hat{R} \sin\hat{\theta}$, the contribution from the axisymmetric component is less dominant. Since the jet thickness parameter is the ratio of the lateral source extent to sound wavelength, the non-axisymmetric component will be important when $\hat{R}$ and λ in Eq. 3.1.24 are comparable. As an illustration let us consider a jet of $D = 12.7$ mm. The space-averaged lateral source extent is assumed to be $\hat{R} = 2D$.

At $\hat{\theta} = 30°$ we have

$$k\hat{R} \sin\hat{\theta} = \frac{2\pi\hat{R}}{\lambda} \sin\hat{\theta} = \frac{4\pi D}{\lambda} \sin 30° = \frac{2\pi D}{\lambda} \quad .$$

Substituting $D = 12.7$ mm and $a_o = 344$ m/sec into the right-hand side of the jet thickness formula, we have λ and f for $k\hat{R} \sin\hat{\theta} = 1$ as

$$\lambda = 2\pi D \simeq 80 \text{ mm} \quad , \quad f = \frac{a_o}{\lambda} \simeq 4.3 \text{ KHz} \quad .$$

Hence, that portion of the sound signal below about 4 KHz is mostly due to the axisymmetric component for a fixed value of $|Q_m(x,r,\omega)|$. The example was intentionally chosen from the experimental work of the present study, and the result obtained here was experimentally verified as discussed in Chapter IV.

One more important feature of $J_m(k\hat{R}\sin\hat{\theta})$ should be mentioned. As is evident from Figure 19, $J_m(k\hat{R}\sin\hat{\theta})$ becomes zero at $\hat{\theta} = 0°$ and $180°$ for $m \neq 0$. This means that only the axisymmetric component is radiated in the jet axis direction. Note that the directivity pattern of the radiated sound is different for each value of m.

The term $\exp\{j\psi_m(x,r,\omega) - jkx\cos\hat{\theta}\}$ represents the effect of convection on the radiated sound. To fully undertand the convection effect, the phase function $\psi_m(x,r,\omega)$ defined by Eq. 3.1.21, must be known. Note from Eq. 3.1.21 that the phase function should be positive for turbulence convection in the flow direction. At a fixed frequency, the value of $(\psi_m - kx\cos\hat{\theta})$ is an increasing function of $\hat{\theta}$, and this results in a reducing influence on the radiation of sound as will be shown in the latter section. Hence, we can say that the convection effect is intensified in the flow direction $\hat{\theta} = 0°$ where $(\psi_m - kx\cos\hat{\theta})$ has a minimum value. As is known, the convection effect depends upon the convection Mach number which is a function of Strouhal number based on jet diameter, jet exit velocity and turbulence frequency. Therefore, for further discussion of the convection effect a suitable model of jet turbulence needs to be introduced.

In recent years, there has been growing evidence that large scale coherent structures contribute significantly to aerodynamic noise. The experimental findings by Mollo-Christensen (1967); Lau, Fuchs and Fisher

(1970); Crow and Champagne (1971) and Chan (1976) suggest that large-scale organized structures can be represented by wave packets with characteristics derived from linear stability theory. This representation infers a similarity between the turbulence structure and those motions in the laminar flow which leads to transition.

Hence, it is reasonable to assume that each azimuth-frequency component of turbulence is wave-like in the jet flow direction and each source term is given by

$$Q_m(x,r,\omega) = \hat{Q}_m(x,r)e^{j\alpha x} \tag{3.1.25}$$

where α is the axial wave number of the turbulent component and can be a function of Mach number, frequency, azimuthal mode and radial coordinate, but is assumed to be independent of x.

Substituting Eq. 3.1.25 into Eq. 3.1.22, we have

$$|P(\omega)|^2 = \sum_{m=o}^{\infty} \frac{1}{4\hat{r}^2}\left|\int_o^L\int_o^R rJ_m(k\hat{R}\sin\hat{\theta}\frac{r}{R})\hat{Q}_m(x,r)e^{j\alpha L(1-M_c\cos\hat{\theta})\frac{x}{L}}dxdr\right|^2 \tag{3.1.26}$$

where Eq. 3.1.16 was taken into account. In Eq. 3.1.26, we have two new parameters. One is the convection Mach number, M_c, and is defined as the ratio of the axial velocity to sound speed as given by

$$M_c = \frac{k}{\alpha} = \frac{(\omega/\alpha)}{a_o} = \frac{C_{ph}}{a_o} \tag{3.1.27}$$

Another new parameter is the axial (longitudinal) extent of source distribution in the jet turbulence and is denoted by L. The argument of the exponent in Eq. 3.1.27, i.e., $\alpha L(1 - M_c\cos\hat{\theta})$ is referred to as the convection parameter. As will be shown, a nonzero value of the convection parameter always causes reduction of the magnitude of $|P(\omega)|^2$ for $M_c < 1$.

However, at $M_c > 1$ and when $\hat{\theta}$ satisfies

$$\hat{\theta}_c = \cos^{-1}\frac{1}{M_c} \tag{3.1.28}$$

there is no interference of sound sources at different longitudinal locations. Thus, the most intense radiation is observed at $\hat{\theta} = \hat{\theta}_c$.

The jet thickness parameter and the convection parameter are two major factors which strongly affect the directivity of radiated sound. The jet thickness parameter $k\hat{R}\sin\hat{\theta}$ determines the magnitude of the Bessel function illustrated in Figure 19. From experimental results it is known that for Strouhal number between 0.1 and 1.0, the values of the lateral source distribution extent $\hat{R}$ falls in the ranges of $D \leq \hat{R} \leq 8D$. As pointed out previously, the jet thickness parameter is the ratio of $\hat{R}$ to sound wavelength and is given by

$$k\hat{R} = \frac{2\pi\hat{R}}{\lambda} = \frac{2\pi f}{a_o}\hat{R} = 2\pi\left(\frac{fD}{a_o}\frac{a_o}{U}\right)\left(\frac{U}{a_o}\right)\left(\frac{\hat{R}}{D}\right) = 2\pi\left(\frac{\hat{R}}{D}\right)(M)(Sh) \quad .$$

Hence, for $M = 0.58$, for example, and $0.1 \leq Sh \leq 1.0$ we have

$$2.9 \leq k\hat{R} \leq 3.6 \quad .$$

This is at least twice as large as that assumed by Michalke and Fuchs (1973). He assumed that the jet diameter is roughly twice the radius $\hat{R}$ of the source region and obtained the value of $k\hat{R}$ being smaller than 1.4 for $Sh < 0.5$ and $M < 0.9$. If we calculate the value of $k\hat{R}\sin\theta$ with his assumed value of $(\hat{R}/D)$ for $M = 0.58$, $\hat{\theta} = 30°$ and $Sh = 1.0$, we obtain $k\hat{R}\sin\hat{\theta} \simeq 0.9$. Evidently, from Figure 19, the mode $m = 0$ is dominant for this argument. However, the experimental results of this investigation show that under the same conditions cited above, the contribution to power spectral density of the radiated sound by the axisymmetric component is less than that by the first non-axisymmetric component ($m = 1$). This indicates that the lateral extent of source distribution in jet turbulence is larger than that assumed by Michalke.

It should be mentioned, therefore, that very careful determination of the value of $\hat{R}$ is essential to the accurate prediction of the sound field.

The convection parameter $\alpha L(1 - M_c \cos\hat{\theta})$ is another important factor in the determination of the directivity of radiated sound. The results of Chan's forced jet measurements (1976) indicate that the value of αL is in the range of 20 and 40 for $0.1 \leq Sh \leq 1.0$ and that larger values of αL corresponds to larger Strouhal number. Here again, we see that the values of αL adopted by Michalke and Fuchs (1973) are too small. According to Fuchs (1974) αL falls in the range of 5 and 50, and this is consistent with Chan's observation.

By using the experimentally determined source function $\hat{Q}_m(x,r)$ in Eq. 3.1.26, the directivity of sound pressure level can be calculated. The results for the axisymmetric and the first helical modes are shown in Figures 20a and 20b, respectively.

In the case of the axisymmetric mode, as shown in Figure 20b, the sound pressure level of the single frequency component has a maximum at $\hat{\theta} = 0°$ for lower frequency ($Sh = 0.2$) and gradually decreases with $\hat{\theta}$. This indicates that lower frequency components are mainly radiated in the downstream direction. This has been experimentally confirmed by many researchers. At higher frequencies the sound pressure level drastically decreases with $\hat{\theta}$ and has a dip between 45° and 90° and then recovers to higher value with further increase of $\hat{\theta}$. Comparing Figures 20a and 20b, we can note that the directivity patterns produced by an axisymmetric source component and that produced by the first azimuthal source component are entirely different. For the $m = 0$ mode a maximum of sound pressure occurs at $\hat{\theta} = 0°$, wheras, for $m = 1$ mode the sound pressure has zero value

at $\hat{\theta} = 0°$ because $J_1(k\hat{R} \sin 0°) = 0$. At low frequencies, the m = 0 mode is dominant at small angles of $\hat{\theta}$. However, at larger values of $\hat{\theta}$, the first non-axisymmetric sound component (m = 1) becomes prominent. As shown in Figure 20a, we have again different directivity patterns at different Strouhal numbers. Higher frequency sound has a peak value at approximately $\hat{\theta} = 40°$ (see Figure 21). This behavior has particular significance as will be discussed in Chapter IV. It is interesting to note that the directivity patterns shown in Figures 20a and 20b are based on a source distribution function $\hat{Q}_m(x,r)$ which is quite different from that used by Michalke (1973). Nevertheless, the resulting directivity patterns are very similar. Michalke used a suitably chosen distribution function $\hat{Q}_m(x,r) = \hat{F}_m(x)\hat{G}(r)$ which, in his calculation was assumed to be independent of m and ω. He also chose the values for αL and $k\hat{R}$ rather arbitrarily without taking into consideration their relationship with Strouhal number.

In the present study, the source distribution functions $\hat{Q}_m(x,r)$ from which the directivity was calculated were determined strictly on the basis of observations. In this formulation, $\hat{Q}_m(x,r)$ is not assumed to be independent of m and ω. Chan's experimental results (1976) show that both the longitudinal and the lateral source extents in the jet turbulence are functions of the azimuthal wave number and Strouhal number. This fact was taken into consideration in the calculation of directivity shown in Figure 20a and 20b.

3.2 Chan's Jet Noise Prediction Method

As discussed in the previous section, once the source term in Michalke's wave model is known, the intensity of the radiated sound due

to a single azimuth-frequency component of the noise source can be readily evaluated by Eq. 3.1.26. Chan (1974a) proposed that this source term can be written in terms of the fluctuating pressure according to the dilation theory of Ribner (1962). Furthermore, the experimental results obtained by Chan (1974b) for the instability pressure waves in an acoustically excited jet can be used to compute a proper form for the source function.

3.2.1 Ribner's dilation theory

As is known, for small disturbances generated in a fluid at rest, $-\rho(\partial u/\partial t) = \partial p/\partial x$ is satisfied. This means that the inertial forces will give rise to pressure gradients. Consequently, in a turbulent flow, the local static pressure will have a different value at a different location. We note that since the fluid is compressible this variance of the local static pressure must be accompanied by the local change of the density. Stated another way, local volume dilations which are inverse of the local density variations are associated with the fluid accelerations. These local volume dilations can be regarded as pulsating spheres which are effective sound generators.

We may, for an acoustical treatment of jet turbulence, replace the extent-limited turbulent flow by an equivalent acoustic medium at rest which includes the local volume dilations. The time rate of the mass flow rate per unit volume, i.e., $(\partial m/\partial t)$ can effectively generate sound in fluid. In the medium considered above, m is related to the dilation rate, which is equal to $-(1/\bar{\rho})(\partial p/\partial t)$ and $\bar{\rho}$ represents the loca mean density. Thus, we have an effective source strength described as

$$\frac{\partial m}{\partial t} = -\frac{\partial^2 \rho(0)}{\partial t^2} \simeq -\frac{1}{a_o^2}\frac{\partial^2 p(0)}{\partial t^2}, \qquad (3.2.1)$$

where for density and pressure fluctuations that part associated with sound propagation is excluded, and the remainder are designated $\rho^{(0)}$ and $p^{(0)}$, respectively. Eq. 3.2.1 shows a relationship between $p^{(0)}$, which is often referred to as the pseudosound pressure that produces the effective dilations and the effective acoustic source strength. In contrast to sound pressure the pseudosound $p^{(0)}$ is dominated by inertial rather than compressible effects and has a spatial decay which is proportional to the cubic of distance.

3.2.2 Prediction formula

The power spectral density of jet noise due to a single azimuthal component of noise source is given from Eq. 3.1.26 as

$$P_m(\omega) = \frac{1}{2\hat{r}}\int_0^L\int_0^R rJ_m(k\hat{R}\sin\hat{\theta}\frac{r}{\hat{R}})\hat{Q}_m(x,r)e^{j\alpha L(1-M_c\cos\hat{\theta})\frac{x}{L}}dxdr \qquad (3.2.2)$$

This expression was derived on the basis of a wave-like model of jet turbulence. To evaluate this integral the source term $\hat{Q}_m(x,r)$ which first appeared in Eq. 3.1.25 has to be known. One of the practical ways to achieve this is to express this quantity in terms of the fluctuating pressure. For this purpose, Chan (1974a) introduced the dilation theory discussed in the previous section. The left-hand-side of Eq. 3.2.1 represents an effective source strength embedded in the turbulent flow, and the Fourier transform of this term must be equal to $\hat{Q}_m(x,r)$.

Hence, we have

$$\hat{Q}_m(x,r) = \text{Fourier transform of } \left(\frac{1}{a_o^2}\frac{\partial^2 p^{(0)}}{\partial t^2}\right)$$

$$= -k^2 P_m^{(0)}(x,r) \quad , \qquad (3.2.3)$$

where $k = \omega/a_o$ represents the wave number of the sound of angular frequency ω. If we assume that the pressure source $P_m^{(0)}(x,r)$ can be separated into single variable functions as

$$P_m^{(0)}(x,r) = F(x)G(r) \quad , \tag{3.2.4}$$

where $F(x)$ and $G(r)$ are the longitudinal and the lateral source distribution functions, respectively, then Eq. 3.2.2 can be modified as follows:

$$P_m(\omega) = \frac{k^2\hat{R}^2L}{2\hat{r}} \int_o^1\int_o^1 I_x I_r \hat{F}(\bar{x})\hat{G}(\bar{r})\bar{r}d\bar{r}d\bar{x} \quad , \tag{3.2.5}$$

where

$$I_x = \frac{\int_o^1 \hat{F}(\bar{x})e^{j\alpha L(1-M_c\cos\hat{\theta})\bar{x}}d\bar{x}}{\int_o^1 \hat{F}(\bar{x})d\bar{x}} \tag{3.2.6}$$

$$I_r = \frac{\int_o^1 \hat{G}(\bar{r})\bar{r}J_m(k\hat{R}\sin\hat{\theta}\cdot\bar{r})d\bar{r}}{\int_o^1 \hat{G}(\bar{r})\bar{r}d\bar{r}} \tag{3.2.7}$$

and

$$\bar{x} = x/L \ , \quad \bar{r} = r/\hat{R} \ , \quad \hat{F}(\bar{x}) = F(\bar{x})/F_{max}(\bar{x})$$

$$\hat{G}(\bar{r}) = G(\bar{r})/G_{max}(\bar{r}) \quad .$$

The axial extent of the source region in the flow L, and the lateral extent of source region $\hat{R}$ are used to normalize the variables x and r, respectively. The two source distribution functions are also normalized by their maximum values, $F_{max}(\bar{x})$ and $G_{max}(\bar{r})$.

To evaluate the expression 3.2.5 at a given observation point $(\hat{r},\hat{\theta})$ and at specified frequency ω, it is necessary to know two source functions,

i.e., $\hat{F}(\bar{x})$, $\hat{G}(\bar{r})$ and four parameters, i.e., $\hat{R}$, L, α and M_c. It is a rather simple task to compute the expression 3.2.5 numerically, given the necessary information about these parameters. The next subsection is devoted to a discussion of the experimental determination of these parameters in an acoustically forced jet.

3.2.3 Pressure wave measurements in acoustically excited jets

Direct measurement of the axisymmetric and helical waves in the turbulent shear layer of a jet was carried out by Chan (1976) at the National Aeronautical Establishment, Ottawa, Canada. The prediction of the directivity of narrow band jet noise in this study is entirely based on his experimental results. Similar instability wave measurements were made during this investigation, but in a quite different way, as will be discussed in Appendix B.

Chan used six equally spaced acoustic drivers mounted circumferentially around the jet exit plane of a 57 mm diameter jet in order to provide periodic forcing at the jet boundary. Each unit consisted of a 40 watt loudspeaker driver and a converging duct. The phase and amplitude of each driver could be adjusted independently so that the whole system could provide any mode of acoustic excitation in the jet flow. The exciting amplitude of the drivers was adjusted to 124 dB (ref: $20\mu N/m^2$) at the duct exit. Two microphones were mounted circumferentially 180° apart within the jet at a distance of one nozzle radius from the centerline. The microphones could be located at various axial positions. Each microphone was equipped with the standard B&K bullet noise fairing for flow measurements. The signals from each of the two microphones were fed into two slave filters. The filtered signals then drove the vertical

displacement of an oscilloscope. At the required phase, determined by the axial position of the microphones the oscilloscope intensity modulation was triggered by timing spikes from a pulse generator. The pulse generator was driven by the same beat frequency oscillator that provided the input to the acoustic drivers. A traversing position potentiometer indicated the horizontal displacement of the microphones on the x-axis of the oscilloscope. Thus, the intensified trace displayed on the oscilloscope represents the spatial change of the pressure signals at a fixed time. This experimental setup permitted the determination of the wave number versus Strouhal number relationship and the lateral and longitudinal source extent. This also permitted the determination of the longitudinal and lateral distributions of the amplitude of the pressure waves for different Strouhal numbers for the first three azimuthal modes. The results are illustrated in Figure 22. Figure 22a shows the relationship between the total wave number and Strouhal number based on excitation frequency. The total wave number for each mode is given by

$$\frac{kD}{2} = [m^2 + (\frac{\alpha D}{2})^2]^{1/2}$$

where m is the mode number and α is the axial wave number for each given mode as measured by the forcing technique described above. The data clearly show a linear relationship between normalized wave number and Strouhal number.

Non-dimensionalized phase velocities of the waves are presented in Figure 22b as a function of Strouhal number. It is interesting to note that, in contrast to the helical modes the phase velocity of the axisymmetric mode tends to decrease with increasing Strouhal number. Furthermore, at high frequencies the phase velocity seems to be independent of the azimuthal mode and to have a limiting value of about 0.55.

Figure 22C includes the axial source distribution functions for the first three modes, m = 0, 1 and 2. These curves were replotted from Chan's original curves. Note that the abscissa is a normalized distance $x \cdot Sh/D\ell$ where ℓ represents the extent of the source distribution in terms of the normalized distance and is approximately equal to 3.0 (Chan, 1976). The value of the ordinate 1.0 corresponds to 124 dB (Chan, 1976). Similarly, Figure 22d shows the lateral source distribution functions plotted in terms of the normalized lateral distance $\bar{r}(= r/\hat{R})$ for the first three modes. Here also $\hat{G}(\bar{r})$ is normalized with the reference sound pressure level of 124 dB. It should be pointed out that the longitudinal and lateral source functions in Figure 22c and 22d are only valid for Strouhal frequencies larger than approximately 0.3, because for smaller frequencies than Sh = 0.3 both $\hat{F}(\bar{x})$ and $\hat{G}(\bar{r})$ cease to be scaled by $\bar{x}(= Sh \cdot x/D\ell)$ and $\bar{r}(= r/\hat{R})$, respectively.

Although Michalke and Fuchs (1973) rather arbitrarily chose values for αL to predict the directivities of jet noise, the quantity αL should be carefully determined by the pressure wave measurements. In the present investigation, the longitudinal extent of the source region in jet turbulence, L, was determined by the relation

$$L = \frac{\ell D}{Sh} \quad \text{for } 3 \leq \ell \leq 4$$

which was derived from the experimental results (see Figure 4 of Chan (1976)). Consequently, we note that L is a function of Strouhal number and proportional to the jet diameter. To be more precise, L is proportional to the jet exit velocity U_j and inversely proportional to the frequency f of the radiated sound.

The jet thickness parameter $k\hat{R}$ is another important parameter along with the convection parameter $\alpha L(1 - M_c \cdot \cos\hat{\theta})$. The radial source

distribution extent $\hat{R}$ can be determined from Figure 22d. It should be pointed out, however, that the lateral source distribution function is dependent on the axial coordinate $\bar{x}$. Consequently, $\hat{R}$ also varies with $\bar{x}$. This is obvious from the fact that the jet spreads out laterally downstream from the nozzle. This dependence of $\hat{R}$ on $\bar{x}$ may be a rather unfortuante limitation on the evaluation of the integrals in Eq. 3.2.5. As an approximation, however, a mean value of $\hat{R}$ can be taken.

Up to this point only the experimental determination of the necessary parameters for the evaluation of $P(\omega)$ in Eq. 3.2.5 has been discussed. As mentioned previously, the prediction formula for $P(\omega)$ can be numerically evaluated for various frequencies with fixed values of $\hat{r}$ and $\hat{\theta}$. The results of the prediction using these parameters will be discussed in Chapter IV.

Chapter IV

RESULTS AND DISCUSSION

In this chapter, the flow and acoustical characteristics of the jet facility used for the present study will be presented in detail with special emphasis on the spectral features of both the jet turbulence and the radiated sound. Comparison with theory is also made. The role of Reynolds number in noise generation will then be discussed. Finally, the results of Fourier decomposition of the jet noise signal into azimuthal components will be presented and compared with the spectral theory of Michalke.

4.1 Flow Characteristics

4.1.1 Mean velocity profile

Quantitative measurements of the mean velocity profiles and the distributions of the velocity fluctuations (u-component) were obtained at ten equally spaced axial stations between X = D and X = 10D from the jet exit plane. Three nozzles of different sizes, 12.7, 6.35 and 3.18 mm in diameter have been used for flow measurements at Mach numbers (nominal) between 0.2 and 0.6. However, only a part of the experimental results obtained under these conditions will be reported here. Before presenting the experimental results, it is profitable to consider probable sources of major errors associated with the flow measurements reported herein.

They can be classified into four categories, namely:

1. Fluctuations of flow rate
2. Unstable response of the instruments

3. Spatial averaging-effect of hot-film (hot-wire) sensor

4. Compressibility effect

The flow rate of air supplied to the settling chamber was constantly monitored with a total pressure probe. The variation of the flow rate recorded was found within $\pm$ 3%.

The flow measurement system composed of the hot-film (hot-wire) anemometer and linearizer was carefully calibrated before and after each test. The fluctuations of the response of the system was carefully monitored with an autoranging digital voltmeter and also with the SD-360 FFT analyzer. Judging from the high degree of repeatability of the data reported herein, the response of the entire system could be reasonably regarded to be quite uniform.

Among the errors associated with hot-wire turbulence measurements the most serious one may be the error due to the finite length of the sensor wire. Since the hot-wire is in a nonuniform velocity field of a jet, the effective cooling velocity varies over the entire length due to its finite length. However, the calibration of a hot-wire is always conducted in an uniform velocity field over the entire wire length. Thus, the measured output voltage always corresponds to the spatially averaged velocity over the wire length. The error in the turbulence intensity measurements due to the nonuniform velocity field can be estimated as follows. Here, it is assumed that the turbulent fluctuations are small compared with the mean velocity and that the compressibility can be neglected. Then the corrected value of the square of the voltage, $\overline{e^2}$, may be related to the measured voltage $(\overline{e^2})_M$ by

$$\overline{e^2} = \kappa(\overline{e^2})_M$$

where κ represents the correction factor defined by

$$\kappa = \frac{1}{1 - \frac{\ell^2}{6\lambda_G^2}}$$

The sensor length and the spatial length scale of jet turbulence are denoted by ℓ and λ_G, respectively (Hinze, 1975). In the present study, ℓ was 1.25 mm and λ_G was 1.27 to 12.7 mm for the 12.7 mm jet. Therefore, the correlation factor to the measured rms voltages varies from 1.002 to 1.19. Thus, the spatial averaging of the effective cooling velocity due to the finite length of the sensor wire introduces a maximum error of about 10% in turbulence intensity measurements.

It has been well established that the compressibility effect of air at room temperature can be neglected in flow measurements when the flow velocity is approximately less than M = 0.3. In the present study, however, some flow quantities were measured at Mach numbers in excess of M = 0.3. At these high flow velocities the resulting data were calibrated according to the method proposed by Norman (1967). The deviation from King's law with respect to the output voltage was found to be less than 5% at a nominal Mach number of M = 0.6.

In summary, it can be argued that the flow measurements reported herein were made as accurately as the state of the art in hot-wire measurements would allow.

During preliminary testing, the true jet axis was determined with a single hot-film probe. As had been discussed in Chapter II, the aerodynamic jet axis is defined as a locus of the points in the flow on a vertical plane to the geometrical jet axis at which turbulence intensity is minimum. Measurements were made at ten equally spaced X stations between X = D and X = 10D from the jet exit plane. The results show that at each X station the deviation from the geometrical jet axis was on the

order of one hundredth of an inch (0.254 mm) and the true jet axis has the form of a helical wave. This helical wave-like jet axis was seen in all of the three jets of 12.7, 6.35 and 3.18 mm diameters. It was further confirmed that rotating of the nozzle or settling chamber does not give any noticeable effect on the profile of the true jet axis and that this profile changed significantly from one day to another. This may indicate that the helical wave-like disturbances are generated far upstream of the nozzle. One may speculate that since turbulence is more sensitive to the variations of flow conditions than mean flow the asymmetry of jet flow must be obviously observed in turbulence intensity measurements. In fact, this was clearly confirmed in the present investigation. It is interesting to note that the asymmetry of the jet flow was observed not only in the flow field but also in the radiated field. It should be added that the circumferential asymmetry of the sound pressure level was more strongly observed in the lateral direction than the downstream direction. The observed asymmetry of the turbulence intensity will be discussed in some detail later in this chapter.

Figure 23 shows mean velocity profiles measured in the 12.7 mm jet at M = 0.297, $R_e = 0.87 \times 10^5$ at various downstream locations between X/D = 1 and 10. These were measured by a single hot-film probe. Identical results were obtained with a single hot-wire probe. The typical top-hat profile of the mean velocity at the jet exit can be noted. Further downstream the velocity profile takes on the appearance of a fully developed jet. The similarity of the mean velocity profiles in the mixing zone of the 12.7 mm jet at Mach number of M = 0.199 and 0.297 is shown in Figure 24. Here the similarity is expressed in terms of non-dimensionalized variables U/U_m and η, where U_m represents the centerline

velocity and $\eta = (Z - Z_{0.5})/X$. The distance $(Z - Z_{0.5})$ corresponds to the lateral distance between any radial point and that for which the velocity is half of the centerline velocity U_m. It is evident that the similarity profile is most likely independent of Mach number. These profiles are consistent with those observed in many other jets. The data statisfy a similarity relationship suggested by Seiner (1974) as

$$U/U_m = \exp[-52.4(\eta + 0.115)^2]$$

This relationship corresponds to the tip of the potential core being at X/D = 4.3. The virtual origin of the jets of this study was found to be a = -1.5D which is consistent with data found in Abramovich (1963).

It is well-known that the velocity profiles in the mixing region are similar at axial distances greater than about two dimaters from the nozzle. Closer to the nozzle the velocity profiles lack similarity because the varied effects of initial conditions such as boundary layer thickness at the nozzle tip. Hence, data are shown only for axial positions of two or more diameters downstream. It should be pointed out that the similarity of the mean velocity profiles has been verified with data gathered at Reynolds numbers in excess of 10^5. However, the Reynolds number corresponding to the data in Figure 24 was either $5.8X10^4$ or $8.7x10^4$. These data show no apparent difference from high Reynolds number data. The axial distribution of the normalized mean velocities for the 12.7 mm jet at three differenet Mach numbers are presented in Figure 25, where U_j represents the jet exit velocity. The length of the potential core appears to be a weak function of the exit Mach number. However, the mean velocity in the core begins to decrease at an axial distance between X/D = 4 and 6, and its decay rate is larger at smaller exit velocities.

Since nozzle diameter was held constant, it is not apparent whether this is a Mach or Reynolds number effect.

A Gaussian error curve and a theoretical radial distribution of the axial velocity component calculated according to the momentum-transport theory are presented in Figure 26 together with two experimental curves. The theoretical curves were plotted according to Eqs. (6-76) and (6-80) of Hinze (1975). These two curves are only valid between X + a = 8D and 20D, where a represents the distance to the vitual origin from the jet exit plane. The dash-dot-line is the measured curved at X/D = 8 with R_e = 8.7×10^4. Both theoretical curves give fairly good agreement with observations across the entire lateral width with larger deviations at further distances from the jet axis.

4.1.2 Turbulence intensity and non-axisymmetry of a round jet

The measurement of the turbulence intensity was conducted with three different nozzles at varying exit Mach numbers. In Figure 27 the u-component turbulence profiles for the 12.7 mm jet at M = 0.297 observed at various downstream locations are depicted. A single hot-film was traversed laterally between $-3D \leq Z \leq 3D$ at equally spaced axial stations between $D \leq X \leq 10D$. The turbulence intensity attains a maximum value near Z/D = 0.5 at any downstream station. The asymmetry of the profiles is evident. This asymmetry of the jet flow is not due to the nozzle configuration. This was confirmed by rotating the nozzle by 180°, yielding the same results. It is debatable whether these results imply a natural asymmetry of the flow due to a helical mode in the jet turbulence or upstream flow conditions. We note in Figure 27 that the turbulence intensity on the jet axis grows almost linearly up to five diameters

downstream, and the intensity becomes approximately doubles over an increment of one diameter. The asymmetry of the turbulence intensity is evident and was observed in all of the three jets of 12.7, 6.35 and 3.18 mm diameters. In Figure 27, the difference of the peak intensity observed in lower and upper mixing layers seems to grow gradually up to five diameters downstream and then to decay slowly with a further increase of downstream distance. This may be attributed to the helical wave-like motion of jet turbulence with a wavelength which is relatively large when compared to jet diameter.

To further explore the asymmetry of a circular jet, a measurement of the circumferential distribution of rms fluctuating velocity signals was undertaken. A hot-wire (DISA 55P11) probe was rotated in the plane vertical to the true jet axis at X/D = 2. The sensor portion of the probe was consistently supported horizontally during the rotation along a circle of radius 0.5D. The results of this experiment are shown in Figure 28, where the ordinate represents linearized output voltage of the hot-wire and the abscissa corresponds to the azimuthal angle (degrees). Here we note a somewhat sinusoidal profile centered at the 400 mV line. The results, however, must be interpreted carefully. The hot-wire sensor whose length and diameter are 1.25 mm and 5 μm, respectively, can be thought to be completely immersed in the very thin mixing layer when the sensor probe is located at ϕ = 0° and 180°. With increasing azimuthal angle, ϕ, the sensor wire will cut the mixing layer with larger angle, and at ϕ = 90° and 270°, the wire cuts across the mixing layer radially. Here, a maximum spatial averaging effect may be observed.

If we assume that the sinusoidal profile of the turbulence (u-component) is only due to the averaging effect of the hot-wire, then we

should have a minimum at $\phi = 90°$ amd 270°. However, this is not consistent with the observations in Figure 28. Here the minimum output voltage is observed at about $\phi = 180°$. It is now obvious that even for a circular jet the turbulence intensity (u-component) is not axisymmetric, and a jet flow may be speculated to have a helical structure to some extent in the downstream direction. As will be discussed in a later section of this chapter, this non-axisymmetry of the flow has a noticeable effect on the radiated field.

We see in Figure 28 that the deviations of rms value about the mean value (400 mV) are within $\pm$ 40 mV. Hence, if we accept the errors of the order of 10% in turbulence measurements, we may regard the circular jet to be axisymmetric as an approximation.

The axial distribution of turbulence intensity (u-component) in the mixing layer at two Mach numbers are presented in Figure 29, together with that obtained by Wooldridge et al. (1971). It can be noted that the intensity is dependent on Reynolds number $R_e = U_j D/\nu$, as well as on Mach number $M = U_j/a_o$. The intensity observed by Wooldridge has a constant value after X/D = 4 while the data observed in the present study keep growing up to about six diameters downstream. The Reynolds number under which Wooldrige et al. measured the intensity is 2.6×10^5, and at this value of Reynolds number the wall boundary layer of the jet nozzle is supposedly turbulent. However, the Reynolds numbers for the data reported herein are $R_e = 8.7 \times 10^4$ (M = 0.297) and 5.8×10^4 (M = 0.199). Under these lower Reynolds numbers the transition from laminar to turbulent flow in the boundary layer presumably occurs in the free shear flow rather than in the nozzle wall boundary layer as pointed out by Mollo-Christensen (1967). This spatial delay of transition may result in the spatial delay

of the growth of the turbulence intensity to a constant magnitude as seen in Figure 29. One may argue that this spatial growth of turbulence intensity is also a function of nozzle design. Therefore, a detailed investigation of the boundary layer of nozzle wall must be done before any decisive conclusion on this point can be made. The intensity profiles illustrated in Figure 29 are favourably consistent with the observation by Davies et al. (1963).

The normalized turbulence (u-component) profiles measured at equally spaced downstream stations for the 12.7 mm jet at M = 0.199 are presented in Figure 30. The dashed line corresponds to the similarity profile given by Seiner (1974) using the 50.8 mm jet at M = 0.32, and this gives a Reynolds number of $R_e = 3.9 \times 10^5$. The abscissa is expressed in terms of $\eta = (Z - Z_{0.5})/X$ and u_m represents the maximum value of fluctuating velocities measured in a vertical plane to the jet axis at each downstream station.

As shown in Figure 30, the turbulence profiles are obviously similar, and an excellent agreement is found with the data obtained by Seiner (1974). The dashed line in Figure 30 can be expressed as

$$\frac{u}{u_m} \simeq 0.16 \left| \frac{\partial (U/U_m)}{\partial \eta} \right|$$

for approximately $\eta > 0.1$ according to Seiner. This is nothing more than an expression of Prandtl's mixing length theory which is valid only where one characteristic length scale is involved.

The lateral distribution of the mean shear calculated from the non-dimensionalized mean velocity profile is illustrated in Figure 31 together with a calculated mean shear obtained by Davies et al. (1963). The solid line represents the mean shear distribution for the 12.7 mm jet at

M = 0.297 at the axial positions $2 \leq X/D \leq 10$. The Reynolds number $R_e = U_j D/\nu$ is 8.7×10^4. The dashed line corresponds to the mean shear distribution computed from the results of the mean velocity measurements of Davies et al. (1963). They used a jet of 25.4 mm at M = 0.3 corresponding to a Reynolds number of 1.7×10^5. In addition, they observed that the mean shear varies with Mach number but not quite in a linear fashion. Note, however, that the Mach number for both sets of data is 0.3, and, nevertheless, there is a significant difference between the two sets of data. This may be attributed to the variations in the initial development of the jets.

4.1.3 Power spectral density of turbulent velocities

As has been discussed in Chapter II, the SD-360 FFT analyzer performs a frequency analysis on any given sample of data with two degrees of freedom. All spectra are the results of ensemble averaging 254 samples. As will be discussed in Appendix A, the 99% confidence interval for the power spectral density estimate is as good as within $\pm$ 1 dB of the true power spectral density with this linear ensemble averaging.

Figure 32 shows narrow band power spectral density of the axial turbulent velocity components measured at ten equally spaced stations on the jet axis of the 12.7 mm jet at M = 0.58, corresponds to a Reynolds number of $R_e = 1.6 \times 10^5$. The filter spacing for the spectral analysis was set at 40 Hz, and signals were always bandpassed in the frequency range, $0.5 \leq f \leq 16$ KHz.

A drastic fall-off at high frequency edge is only due to the aliasing lowpass filter. Linear ensemble averaging of 256 ensembles of frequency data was found to be adequate for this analysis. High repeatability of

the results has confirmed this. Two peaks were observed in the spectrum of the fluctuating velocities sampled in the core within two diameters from the jet exit plane. A narrow peak is noted at about 15 KHz and a broadpeak at about 5 KHz, which correspond to Strouhal number $Sh = fD/U_j \simeq$ 1.0 and 0.3, respectively. Wooldridge et al. (1971) also reported the existence of the similar high frequency peak which decreases in magnitude with an increase of distance from the nozzle exit. However, it is open to question whether this high frequency peak is due to the instrinsic structure of jet turbulence or to some anomalous signal. No further attempt to investigate this point was done in the present study. It may be worth noting that the high frequency peak shown in Figure 32 is low enough in magnitude to be buried in, for example, electronic noise.

According to Lau et al. (1972), the microphone spectra and those of the hot-wire have a close resemblance to each other and in each case the peak locates at almost the same frequency. The peak in the core spectra is then supposedly associated with the radiated sound signals. Further downstream on the jet axis, this peak shows a trend to shift gradually to lower frequencies with increasing downstream distance. Comparing Figures 32 and 33, it can be noted that the axial distance where the profile of the lower part of the spectrum becomes uniform depends on Mach number. This was also confirmed by Wooldridge et al. (1971). This distance may be related to the length of the jet core region (see Figure 29 for comparison). In Figure 32, the jet diameter is 12.7 mm, and the exit Mach number is 0.58 which gives a Reynolds number of $R_e = 1.6 \times 10^5$. Here, the peak observed at the end of the jet core (X/D = 5) locates at about Sh = 0.3. The corresponding peak in Figure 33 is found at about Sh = 0.33 where Reynolds number is 0.54×10^5. The axial variation of the peak

amplitude between X/D = 1 and X/D = 5 is approximately 15 dB in both cases. This is significantly smaller when compared with the value of 22 dB obtained by Wooldrige et al. (1971) who measured variation of energy in band centered at Sh = 0.48 along the jet center line between the jet exit and the tip of the core (X/D = 4) using a 38 mm jet at Mach number of M = 0.3 which gives a Reynolds number of $R_e = 2.6 \times 10^5$. It is not likely, however, that this axial variation of peak amplitude can be scaled either by Mach number or by Reynolds number.

With increasing axial distance, the turbulence intensity observed on the jet axis grows rapidly which results in masking lower energy signals observed in the core region.

It should be remarked that the measured energy spectrum for higher frequency end falls off not like $\omega^{-5/3}$ but like $\omega^{-4/3}$ as seen in Figure 32. This corresponds to the decay of a sound spectrum like $\omega^{-2/3}$ according to Meechan (1969). Later sections will deal with the comparison of the spectrum observed in the near and far fields. It should be noted that in Figure 33 a broad peak of Sh = 0.7 at one diameter downstream from the jet exit shifts more drastically with axial distance than in the case shown in Figure 32. At the tip of the potential core a peak is observed with a frequency of Sh = 0.33, which is nearly half of the frequency of the peak seen at X/D = 1. The measured spectra show the same energy fall-off with frequency in both cases, and the high frequency content varies as $\omega^{-4/3}$.

Lau, Fisher and Fuchs (1972) proposed a model of turbulent flow to explain a fairly regular structure in a jet on the basis of their slow speed jet measurements. They assumed an axial disposition of discrete vortices in the jet spaced at about one and one-quarter nozzle diameters

apart travelling downstream in the center of the mixing layer. This assumption was presumably derived from their knowledge about turbulence spectrum of jets. As is seen in Figures 32 and 33, the spectrum observed in the core region has a pronounced peak. According to their calculation, the Strouhal number of the peak based on jet diameter and convection velocity gives a value of nearly one. If this is the case, since $Sh = f_p D/U_c \simeq 1$, it follows that $D = U_c/f_p \equiv \lambda$ indicating that the wavelength of the disturbances is of the same order of magnitude as the jet diameter. With this model, certain physical features of the jet turbulence could be explained. They also suggest the usefulness of this model even for high subsonic jets (Lau, 1971).

The results of the present study, however, do not support their model. The vortex passing frequency is not simply proportional to the jet efflux speed, and this can be seen by comparing the spectrum at X/D = 4 in Figure 33 with that observed at Z/D = 0 in Figure 36. Probably, a crucial drawback of this model exists in that it cannot give any reasonable explanation for the helical structure observed in the mixing layer of the jet. It may be remarked, on the basis of the present study, that the structure of the jet turbulence is much too complicated to be modelled by such a relatively simple vortex model.

Figure 34 shows turbulent energy spectra for this 12.7 mm jet in the mixing layer observed at various axial locations at Mach number M = 0.58. This figure serves to illustrate that high frequency noise is predominantly generated by the jet within a few diameters from the nozzle. This is also seen in the results of the coherent output power measurements which will be reported in a later section. Similar profiles are seen in Figure 35 for the 6.35 mm jet at M = 0.394. In Figure 36, the frequency analysis has

been extended up to 40 KHz with the filter spacing of Δf = 100 Hz. Here, we see that near the center of the shear layer, namely at X/D = 4, Z/D = 0.4, the spectrum shows a uniform profile up to 20 KHz. The energy then falls off drastically as ω^2 which is a typical decaying profile observed in the inertial subrange of an isotropic turbulence (Tennekes and Lumley, 1972). Figure 37 shows the similiar profile for the 6.35 mm jet at M = 0.394.

It may be remarked that the energy centered at the peak observed on the axis corresponds to the disturbance generated by the interaction of individual vortices within the large-scale structure while the energy distributed over the lower frequency region corresponds to the convection of the large-scale structures downstream (Winant and Browand, 1974).

The spectra in the intermittent region are presented in Figures 38 and 39. Note that they completely lack high frequency energy components throughout the entire noise generating region of jet turbulence. As pointed out by Lau et al. (1972), there is a radially inward mean flow in the entrainment region, and this may give, more or less, an influence on the hot-wire signals sampled in this region. Therefore, the spectra plotted in Figures 38 and 39 should be interpreted with caution.

4.2 Acoustical Characteristics

4.2.1 Overall sound pressure level, 1/3 octave spectrum and directivity

The following expression for the far field intensity is a result of Lighthill's work (1952) with a slight modification on the convection term:

$$I = K \frac{\rho_m^2 U_j^8 D^2}{\rho_o a^5 R} \frac{\psi(\theta)}{(1 - M_c \cos\theta)^5} \qquad (4.2.1)$$

where D is the nozzle diameter, U_j the jet exit velocity, ρ_m the air density in the mixing region, ρ_o and a_o the ambient air density and sound

speed in the medium at rest, R the distance from the nozzle exit to the observer and $\hat{\theta}$ the angle between the direction of sound emission and the downstream jet axis. M_c is the convection Mach number and $\psi(\hat{\theta})$ represents the directivity factor which is given by

$$\psi(\hat{\theta}) = 1 + \left(\frac{\cos^4\theta + \cos^2\theta}{2}\right)W \qquad (4.2.2)$$

where W is the ratio of the maximum value of shear noise to the self noise. K is a numerical constant of the order of 10^{-6}.

It should be pointed out that Eq. 4.2.1 has been derived for axisymmetric jets based on such simplifing assumptions as isotropy and incompressibility of the jet turbulence and a Gaussian distribution of the joint probability of the velocities at two points. If we can approximate W to be nearly unity as claimed by Ribner (1969), then $\psi(\hat{\theta})$ also becomes approximately unity except for small radiation angles $\hat{\theta}$.

Mollo-Christensen et al. (1964) analyzed the results of a series of their sound pressure measurements to find the Mach number dependence of the overall sound pressure level (OASPL) on the presumption that

$$\frac{p}{K\rho_o a_o^2} = \frac{D}{R} G(M,R_e,\hat{\theta}) \sim M^{n(\hat{\theta})} F(R_e) \qquad (4.2.3)$$

where p represents the sound pressure observed in the far field. In this study, measurements of the overall sound pressure level were made at non-dimensional distances R/D of 50 and 100, and Mach numbers M = 0.4 to 0.9 for jets of five different nozzle diameters. Figure 40 shows the variation of OASPL with Mach numbers 0.4 to 0.9 at several observation angles for the 12.7 mm jet. We note that the value of $n(\hat{\theta})$ varies between 7.55 at $\hat{\theta} = 90°$ and 9.56 at $\hat{\theta} = 15°$, being an increasing function of emission angle $\hat{\theta}$. Corresponding values of $n(\hat{\theta})$ for the same range of the emission

angle obtained by Mollo-Christensen et al. (1964) fall between 6.64 and 8.22. These values are noticeably smaller than those reported herein. It has been well established that the effect of convection is to increase the overall sound generation, and, consequently, the predicted overall power should have a higher power of the jet velocity than the eighth. On the other hand, there is evidence that the relative turbulence intensity decreases with increasing Mach number. This fact has been cited as the primary factor involved in modifying the basic sound power with convection from an eight power to a sixth power dependence on velocity. If this is the case, the sound intensity observed at $\hat{\theta} = 90°$ where no convection effects are present should be proportional to the sixth power of the jet exit velocity. The results shown in Figure 40 are consistant with the prediction mentioned above in that $n(\hat{\theta})$ increases with decreasing $\hat{\theta}$ due to the convection effects. However, the $n(\hat{\theta}) = 7.55$ observed at $\hat{\theta} = 90°$ is in disagreement with the hypothetical sixth power law. It may be remarked that $n(\hat{\theta})$ is independent of Mach number as seen from Figure 40, but obviously dependent on Reynolds number as shown in Figure 41 where normalized sound intensity is plotted versus Mach number for various Reynolds numbers. Note that the normalized sound intensity increases with increasing Reynolds number. This trend is observed at either $\hat{\theta} = 30°$ or 90°. A rather unusually low intensity level of the data for the 3.18 mm jet observed at $\hat{\theta} = 90°$ may be attributed to the fact that the large diameter plate on which the nozzle was mounted acoustically shadowed the microphone located in the lateral direction ($\hat{\theta} = 90°$).

Directivity patterns for the 12.7, 6.35 and 3.18 mm jets are presented in Figure 42-44, together with the predictions by Lighthill (1952), Philips (1960) and Lilley (1971). The level of the predicted curves was adjusted

to go through the data point at $\hat{\theta} = 90°$. In Figure 42, the directivities of the radiated sound observed at locations 50 diameters away from the jet exit plane for four different Mach numbers are illustrated, where Reynolds numbers fall in the range of $1.43\text{x}10^5 \leq R_e \leq 2.21\text{x}10^5$. It is seen in Figure 42 that the intensity is directional with a peak more or less along the jet axis. With increasing Mach number the directivity becomes more pronounced, and the amount of amplification from $\hat{\theta} = 90°$ to $\hat{\theta} = 15°$ at the highest exit velocity is approximately 10 dB. Apparently, Lighthill's prediction overestimates the amplification at any Mach number, where the directivity factor $\psi(\hat{\theta})$ in Eq. 4.2.2 is assumed to be unity. The observed inconsistency between the experiments and Lighthill's theory may be partly attributed to the assumption that all the quadrupoles are randomly oriented so that $\psi(\hat{\theta})$ is unity. However, the general consensus of opinion is that the discrepancy can be attributed to the exclusion of the acoustic-mean flow interaction effect in the prediction formulation. In fact, Phillips (1960) and Lilly (1971) showed that Lighthill's theory could be improved by transforming the full nonlinear equations into the form of the wave equation travelling in a moving medium. The theory then shows that the convection factor $(1 - M_c \cos\hat{\theta})^{-5}$ in Eq. 4.2.1 should be replaced by $(1 - M_c \cos\hat{\theta})^{-3}$ (Goldstein, 1976).

The dashed line seen in Figure 42 was plotted based on the Phillips and Lilly's equation. Evidently, the additional Doppler factor which appears in the denominator of the expression for directivity reduces the gap between theory and observation, yielding a favourable agreement. The rather rapid fall-off seen at larger angles than $\hat{\theta} = 90°$, particularly for smaller nozzles (see Figures 43 and 44), is due to the experimental setup and is not a fundamental feature of the jet noise signals. The

resulting discrepancy is due to an acoustic shadow created by the large diameter plate on which the nozzles were mounted.

A comparison of the data reported herein, and those available in the literature (Lush, 1971, Olsen and Karchmer, 1976) show general agreement, but also minor differences, particularly for smaller jets. The directivity due to a single azimuthal components of jet noise will be discussed in a later section.

Typical 1/3 octave spectra obtained for three jets of different diameters are illustrated in Figures 45-54 for various jet exit velocities. These data are lossless and have been obtained directly with the Real-Time Aanlyzer Type 1921 (General Radio). The analysis frequency range was 500 Hz $\leq$ f $\leq$ 80 KHz. Comparing the spectra for three different emission angles (Figures 45-47), we note that the spectrum changes its shape noticeably with radiation angle. The spectra observed at acute angles are fairly peaky, while at sideline positions the spectra have a rather broad shape.

The growth rate of the spectrum at low frequencies is about 6 dB/ octave and the decay rate is nearly half of the growth rate (see Figure 47). This is consistent with the results reported by previous experimentalists (Lush, 1971; Olsen and Karchmer, 1976). At $\hat{\theta}$ = 15°, the peak frequency is independent of the jet exit velocity and locates at about f = 3.2 KHz (see Figure 45). This indicates that the peak frequency does not scale as a Strouhal number at this emission angle. Moreover, the decay of the spectrum at the high frequency end is more extreme and is about 5 dB per octave. In contrast to the spectrum observed at $\hat{\theta}$ = 15°, the spectrum obtained at $\hat{\theta}$ = 30° does not fall off monotonically but rather has another peak which shifts to higher frequency

with increasing jet exit velocity (see Figure 46). It should be pointed out that the raw data, on the basis of which the spectra shown in Figures 45-54 have been depicted, behave like any previously reported results. However, necessary corrections to the data mainly due to air absorption, give rise to the peculiar results shown. At this point, no explanation can be made for this anomalous behavior at higher frequencies. The peak frequency again does not scale as a Strouhal number at this radiation angle, and remains almost constant at f = 5 KHz (Figure 46). We note that the peak shifts progressively to higher frequency with increasing emission angle and at $\hat{\theta} = 90°$ to the jet axis peak scales with Strouhal number (Figure 47).

Figures 48-50 show the 1/3 octave spectra for the 6.35 mm jet observed at three different radiation angles. The general trend is similar to that of the spectrum for the 12.7 mm jet except in that the corrected spectrum at $\hat{\theta} = 90°$ seems to have a stronger second peak than the peak expected to appear at about f = 15 KHz. This may be attributed to possible extra sources at frequencies beyond f = 30 KHz. It is likely that the spectrum in Figure 50 would begin decaying at about f = 30 KHz, were it not for the effect of additional apparent noise sources. Since the spectrum observed at $\hat{\theta} = 90°$, in the case of smaller nozzles (Figures 50 and 52), is too broad to locate the peak; it is rather difficult to see whether or note the peak scales as a Strouhal number. This point will be discussed again in detail in a later part of this section with the results of narrowband spectral measurements.

A limited amount of spectral data for the smaller nozzles are presented in Figures 51-54. As has been discussed in Chapter III, the analysis frequency range for the spectral measurements reported in this

section was limited to 300 Hz $\leq$ f $\leq$ 80 KHz, mainly due to limitation on frequency response of the microphones utilized in this study. Observations indicate that the low frequency end of the spectrum seems to be independent of Reynolds number in the Reynolds number range studied. However, as is seen from Figure 46 and 51, the high frequency end is apparently different from one jet to another. This probably indicates that high frequency sound mostly produced in the mixing region is strongly influenced by the jet exit conditions. Moreover, as has been pointed out by Mollo-Christensen (1967), the boundary layer in the nozzle wall is presumably laminar for the small jet at low exit velocities and transition from laminar to turbulent flow may take place in the free shear layer. If this is the case, the sound generated in the vicinity of the orifice would be more or less influenced by such flow conditions.

Normalized sound pressure level spectra at $\hat{\theta} = 90°$ are shown in Figures 55-57 for the three jets of different diameters, together with the recommended curve given by Stone (1974). Stone proposed that the effect of jet temperature on the spectral shape is accounted for by multiplying the Strouhal number by the ratio of jet total temperature to ambient temperature to the 0.4 power. This gives the non-dimensional frequency parameter

$$S = \left(\frac{fD}{U_j}\right)\left(\frac{T_j}{T_a}\right)^{0.4} . \qquad (4.2.4)$$

In the present study, the jet total temperature is assumed to be equal to the ambient temperature, to give $S = fD/U_j = Sh$. The abscissa log S in Figures 55-57 is given by Eq. 4.2.4, and the normalized sound pressure level spectrum appearing as the ordinate is defined by

(1/3 octave spectrum level) $-$ (overall sound pressure level).

The experimental conditions under which the data in Figure 55 were obtained are shown in the figure, namely D = 12.7 mm, R = 50D and $\hat{\theta}$ = 90°. At $\hat{\theta}$ = 90°, a point 50 diameters away from the center of the jet exit plane can be considered to be in the far field with a considerable confidence. We note in Figure 55 that the experimental results are in good agreement with the recommended curve up to about log S = 0.4. For higher frequencies, the spectra are strongly affected by atmospheric absorption. This may imply that the correction due to the air absorption may be too high, provided that the recommended curve is valid for high frequencies.

Spectra for the 6.35 mm jet are similarly illustrated in Figure 56 where the observation angle and location are $\hat{\theta}$ = 90° and R = 100D, respectively. Here, we note that the scatter of data points is more remarkable than in the case of the 12.7 mm jet. Particularly, for the lowest exit Mach number the deviation from the recommended curve is largest. This may be attributed to the low intensity which is possibly masked by background noise. A rather noticeable deviation at the high frequency end is conceivably due to unidentified extraneous noise.

Figure 57 represents normalized spectra for the 3.18 mm jet measured at R = 100D and $\hat{\theta}$ = 90° to the jet axis. Before comparing the experimental data with the prediction, we have to return to Figure 57 which illustrates 1/3 octave spectra at $\hat{\theta}$ = 90° for the 3.18 mm jet. It should be pointed out that since the frequency range of the spectral analysis has been limited to lower than 80 KHz (1/3 octave band range) in the present study, a fraction of the radiated energy is missing in the summation of total energy, yielding lower intensity by presumably a few dB than the true overall sound pressure level. Hence, if the correction of this amount

is considered in Figure 57, the agreement is seen within about $\pm$ 2 dB for low frequencies. However, the peak frequency of the experimental data is apparently shifted to the lower side by about 0.4 in terms of log S. Accordingly, the high frequency end of the measured profile would largely deviate from the recommended profile. This discrepancy may indicate that the normalized sound pressure level spectrum does not scale as a non-dimensional frequency parameter S for the low Reynolds number jets. This has been experimentally confirmed by the present author by means of the analysis of the power spectral density of the radiated sound at low Reynolds numbers and will be discussed in Section 4.3 in some detail.

4.2.2 Power spectral density of jet noise

One of the interesting and important problems relevant to jet noise is that of predicting the spectrum of the emitted sound. However, this has been proved to be a particularly difficult problem because the theoretically derived power spectrum includes the space-time correlation function of fluctuating velocities which is an almost intractable quantity to determine without recourse to some simplifying assumptions. Starting from Lighthill's integral solution for the density fluctuations observed in the far field caused by the turbulent motion in the near field Meecham (1969) derived the following expression for the power spectrum, based on the assumption that the turbulent jet is locally and statistically homogeneous:

$$I(\hat{\mathbf{x}},\omega) = \frac{\rho_o \overline{v}}{32\bar{u}^3 a_o^5} \frac{\hat{x}_i \hat{x}_j \hat{x}_k \hat{x}_\ell}{\hat{r}^6} \int^6 d\xi \int d\tau e^{i\omega\tau} \frac{\partial^4}{\partial\tau^4} Q_{ij,k\ell}(\xi,\tau) \quad , \quad (4.2.5)$$

where the effective volume of turbulence $\overline{v}$ and the fourth order correlation $Q_{ij,k\ell}$ are defined by

$$\overline{v} = \int dy[\langle u^8(y)\rangle / \langle u^8(y_o)\rangle] \qquad (4.2.6)$$

and

$$Q_{ij',k\ell}(\xi,\tau) = \langle u_i u_j(y,t) u_k u_\ell(y+\xi,\ t+\tau)\rangle \ , \qquad (4.2.7)$$

respectively.

He further assumed that the fourth order, space-time velocity correlation $Q_{ij',k\ell}$ could be expressed in terms of the second order velocity correlation and furthermore, the jet turbulence had a frozen pattern. After several stages of manipulation he obtained the following high frequency sound spectrum:

$$I(\hat{r},\omega) = \frac{16\rho_o \overline{v} U_j^3}{15 a_o^5 \hat{r}^2}\left(\frac{2U_j}{\omega}\right)^{2\alpha-2} c_\alpha^2 \frac{\Gamma(2\alpha+2)}{\Gamma(\alpha+\frac{3}{2})} \ , \qquad (4.2.8)$$

where Γ represents the gamma function and α comes from the energy spectra $E(k) \sim c_\alpha k^{-\alpha}$.

It should be pointed out that Eq. 4.2.8 has been derived on several simplying assumptions summarized below:

1. Incompressibility of jet flow
2. No thermal effect
3. Statistical stationarity
4. Gaussian distribution of fluctuating velocity
5. Neglect of retarded time
6. Frozen-turbulence approximation

For high Reynolds number flows the well-known five-thirds law $E(k) = \alpha\varepsilon^{2/3}k^{-5/3}$ is satisfied in the inertial subrange. If we substitute this into Eq. 4.2.8, we obtain $I(\hat{r},\omega) \sim \omega^{-4/3}$.

However, as pointed out by Tennekes and Lumley (1972), it is unlikely that we would encounter the inertial subrange in laboratory flows where

the five-thirds law can be applied. It has been known that a measured energy spectrum decays like k^{-2} in high wave number region of low Reynolds number flows. If this is the case, we find $I(\hat{r},\omega) \sim \omega^{-2}$.

Narrow band acoustical spectra are presented in Figure 58 observed at $\hat{\theta} = 30°$ for various exit Mach numbers. At the highest velocity shown in Figure 58, the spectrum falls off as f^{-2} at the higher frequency end, and it is likely that the decaying slope is a weak function of Mach number. This is favourably consistent with Seiner's (1974) results obtained by using a 50.8 mm jet at M = 0.32 and 0.6.

If Meecham's (1969) argument is correct, and the energy spectrum function for higher wave numbers falls off like k^{-2}, then the acoustic spectrum $I(\hat{r},\omega)$ would decay as f^{-2} and agree with the observations in Figure 58. Of the various simplifying assumptions Meecham (1969) adopted in his formulation of the acoustic spectrum the Gaussian distribution of velocity fluctuations is probably the most acceptable. Probability density measurements made during this study (not reported herein) have confirmed this assumption for most of the jet flows. However, the assumption of nearly frozen-flow is presumably open to question in the present study. In the vicinity of the orifice, as has been discussed in Section 4.1.2, jet turbulence is found to be asymmetric, being far from locally homogeneous.

We note in Figure 58 that, just as in the 1/3 octave spectrum, the peak of the narrow band spectrum does not scale as a Strouhal number and remains almost constant at f = 4 KHz over the whole velocity range.

The relationship between peak frequency and emission angle is presented in Figures 59 and 60. In Figure 59, the power spectral density of the 12.7 mm jet at M = 0.58 is given. Here, the Reynolds number

$R_e = U_j D/\nu$ is 1.69×10^5. We see in this figure that the acoustic energy in the low frequency range decreases with emission angle and at $\hat{\theta} = 15°$ the high frequency end of the spectrum falls off most drastically, indicating that the lower frequency content of noise is mainly radiated to the downstream direction and higher frequency sound, on the contrary, is radiated with larger emission angle due to the refraction effect.

According to Ribner (1969) the self noise peaks at a higher frequency than the shear noise, and the shear noise is always beamed in a downstream direction. If this is true, the sound intensity measured at $\hat{\theta} = 15°$ may be mainly a result of shear noise and this shear noise seems to be stronger than the self noise (see Figure 59). It is clearly shown there that the peak shifts to higher frequency with emission angle. However, this is not true for jets at low Reynolds numbers as seen from Figure 60, where the peak remains almost constant at f = 7 KHz over the whole range of emission angle. This will be further discussed in the next section. Another remarkable difference between the two sets of data shown in Figures 59 and 60 is that for the jet of $R_e = 0.845 \times 10^5$, the spectrum observed at $\hat{\theta} = 30°$ is dominant over the whole frequency range whereas in the case of the 12.7 mm jet the spectrum measured at $\hat{\theta} = 30°$ is only dominant at higher frequencies greater than about 7 KHz. Furthermore, for the 6.35 mm jet the spectrum at $\hat{\theta} = 15°$ falls off much more drastically than that seen in Figure 59. As has been already pointed out, the boundary layer on the nozzle walls is presumably laminar for the smaller jet at low exit velocities and transition from laminar to turbulent flow may occur in the free shear layer. Hence, the acoustic spectrum will possibly be affected by where the transition occurs.

4.2.3 Coherent output power

Coherent output power (COP) is nothing more than the portion of the output power produced by a given input. Here, we are concerned with what portion of the sound energy observed at a specified microphone location is contributed by the pressure (or velocity) fluctuations at a specified hot-wire location. In these correlation measurements, a microphone was located at R = 317.5 mm, $\hat{\theta}$ = 30° as illustrated in Figure 12. A DISA hot-wire probe mounted on a traversing mechanism, which is movable three dimensionally, was inserted in the flow of the 6.35 mm jet at M = 0.394. The coherent output power is expressed in terms of dB with 0.1 volt peak voltage of a sinusoidal signal at 1000 Hz being a reference (0 dB).

Figure 61 shows the lateral distribution of coherent output power. It should be pointed out that the noise sources which most effectively radiate sound in the direction inclined at 30° to the downstream jet axis are located at X/D = 4 and close to the jet axis. The axial distribution of coherent output power is presented in Figure 62. On the jet axis, the fluctuating velocities in the region within the first six diameters predominantly contribute to the sound radiated at $\hat{\theta}$ = 30° except for the lowest measured frequency component, Sh = 0.15 which is most likely dominated by noise sources in the fully developed region.

As compared with the distribution profile at Z/D = 0, the coherent output power has a more uniform profile in the center of the shear layer. This is consistent with the profile of the power spectral density in the shear layer which has an uniform profile in the low frequency range (see Figure 35).

As is expected, lower frequency sound is radiated preferably in the downstream direction as seen in Figures 61 and 62. It should be noted

that the power spectral density observed at the microphone location has a peak at about Sh = 0.3, and this frequency component has the highest value of coherent output power at X/D = 4 except on the jet axis.

Judging from the general trend of the profiles shown in Figure 62B, we may speculate that high frequency sound is predominantly produced in the region close to the orifice. The results are consistent with both theory and previous experiments.

4.3 Reynolds Number Dependence of Jet Noise

As is discussed in Chapter I, Mollo-Christensen et al. (1964) pointed out that the rms value of the far field sound pressure was a function of Reynolds number, showing that $p \sim M^{n-m}(R_e)^m$, where m takes on values $1 \leq m \leq 3$. In addition, they observed that non-dimensionalized narrow band spectra of noise varied with Reynolds number over a rather broad range of Strouhal number. This observation was considered worthy of further study particularly in a more quantitative way. In this section, narrow band spectral characteristics of jet noise which apparently depend upon the Reynolds number will be discussed with a particular emphasis on the peak frequency in the noise spectrum. In order to study the Reynolds number dependence of the power spectral density of jet noise, the dimensionless power spectral density has been extensively used in the present study which is defined by

$$10 \log_{10} \frac{p_f^2/(\rho_o U_j^2)^2}{D \cdot \Delta f / U_j} \cdot \left(\frac{R}{D}\right)^2 \qquad (4.3.1)$$

in logarithmic scale, where p_f^2 represents the mean square of the pressure fluctuations at frequency f observed in the far field.

Figures 63 and 64 contain dimensionless spectra plotted as a function of the Strouhal number $Sh = fD/U_j$ for various Reynolds numbers and two Mach numbers. As has been already pointed out by Mollo-Christensen et al. (1964), the variation of the sound spectrum with Reynolds number is evident. Three important features should be mentioned. First, the magnitude of the spectrum is an increasing function of the Reynolds number. This is consistent with the observation by Mollo-Christensen et al. (1964). Secondly, the maximum level of the spectrum is not a linear function of Reynolds number. One could conjecture that, at a sufficiently low Reynolds number, the flow is completely laminar and no sound is radiated. However, it is questionable whether a jet flow can be completely laminar over all space at any Reynolds number greather than zero. For our purposes this conjecture is probably irrelevant. Thirdly, the profile of the spectrum is similar, irrespective of Reynolds number, providing its value is approximately larger than 10^5. For lower Reynolds numbers, both the low and high frequency ends of the spectral profile are more or less affected by variations of the Reynolds number. This is inconsistent with the view adopted by Meecham (1969) in his formulation of the expression for the predicted sound intensity. He argues that the large scale characteristics of jet turbulence is dependent on the way the jet is generated and since most of the low frequency sound is related to the large eddies, the low frequency end of the sound spectrum will depend upon the driving mechanism of the jet turbulence. On the other hand, he suspects that the high frequency end of the spectrum may be independent of the driving forces. The results shown in Figures 63 and 64 do not support his argument. The decaying profiles of the high frequency end of the spectrum shown in these figures obviously depends upon the jet diameter, and for smaller nozzles

the decaying rate of the normalized power spectral density was found to be larger.

This indicates that the driving mechanism of the jet turbulence may be relevant to the sound which is mostly produced in the region close to the jet orifice. Although the spectral shape of jet noise is apparently dependent on Reynolds number in some cases, it is not likely that the spectrum is related to the Reynolds number in a simple way so that the spectrum scales with Reynolds number for a given Mach number and emission angle. Since a low Reynolds number flow is likely to be very sensitive to the fluctuations of upstream conditions, however small they may be, the acoustic characteristics may be different from one jet to another, even when Reynolds number is held constant.

Figure 65 shows how the normalized maximum shear varies with Reynolds number, where the normalized maximum shear is defined by $(X/U_j)(\partial U/\partial Z)$. In spite of scatter of the data points, a general trend of growth of the normalized maximum shear with Reynolds number can be observed. Since jet noise is predominantly produced in the mixing layer as a whole, the intensity of the radiated sound is probably related to the maximum shear in the jet flow. Hence, the dependence of the maximum shear on Reynolds number may partly serve to explain the dependence of the normalized energy spectrum on Reynolds number.

One of the most important findings in this jet noise study was that the narrow band peak frequency of the radiated sound is an increasing function of the Reynolds number (Arndt and Yamamoto, 1976). It has been well established that the peak shifts to higher frequencies with increasing observation angles measured from the downstream jet axis. During the present investigation, it was also found that this is true for the jets

having Reynolds number greater than approximately 10^5. If the Reynolds number is less than 10^5, then the peak lacks a distinct directivity. This can be seen in Figures 59 and 60. As has been discussed in Chapter I, 1/3 octave spectra obtained by Ahuja et al. (1973) also show this trend. Figure 66 presents their results. Although they did not give any comment on this point, it is quite obvious that with decreasing Reynolds number, the amount of shift of the peak frequency with emission angle decreases, and the peak shows a trend to locate at a certain frequency irrespective of the emission angle.

Figure 67 illustrates the narrow band peak frequency of jet noise as a function of Reynolds number at various Mach numbers. Seiner's (1974) narrow band data and Lush's (1971) 1/3 octave band data are also presented in the figure. Here we see that up to $R_e = U_j D/\nu \simeq 10^5$, the peak Strouhal frequency observed at $\hat{\theta} = 30°$ is identical with that at $\hat{\theta} = 90°$ for any exit Mach number. However, at Reynolds numbers larger than $R_e \simeq 10^5$ the situation becomes entirely different. Then, as is seen in Figure 67, the peak Strouhal number increases with increasing emission angle. Although the peak Strouhal frequency is a weak function of Reynolds number, the effect is definitely measurable. According to Lush (1971), the peak frequency does not scale very well with U_j/D at angles between 15° and 45°, and the peak moves progressively to higher frequencies as the emission angle is increased. At the sideline, the peak scales as a Strouhal number. In this case (see Figure 20 of Lush, 1971), the peak Strouhal numbers lay between 0.75 and 0.93 at $\hat{\theta} = 90°$. If one is allowed to say that the peak frequency scales as a Strouhal number with this degree of scatter for jets below a Reynolds number of about 10^5, then it can be said that the peak Strouhal number is approximately 0.25 at any emission

angle. However, this may be too crude a statement and might lead to a misunderstanding of the nature of the jet generation mechanism.

According to McCartney (1975), the peak frequencies of self and shear noise spectra can be expressed in terms of the derivatives of a Fourier transform of the second order moving frame correlation tensor of turbulent velocities at two points at different times. He proposed, furthermore, that if the space and time dependence of the correlation tensor can be separated the peak frequency can be calculated for any given time decay of the correlation tensor. Hence, if the peak frequency shift with Reynolds number, observed in the present study, is one of the intrinsic properties of jet noise, the decaying profile of the second order moving frame correlation tensor of turbulent velocities would be dependent on Reynolds number $R_e = UD/\nu$. However, no attempt to experimentally confirm this has been made in the present investigation.

It is difficult to explain in a precise way why the viscous effects are apparently negligible above a Reynolds number of about 10^5. As has been repeatedly discussed, if the turbulence level in the air supply is reasonably low, the boundary layer on the nozzle wall is possibly laminar for the smaller diameter nozzles. Thus, transition may take place in the free shear flow. One may speculate, however, that for larger jets and at high Mach numbers, transition occurs in the nozzle boundary layer. Then, there must be a critical Reynolds number associated with where transition takes place, in the wall boundary or in the free shear layer. It may, therefore, be surmised that the critical value of $R_e = 10^5$, is associated with transition. The result of Mollo-Christensen's (1967) experiments also show that the critical Reynolds number associated with the narrow band spectrum of jet noise is of the order of 10^5. It is interesting to note

that the calculated transition Reynolds number, assuming that the circular jet nozzle wall can be approximated by flat plate, also has a value of the order of 10^5.

McLaughin et al. (1976) investigated the Reynolds number dependence in supersonic jet noise, and found that a few discrete modes in a low Reynolds number jet are powerful noise generators. It is surprising to note that the spectrum of noise radiated from low Reynolds number jets (see Figure 2 of McLaughlin et al., 1976) has a few discrete modes near Sh = 0.2, which is almost identical with peak Strouhal number of the low Reynolds number subsonic jets as shown in Figure 67. Apparently, the octave and the 1/3 octave band analysis is too crude for detailed analysis of the jet noise, and only the narrow band spectral analysis may unveil certain details of jet noise which have received scant attention in the literature.

4.4 Prediction of Single Azimuth-Frequency Component of Jet Noise

In this section, the coherent structure of jet turbulence will be discussed in conjunction with the prediction of the sound intensity due to a single azimuth-frequency component of noise source utilizing Michalke's spectral theory.

4.4.1 Circumferential cross-correlation measurements in far field

With the experimental setup shown in Figure 16, the measurement of the circumferential cross-correlation of the noise signals sampled by two microphones has been conducted, yielding coherence functions as illustrated in Figures 68 and 69. Here, the coherence functions defined in Section 2.3.5 are plotted versus frequency for various azimuthal

separation angles. Evidently, at $\phi = 0$, the coherency is perfect and, therefore, $\gamma^2 = 1$. With an increase of the azimuthal separation angle, the coherency decreases. Note that in the high frequency range the coherency falls off drastically. The strongest coherency is seen at about 2 KHz, which gives a Strouhal number of Sh = 0.127. From this, one may deduce that the sound most strongly radiated to $\hat{\theta} = 30°$ to the jet axis is generated in the fully developed region of jet turbulence as seen in Figures 61 and 62. This is also consistent with the experimental results of near field pressure fluctuation measurements obtained by Michalke and Fuchs (1975) in which they observed that a component of fluctuating pressure at Sh = 0.113 reaches a maximum as far as eight diameters downstream. Furthermore, a strong azimuthal coherency over a rather broad range of low frequency may indicate the existence of large scale coherent structures in the fully developed region. This is qualitatively consistent with Fuch's (1972) near field data which indicates high coherence of turbulent fluctuations at widely displaced locations in a jet.

Figure 70 illustrates the cross spectral density (CSD) of jet noise for the first three azimuthal separation angles measured under similar experimental conditions with those for Figures 68 and 69. Here we see a definite phase lag between two signals. This is evidently incompatible with the assumption of the axisymmetry of a circular jet which is a major assumption in Michalke's spectral theory. However, since the magnitude of the quad-spectrum is almost negligible compared to that of co-spectrum, we may conclude that for practical purposes the jet is axisymmetric.

4.4.2 Fourier decomposition of coherence function

The coherence data shown in Figure 68 and 69 were then sampled at thirteen arbitrarily selected frequencies and expanded in terms of a Fourier series with respect to the azimuthal angle.

$$\gamma = \sum_{m=o}^{\infty} b_{\omega m} \cos m\Delta\phi \qquad (4.4.1)$$

For a strictly axisymmetric circular jet, the coherence function is equivalent to the co-spectrum of the cross spectral density. Then we have

$$\gamma = \frac{c_{\omega}(\Delta\phi)}{G_x(\omega)} = \sum_{m=0}^{\infty} \frac{c_{\omega m}}{G_x(m)} \cos m\Delta\phi \ , \qquad (4.4.2)$$

where $c_{\omega}(\Delta\phi)$ is the co-spectrum of the cross spectral density of the signals sampled when the moving microphone is separated from the stationary one by $\phi = \Delta\phi$ and $G_x(\omega)$ represents the power spectral density.

For $\Delta\phi = 0$, Eq. 4.4.2 can be written as

$$\sum_{m=o}^{\infty} \frac{c_{\omega m}}{G_x(\omega)} = 1 \ . \qquad (4.4.3)$$

This means that Fourier coefficients in Eq. 4.4.2 are nothing more than the PSD of the individual azimuthal components of the radiated sound. These components will be designated as $\{G_x(\omega)\}_m$ (Michalke and Fuchs, 1975).

Combining Eqs. 4.4.1, 4.4.2 and 4.4.3, we obtain

$$\{G_x(\omega)\}_m = C_{\omega m} = G_x(\omega) b_{\omega m}$$

or, in a logarithmic form,

$$(PSD)_{\omega m} = 10 \log b_{\omega m} + PSD \ (dB) \qquad (4.4.4)$$

where PSD is an overall power spectral density and $(PSD)_{\omega m}$ corresponds to a single azimuth-frequency component of the PSD.

Figure 71 displays normalized azimuthal coefficients for two Strouhal numbers computed from the coherence data. The ordinate in Figure 71 represents a normalized co-spectrum, namely the co-spectrum c_ω divided by power spectral density $\hat{p}^2_\omega$. Near field data obtained by Fuchs (1973) are also illustrated. It is seen that higher frequency component falls off more rapidly with increasing azimuthal angle. It is interesting to note that the far field decaying profile is fairly similiar to that of the near field observed in the center of shear layer at X/D = 3. From this we may speculate that that portion of the mixing layer where the mean velocity gradient is the largest is the dominant noise source region.

Figure 72 contains the Fourier coefficients of the decomposed coherence function for four different Strouhal numbers. In the present study, the first fifteen azimuthal modes were considered. Only the first few modes have any practical importance for Strouhal frequencies lower than Sh = 1.0, and the m = 0 and m = 1 modes are noticeably dominant at such low frequencies. However, for higher frequencies the higher azimuthal components have equal importance in the radiated sound.

These results are favourably in agreement with the near field data reported by Fuchs (1973). For very low frequencies, the axisymmetric mode is overwhelmingly strong. This may justify the concept of the ring model of jet turbulence in limited regions of flow where low frequency sound is predominantly produced.

Normalized Fourier coefficients of the coherence functions for the Strouhal frequencies $0.074 \leq Sh \leq 1.284$ are shown in Figure 73. We see that at about Sh = 1.0, the first helical model (m = 1) becomes predominant. It may be remarked, therefore, that the ring model is not appropriate to

describe the statistical behavior of jet turbulence near the orifice where most of the high frequency sound is produced.

4.4.3 Fourier decomposition of power spectral density

A measured power spectral density can be readily expanded into single azimuthal components by means of Eq. 4.4.4. The results are presented in Figure 74 together with the prediction for the axisymmetric component. Here, the solid line (top) is the directly measured power spectral density of the 12.7 mm jet at M = 0.58 and $\hat{\theta}$ = 30° to the jet axis. The line with circles represents the contribution to the overall spectrum by the axisymmetric component. Similarly, the line with crosses represents the m = 1 mode, while the line with triangles corresponds to the m = 2 mode. The dotted-line is the prediction for the m = 0 mode. We see that in the most important Strouhal number range $0.1 \leq Sh \leq 1.0$, within which most of the radiated sound is contained, only the first two modes have any practical importance, and the difference in the intensity between these two modes falls between 2 and 5 dB. The m = 1 mode is stronger than the m = 2 mode by a factor of 4 to 10 dB. One may deduce that increasing the mode number by one is coupled with, roughly, doubling the difference in the intensity for the range of Strouhal numbers $0.1 \leq Sh \leq 1.0$. A rather drastic decay of the profiles for Sh > 0.5 was unexpected. At about Sh = 1.2, the dominance of the axisymmetric modes ceases and the first helical mode becomes dominant. Hence, as previously discussed, the turbulence structure of a jet near the orifice seems to be inadequately modelled by the evenly spaced ring votices which always remain phase-locked circumferentially as proposed by Lau et al. (1972).

As is evidenced from Chan's experimental results (Chan, 1976), the lateral source extent $\hat{R}$ is a function of Strouhal number, as well as, distance X. As an approximation, however, a mean value of $\hat{R}$ over $0.1 \leq Sh \leq 1.0$ and $0 \leq X/D \leq 10$ may be used for the evaluation of the predicted intensity. The dotted-line in Figure 74 and the dash-two dots-line in Figure 75 are the predicted intensities for the $m = 0$ computed with $\hat{R}$ which is assumed to be independent of Sh and X. The solid-line in Figure 75 was derived with $\hat{R}$ which is considered to be a function of Strouhal number. In Figure 74, the prediction was fitted so as to make the data coincide at $Sh = 0.340$, while in Figure 75 the theoretical curves are fitted at $Sh = 0.5$. It is seen in Figure 74 that the theory apparently overestimates in the high frequency range by a factor of about 2 dB while for low frequencies it falls off drastically, yielding a noticeable disagreement with the observations. However, as can be noted from Figure 75, this inconsistency observed in lower frequency range may be reduced by adopting $\hat{R}$ which is a function of frequency. This is rather reasonable consequence of the fact that $\hat{R}$ is, approximately, inversely proportional to frequency. Stated another way, the lateral source extent $\hat{R}$ is more sensitive to frequency at lower frequencies. It has been confirmed that the wavy profile of the solid-line seen in Figure 75 can be smoothed out with increasing accuracy of the numerical computation of Eq. 3.2.5, and that this is not a real property of the noise signal. Although the analysis reported herein is limited to a rather narrow frequency range, it may be remarked that the predictions are in good agreement with the observations.

4.4.4 Predicted directivity of radiated sound compared with experiments

As has been discussed in Chapter III, the directivity of a sound pressure component $P_m(\omega)$ given by Eq. 3.2.5 is considerably sensitive to the jet thickness parameter $k\hat{R}\sin\hat{\theta}$ and the convection parameter $\alpha L[1 - M_c\cos\hat{\theta}]$ as well. It also depends on the azimuthal mode m, but is generally not very sensitive to the axial and lateral source distribution functions. This has been already pointed out by Michalke (1970a) and can be seen in Figure 76 where the longitudinal and lateral source integrals defined by Eqs. 3.2.6 and 3.2.7 are shown in terms of $\alpha L[1 - M_c\cos\hat{\theta}]$ and $k\hat{R}\sin\hat{\theta}$, respectively. Here, $|I_x|^2$ is common to all the azimuthal modes, and $|I_r|_o^2$, $|I_r|_1^2$ and $|I_r|_2^2$ correspond to the m = 0, 1 and 2, respectively. It may be surprising to note how the values of these integrals drastically decay with the parameters for the m = 0 mode. The low efficiency of jet turbulence as a noise source is obviously attributed to this abrupt decaying character of the source integrals. From a practical viewpoint, this strong dependence of sound pressure on these parameters is one of the major drawbacks of Michalke's spectral theory. For a given frequency and emission angle in a specified jet, we may write as $k\hat{R}\sin\hat{\theta}\propto\hat{R}$ and $\alpha L[1 - M_c\cos\hat{\theta}]\propto L$. This means that even small errors associated with the $\hat{R}$ and L will strongly affect the prediction of the intensity of the radiated sound. A close examination of Chan's (1976) experimental works tells us that at the present state of art, a precise determination of $\hat{R}$ and L cannot be expected.

Figure 76 shows that at $\hat{\theta} = 90°$ and for $k\hat{R} \leq 3$, the lateral source integral of the m = 0 mode, i.e. $|I_r|_o^2$ is predominant. The most effective source of sound with wavelengths that are large compared with $2\hat{R}$ is evidently the first azimuthal constituent of turbulence (m = 0).

For smaller wavelengths, the contributions by higher modes become more important.

The directivities of narrow band jet noise of the 12.7 mm jet at M = 0.58 are illustrated in Figure 77 for four different Strouhal numbers together with the predictions for the m = 0 and 1 modes. These directivities were directly computed with an IBM 370 using Eq. 3.2.5. The dotted-line is the measured power spectral density which is nothing more than a synthesis of an infinite number of frequencies and modes. The solid-line represents the predicted directivity for m = 0, whereas the dashed-line corresponds to the prediction for the m = 1. The prediction for the m = 0 mode was fitted so as to make data coincide at $\hat{\theta} = 30°$ and Sh = 0.5. The absolute magnitude of the predicted intensity for the m = 1 mode was then automatically determined. It has been confirmed in the present study that the directivity of narrow band limited noise is dominated by the contribution of the axisymmetric and the first helical modes in the Strouhal number range $0.1 \leq Sh \leq 1.0$. This is the reason why only the first two modes are shown in Figure 77.

In Figure 77a, a monotonic decaying profile of the m = 0 mode with increasing emission angle is illustrated for Strouhal number Sh = 0.4. The contribution by the m = 0 mode to the overall power spectral density is at least 5 dB larger than that by the m = 1 mode for the emission angle, $0° \leq \hat{\theta} \leq 60°$. This apparently indicates that the sound energy radiated in this range of emission angle is mostly attributed to the axisymmetric constituent of the noise sources in jet turbulence.

Next, it should be noted that the directivity pattern of the m = 0 mode falls off drastically at about $\hat{\theta} = 70°$. This seems to be not realistic, but at this point no explanation is available on this peculiar

behavior. With increasing emission angle, the contribution by the m = 1 becomes stronger and at about $\hat{\theta}$ = 70° the m = 1 mode overpowers the m = 0 mode. In fact, at $\hat{\theta}$ = 90° we see more than a 25 dB difference between the two.

Apparently, the prediction overestimates near $\hat{\theta}$ = 90°. A peak observed at $\hat{\theta}$ = 30° in the profile of the m = 1 mode (Figure 77a) shows a trend to shift to larger radiation angle with increasing frequency. Figure 77b represents directivities for Sh = 0.6. Note a quite different profile of the m = 0 mode in this case. It has a dip at about $\hat{\theta}$ = 75° and then recovers to -20 dB level with further increasing angle. For this frequency, its dominance ceases at about $\hat{\theta}$ = 62° and for larger angles the m = 1 mode overpowers the m = 0 mode. Again, the prediction scheme considerably overestimates the sideline noise. The peak seen in the profile of the m = 1 mode is now located near $\hat{\theta}$ = 40°, and its magnitude also has increased by a factor of 2 dB. The observed power spectral density still has a maximum value at the smallest emission angle. The directivities for Sh = 0.8 are seen in Figure 77c where the m = 0 mode becomes less important. Here we see that the maximum of the measured power spectral density now has moved to $\hat{\theta}$ = 30° to the jet axis. This effect is usually attributed to refraction. At large Strouhal numbers, the theory predicts that the maximum shifts further to $\hat{\theta}$ = 40°. This trend is found in the data of Mollo-Christensen et al., as shown in Figure 21. In Figure 77c, the contribution by the m = 1 mode becomes identical with that by the m = 0 mode at $\hat{\theta}$ = 60°, and for larger emission angles the directivity is dominated by the m = 1 mode. It should be pointed out here that the theory (m = 0) now overestimates at smaller emission angles too. This trend is also seen in Michalke's results

(Michalke and Fuchs, 1973) where the rms sound pressure directivities at a high frequency are strongest in the downstream direction. The overall power spectral density now has its maximum at near $\hat{\theta} = 40°$ for Sh = 1.0, as shown in Figure 77d. As has already been discussed in Chapter III, a pronounced peak at $\hat{\theta} = 40°$ for high frequency has been widely recognized, and this is evidently due to the peak of the m = 1 mode observed at about $\hat{\theta} = 40°$. In Figure 77d, at this emission angle the intensity of the m = 1 mode is almost identical with that of the m = 0. However, it has been confirmed by means of extrapolated data that for frequencies higher than Sh = 1.0, the contributions from the m = 1 mode overwhelm those by the m = 0 at this emission angle.

Similar directivity patterns are seen in Figure 78 for the 6.35 mm jet. However, in this case the measured power spectral density for Sh = 0.4 is not a monotonic decreasing function of the emission angle but has already a peak near $\hat{\theta} = 40°$. Although the prediction is in good agreement for the emission angles, $30° \leq \hat{\theta} \leq 70°$, the theory is not consistent with the observations for the axial and lateral emissions. Comparing Figures 77 and 78, we note the Reynolds number dependence of the power spectral density. However, the predictions do not take this dependency into account.

It has been confirmed in the present study, that even for far lower Reynolds numbers, the predicted directivities have similar profiles with those obtained for high Reynolds number jets. A discussion of the influence of variations in the parameters associated with Eq. 3.2.5 on the predicted directivity follows.

Michalke and Fuchs (1973) remakred, ". . . the directivity of a sound pressure component depends strongly on the jet thickness and

on the convection parameters, as well as on m, but seems to be not very sensitive to the spatial amplitude distributions of the source term component". Then they adopted suitably chosen amplitude distributions which were assumed to be independent of m and ω to calculate the directivities. However, the latter part of their statement does not hold true for high frequencies. Figure 79 contains directivity predictions for the m = 0 mode which are based on two different assumptions. The solid line was obtained with $\hat{G}(\bar{r})$ assumed to be independent of ω, whereas the dashed line was derived using $\hat{G}(\bar{r})$, which is a function of frequency. Evidently, for lower frequencies both are almost identical, but with increasing Strouhal number the difference between the two becomes pronounced. This may be attributed to the fact that near the jet center line the pressure distributions for high frequencies show a remarkable scattering and do not scale as any parameter involving Strouhal number (see Figure 7 of Chan, 1976). The axial pressure amplitude distribution $\hat{F}(\bar{x})$, on the contrary, scales considerably well with the normalized Strouhal number X(Sh)/D for higher frequencies than Sh = 0.3 as shown by Chan (1976).

As has been repeatedly pointed out, both the axial and lateral source extents are very sensitive to the prediction of directivity, particularly for small emission angles. Hence, precise determination of these parameters is essential for the accurate prediction of the acoustic field.

4.4.5 Coherent structure of jet turbulence deduced from circumferential cross-correlation measurements

The eddy-model of jet turbulence formulated on the assumptions of an isotropic structure and small correlation volumes has been widely accepted because it enables one to predict the sound intensity contributed by the whole jet in a simple way.

However, as pointed out by Michalke (1970a), the assumption of a spatially random jet structure is not self-evident. Experimental results rather suggest the existence of turbulence components with high space correlation (Fuchs, 1971). Moreover, correlation measurements in the sound field also provide some evidence that jet turbulence has an orderly wave-like structure rather than being random in nature.

The coherence functions shown in Figures 68 and 69 were obtained from the circumferential cross-correlation measurements. There we note a strong azimuthal coherency over a rather broad range of Strouhal frequency. As has been pointed out previously, the strong azimuthal coherency is closely associated with the dominance of the axisymmetric mode in the radiated sound. This observation is one of the main results of the present investigation.

It is seen in Figure 74 that for Strouhal numbers lower than about Sh = 0.5, the measured power spectral density is dominated by the m = 0 mode. Moreover, most of the low frequency sound radiated to the downstream direction is produced in the fully developed region as is seen in the results of the coherent output power measurements (Figure 62b). Hence, one may speculate that the fully developed region of jet turbulence has a coherent recurring structure rather than being spatially random, and that this orderly structure may be properly modelled by axisymmetric ring vortices. Measurements in a wake also support this view. Namely, the far wake becomes increasingly coherent.

On the other hand, it has been confirmed that the sound radiated in the lateral direction has a higher frequency content than sound radiated at angles close to the jet axis, and, moreover, most of the high frequency sound is produced in the flow region near the jet exit. As is clearly

shown in Figures 77 and 78, the dominant mode which is observed in the lateral direction is not the axisymmetric one but the first helical mode of the source term in the Strouhal number range, $0,1 \leq Sh \leq 1,0$. This may reveal that jet turbulence in the region close to the nozzle orifice is less coherent in its structure than the flow structure observed further downstream. This is completely consistent with the conclusions obtained by Maestrello (1976) by means of his two-point correlations of sound pressure in the radiated field. We may argue, therefore, that this consistency between these two independent works would directly show the validity of Michalke's spectral theory on the basis of which the conclusions reported herein have been derived.

Chapter V

SUMMARY AND CONCLUSIONS

5.1 Summary

The objectives of this study were the quantitative investigation of the dependency of jet noise on Reynolds number, and the experimental verification of the validity of Michalke's spectral theory which is formulated on the assumption that the major noise sources in jet turbulence are orderly in its structure. The original reason for studying low Reynolds number jet flow was the conjecture that coherent structure would be more dominant at lower Reynolds numbers.

With these objectives in mind, an extensive series of flow and acoustic measurements in low Reynolds number turbulent jets has been carried out. Particular emphasis has been placed on the quantitative study of the narrow band spectrum characteristics of the flow and acoustic fields. All the experimental work reported herein was conducted in the anechoic chamber at NASA Lewis Research Center, Cleveland, Ohio.

Single hot-wire and hot-film probes were mainly used for flow measurements whereas B&K 6.35 mm condenser microphones were exclusively employed for acoustical measurements. Spectrum analysis of the signals sampled both in the flow and the acoustic field was accomplished with a Fast Fourier Transform (FFT) digital signal processor. Coherent output power measurements and circumferential cross-correlation measurements were conducted with the aim of detecting coherent structure in the jet turbulence. Much of this work would have been impossible without the full uitilization of the capability of the FFT analyzer.

5.2 Conclusions

In the present study, the Reynolds numbers under which flow and acoustic measurements were conducted were in the range of $8.93 \times 10^3 \leq R_e \leq 2.20 \times 10^5$. At these low Reynolds numbers, the jet axis was found to be helical-wave-like, and its deviation from the geometrical jet axis was found to be of the order of 1/50 of a diameter.

The results of the measurements of the circumferential distribution of turbulence intensity (u-component) indicate that the asymmetry of flow is obviously observed in a circular jet, and that this asymmetry of the jet flow has an effect on the radiated acoustic field. This was confirmed by the measurements of the cross spectral density of the circumferentially cross-correlated signals sampled in the far field. The results of the power spectral density measurements of jet turbulence are generally in good agreement with previously reported results (Lawrence, 1956; Davies et al., 1963).

Results of flow and acoustic far field measurements are as follows:

1. Mean velocity similarity in the transition and fully developed regions was observed in the jets with Reynolds number of the order of 10^4.
2. Results of the turbulence intensity measurements also indicate the existence of the helical-wave-like motion of jet turbulence, and its wavelength was found to be relatively large when compared with jet diameter.
3. The high frequency end of the near field energy spectrum observed on jet axis falls off not like $\omega^{-5/3}$ but like $\omega^{-4/3}$.
4. Vortex passing frequency was found to be not simply proportional to the jet efflux speed.

5. The observed directivity of radiated sound is consistent with the Phillips and Lilley's prediction.

In the present study, the validity of Michalke's spectral theory was first verified entirely with the experimental data obtained by Chan (1976) and Yamamoto and Arndt (1977). Chan's (1974a) prediction formula, Eq. 3.2.5 for the single azimuth-frequency component of jet noise based on the Michalke's expansion scheme was found to predict the power spectral density of the jet noise quite well. The predicted directivity of the radiated sound by the same formula is generally in good agreement with observations except at large emission angles.

To summarize, the results of the coherent output power and circumferential cross-correlation measurements are as follows:

1. For Strouhal numbers between 0.1 and 1.0, only the axisymmetric and the first helical modes have any practical importance in jet noise. Since an axisymmetric ring vortex model does not take into account this helical mode (Fuchs, 1974), this model is not adequate to describe jet flows, even at low Reynolds numbers.
2. The axisymmetric component radiates strongly in the downstream direction. In the lateral direction, however, the first non-axisymmetric component is dominant.
3. The peak directivity of high frequency sound can be explained by the m = 1 mode. This result is consistent with that observed by Michalke and Fuchs (1973).
4. A significant contribution from the potential core to the radiated sound was observed at directions close to jet axis.

5. The prediction based on Chan's (1974a) formula is in good agreement with observations for $0.2 \leq Sh \leq 1.0$ and $\hat{\theta} < 75°$. The predicted power spectral density for the m = 0 mode overestimates by as much as 3 dB at high frequencies.
6. The prediction of the sound intensity is found to be remarkably sensitive to the extent of longitudinal and lateral source distribution. Therefore, precise determination of these parameters is essential for the accurate prediction of the acoustic field.
7. Coherency is observed over a rather broad range of frequency at $\hat{\theta} = 30°$. From the directivity patterns, one may reasonably conclude that stronger coherency can be observed to be in the downstream direction rather than the lateral direction. This is consistent with the findings of Maestrello (1976).

The following conclusions may be made about the study of the dependence of jet noise on Reynolds number:

1. One of the most striking findings made in this regard is the existence of the critical Reynolds number associated with the narrow band peak frequency of jet noise. The critical value is approximately 10^5.
2. The peak frequency of narrow band spectrum of jet noise shifts to higher frequency with increasing emission angle only when Reynolds number based on exit velocity and jet diameter is in excess of approximately 10^5. At lower Reynolds numbers, the peak remains at a certain frequency irrespective of emission angle.
3. The peak Strouhal frequency increases monotonically with increasing Reynolds number. It would not be feasible to detect this peculiar property of jet noise with the octave or 1/3 octave band spectrum

analyzer, for the peak Strouhal frequency is a rather weak function of the Reynolds number, and the peak shift with Reynolds number may occur in the filter bandwidth of such a broad band analyzer.

5.3 Recommendations for Future Study

In the present study, the circumferential cross-correlation measurements are limited to the emission angle $\hat{\theta} = 30°$ from the downstream jet axis. A more complete comparison of the predicted directivity of sound intensity due to a single azimuth-frequency component of noise source with the experimental data would require that the correlation measurements be made over all space at emission angles between $\hat{\theta} = 0°$ and 180°.

As has been pointed out by Mollo-Christensen et al. (1964), the process of generation of turbulence may determine the structure of the sound field partly by sound emission from the transition process in jet flow. Therefore, a cross-correlation between fluctuating pressure or velocity signals sampled in the wall boundary layer of a jet nozzle, as well as, in the free shear layer and the sound signals in the far field will surely provide more useful information about the dependency of jet noise on Reynolds number, presumably revealing some key facts for the understanding of the nature of the peak frequency of jet turbulence.

REFERENCES

Abramovich, G. N., The Theory of Turbulent Jets, The MIT Press, Cambridge, Mass. (1963).

Ackerman, C. L., "Signal Processing," unpublished graduate lecture at The Pennsylvania State University (1974).

Ahuja K. K. and Bushell, K. W., "An Experimental Study of Subsonic Jet Noise and Comparison with Theory," J. S. and Vib., 30(3) (1973).

Arndt, R. E. A. and Yamamoto, K., Semi-Annual Progress Report submitted to NASA Lewis Research Center (1976).

Bendat, J. S. and Piersol, A. G., Random Data, Analysis and Measurement Procedures, Wiley Interscience, New York (1971).

Chan, Y. Y., "Pressure Sources for a Wave Model of Jet Noise," AIAA J., Vol. 12, No. 2 (1974a).

Chan, Y. Y., "Spatial Waves in Turbulent Jets," Physics of Fluids, Vol. 17, No. 1 (1974b).

Chan, Y. Y., "Noise Generated Wavelike Eddies in a Turbulent Jet," ICAS paper, No. 76-42 (1976).

Crow, S. C. and Champagne, F. H., "Orderly Structure in Jet Turbulence," J. Fluid Mech., 48, 3 (1971).

Davies, P. O. A. L., Fisher, M. J., and Barratt, M. J., "The Characteristics of the Turbulence in the Mixing Region of a Round Jet," J. Fluid Mech., 15, 337-367 (1963).

Enochson, L. D. and Goodman, N. R., "Gaussian Approximation to the Distribution of Sample Coherence," AFFDL TR65-57 (1965).

Ffowcs-Williams, J. E., "Impulsive Sources of Aerodyanmic Sound," AGARD-CP-131, Tech. Eval. Rep. (1974).

Fuchs, H. V., "Eigenshaften der Druckschwankungen in subsonischen Freistrahl," Paper Code No. N6, presented at the 7th Intern. Cong. Acoustics CI(A), Budapest (1971).

Fuchs, H. V., "Measurements of Pressure Fluctuations Within Subsonic Turbulent Jets," J. S. and Vib.22(3) (1972).

Fuchs, H. V., "Resolution of Turbulent Jet Pressure into Azimuthal Components," presented at AGARD Specialists' Meeting, Brussel, 19-21 (1973).

Fuchs, H. V., "Analysis of Circumferentially Coherent Pressure Fluctuations Relevant to Jet Noise," Colloquium on Coherent Structure in Turbulence, Southampton (1974).

Goldstein, M. E., Aeroacoustics, McGarw-Hill, New York, NY (1976).

Gradshteyn, I. S. and Ryzhik, I. M., Table of Integrals, Series and Products, Academic Press, New York (1965).

Hinze, J. O., Turbulence, 2nd Edition, McGraw-Hill, New York (1975).

Jenkins, G. M. and Watts, D. C., Spectral Analysis, Holden-Day (1969).

Lau, J. C., Fuchs, H. V., and Fisher, M. J., "A Study of Pressure and Velocity Fluctuations Associated with Jet Flows," Univ. Southampton, ISVR, Techn. Rep. 28 (1970).

Lau, J. C., "The Coherent Structure of Jets," Ph.D. Thesis, University of Southampton (1971).

Lau, J. C., Fisher, M. J., and Fuchs, H. V., "The Intrinsic Structure of Turbulent Jets," J. S. and Vib., 22(4) (1972).

Lawrence, J. C., "Intensity, Scale and Spectra of Turbulence in Mixing Region of Free Subsonic Jet," NACA Rep. 1292 (1956).

Lee, H. K., "Correlation of Noise and Flow of a Jet," UTIAS Rep. 168 (1971).

Lighthill, M. J., "On Sound Generated Aerodynamically I, General Theory," Proc. Roy. Soc. London, 211, Ser. A (1952).

Lilley, G. M., "Generation of Sound in a Mixing Region," 4th Monthly Prog. Rep. on Contract F-33615-71C-1663, Lockheed Aircraft Co., Marietta, GA (1971).

Liu, J. T. C., "Developing Large Scale Wavelike Eddies and the Near Jet Noise Field," J. Fluid Mech., 62, 3 (1974).

Liu, J. T. C., "The Large Scale Wavelike Eddies and Their New and Far Jet Noise Field," Proc. 3rd Interagency Symposium on University Research in Transporation Noise, U. of Utah (1975).

Lush, P. A., "Measurements of Subsonic Jet Noise and Comparison with Theory," J. Fluid Mech., 46.3 (1971).

Maestrello, L., "Two-Point Correlations of Sound Pressure in the Far Field of a Jet: Experiment," NASA TMX-72835 (1976).

MacLaughlin, O. K., Morrison, G. L., and Troutt, T. R., "Reynolds Number Dependence in Supersonic Jet Noise," AIAA Paper No. 76-491 (1976).

McCartney, J. R., "Ratio of Peak Frequencies of Jet Self and Shear Noise Spectra," Sound and Vib., 39 (2) (1975).

Meecham, W. C., "Acoustic Spectra from Turbulent Jets," NASA SP-207 (1969).

Michalke, A., "A Wave Model for Sound Generation in Circular Jets," DLR FB 70-57 (1970a).

Michalke, A., "A Note on the Spatial Jet Instability of the Compressible Cylindrical Vortex Sheet," DRL FB 70-51 (1970b).

Michalke, A., "Instabität eines kompressiblen runden Freistrahls unter Berücksichtigung des Einflusses der Strahlgrenzschicht," Z. Flugwiss., 19 (1971).

Michalke, A., "An Expansion Scheme for the Noise from Circular Jets," Z. Flugwiss., 20 (1972a).

Michalke, A., "New Aspects of Sound Generation by Circular Jets," Fluid Dynamics Transaction 6 (1972b).

Michalke, A. and Fuchs, H. V., "Aerodynamic Noise Theory," In Prog. Aero. Sci., Pergamon Press, Oxford, 14 (1973).

Michalke, A., "On the Instability of the Turbulent Jet Boundary Layer," DLR-Mitt, 74-25 (1974).

Michalke, A. and Fuchs, H. V., "On Turbulence and Noise of an Axisymmetric Shear Flow," J. Fluid Mech., 70, 1 (1975).

Mollo-Christensen, E., Kolpin, M. A., and Martuccelli, J. R., "Experiment in Jet Flow and Jet Noise Far-Field Spectra and Directivity Patterns," J. Fluid Mech., 18 (1964).

Mollo-Christensen, E., "Jet Noise and Shear Flow Instability Seen from an Experimenter's Viewpoint," ASME J. Appl. Mech., Ser. E, 89 (1967).

Norman, B. O., "Hot-Wire Anemometer Calibration at High Subsonic Speeds," DISA Information, No. 5 (1967).

Olsen, W. and Karchmer, A., "Lip Noise Generated by Flow Separation from Nozzle Surfaces," AIAA paper No. 76-3 (1976).

Pao, S. P. and Lowson, M. V., "Spectral Technique in Jet Noise Theory," Wyle Laboratories Rep. WR68-21 (1969).

Pfizenmaier, E., "On the Structure of Velocity and Pressure Fluctuations in a Sound Influenced Free Jets," Colloquium on Coherent Structures in Turbulence, Southampton (1974).

Phillips, O. M., "On the Generation of Sound by Supersonic Turbulent Shear Layers," J. Fluid Mech., 9, 1 (1960).

Ribner, H. S., "Aerodynamic Sound from Fluid Dilations," UTIA Rept. 86, AFOSRTN 3430 (1962).

Ribner, H. S., "Quadrupole Correlations Governing the Pattern of Jet Noise," J. Fluid Mech., 38, 1 (1969).

Ribner, H. S and Lee, H. K., "Direct Correlation of Noise and Flow of a Jet, " AIAA Paper No. 72-640 (1972).

Seiner, J. M., "The Distribution of Jet Source Strength Intensity by Means of a Direct Correlation Technique," Ph.D. Thesis, The Pennsylvania State University (1974).

Smith, R. H. and Wang, C. T., "Contracting Cones Giving Uniform Throat Speeds," J. Aeron. Sc. (1944).

Spectral Dynamics Corporation, Instruction Manual Vol. 2, SD-360 Digital Signal Processor Operation (1975).

Stone, J. R., "Interim Prediction Method for Jet Noise," NASA TMX-71618 (1974).

Tennekes, H. and Lumley, J. L., A First Course in Turbulence, The MIT Press, Cambridge, Mass. (1972).

Winant, C. D. and Browand, F. K., "Vortex Pairing: the Mechanism of Turbulent Mixing Layer Growth at Moderate Reynolds Number," J. Fluid Mech., 63, 2 (1974).

Wooldridge, C. E., Wooten, D. C., and Amaro, A. J., "The Structure of Jet Turbulence Producing Jet Noise," NASA Annual Report, N72-15625 (1971).

Yamamoto, K. and Arndt, R. E. A., "Azimuthal Decomposition of the Power Spectral Density of Jet Noise," presented at the 93rd Meeting of ASA, June 7 (1977).

Appendix A

ERROR ESTIMATE FOR POWER SPECTRAL DENSITY AND COHERENCE FUNCTION

One of the most common performance measures for evaluating broadband spectral estimates is the confidence interval. Suppose a quantity A is expected to fall within $A \pm \delta$, where δ represents a small degree of uncertainty. Then, the interval $[A - \delta, A + \delta]$ associated with this confidence statement is referred to as a confidence interval, while the degree of trust associated with the confidence statement is called a confidence coefficient.

Distribution of the power spectral density (PSD) estimate about the true value follows a Chi-square distribution with the statistical confidence of the data estimate increasing as the number of ensembles increases. However, the improvement in the PSD estimates is a converging function of the number of ensembles included and generally a number between 64 and 512 is considered adequate for the ensembles.

The SD-360 Digital Signal Processor performs a frequency analysis on any given sample of data with two statistical degrees of freedom, and by averaging the spectral ensembles the statistical degrees of freedom figure is increased by the number of independent samples averaged. Throughout the entire spectral meaurements of the present study, a number, 256, has been adopted for ensembles.

The confidence interval for PSD estimate expressed in terms of decibel is given by

$$\left[10\log\hat{G} + 10\log\frac{\eta}{\chi_\eta(1-\frac{\alpha}{2})}\ ,\ 10\log\hat{G} + 10\log\frac{\eta}{\chi_\eta(\frac{\alpha}{2})}\right]\ , \qquad (A.1)$$

where $\hat{G}$ is a PSD estimate and η represents the degrees of freedom. The confidence coefficients are determined based on the Chi-square distribution with η degrees of freedom (Jenkins and Watts, 1969). In the present study, the degrees of freedom was 512, yielding the 99% confidence interval of

$$[10\log\hat{G} - 0.46,\ 10\log\hat{G} + 0.53]\text{dB} \quad .$$

The coherence function estimate $\hat{\gamma}^2(f)$ for two random processes is defined by

$$\hat{\gamma}^2(f) = \frac{|\hat{G}_{xy}(f)|^2}{\hat{G}_x(f)\hat{G}_y(f)} \tag{A.2}$$

where $\hat{G}_{xy}(f)$ represents a cross spectral density estimate. It has been established that the $(1 - \alpha)$ confidence interval for $\gamma^2(f)$ is given by

$$\tanh[H(f) - (\eta - 2)^{-1} - \sigma_h Z_{\alpha/2}] < \gamma(f)$$

$$\leq \tanh[H(f) - (\eta - 2)^{-1} + \sigma_h Z_{\alpha/2}] \quad , \tag{A.3}$$

where

$$H(f) = \tanh^{-1}\hat{\gamma}(f) \quad , \tag{A.4}$$

$$\sigma_h^2 = (\eta - 2)^{-1}$$

and Z_α is the $100\alpha\%$ point of the standardized normal distribution (Enochson and Goodman, 1965).

The number of ensembles used for the measurements of the coherence functions reported in Section 4.4 was 2048. In this case, the 99% confidence interval for $\gamma^2(f)$ is given by

$$\tanh\{H(f) - 0.0402\} \leq \gamma(f) \leq \tanh\{H(f) + 0.0398\} \quad ,$$

where H(f) can be determined by Eq. A.4.

Appendix B

PHASE VELOCITY MEASUREMENTS IN ACOUSTICALLY FORCED JETS

As has been discussed in Chapter III, the intensity of sound due to a single azimuth-frequency component of noise source in a jet turbulence is dependent on several parameters associated with the pressure fluctuations in the flow. The results presented in Section 4.4 are based on Chan's (1976) observations in an acoustically excited jet. Before adopting his results to evaluate Eq. 3.2.5, phase velocity measurements in an acoustically forced jet were undertaken to confirm his results with the 12.7 mm jet at selected exit Mach numbers.

Figure 80 shows the schematic diagram of the phase velocity measurements. An acoustic driver was located in the settling chamber to provide periodic forcing in the flow. In this experiment, two forcing frequencies (f = 4.26 and 6.72 KHz) were used. The input power from an audio-frequency generator was set to 0.9 watts. A B&K 6.35 mm microphone was located in the settling chamber. The signals from this sensor were cross-correlated with those sampled by a hot-wire traversing along the jet axis.

The phase of the cross spectral density (CSD) of the cross-correlated signals was directly plotted on the XY-recorder by way of the SD-360 FFT analyzer as a function of the hot-wire distance. Exponential averaging was used in this experiment which produces a time-running average of the data, and the number of the ensembles selected was 64. The traversing speed of the hot-wire probe was set to 0.254 mm/sec. The phase shift between microphone and hot-wire signals is illustrated as a function of axial distance in Figure 81. Plotting of the phase shift shown in the

figure was conducted as follows. An analysis Function 5 on the SD-360 was selected. The sampled signals from the microphone and the hot-wire probe were then introduced into the SD-360 through two channels. Exponential averaging was selected, and after the averaging was completed, the XY-recorder displayed the averaged CSD of the input signals as log-amplitude versus linear frequency in the lower trace. In the upper trace, the corresponding phase angle between the two input data signals was displayed. Then, the cursor (intensity marker) was fixed at the specified forcing frequency in the upper trace of the scope display. During the time that the output singals from the Y-terminal of the SD-360 was being introduced into the XY-recorder, giving a phase angle (degrees) in linear Y-scale, the hot-wire probe was being traversed downstream along the jet axis with a speed of 0.254 mm/sec. The cursor can follow the processed data on the scope to any selected location. The actuator signals were introduced into the x axis of the plotter. Thus, simultaneously with the probe traversing, phase shifts versus axial distance were recorded on the XY-recorder.

The wavelength and the phase velocity of the spatial pressure waves along the jet can be readily evaluated from the results shown in Figure 81. In this case, the Strouhal number of the pressure wave is 0.39, and the corresponding normalized phase velocity c_{ph}/U_j has a value between 0.69 and 0.75. This agrees quite favorably with Chan's results for the m = 0 mode (Chan, 1976).

The axial distributions of the peak value of PSD of the velocity fluctuations with and without forcing are shown in Figures 82-84. We note in Figure 82 that the disturbances given by forcing first amplify up to about X/D = 4 and then gradually decay off, and completely lose

their energy before arriving at about X/D = 10. A similar trend is seen in Figure 83 with a forcing frequency f = 6.72 KHz. It should be pointed out that there exists a preferable forcing frequency for each jet. This can be seen by comparing Figures 83 and 84. The most effective forcing frequency was found to be identical with the peak frequency of the velocity fluctuations observed at X/D = 4 on the jet axis.

Table 1

Nozzle Characteristics

SIZE		0.79 mm	1.59	3.18	6.35	12.7
M	0.2	0.36×10^4	0.73×10^4	1.45×10^4	0.29×10^5	0.58×10^5
R_e	0.5	0.90×10^4	1.82×10^4	3.63×10^4	0.73×10^5	1.45×10^5
	0.8	1.45×10^4	2.90×10^4	5.83×10^4	1.16×10^5	2.32×10^5
	0.2	26.1 KHz	12.9	6.5	3.2	1.6
f_p	0.5	65.1	32.4	16.2	8.1	4.1
	0.8	104.2	51.8	25.9	12.9	6.5
	0.2	0.02 m	0.05	0.09	0.18	0.37
R	0.5	0.89	1.8	3.6	7.2	14.4
	0.8	5.86	11.7	23.6	47.1	94.2
	0.2	0.07	0.29	1.14	4.56	18.24
CFM	0.5	0.18	0.71	2.85	11.41	45.6
	0.8	0.29	1.14	4.56	18.24	72.9

Reynolds number: $R_e = \frac{UD}{\nu}$

Peak frequency: $f_p = \frac{0.3U}{D}$

Mach number: $M = \frac{U}{343}$

Microphone distance from nozzle where OASPL is 60 dB at $\hat{\theta} = 90°$: R

Volume flow rate: CFM

Table 2

Experimental Conditions for Coherent Output Power Measurements

Jet exit diameter	$D = 6.35$ mm
Jet exit velocity	$U_j = 136.3$ m/sec
Resolution bandwidth	$\Delta f = 60$ Hz
Bandpass filter range	$1 \text{ KHz} \leq f \leq 24 \text{ KHz}$
Correlation delay	$\Delta\tau = 16.28$ μsec
Memory period	$T = 1.667 \times 10^{-2}$ sec
Mode of averaging	Linear ensemble (2^8)
Hot-wire probe	DISA 55P11
Microphone	B&K 6.35 mm Type 4135
Axial probe position	$2 \leq X/D \leq 10$
Radial probe position	$0 \leq Z/D \leq 1.0$
Strouhal number	$0.15 \leq Sh \leq 0.9$

Table 3

Experimental Conditions for Coherence Function Measurements

Jet exit diameter	D = 12.7 mm, 6.35 mm
Jet exit velocity	U_j = 201 m/sec
Resolution bandwidth	Δf = 100 Hz
Bandpass filter range	1 KHz $\leq$ f $\leq$ 40 KHz
Correlation delay	$\Delta\tau$ = 9.77 μsec
Memory period	T = 1.00×10^{-2} sec
Mode of averaging	Linear ensemble (2^{11})
Microphone	B&K 6.35 mm Type 4135
Stationary microphone position	R = 60 D, $\hat{\theta}$ = 30°
Rotating microphone position	R = 60 D, $\hat{\theta}$ = 30°, $0° \leq \phi \leq 360°$
Strouhal number	$0.06 \leq Sh \leq 2.53$ $0.03 \leq Sh \leq 1.27$
Reynolds number	1.70×10^5 0.85×10^5

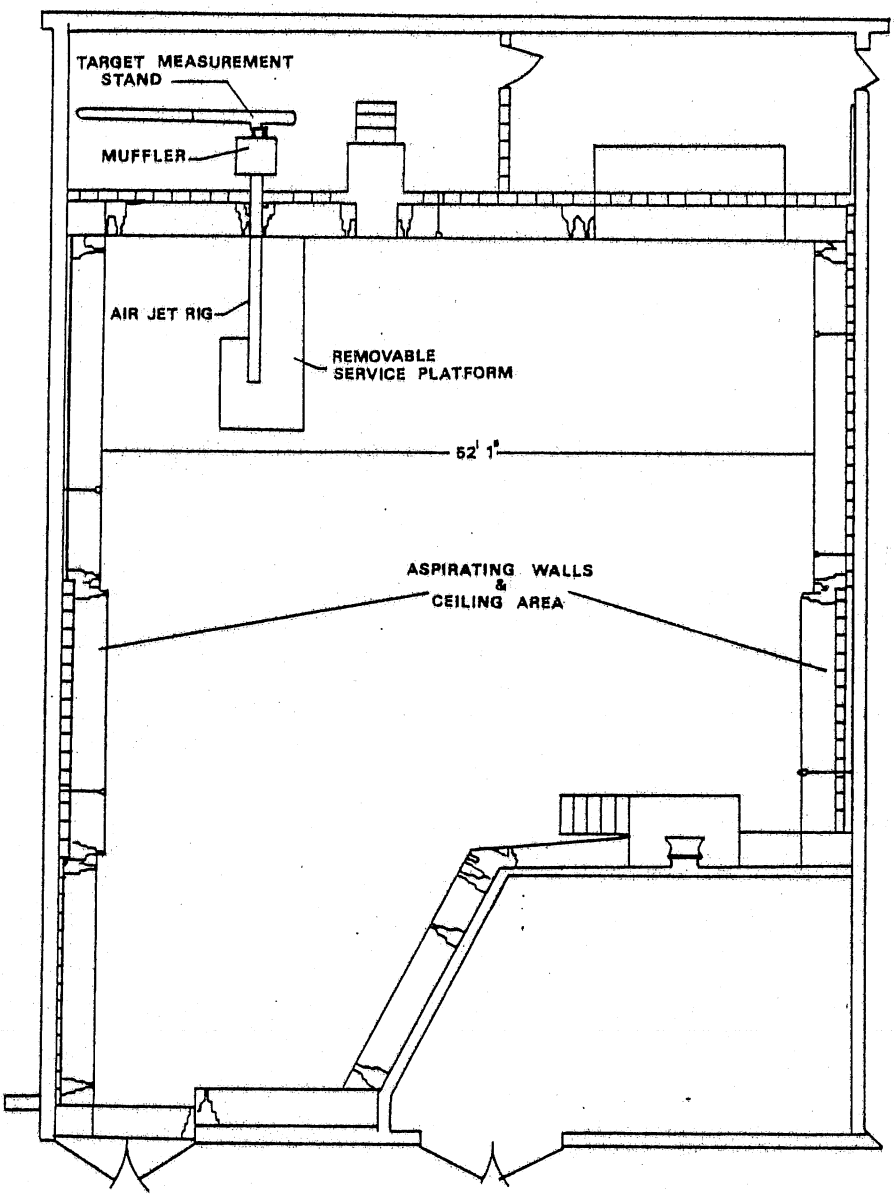

Figure 1: General Flow Plan of Anechoic Chamber

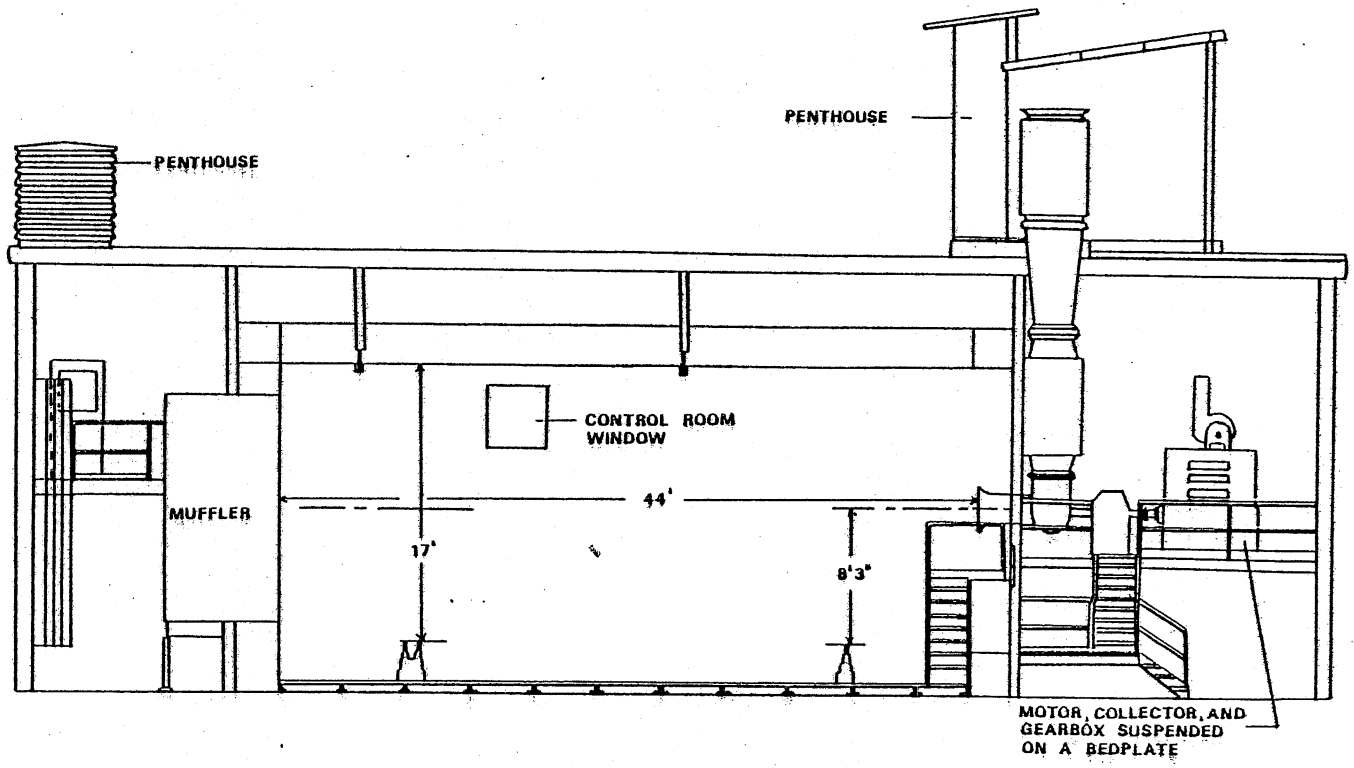

Figure 2: Elevation View of Anechoic Chamber

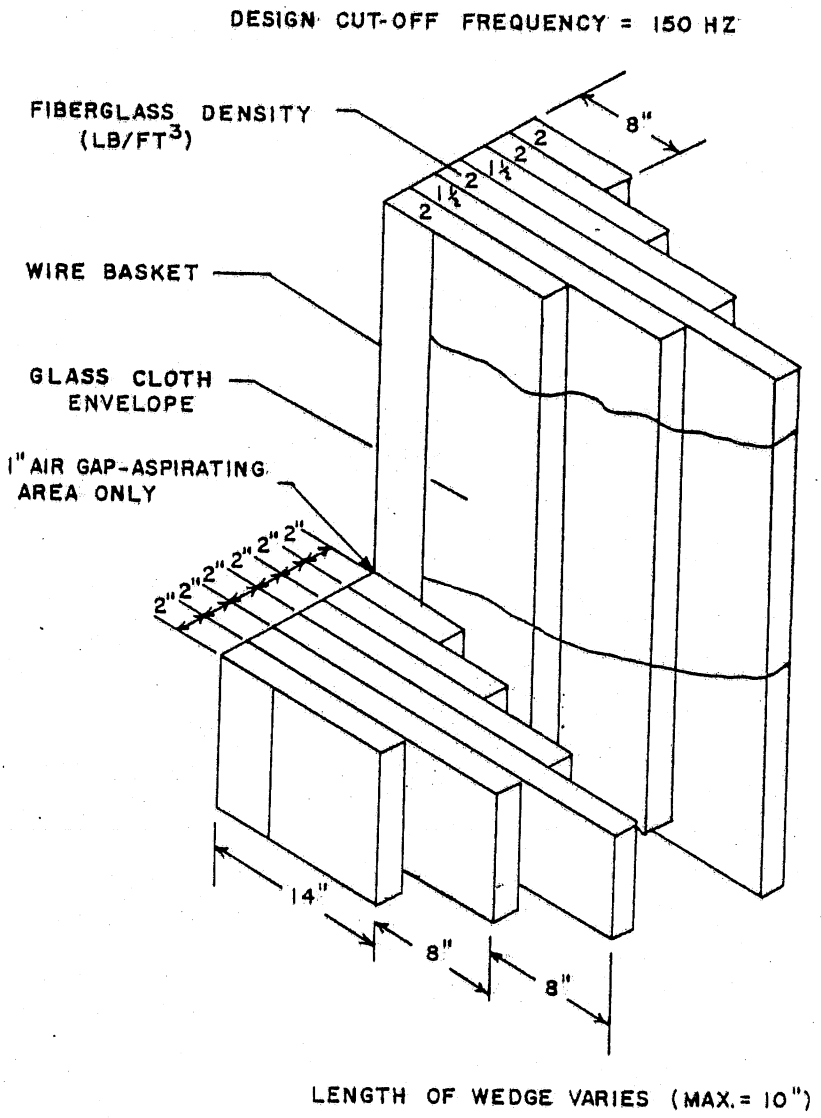

Figure 3: Isometric View of Acoustic Wedge

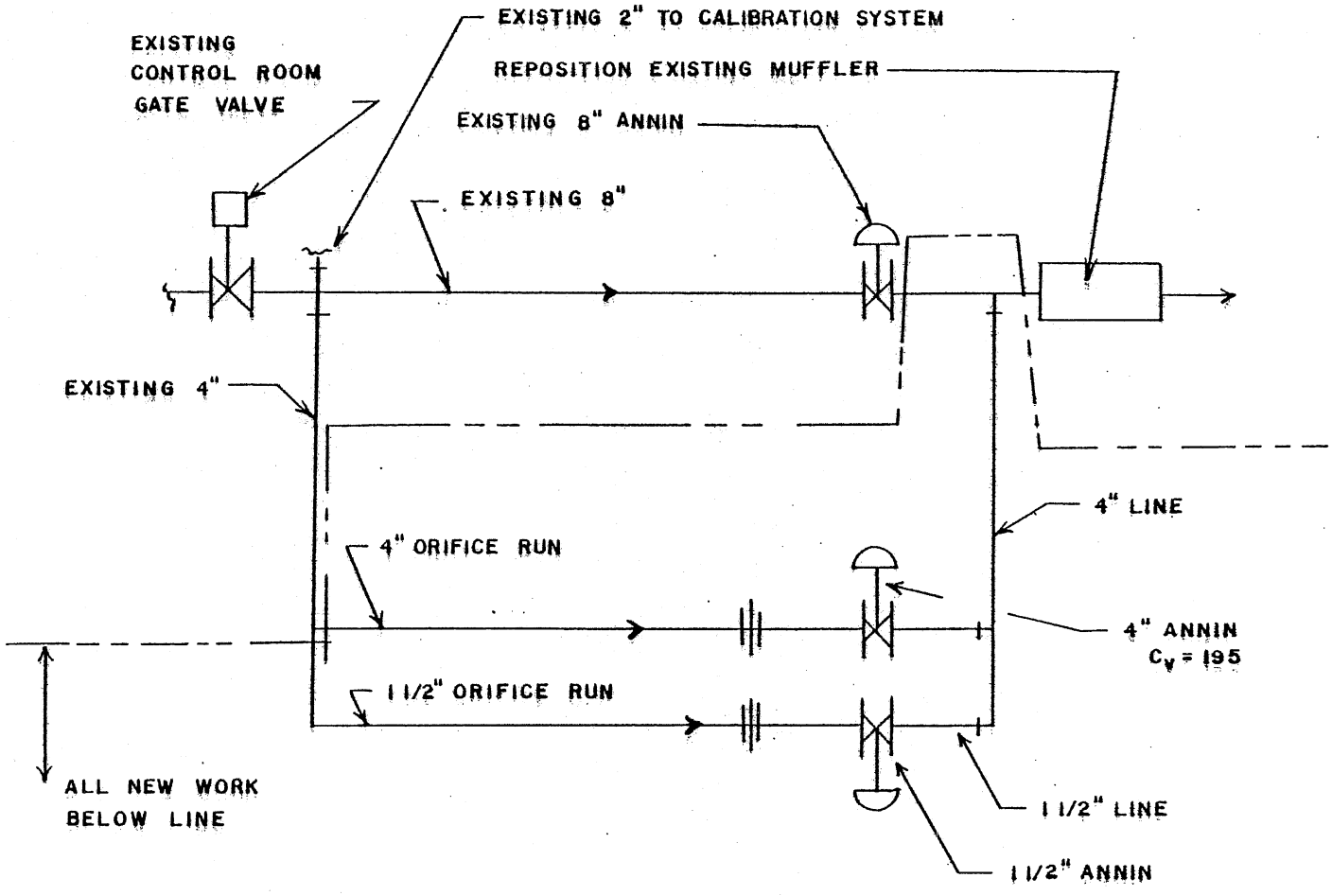

Figure 4: Flow Control System

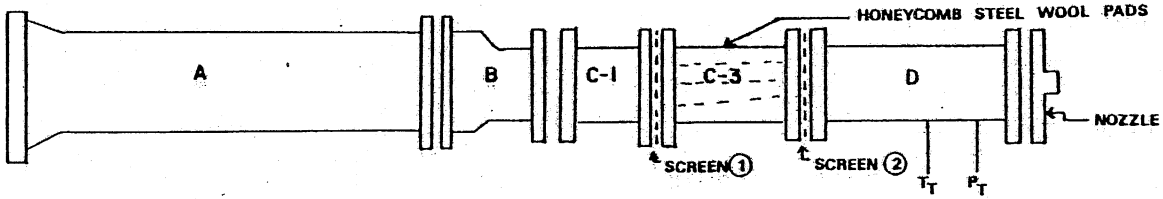

PIPE	LENGTH	NOMINAL DIAMETER
A	11' $3\frac{3}{4}$"	6"
B	7"	4"-6"
C-1	$5\frac{1}{2}$"	4"
C-3	$11\frac{1}{2}$"	4"
D	$31\frac{3}{4}$"	4"

NOZZLE	$\frac{1}{2}$"(12.7mm) $\sim\frac{1}{32}$" (0.79mm)					
SCREEN (1)	14 MESH,	0.025 WIRE,	0.046 OPENING,	41.5% OPEN AREA		
SCREEN (2)	20 MESH,	0.025 WIRE,	0.025 OPENING,	25% OPEN AREA		

Figure 5: Jet Nozzle Assembly

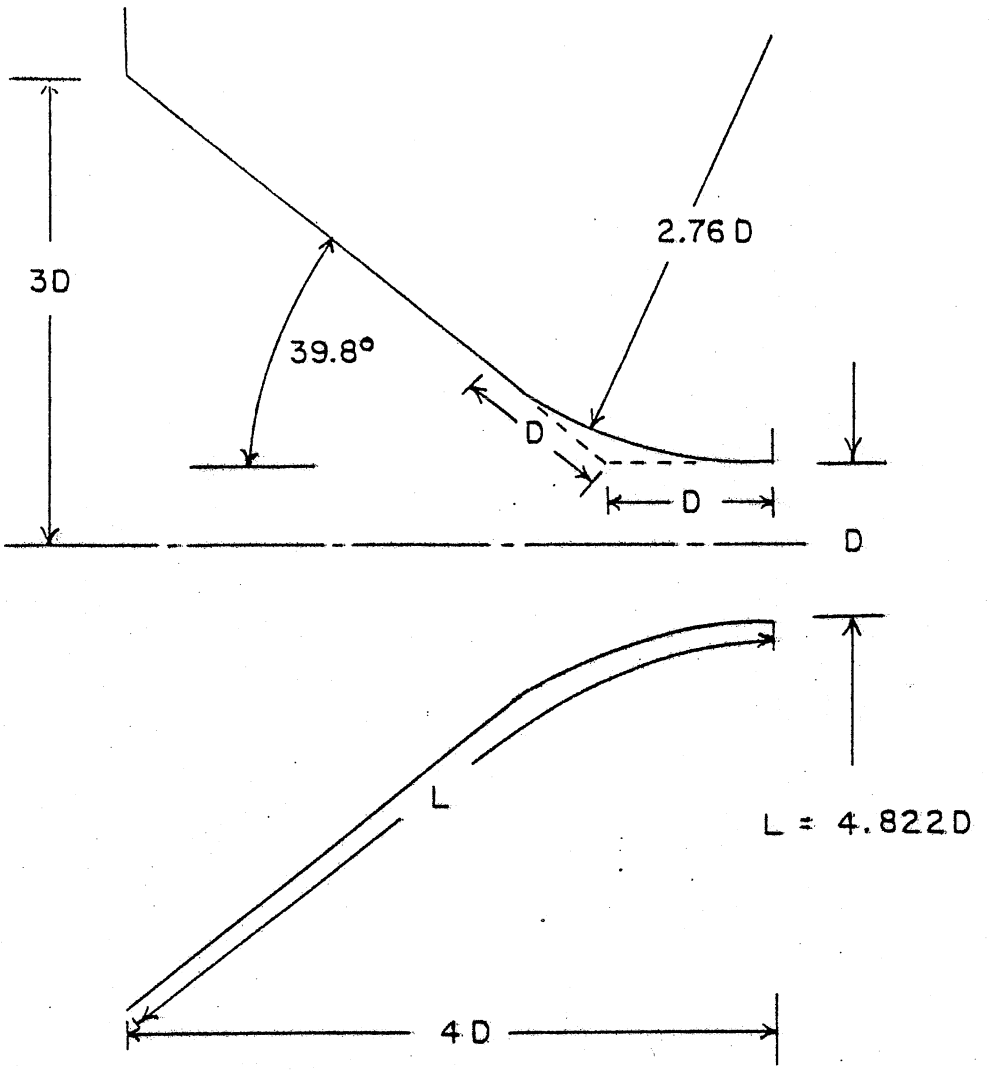

Figure 6: Jet Nozzle

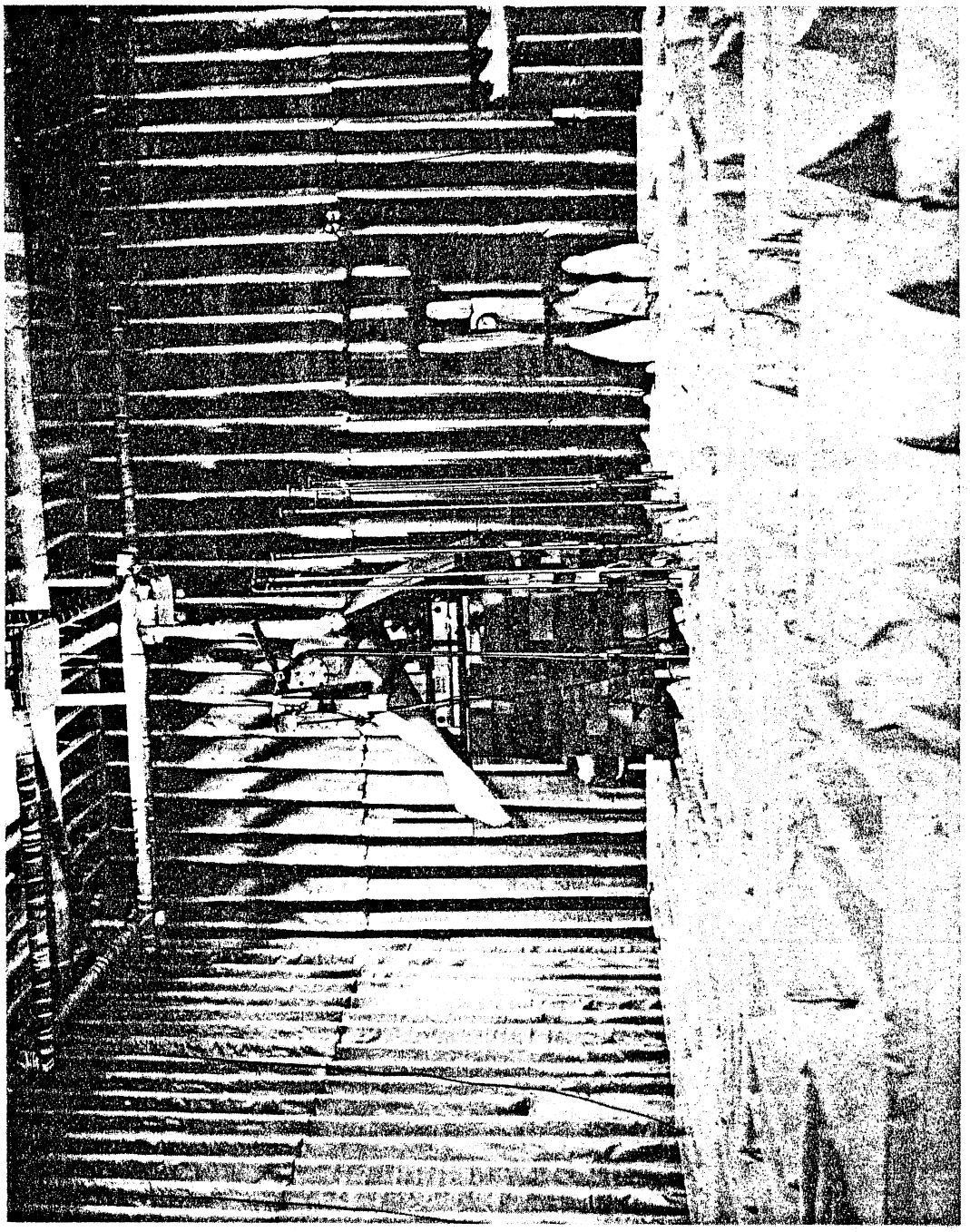

Figure 7: Overall Picture of Chamber

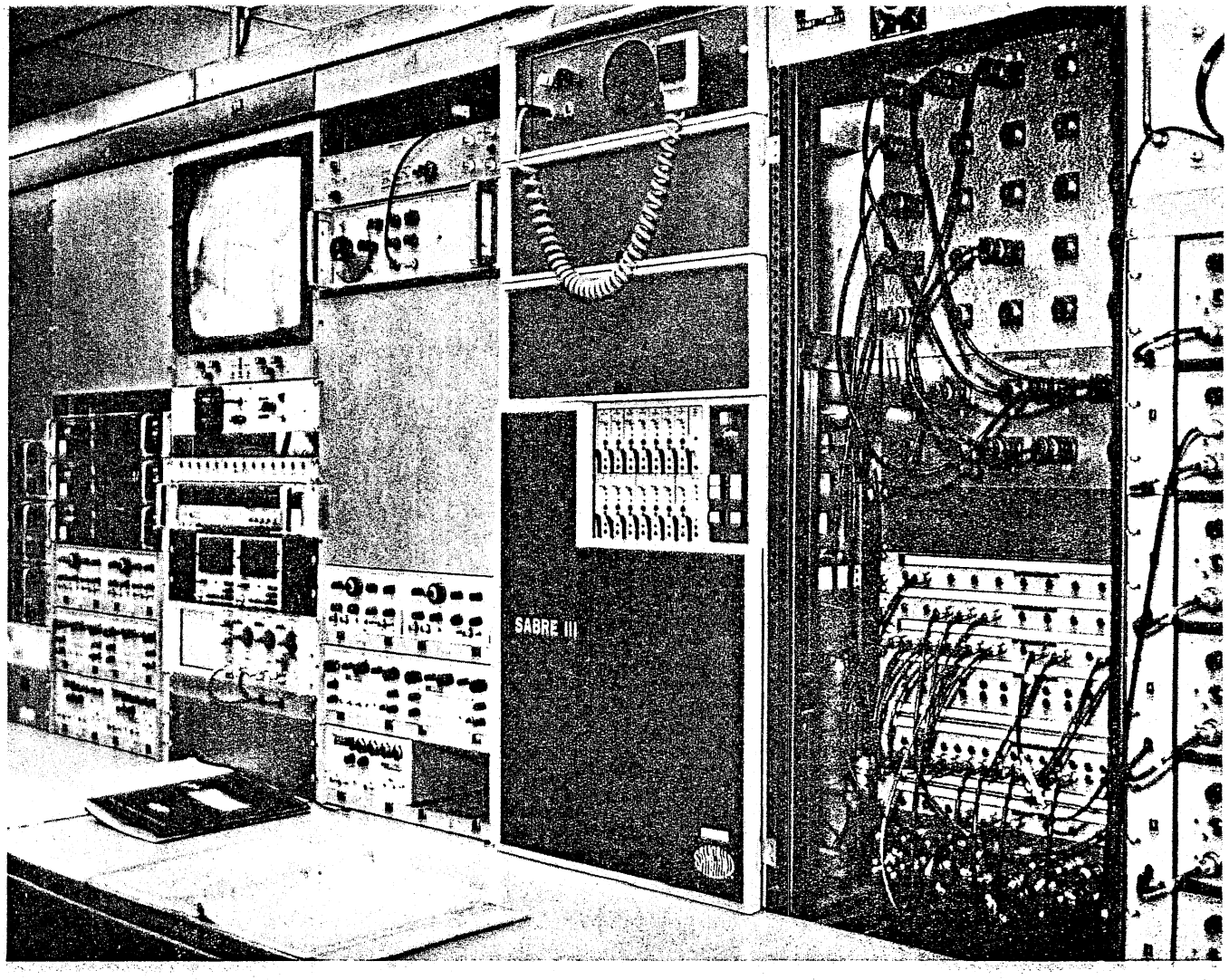

Figure 8: Electronic Instrumentation for Flow Measurements

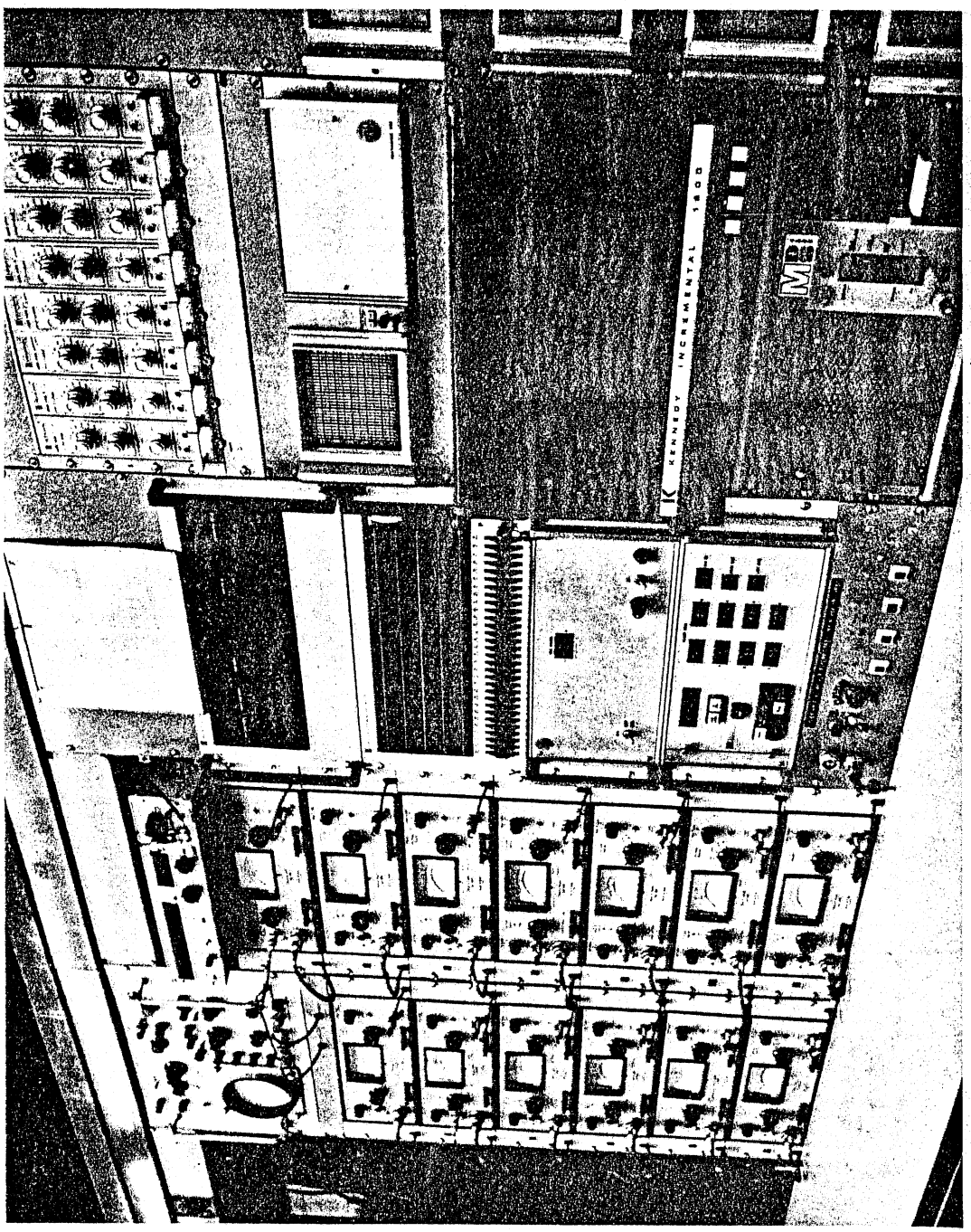

Figure 9: Electronic Instrumenation for Acoustical Measurements

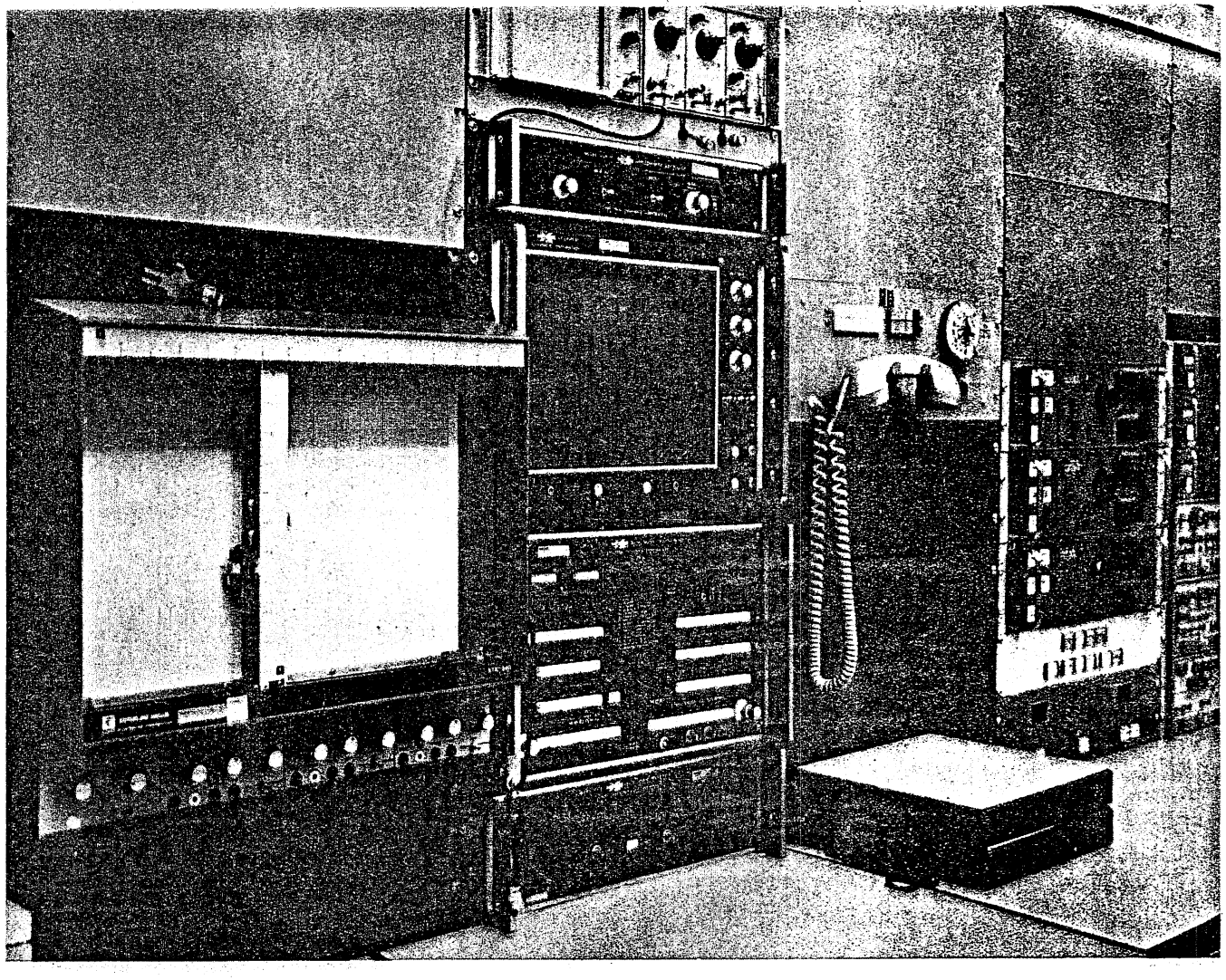

Figure 10: Electronic Instrumentation for Signal Analysis

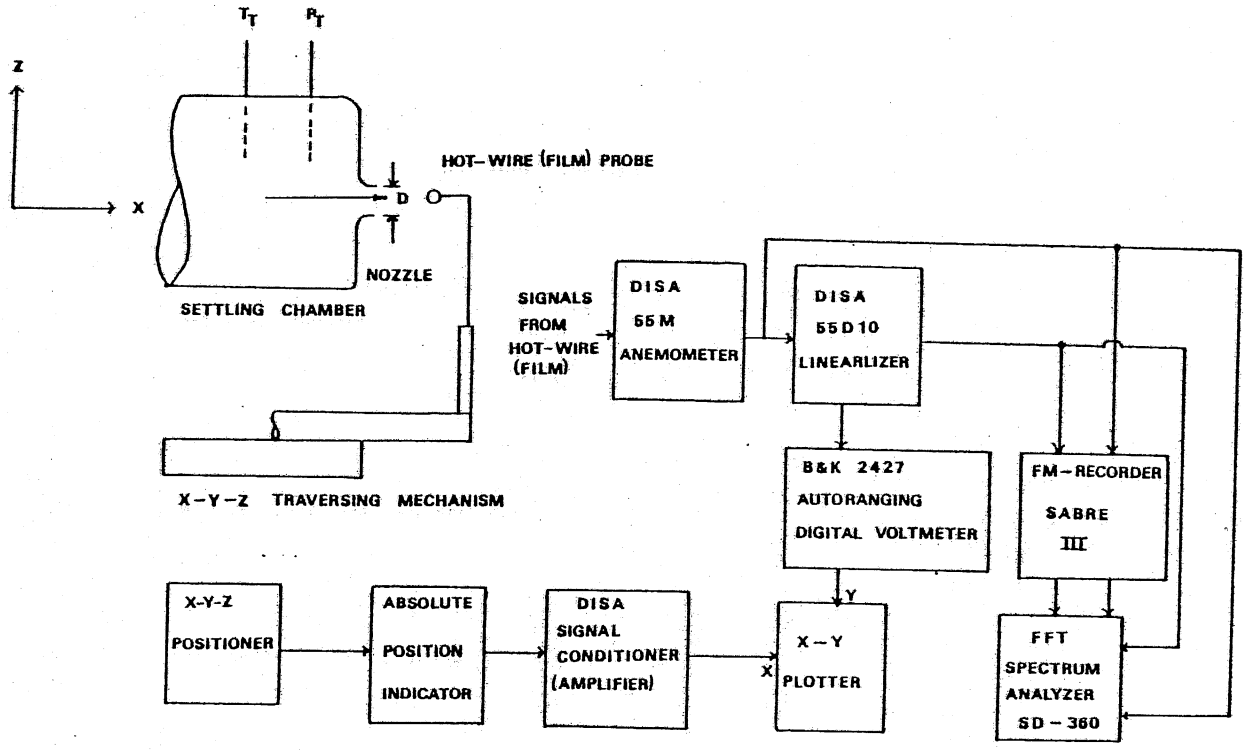

Figure 11: Experimental Setup and Schematic Diagram of Instrumentation for Mean Velocity, Turbulence Intensity and Power Spectral Density Measurements

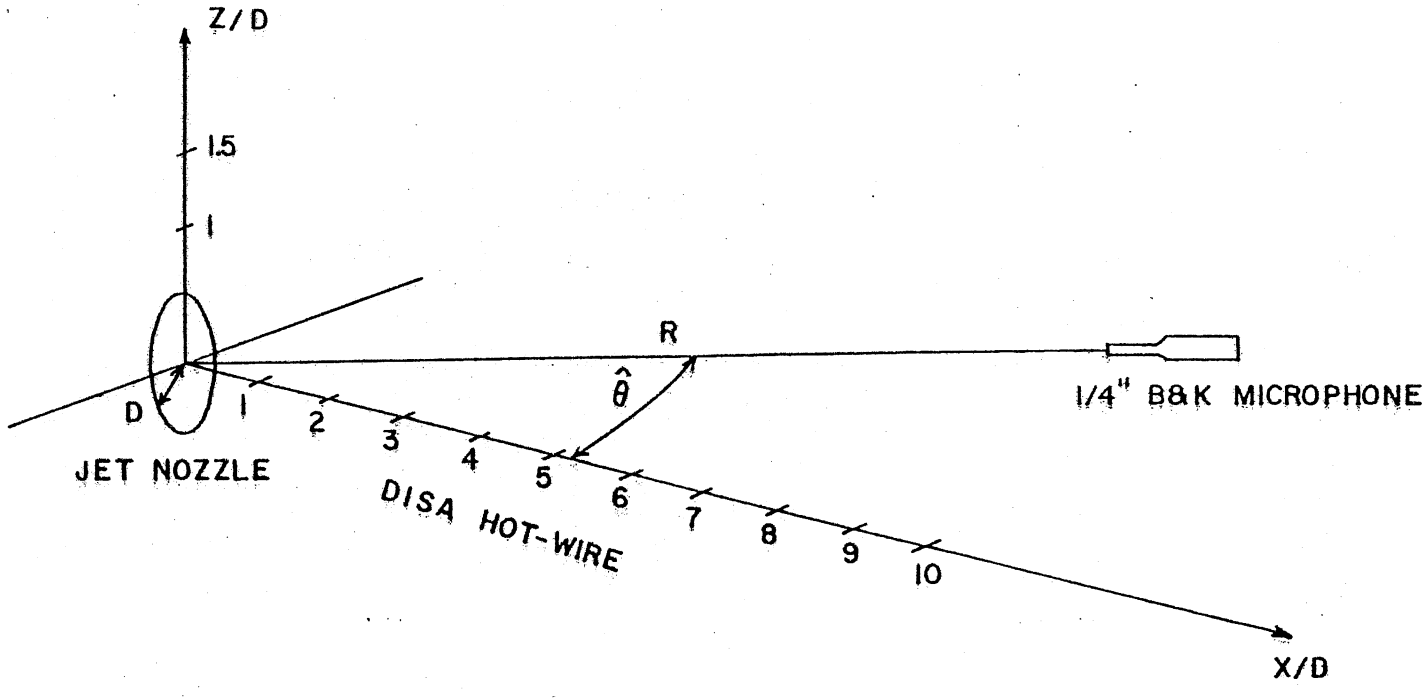

Figure 12: Coordinate System (I)

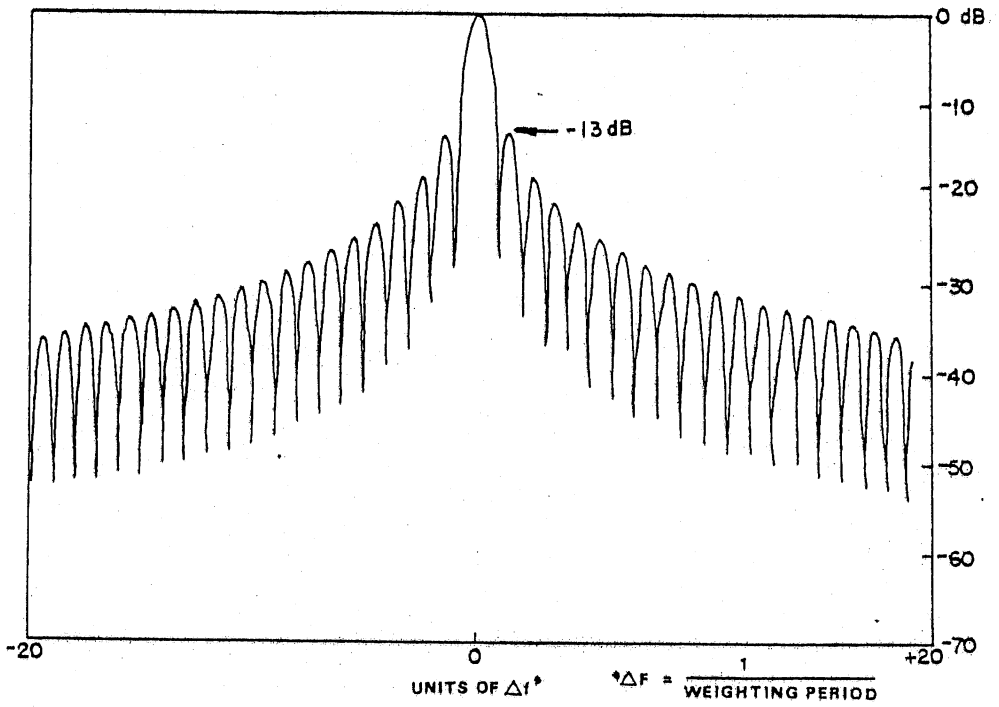

Figure 13a: Rectangular Weighting (Spectral Dynamics Corporation, 1975)

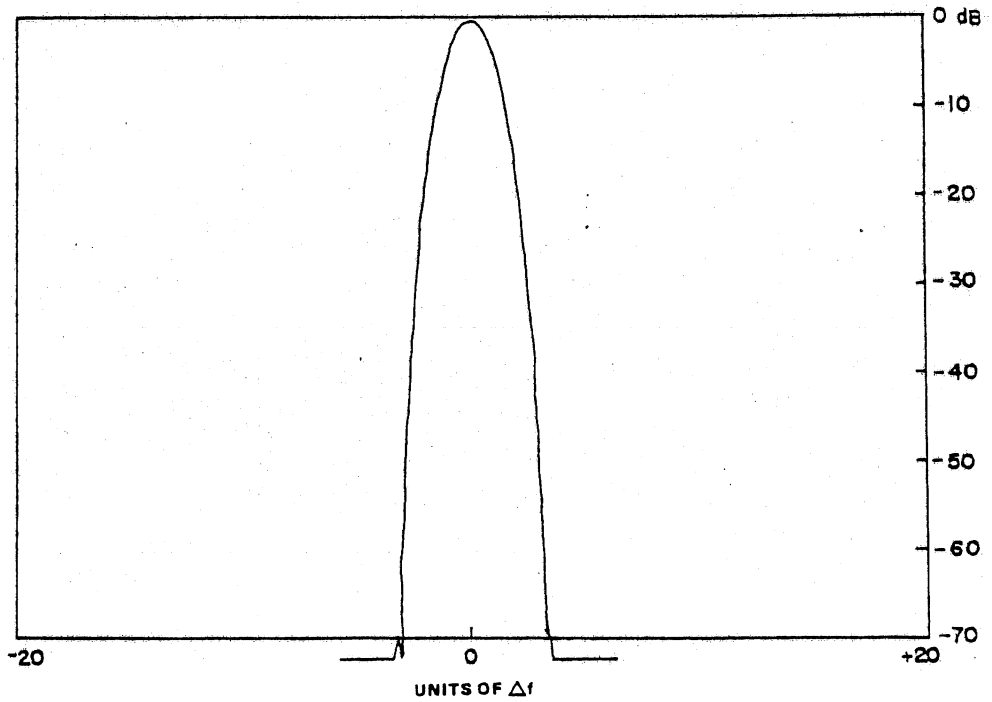

Figure 13b: Kaiser-Bessel Weighting (Spectral Dynamics Corporation, 1975)

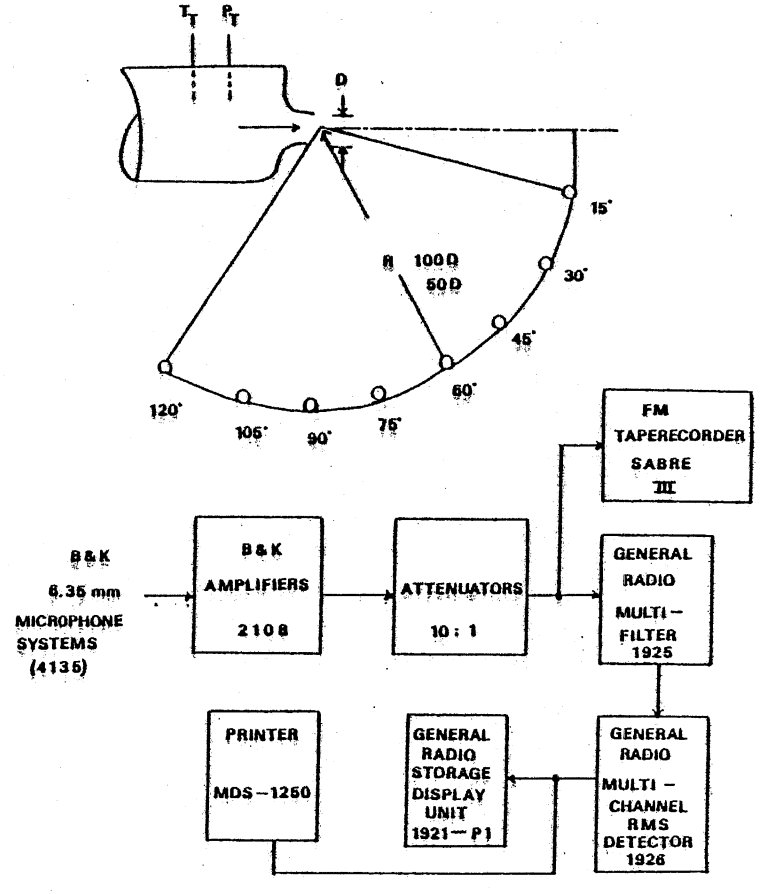

Figure 14: Experimental Setup and Schematic Diagram of Instrumentation for Overall Sound Pressure Level and 1/3 Octave Spectra Measurements

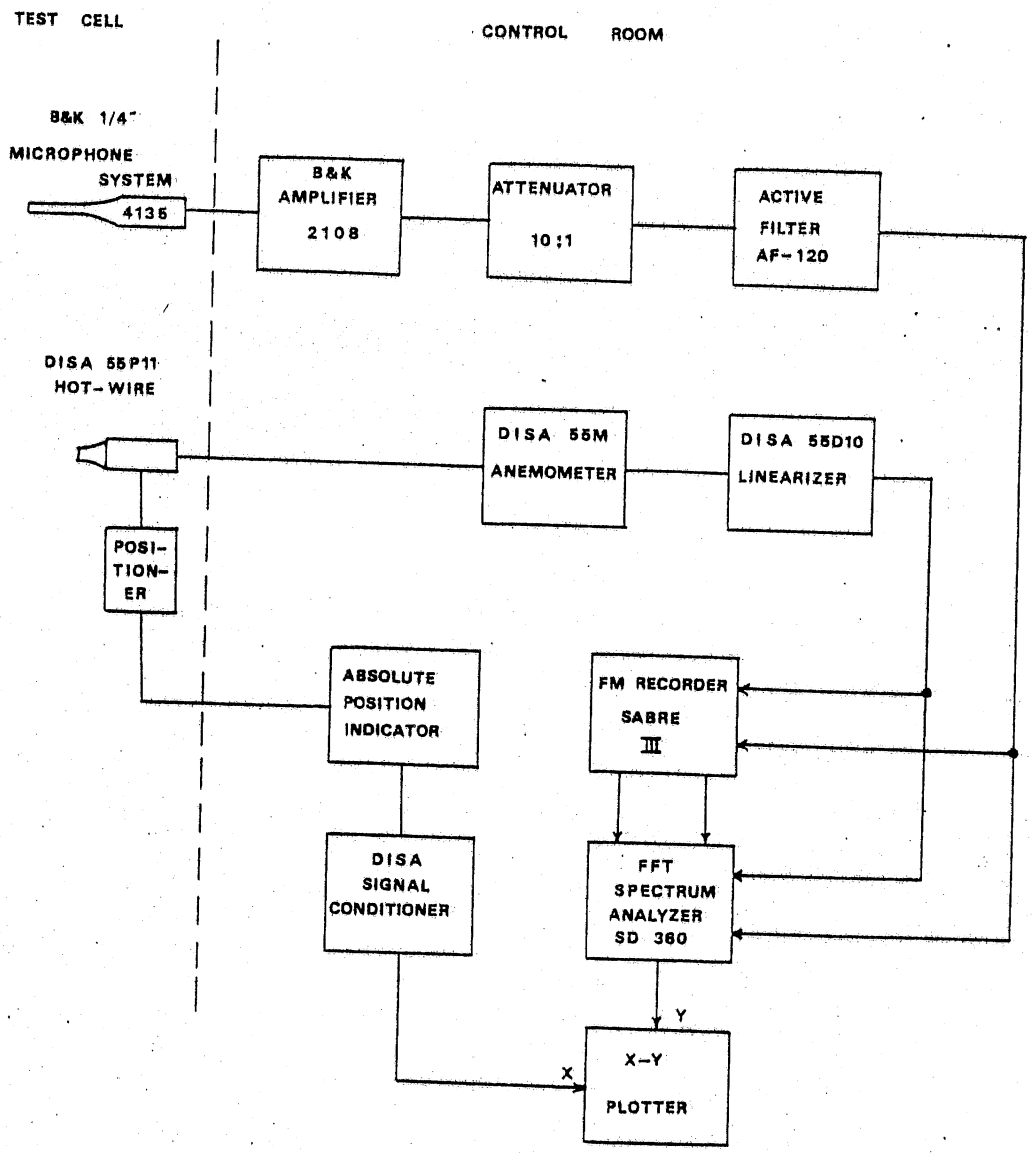

Figure 15: Block Diagram of Hot-Wire and Microphone Cross-Correlation Measurement System

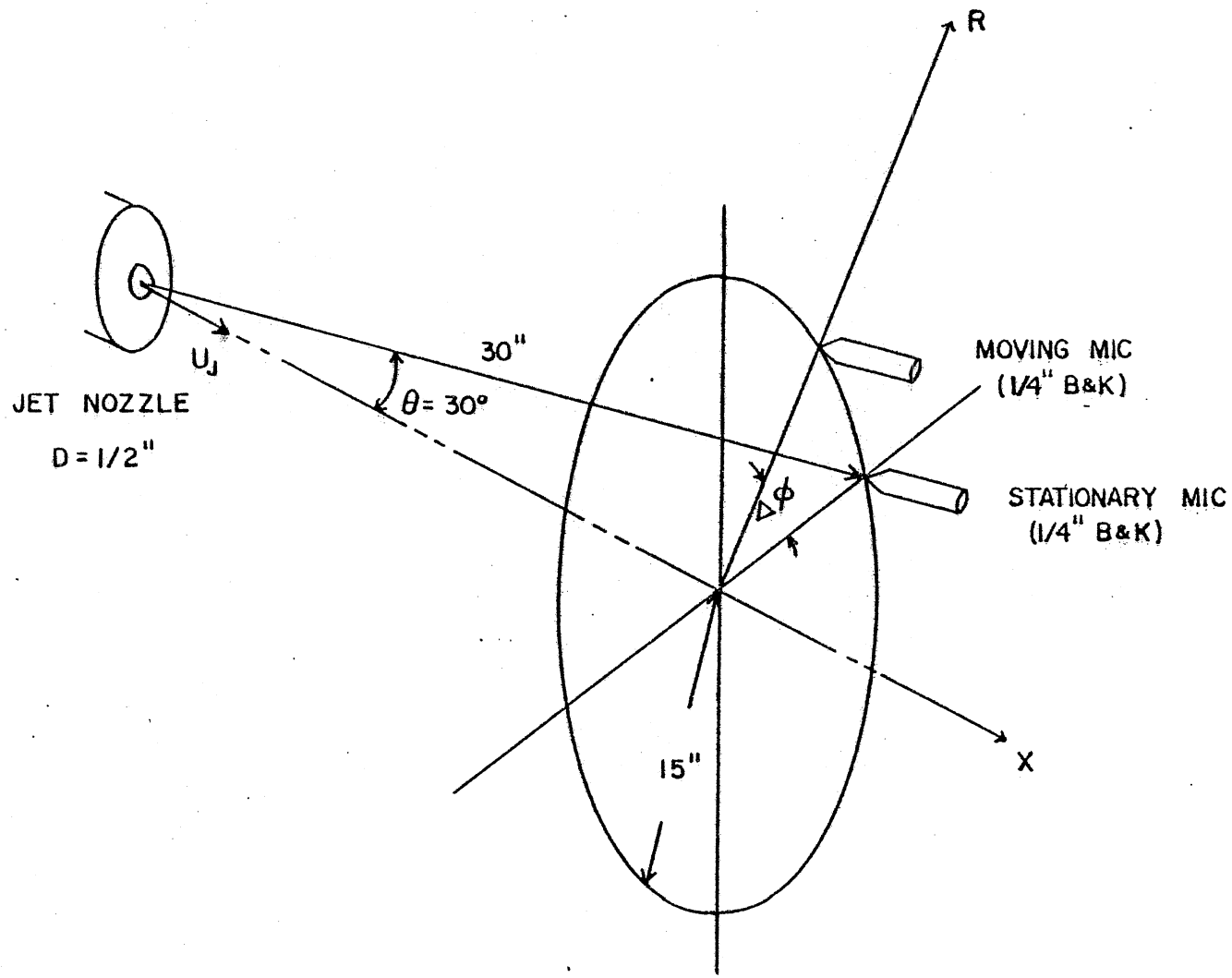

Figure 16: Microphone Arrangement in Azimuthal Cross-Correlation Measurements in Radiated Field

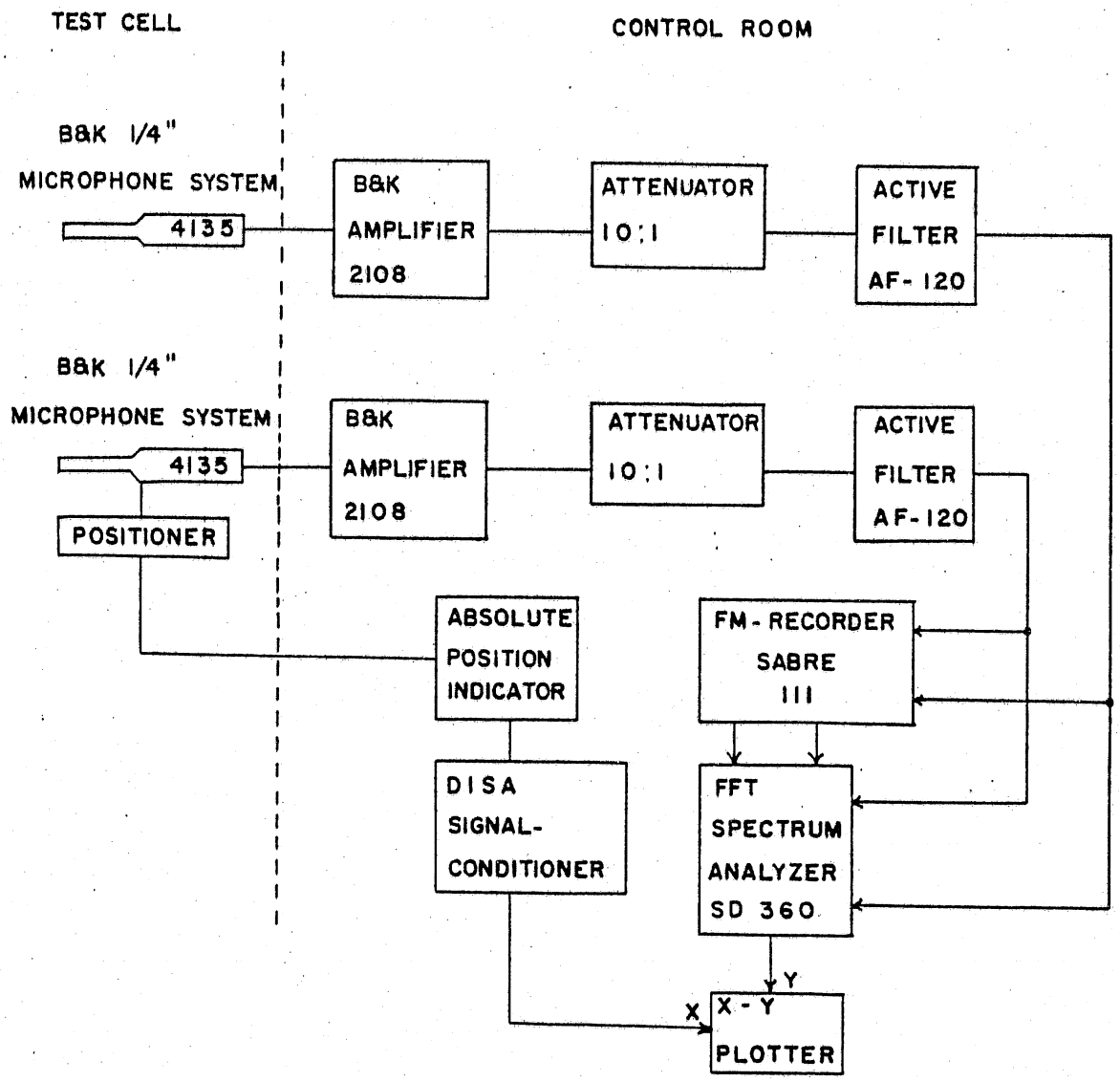

Figure 17: Block Diagram of Digital Narrowband Cross-Correlation System

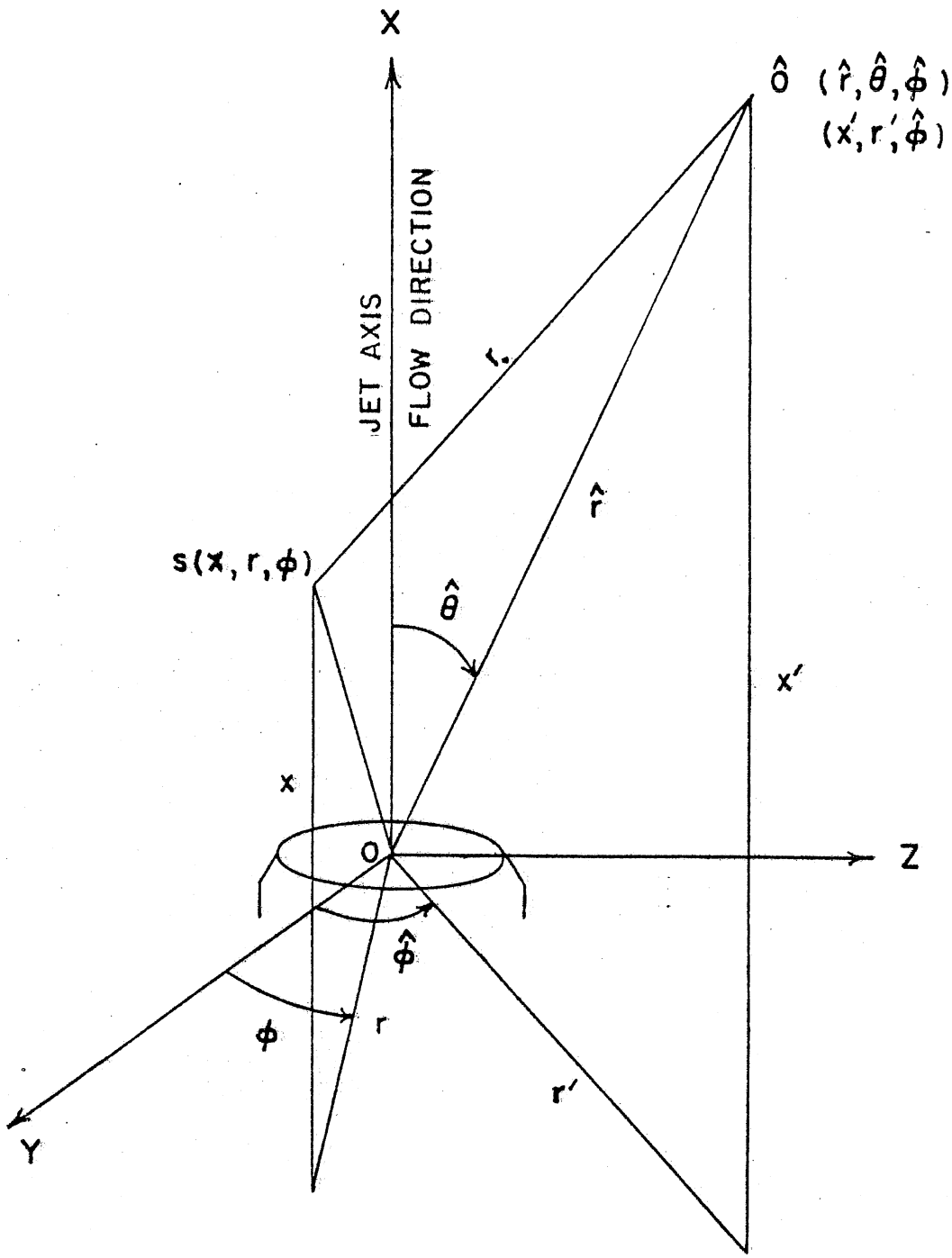

Figure 18: Coordinate System (II)

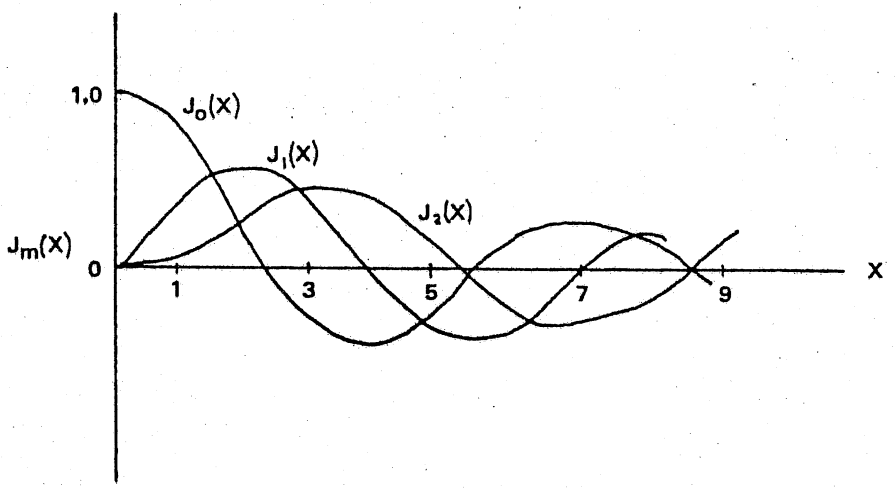

Figure 19: Bessel Function of First Kind and mth Order (m = 0, 1 and 2)

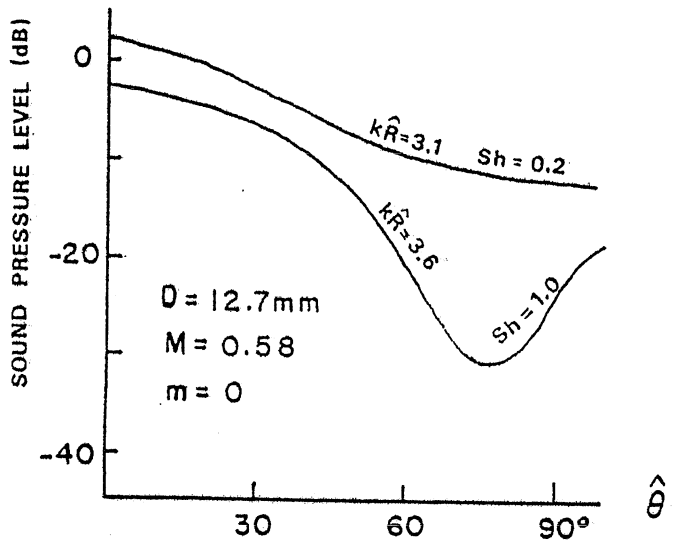

Figure 20a: Sound Pressure Level-Directivities of Single Azimuth-Frequency Components for Mode = 0

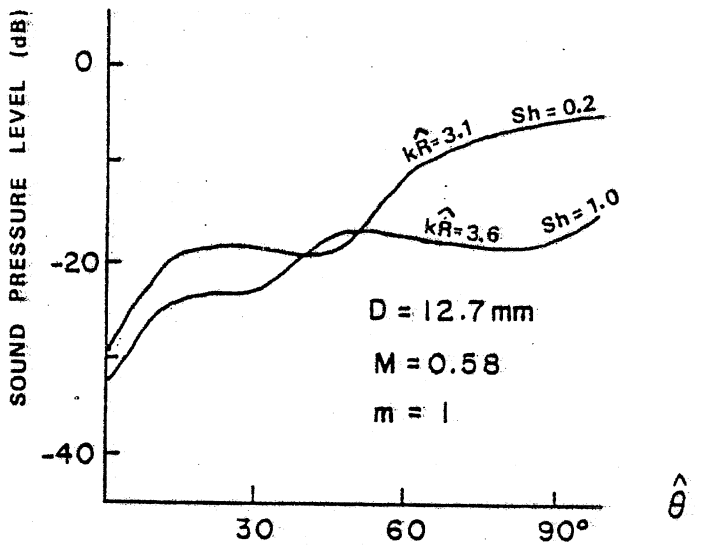

Figure 20b: Sound Pressure Level-Directivities of Single Azimuth-Frequency Components for Mode = 1

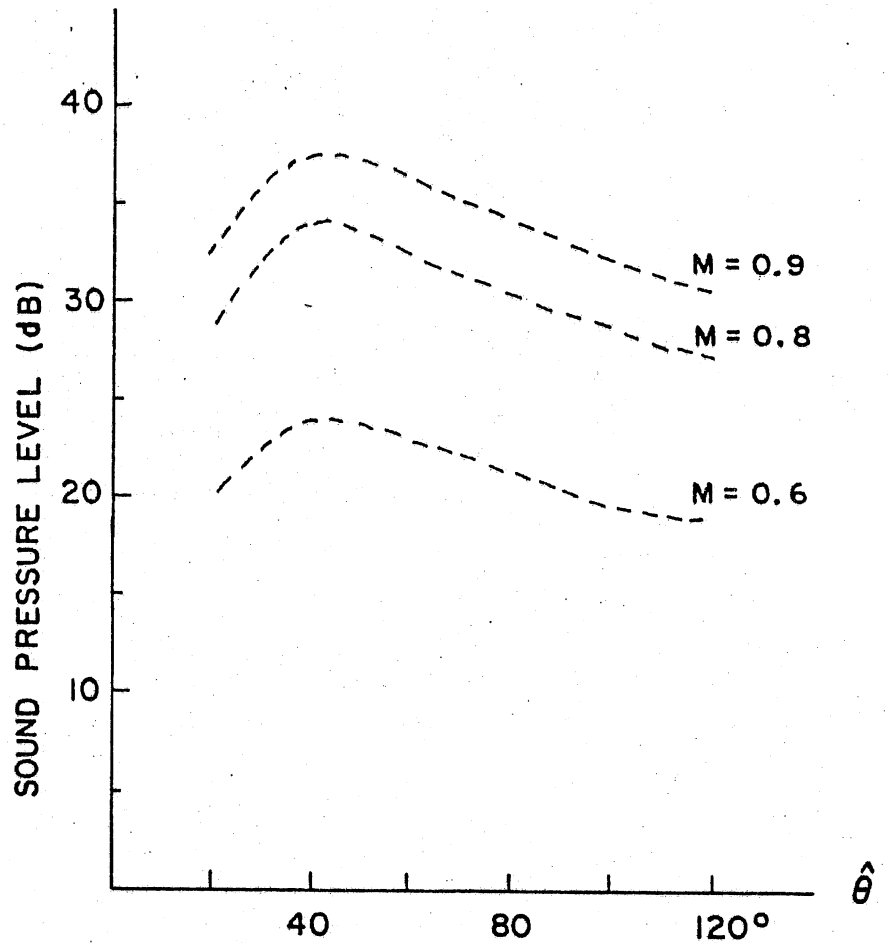

Figure 21: Sound Pressure Level-Directivites for High Frequencies (Sh > 2) and Various Mach Numbers M (Measured by Mollo-Christensen, Kolpin and Martuccelli, 1964)

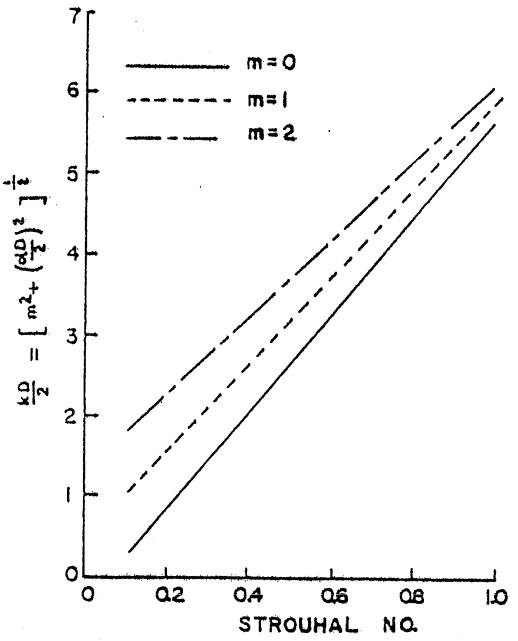

Figure 22a: Wave Number Versus Strouhal Number (Chan, 1976)

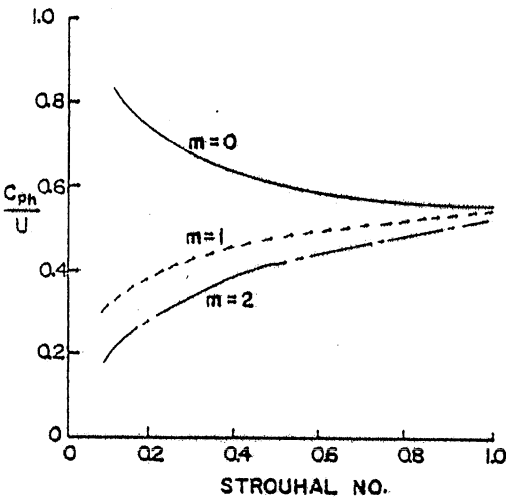

Figure 22b: Phase Velocity Versus Strouhal Number (Chan, 1976)

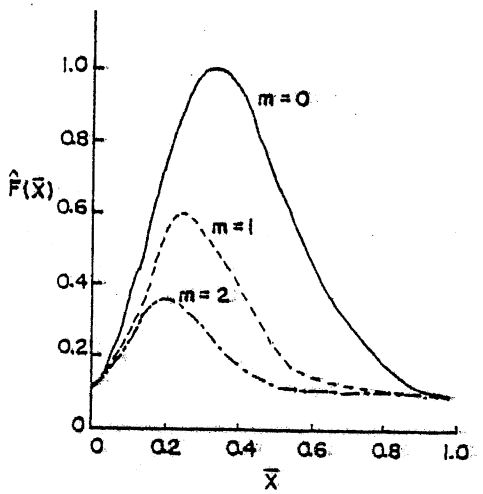

Figure 22c: Axial Source Distribution Function (Replotted Based on Figure 9 of Chan, 1976)

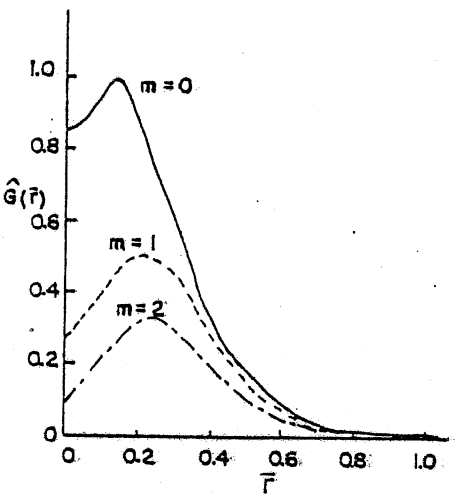

Figure 22d: Lateral Source Distribution Function at X = L/2 (Replotted Based on Figure 10 of Chan, 1976)

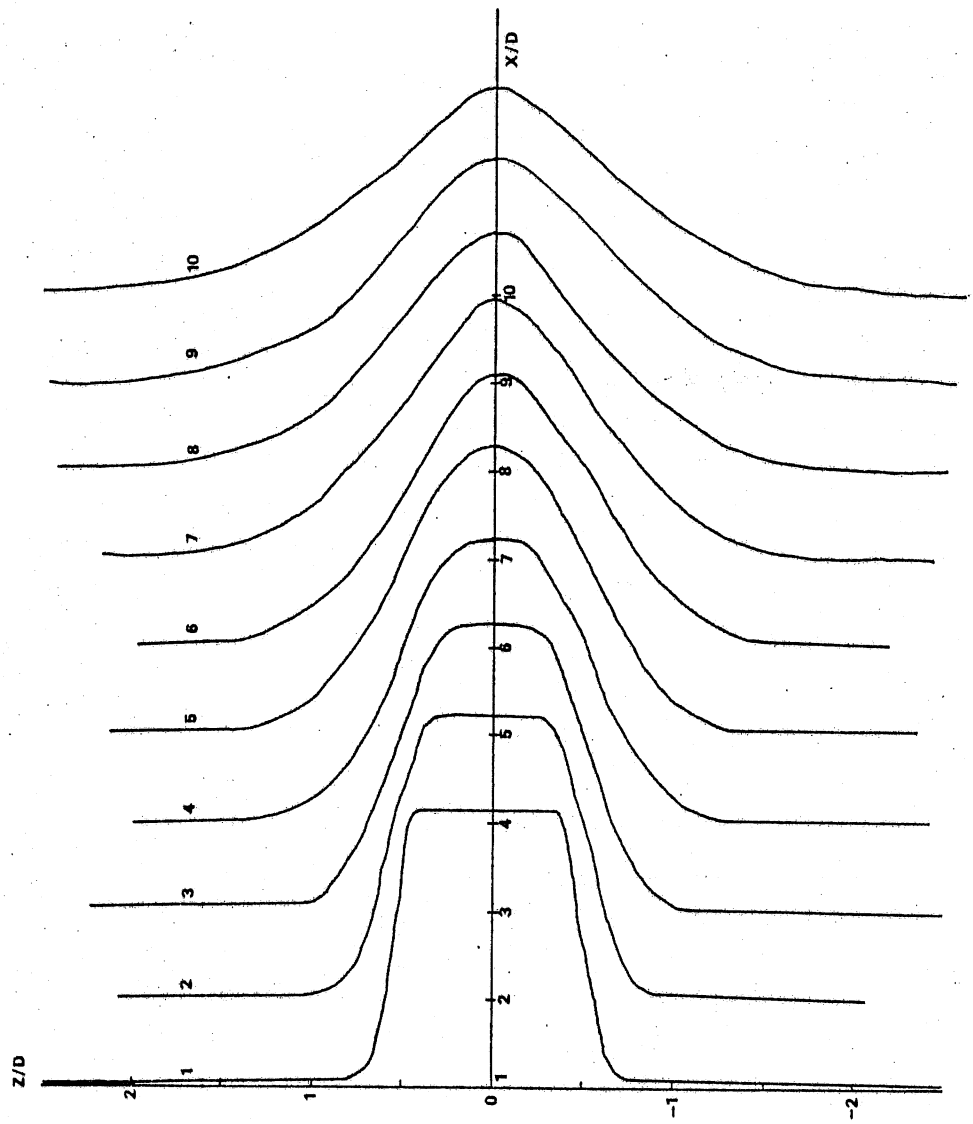

Figure 23: Mean Velocity Profiles at Various Downstream Locations for the 12.7 mm Jet at M = 0.297

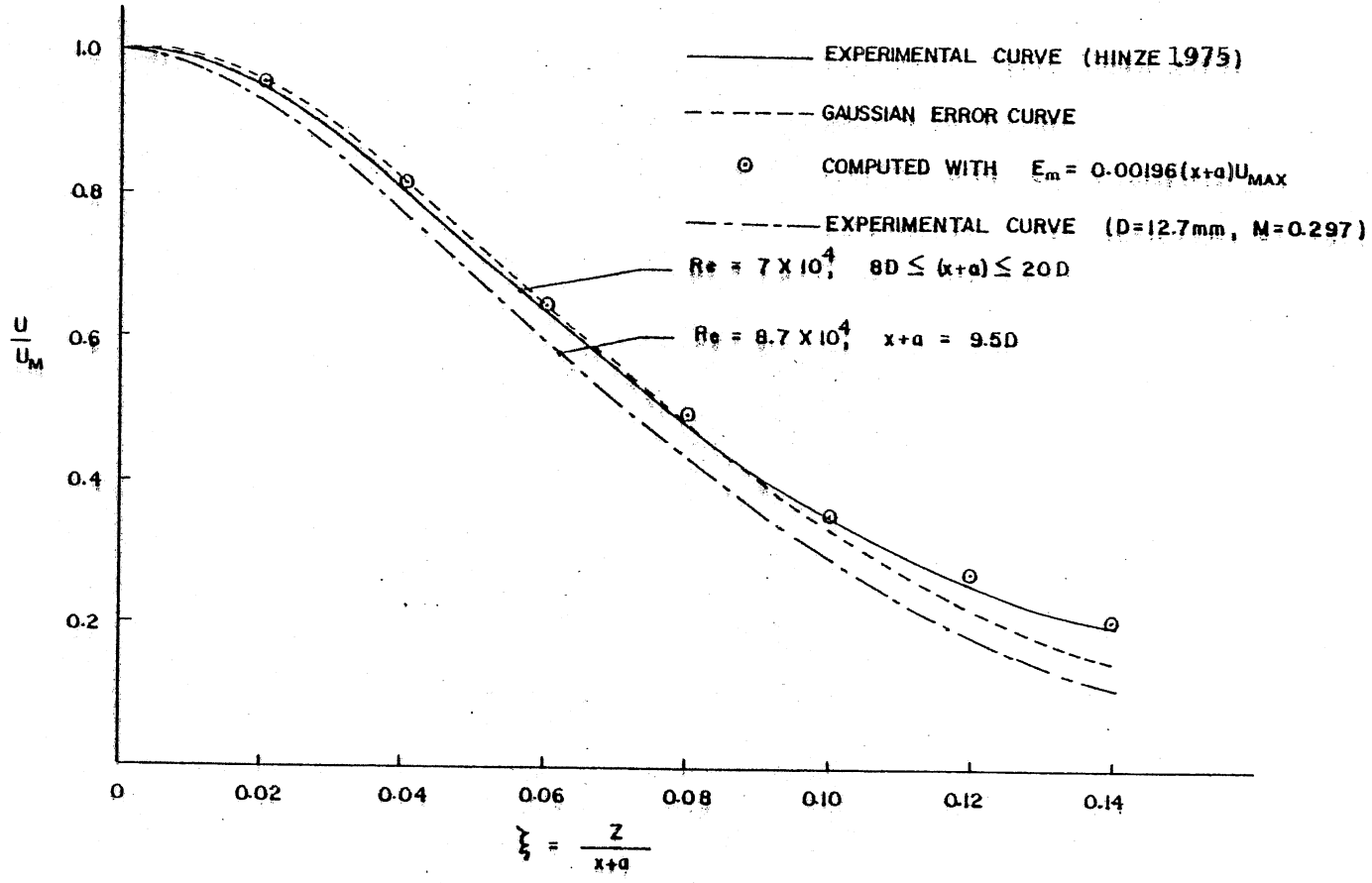

Figure 26: Mean Velocity Distribution in the Self-Preserving Region (X = 8D) (Gaussian Error Curve and Computed Data Were Obtained by Hinze, 1975)

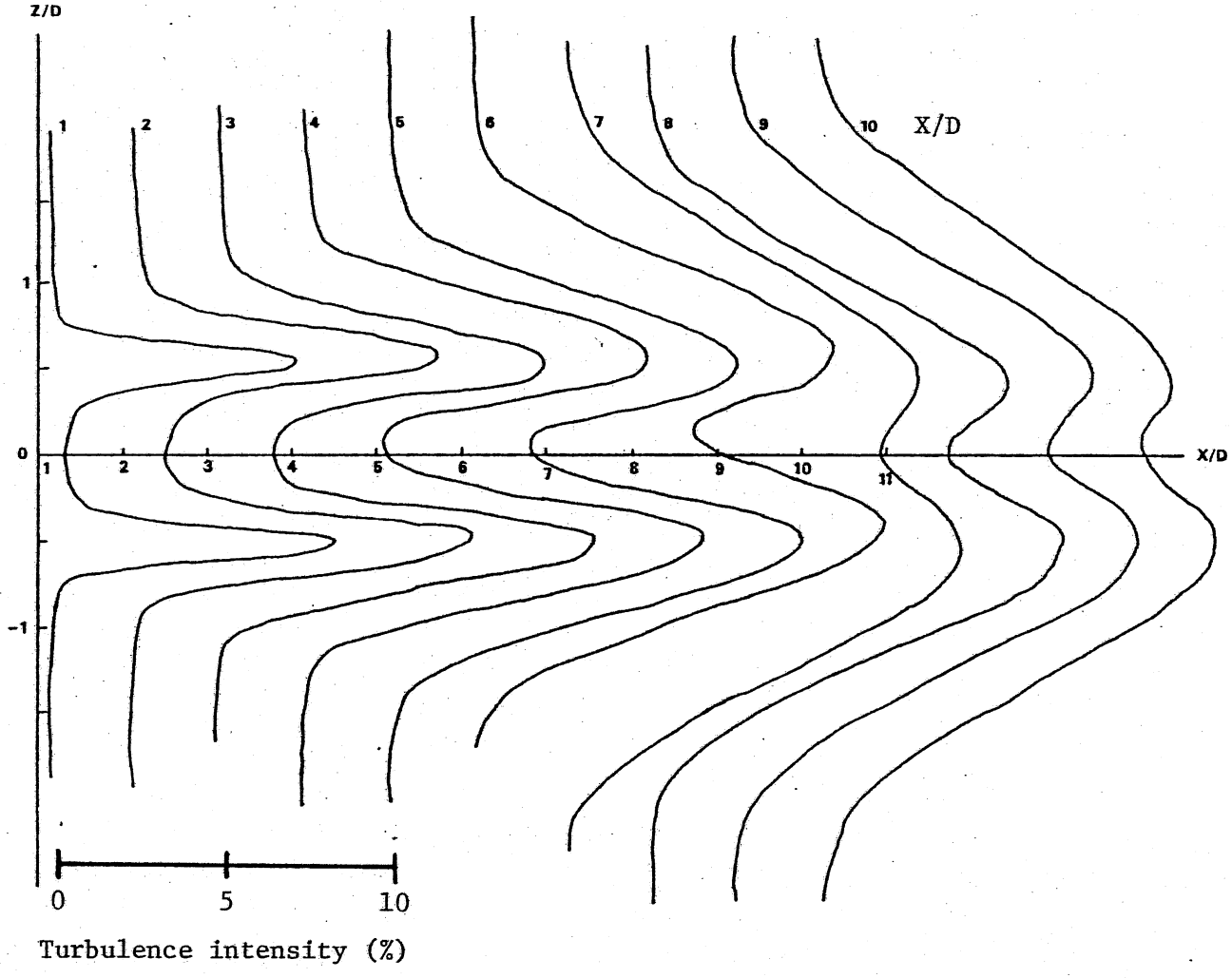

Figure 27: Turbulence u-Component Profiles at Various Downstream Locations for the 12.7 mm Jet at M = 0.297

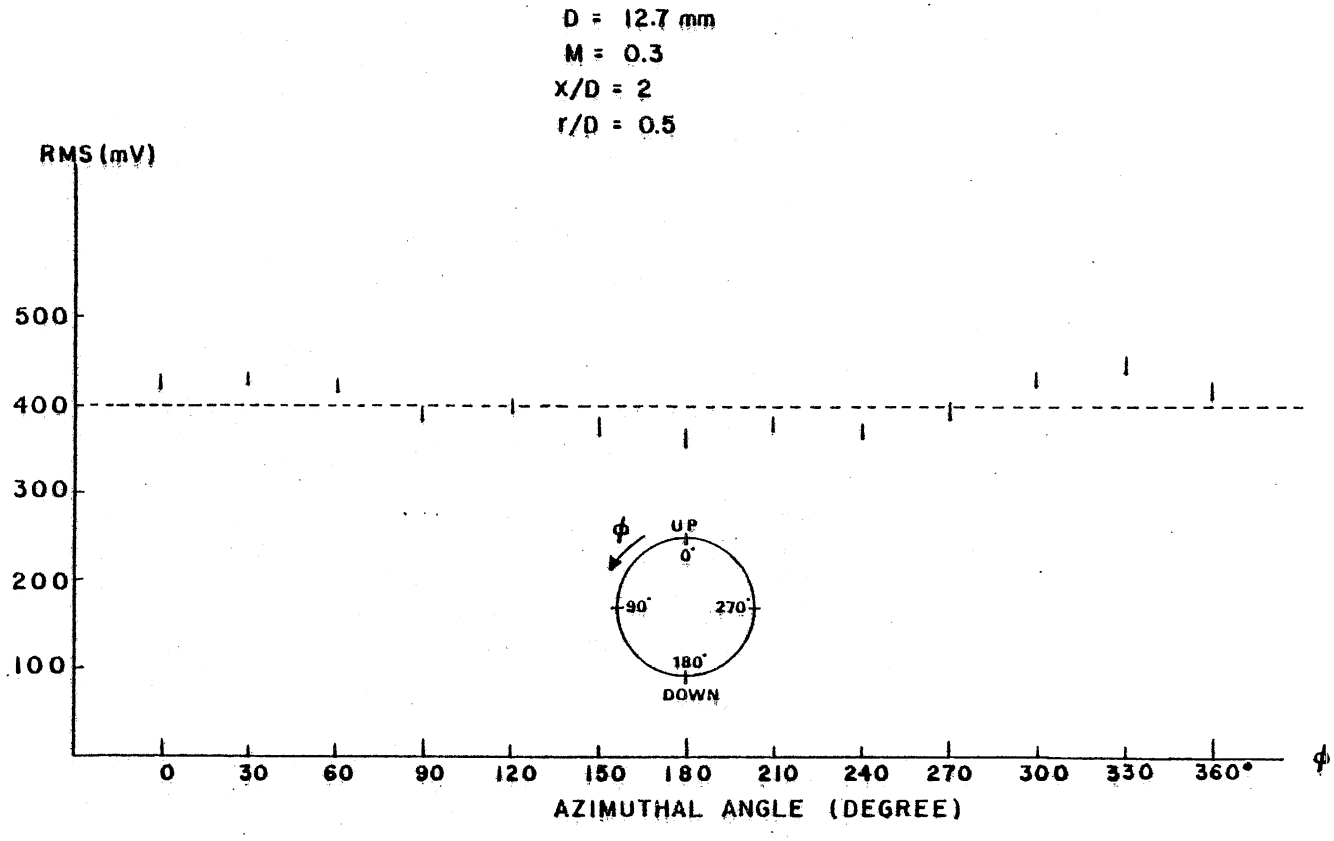

Figure 28: Circumferential Distribution of RMS Voltage of Fluctuating Velocity Signals (u-Component)

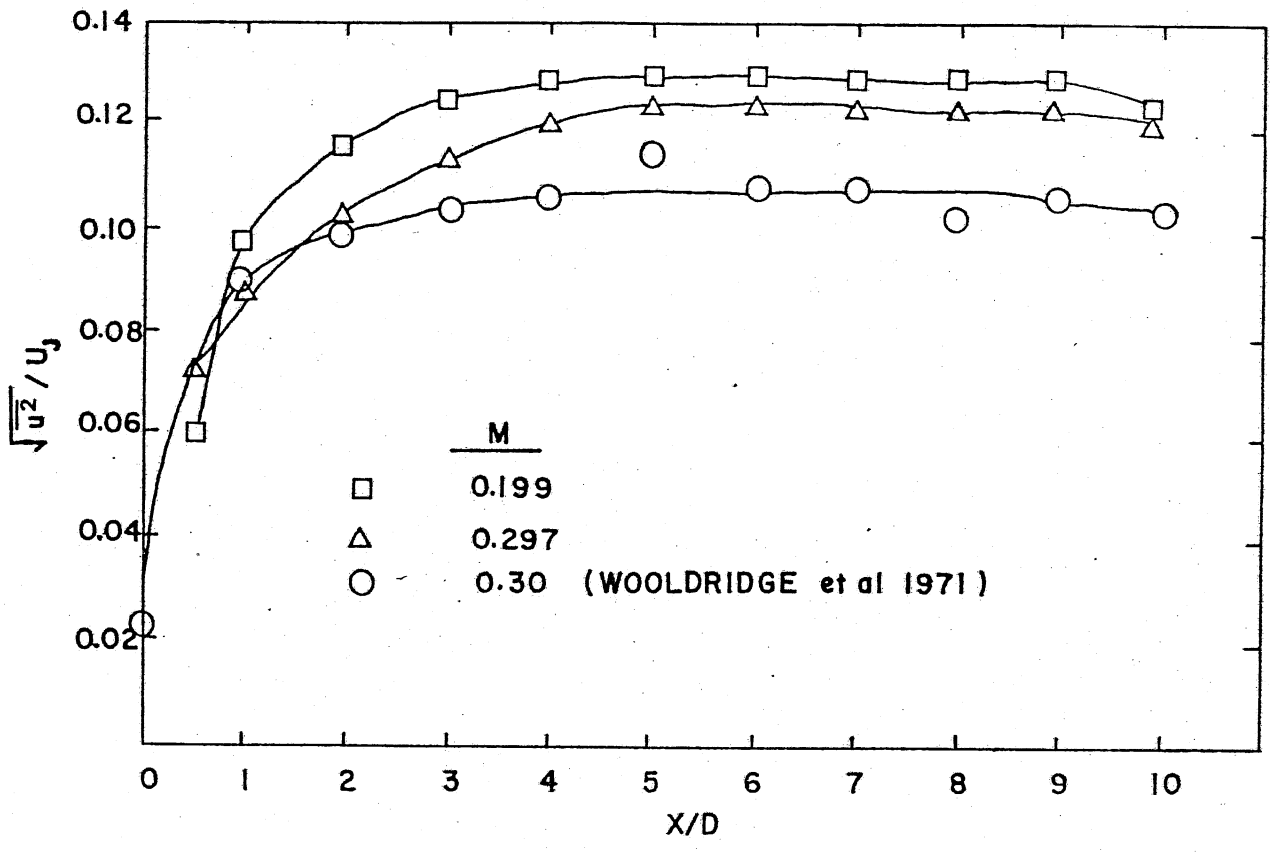

Figure 29: Axial Distribution of Turbulence Intensity for Various Mach Numbers at Z/D = 0.5

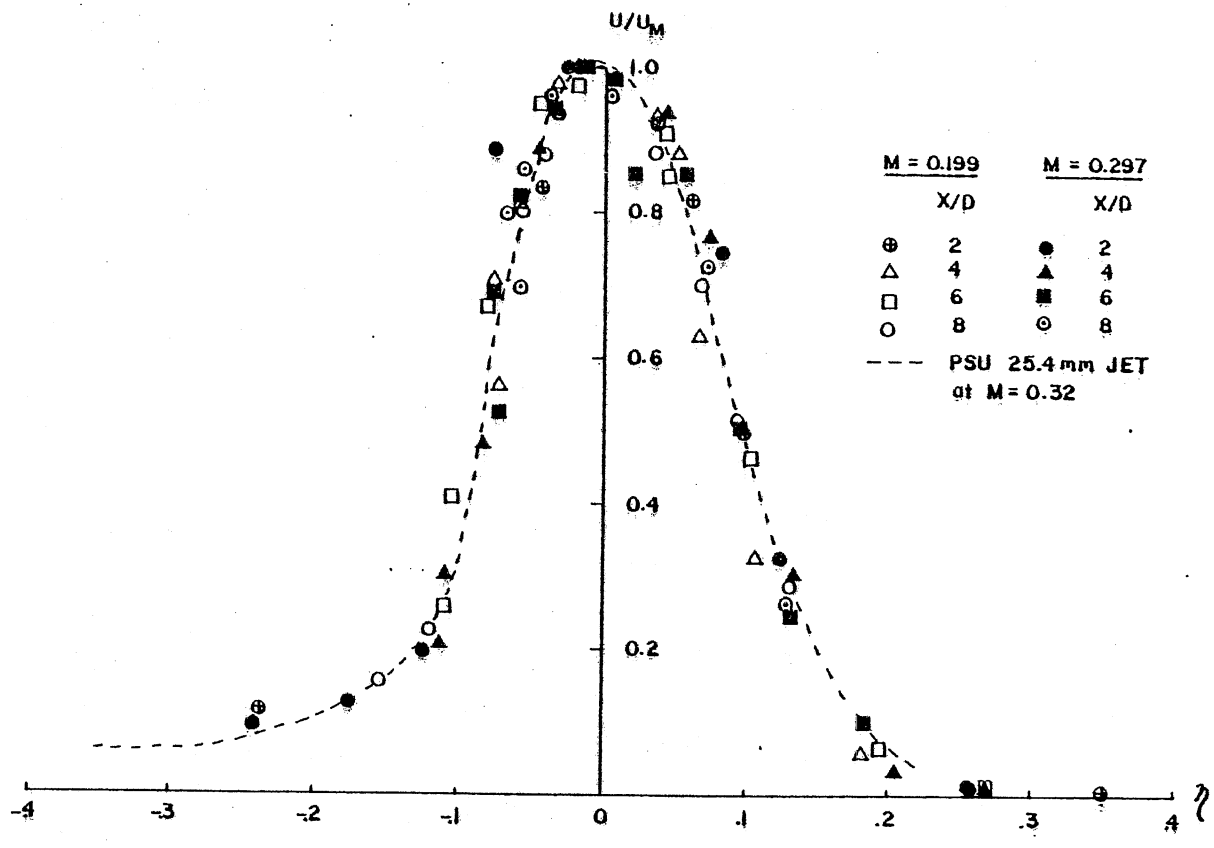

Figure 30: Similarity of Turbulence u-Component Profile of the 12.7 mm Jet at M = 0.199 and 0.297

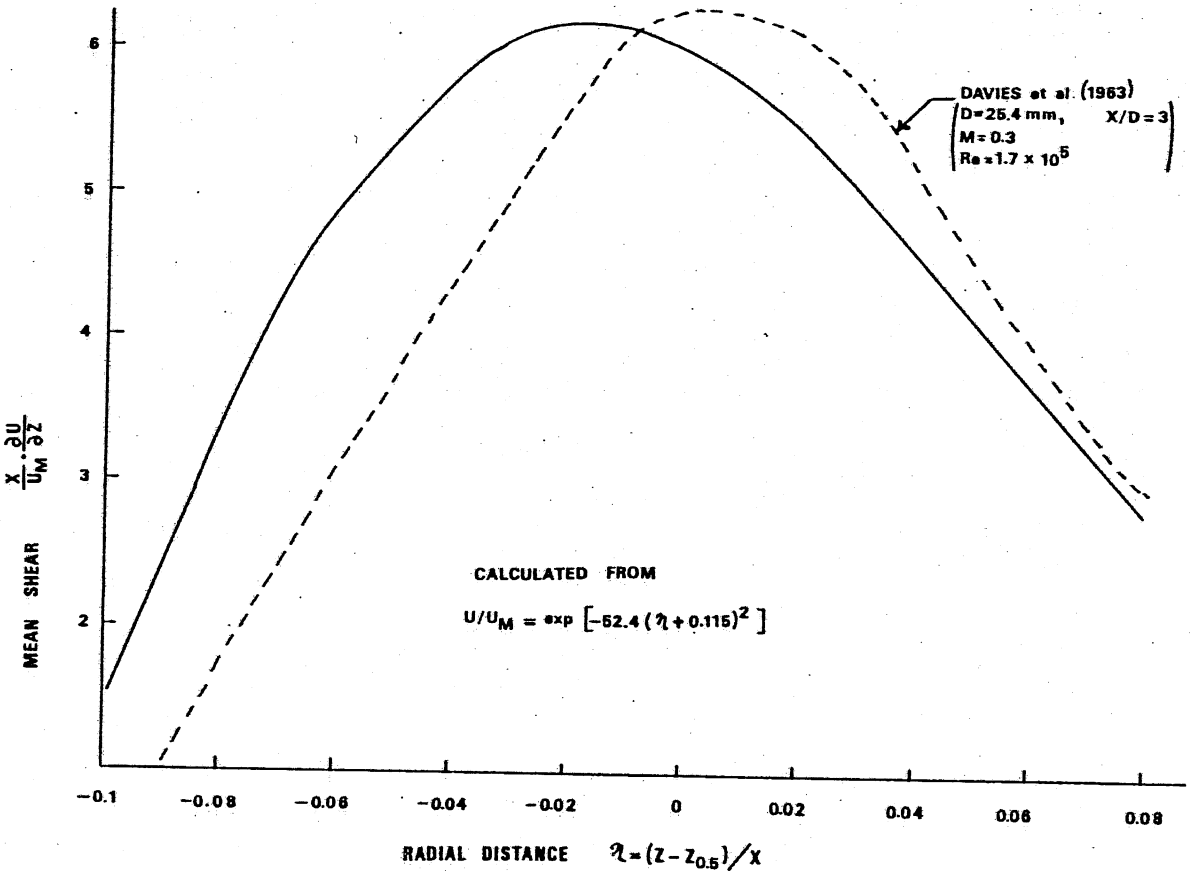

Figure 31: Lateral Distribution of Mean Shear (12.7 mm Jet, M = 0.297, $R_e = 8.7 \times 10^4$)

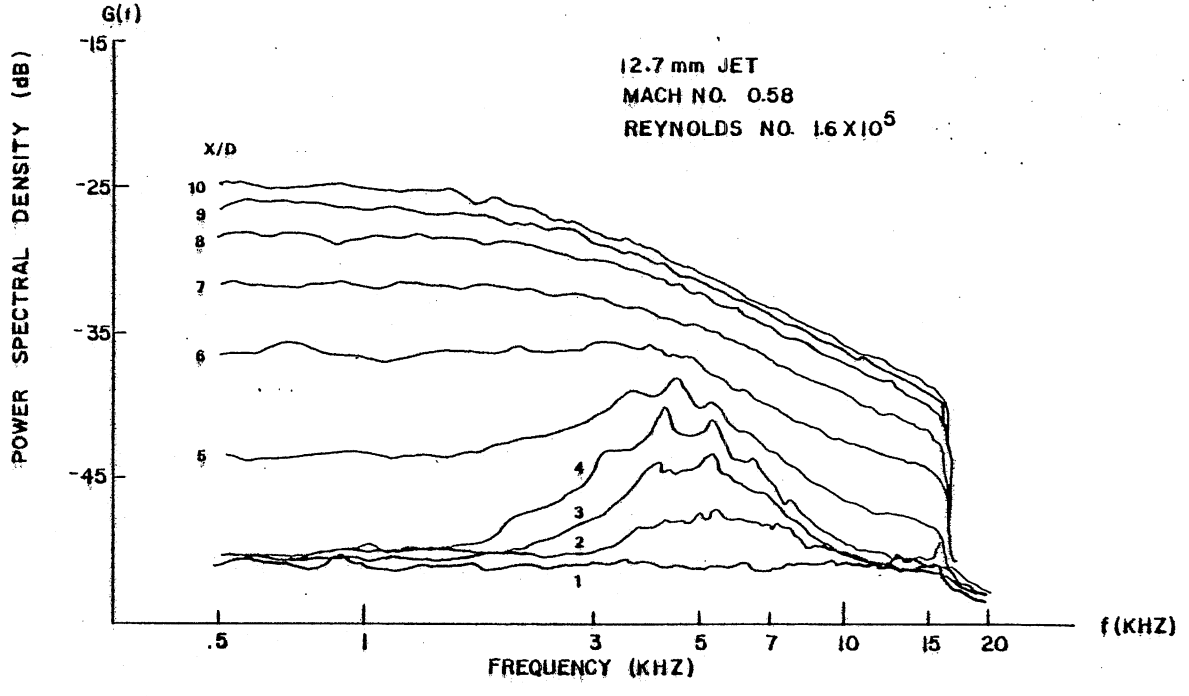

Figure 32: Turbulence u-Component Power Spectral Density Along Jet Axis (D = 12.7 mm)

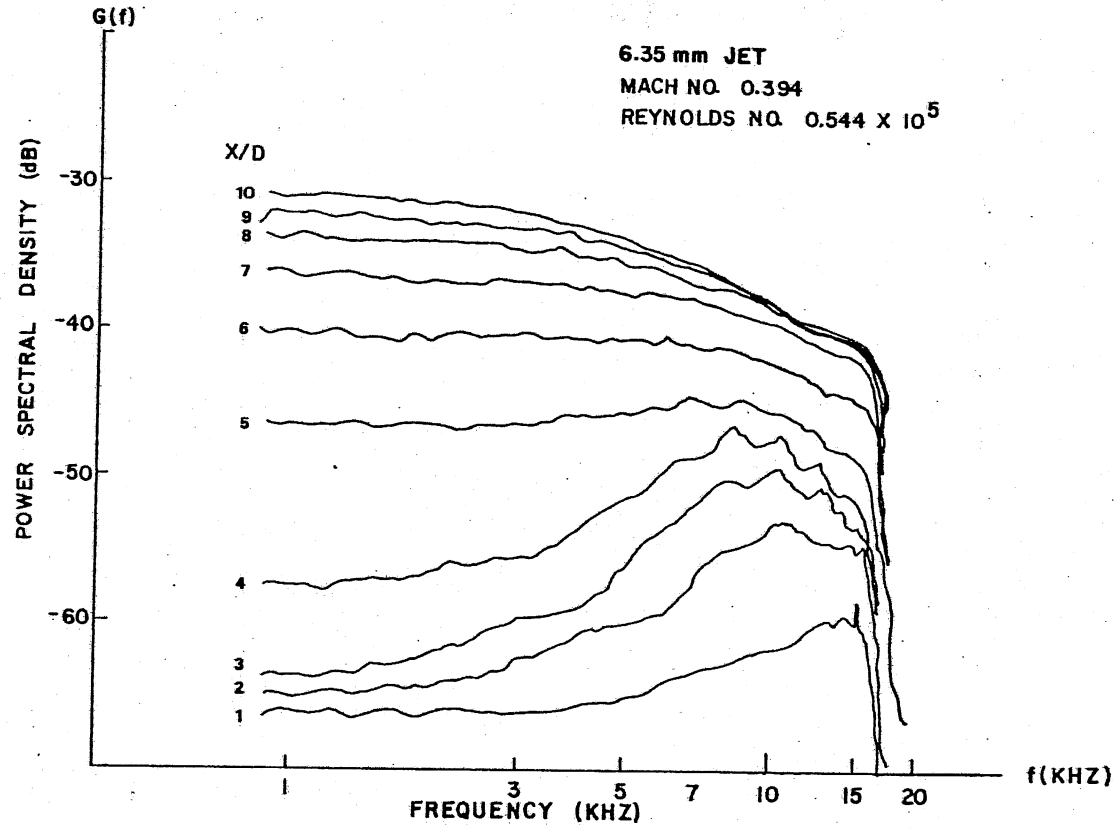

Figure 33: Turbulence u-Component Power Spectral Density Along Jet Axis (D = 6.35 mm)

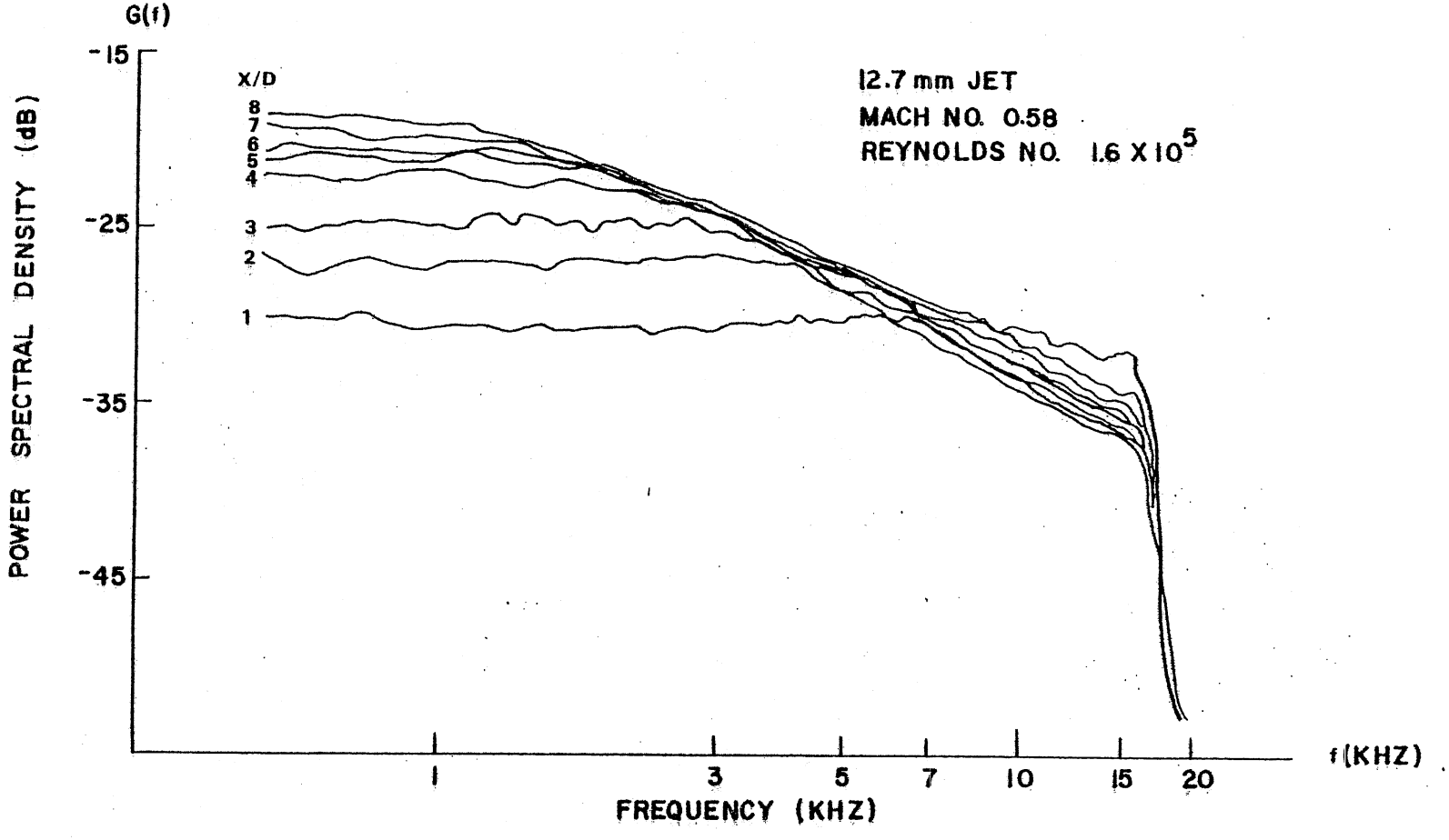

Figure 34: Turbulence u-Component Power Spectral Density in the Center of Mixing Layer (D = 12.7 mm)

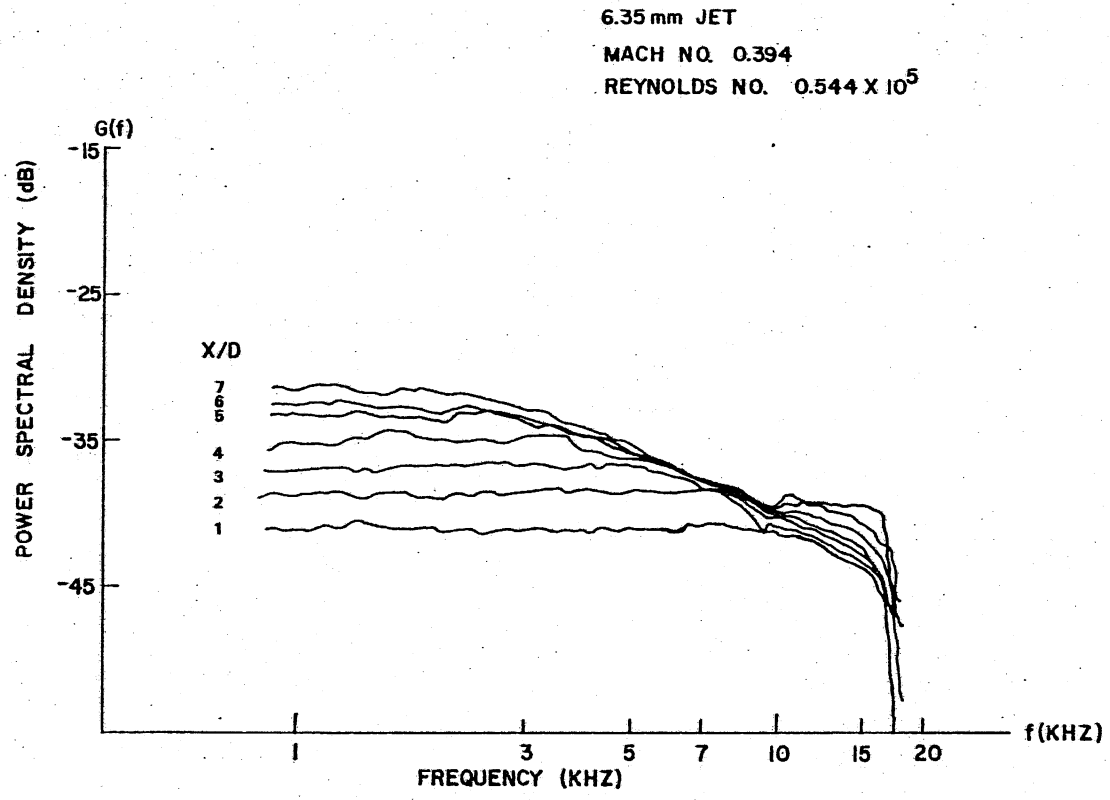

Figure 35: Turbulence u-Component Power Spectral Density in the Center of Mixing Layer (D = 6.35mm)

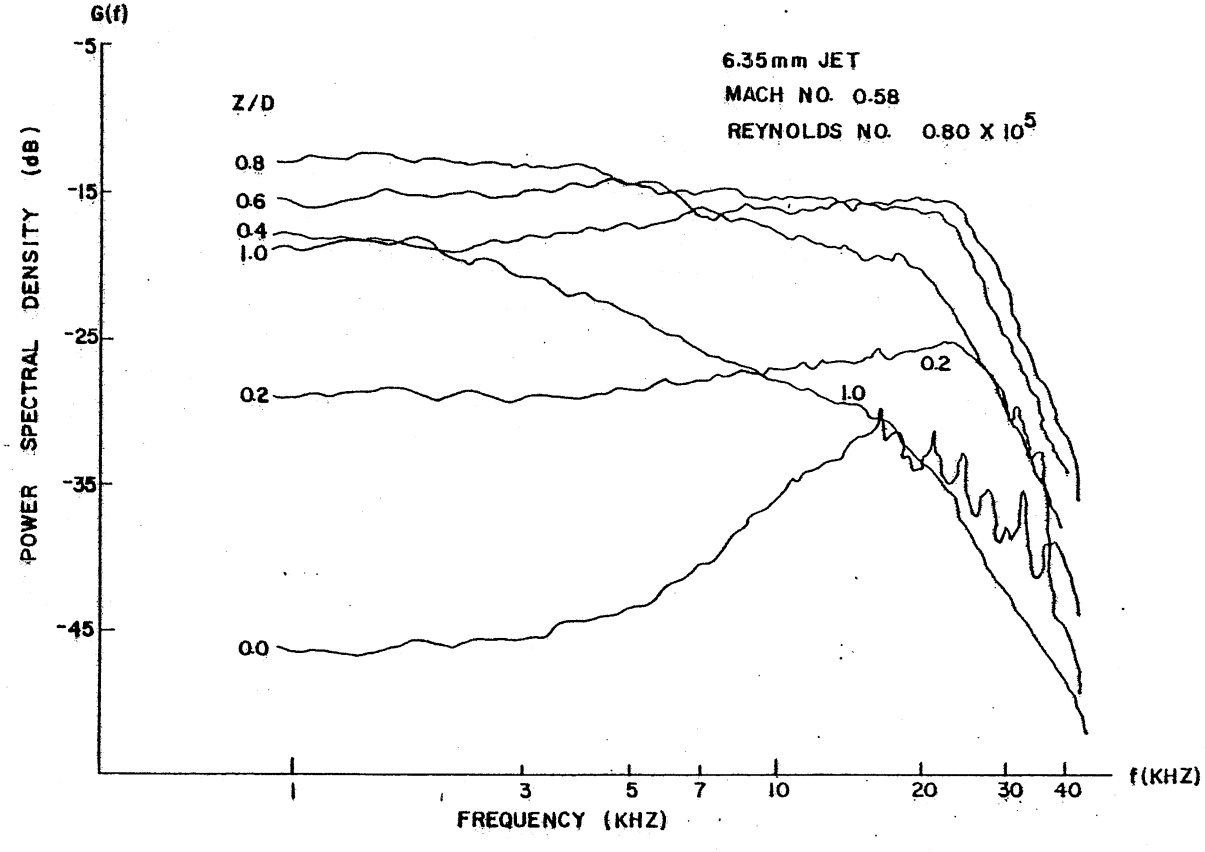

Figure 36: Turbulence u-Component Power Spectral Density for Various Lateral Locations at X/D = 4 (D = 6.35 mm, M = 0.58)

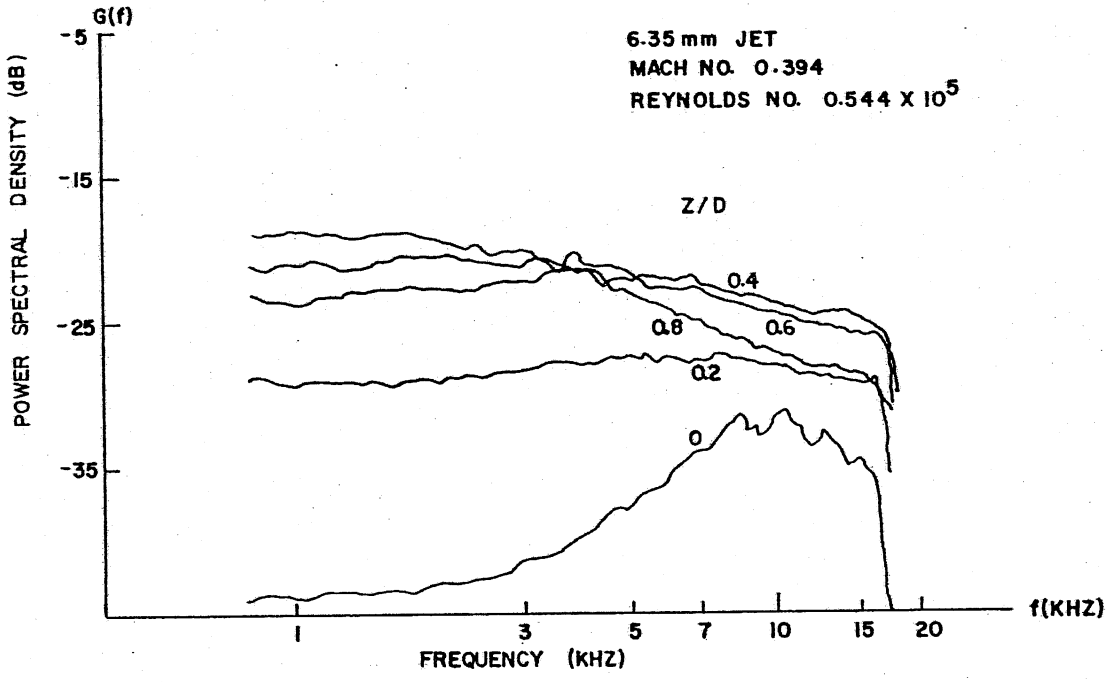

Figure 37: Turbulence u-Component Power Spectral Density for Various Lateral Locations at X/D = 4 (D = 6.35 mm, M = 0.394)

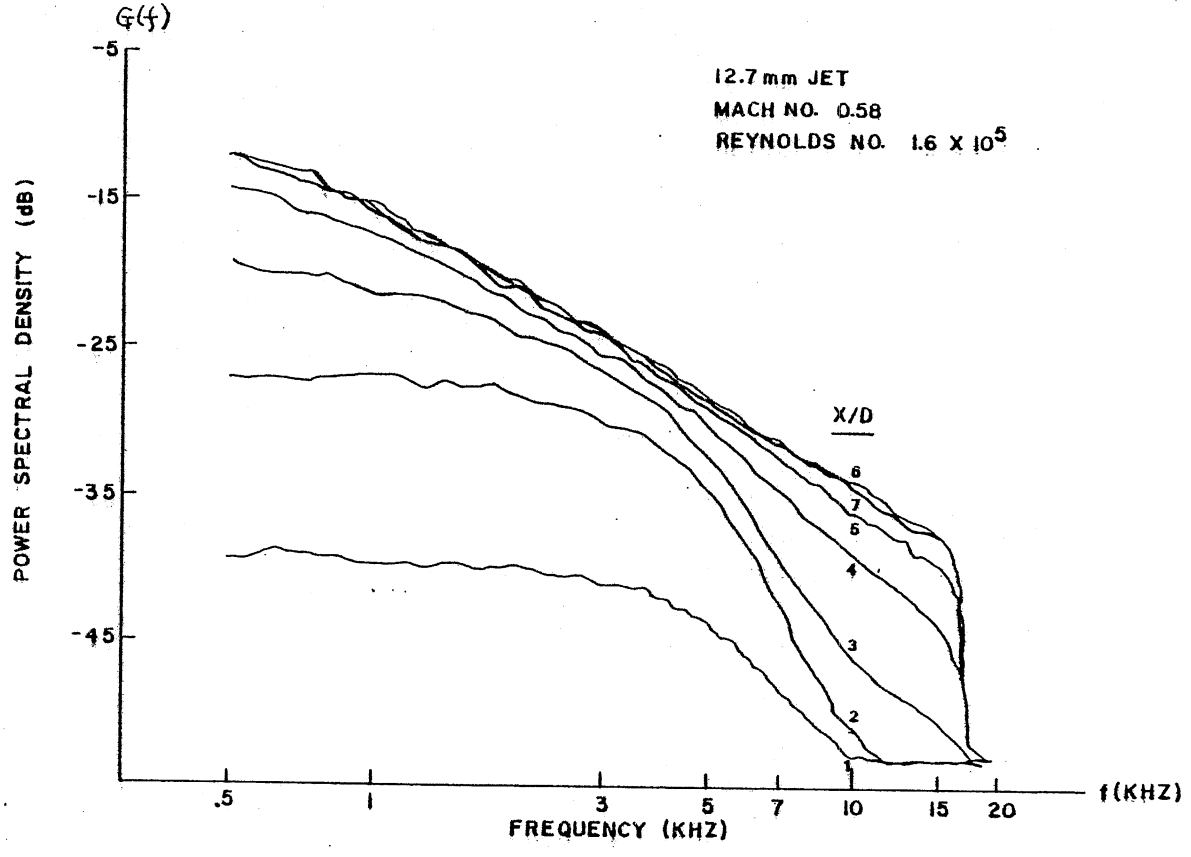

Figure 38: Turbulence u-Component Power Spectral Density at Z/D = 1 (D = 12.7 mm)

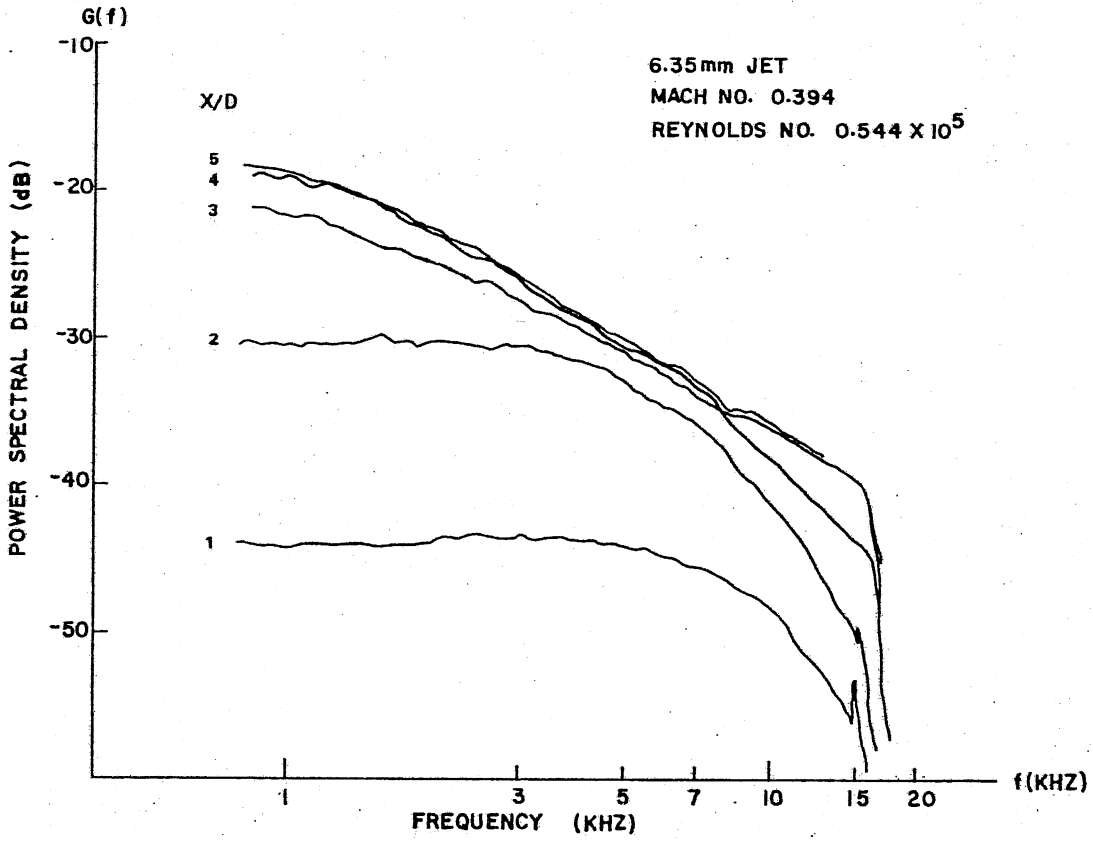

Figure 39: Turbulence u-Component Power Spectral Density at Z/D = 1 (D = 6.35 mm)

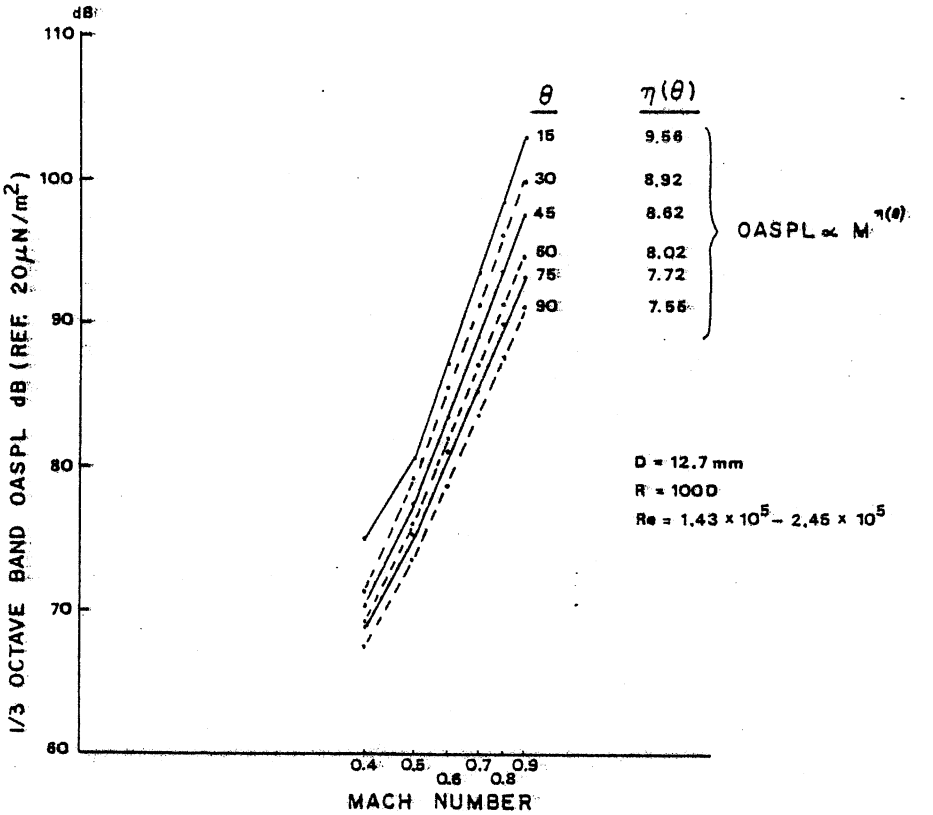

Figure 40: Variation of Overall Sound Pressure Level (OASPL) with Jet Exit Velocity (D = 12.7 mm)

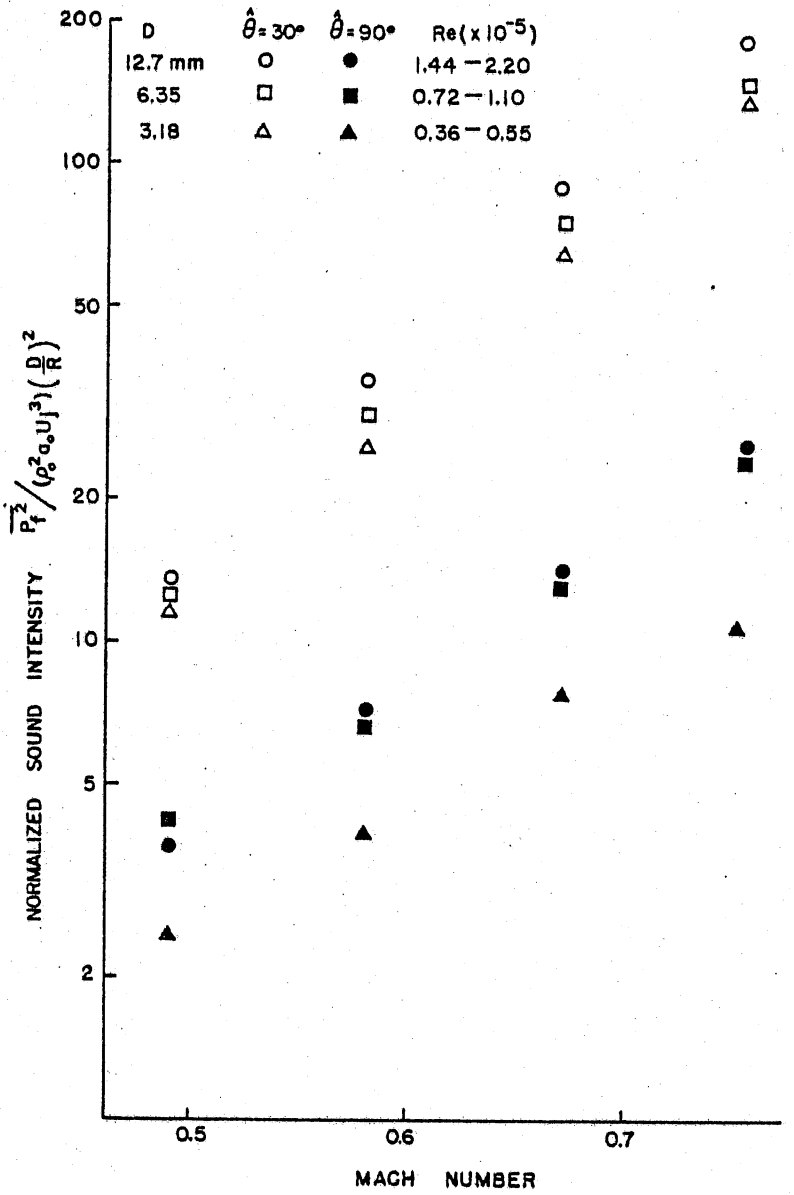

Figure 41: Normalized Sound Intensity Versus Jet Exit Mach Number

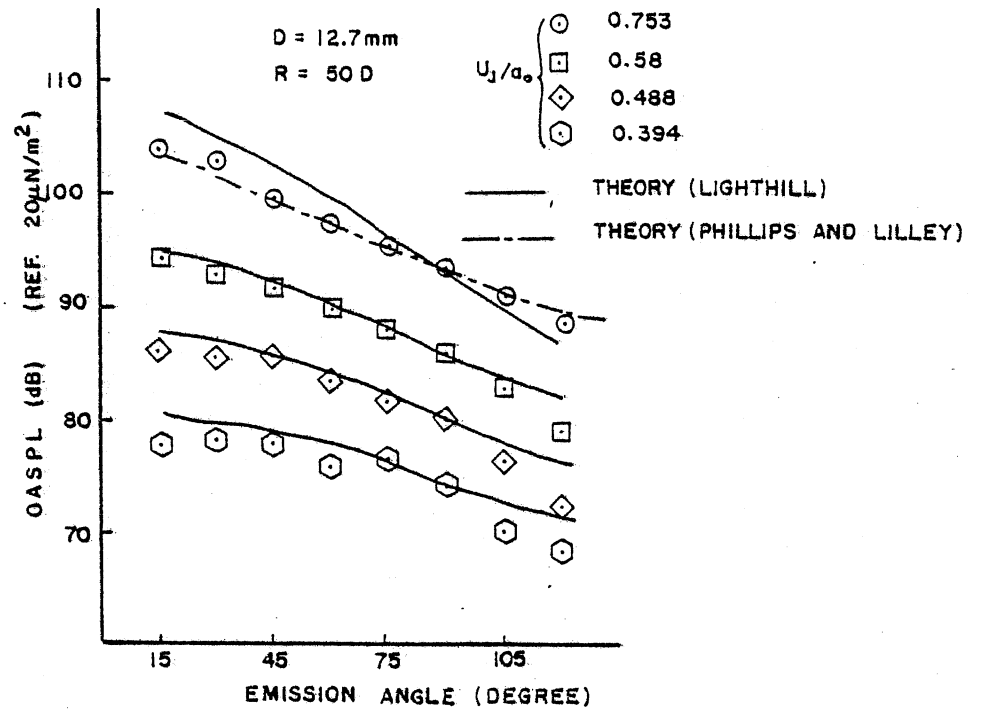

Figure 42: Directivities of the 12.7 mm Jet Compared with Theories

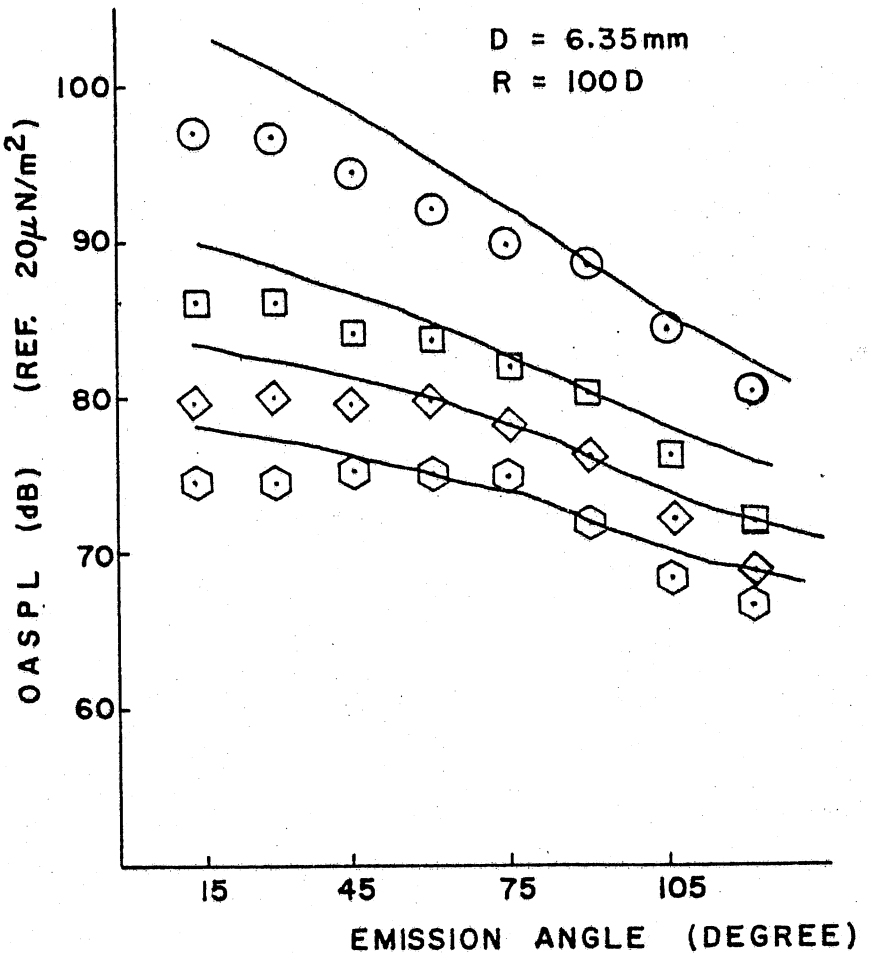

Figure 43: Directivities of the 6.35 mm Jet Compared with Theory (see Figure 42 for Symbols)

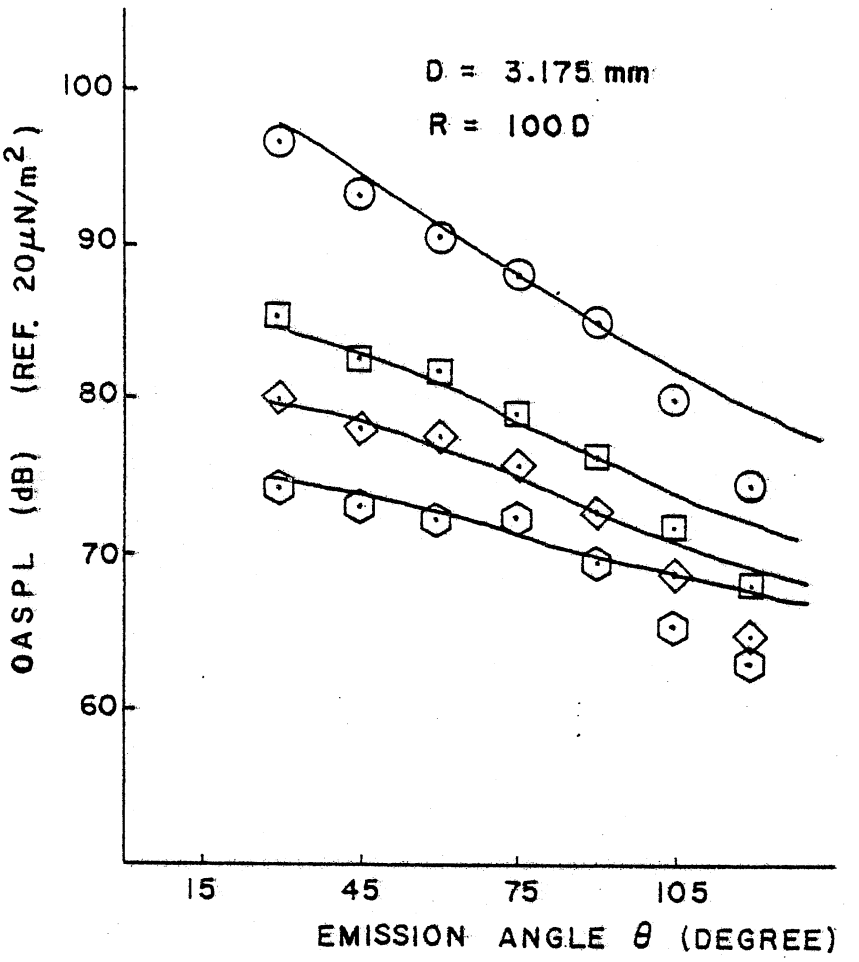

Figure 44: Directivities of the 3.175 mm Jet Compared with Theory (see Figure 42 for Symbols)

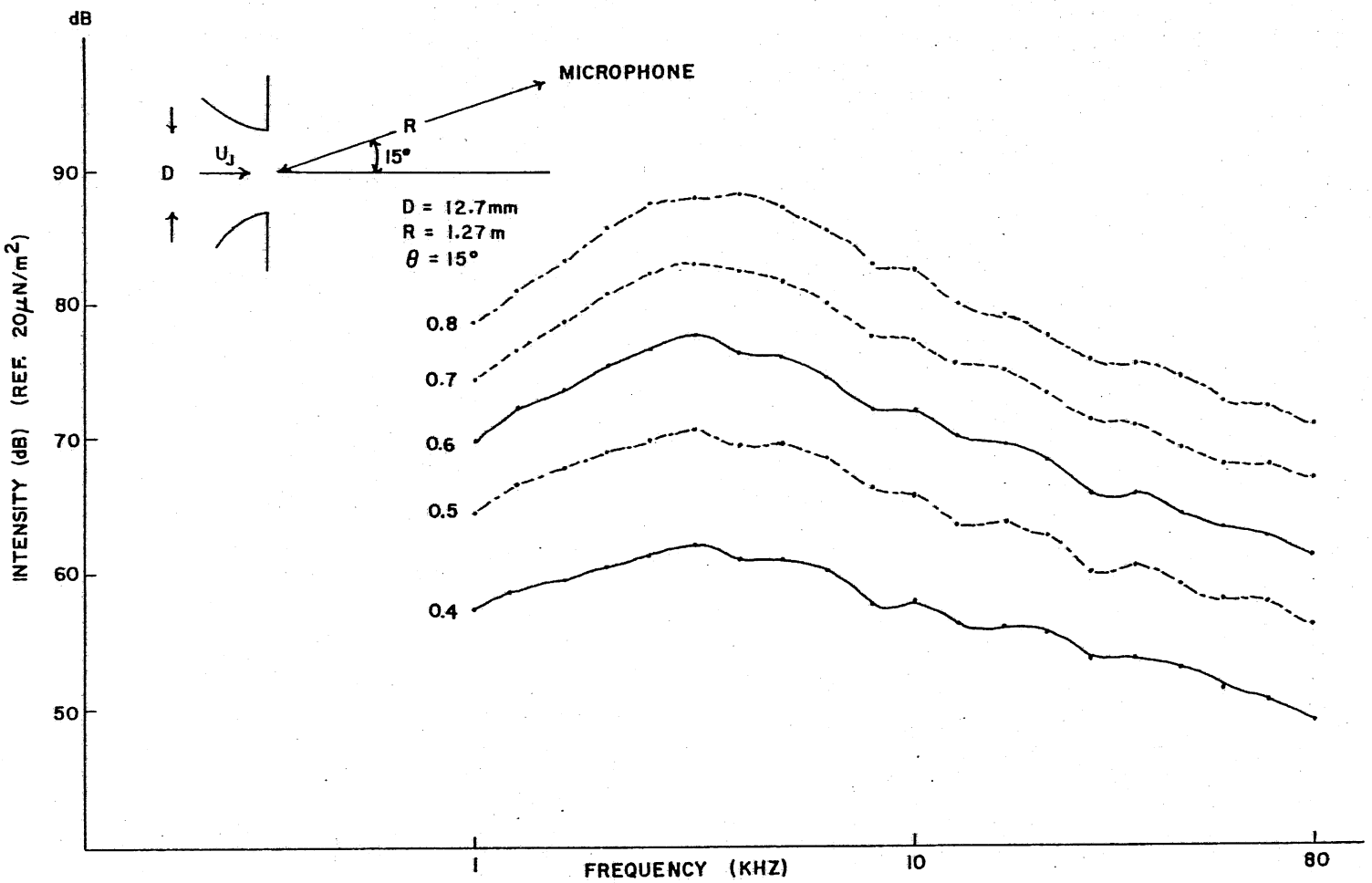

Figure 45: 1/3 Octave Spectra at $\hat{\theta} = 15°$ for Various Jet Exit Velocities (D = 12.7 mm)

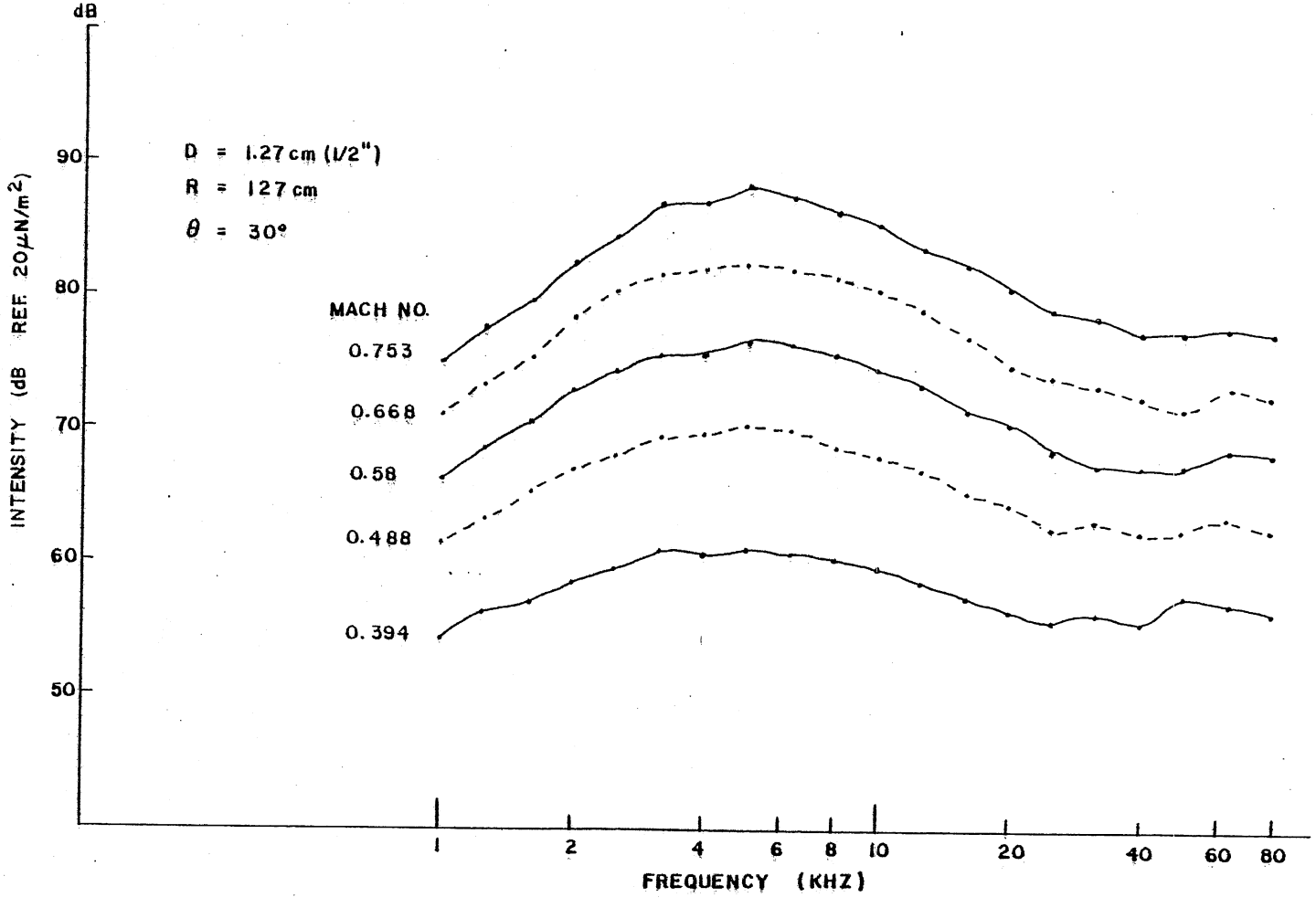

Figure 46: 1/3 Octave Spectra at $\hat{\theta}$ = 30° for Various Jet Exit Velocities (D = 12.7 mm)

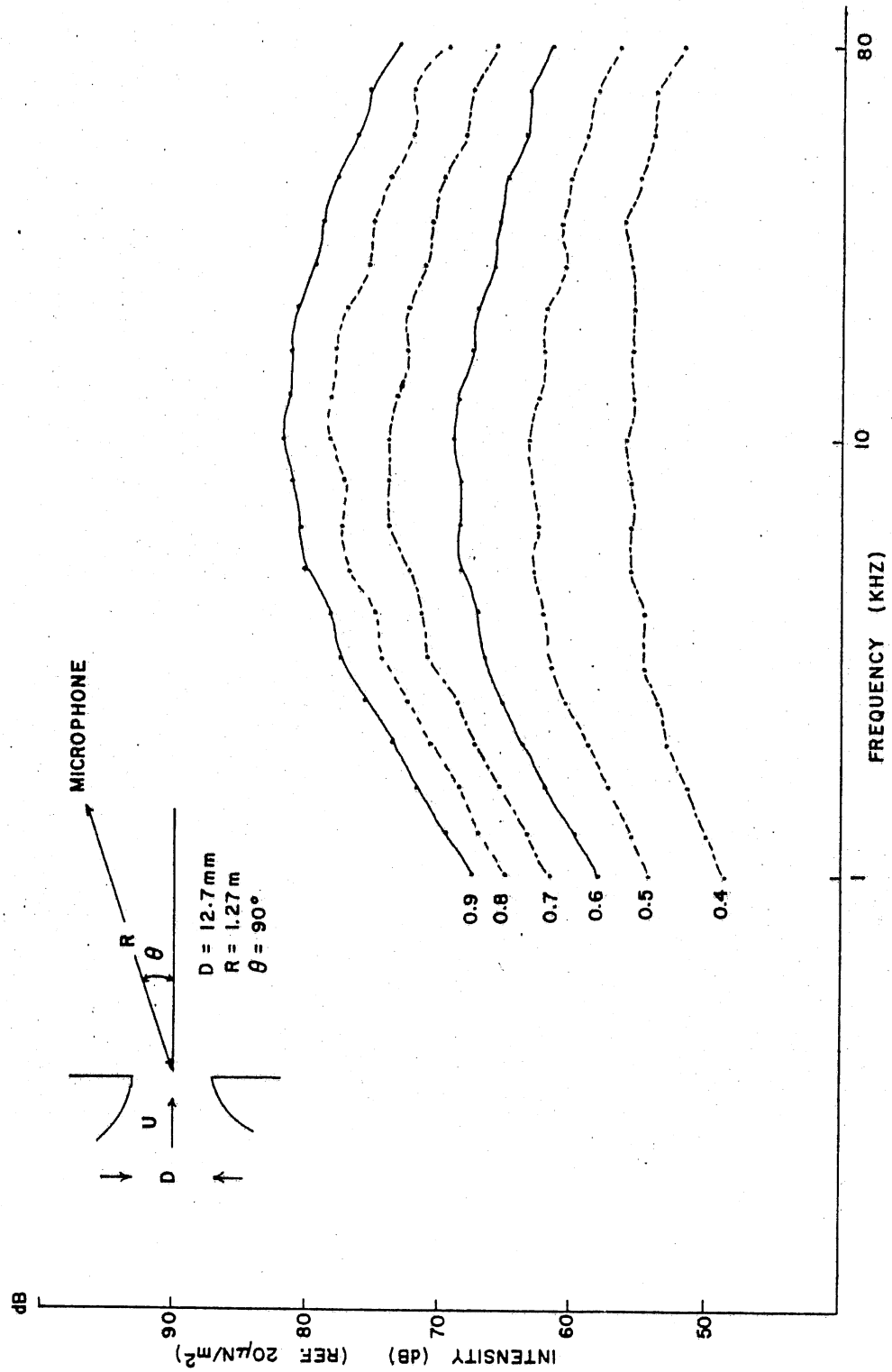

Figure 47: 1/3 Octave Spectra at $\hat{\theta} = 90°$ for Various Jet Exit Velocities (D = 12.7 mm)

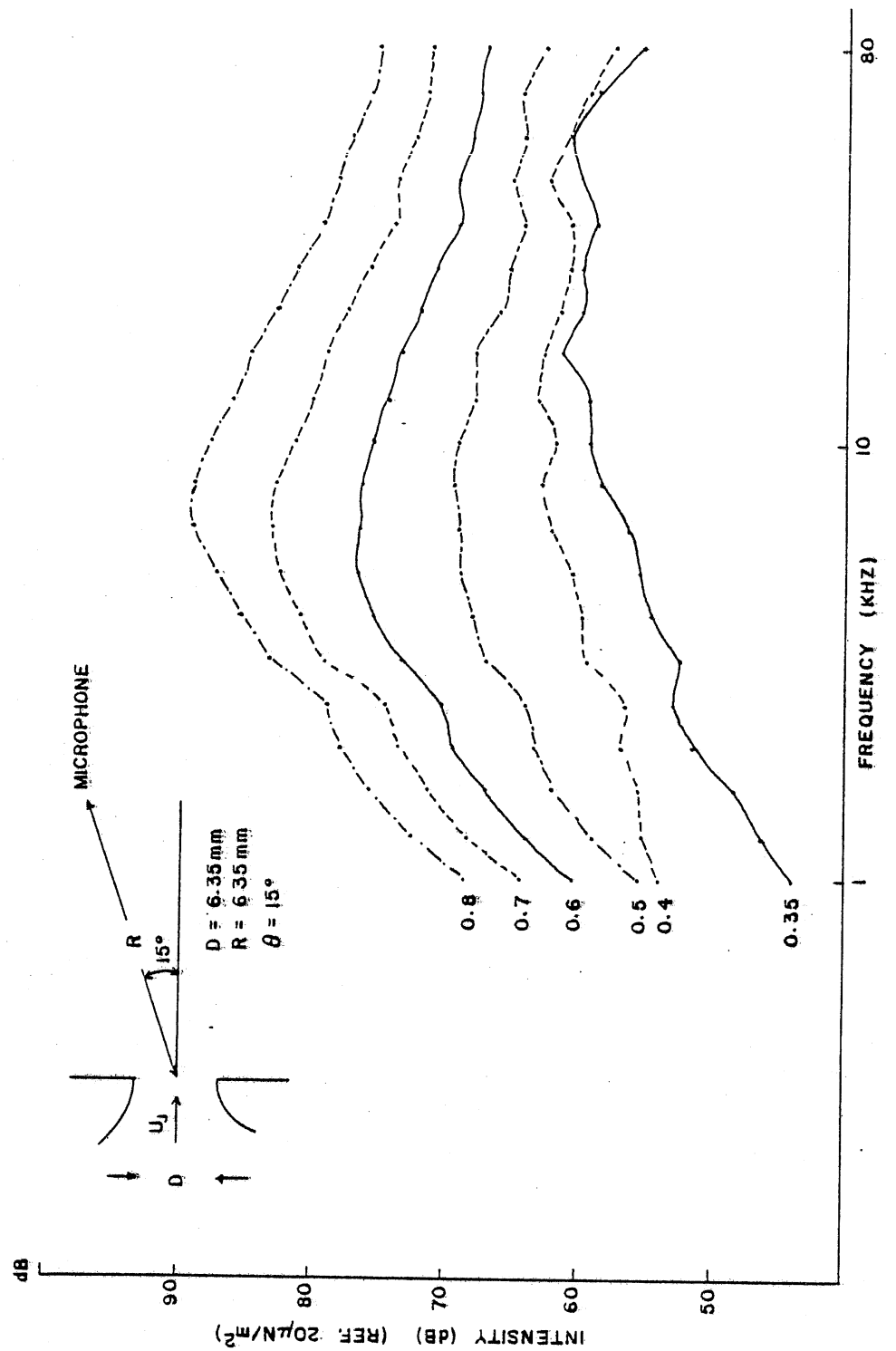

Figure 48: 1/3 Octave Spectra at $\hat{\theta} = 15°$ for Various Jet Exit Velocities (D = 6.35 mm)

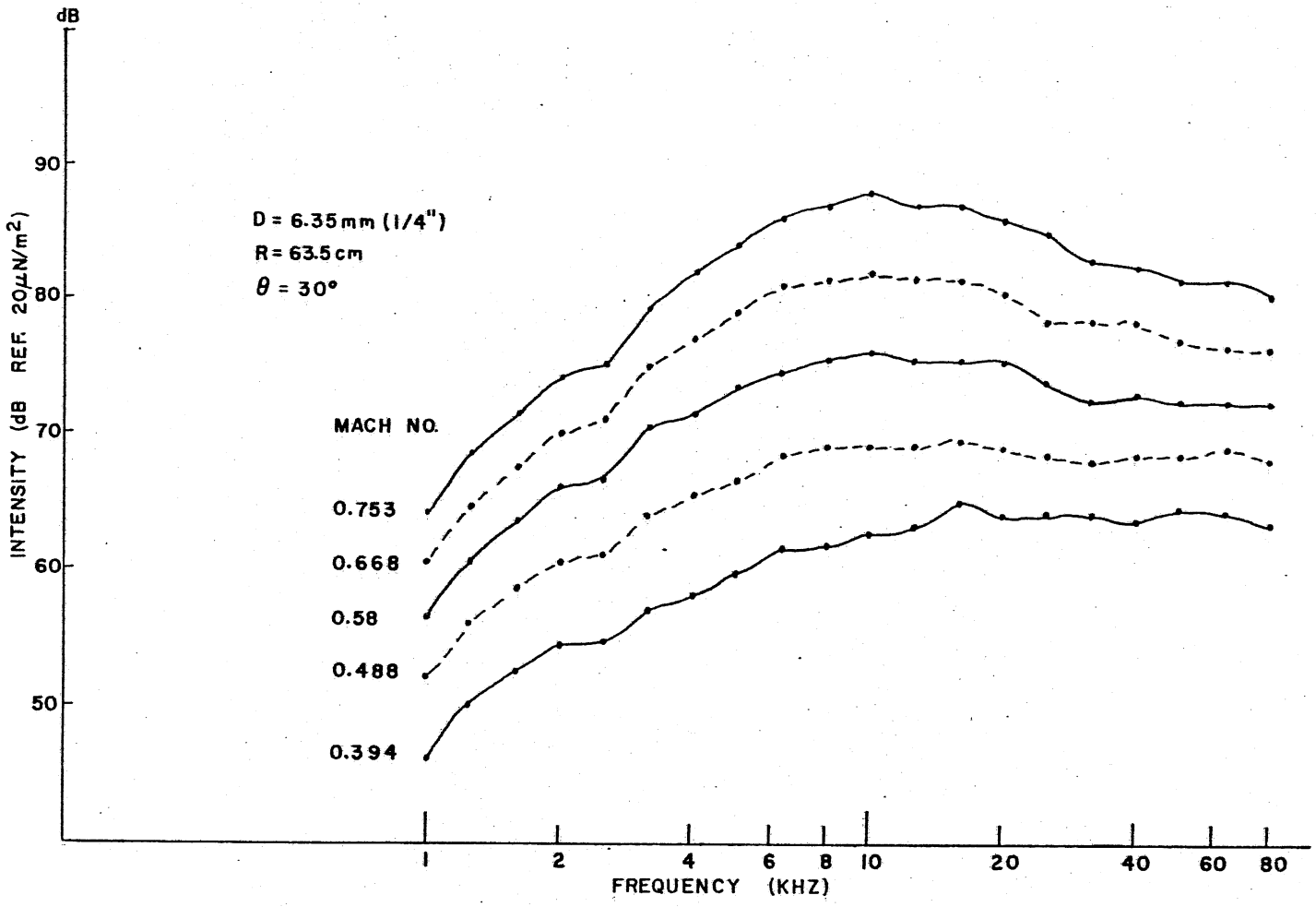

Figure 49: 1/3 Octave Spectra at $\hat{\theta}$ = 30° for Various Jet Exit Velocities (D = 6.35 mm)

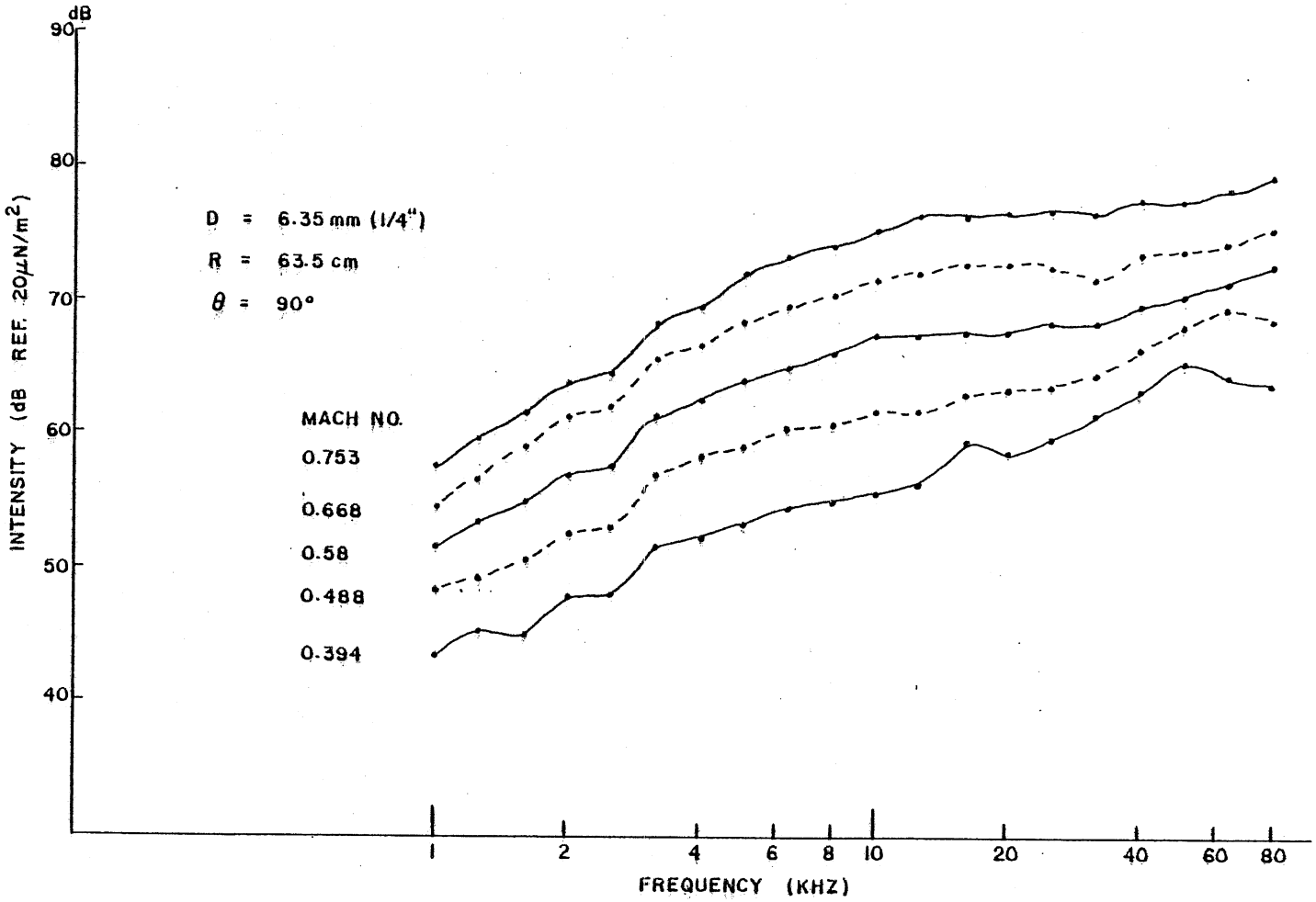

Figure 50: 1/3 Octave Spectra at $\hat{\theta} = 90°$ for Various Jet Exit Velocities (D = 6.35 mm)

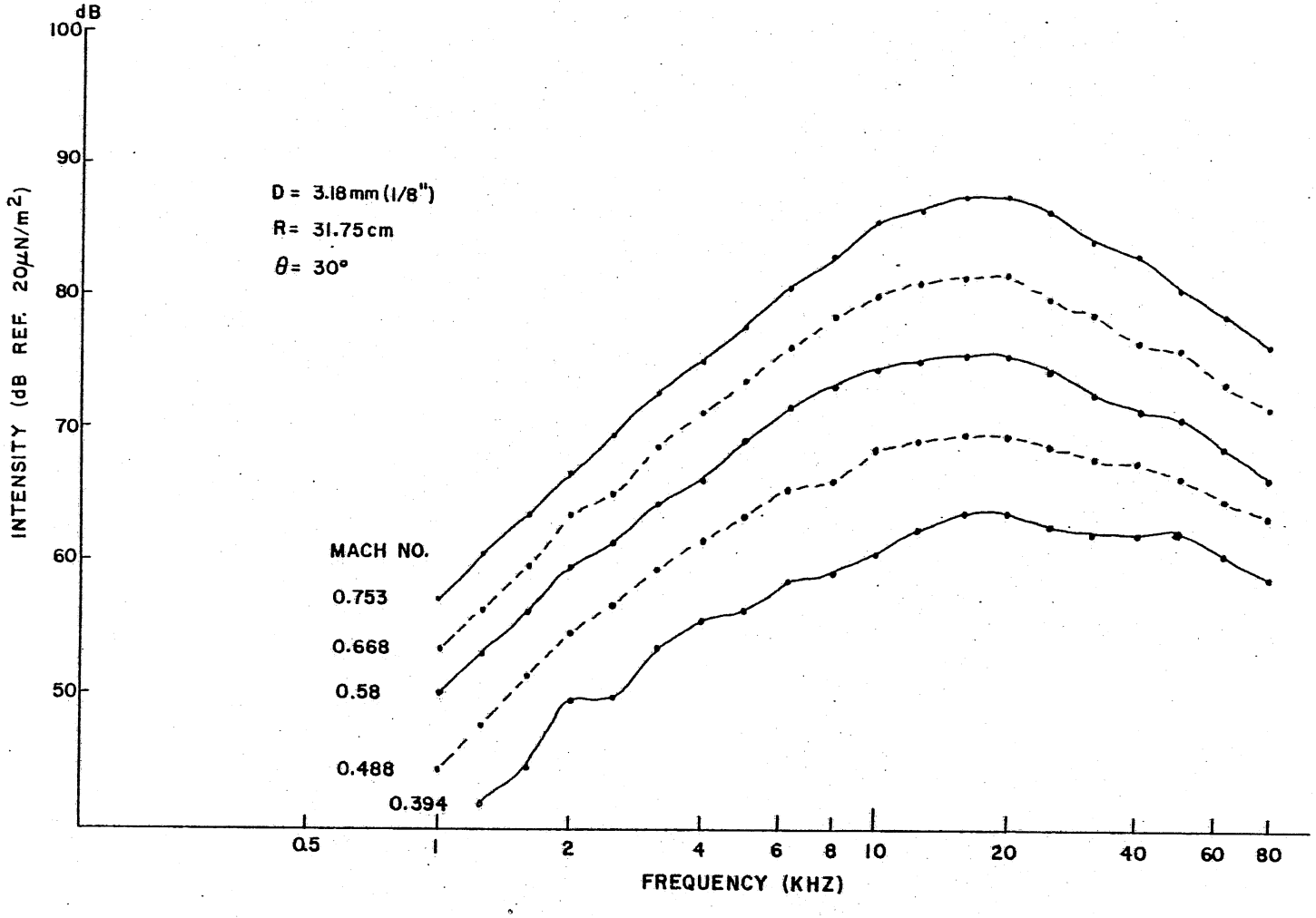

Figure 51: 1/3 Octave Spectra at $\hat{\theta}$ = 30° for Various Jet Exit Velocities (D = 3.18 mm)

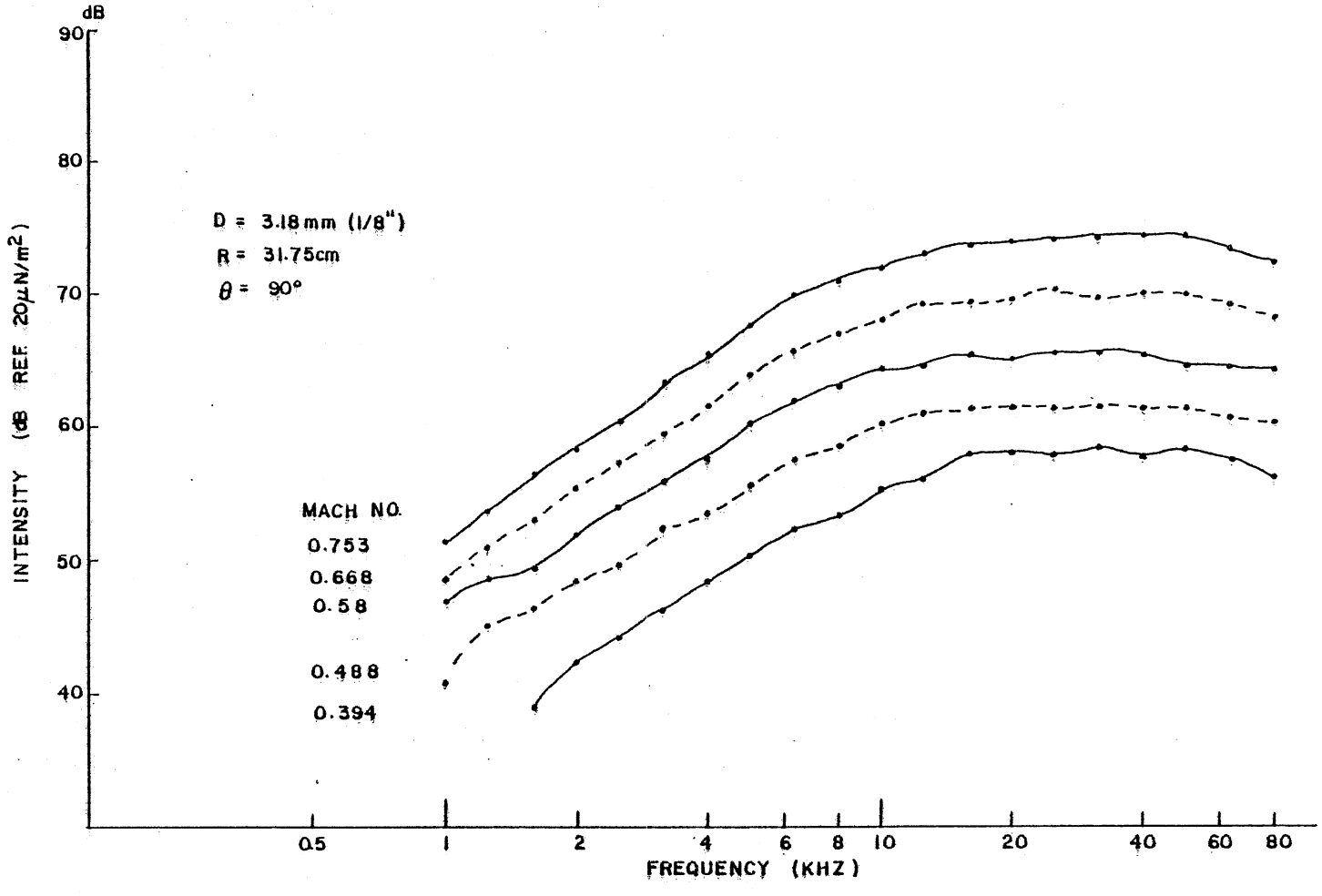

Figure 52: 1/3 Octave Spectra at $\hat{\theta} = 90°$ for Various Jet Exit Velocities (D = 3.18 mm)

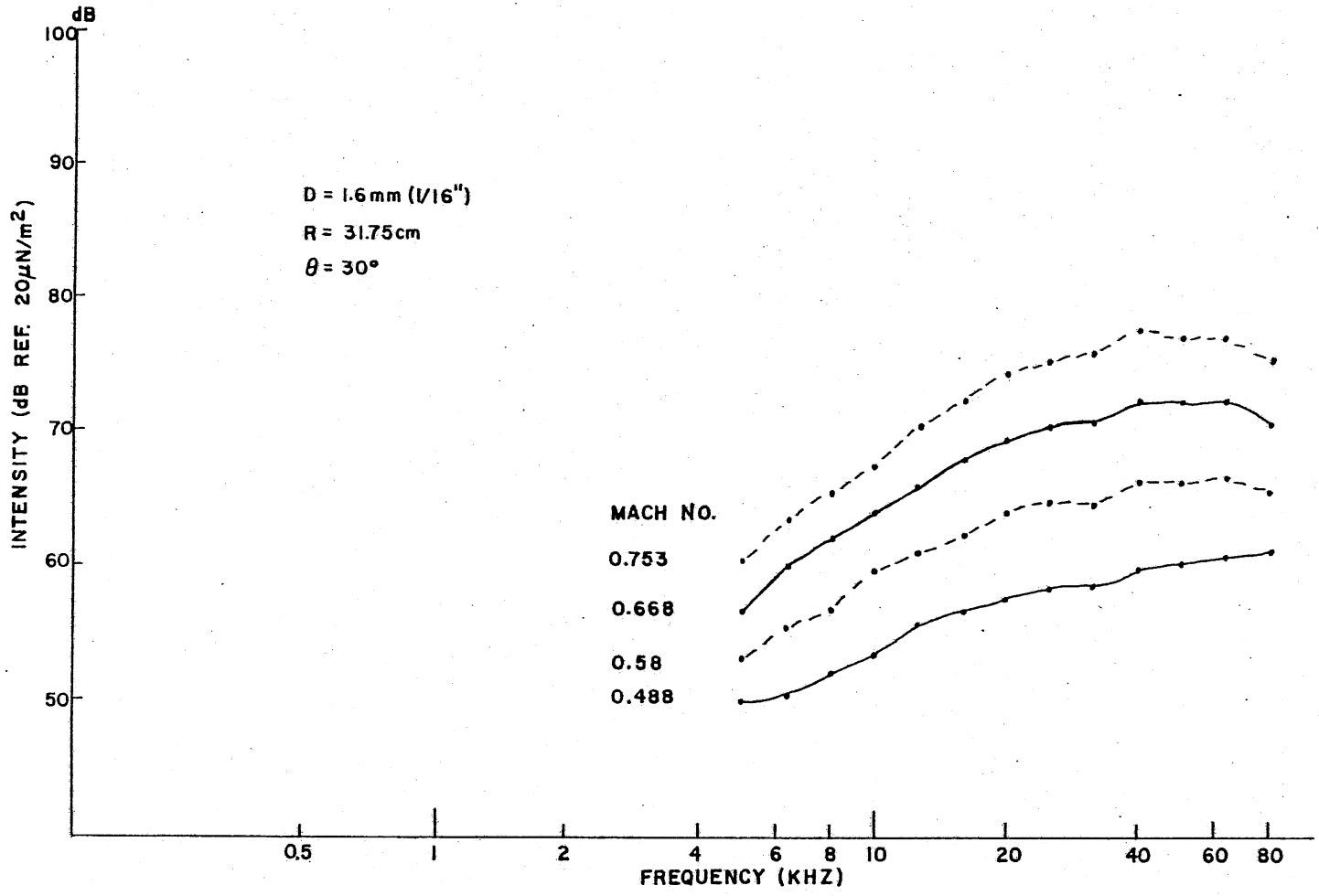

Figure 53: 1/3 Octave Spectra at $\hat{\theta}$ = 30° for Various Jet Exit Velocities (D = 1.6 mm)

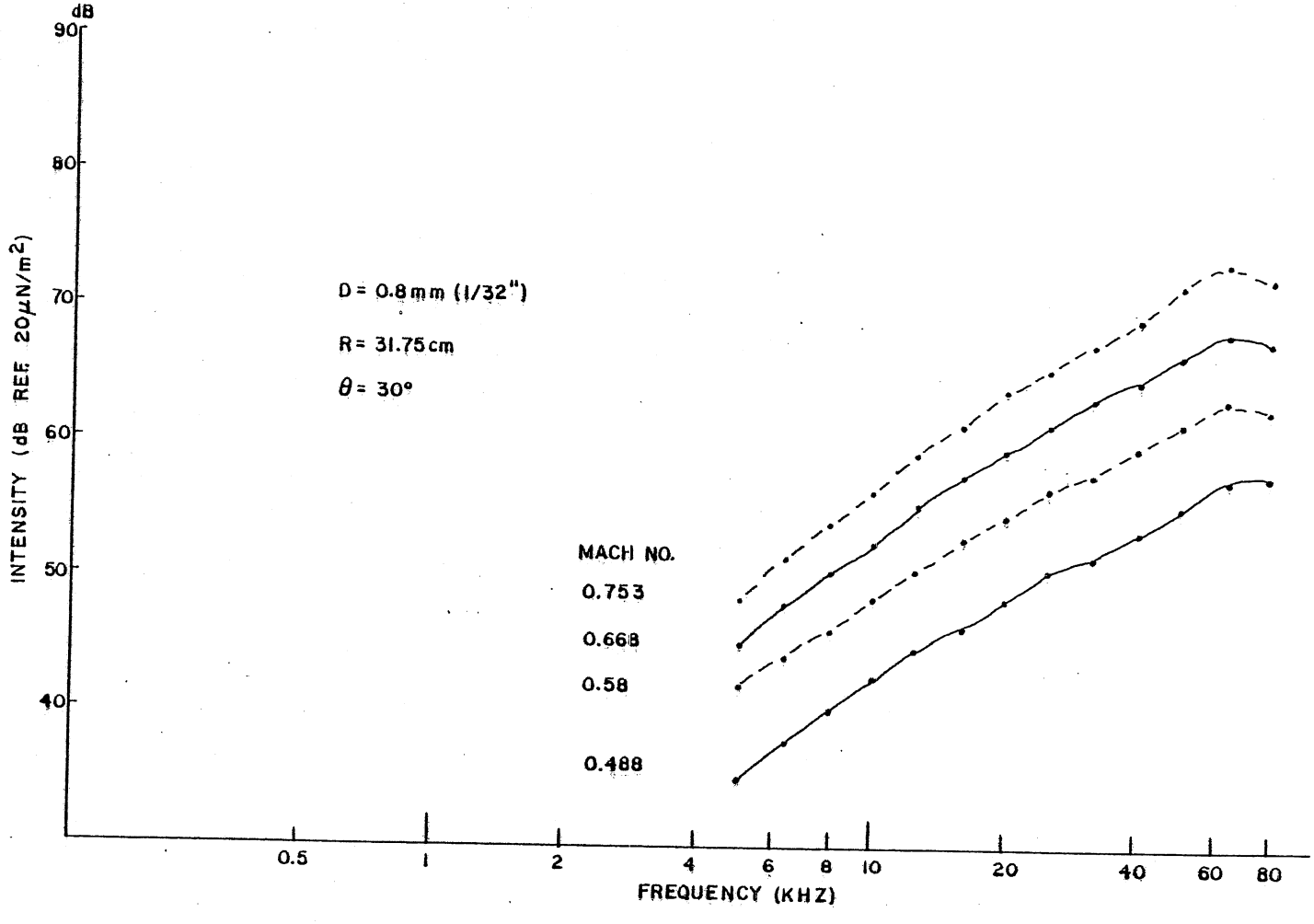

Figure 54: 1/3 Octave Spectra at $\hat{\theta}$ = 30° for Various Jet Exit Velocities (D = 0.8 mm)

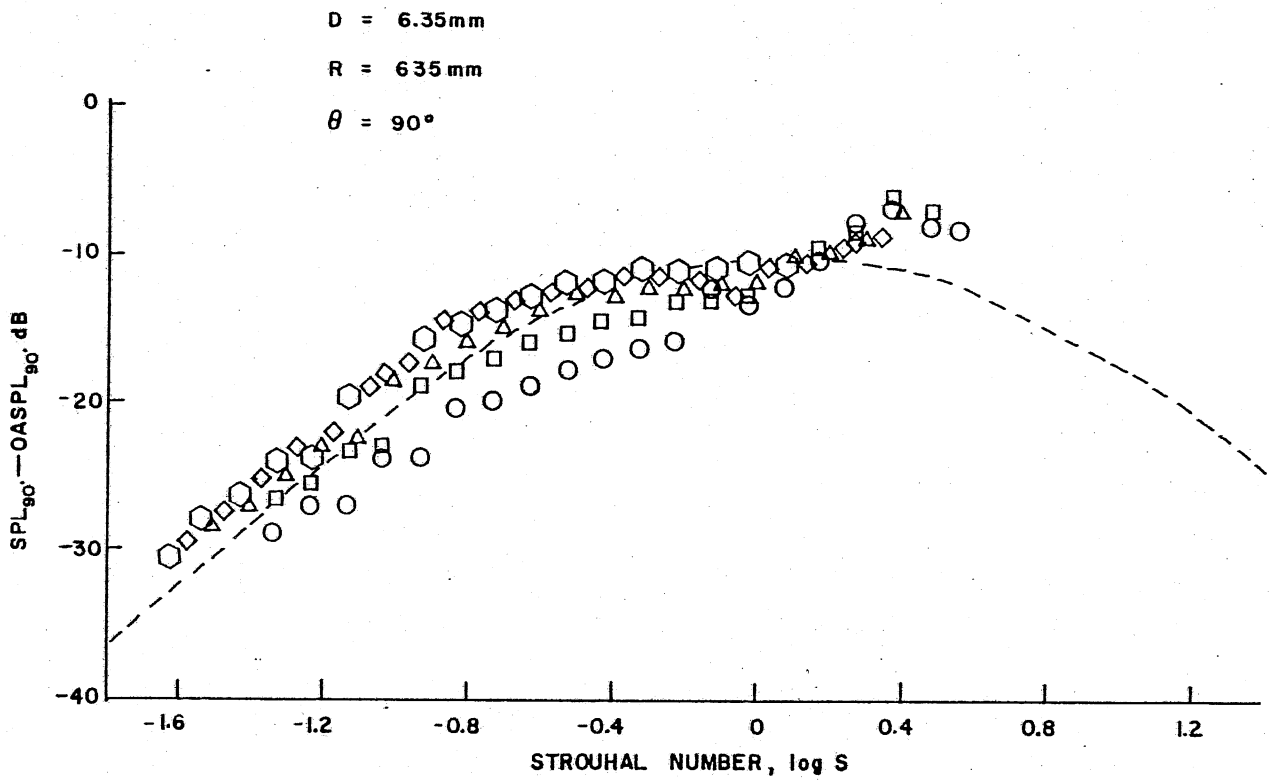

Figure 55: Sound Pressure Level Spectra of the 12.7 mm Jet at $\hat{\theta} = 90°$ for Various Jet Velocities

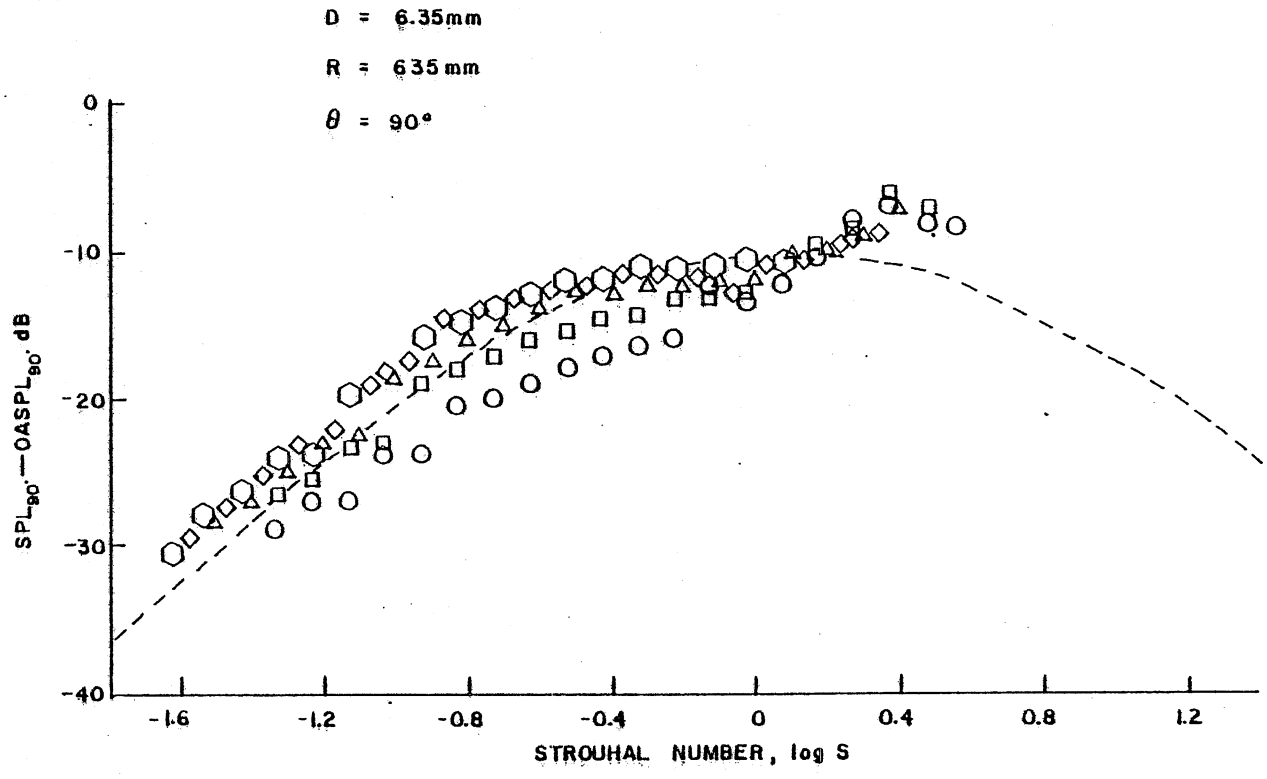

Figure 56: Sound Pressure Level Spectra of the 6.35 mm Jet at $\hat{\theta} = 90°$ for Various Jet Velocities (See Figure 55 for Symbols)

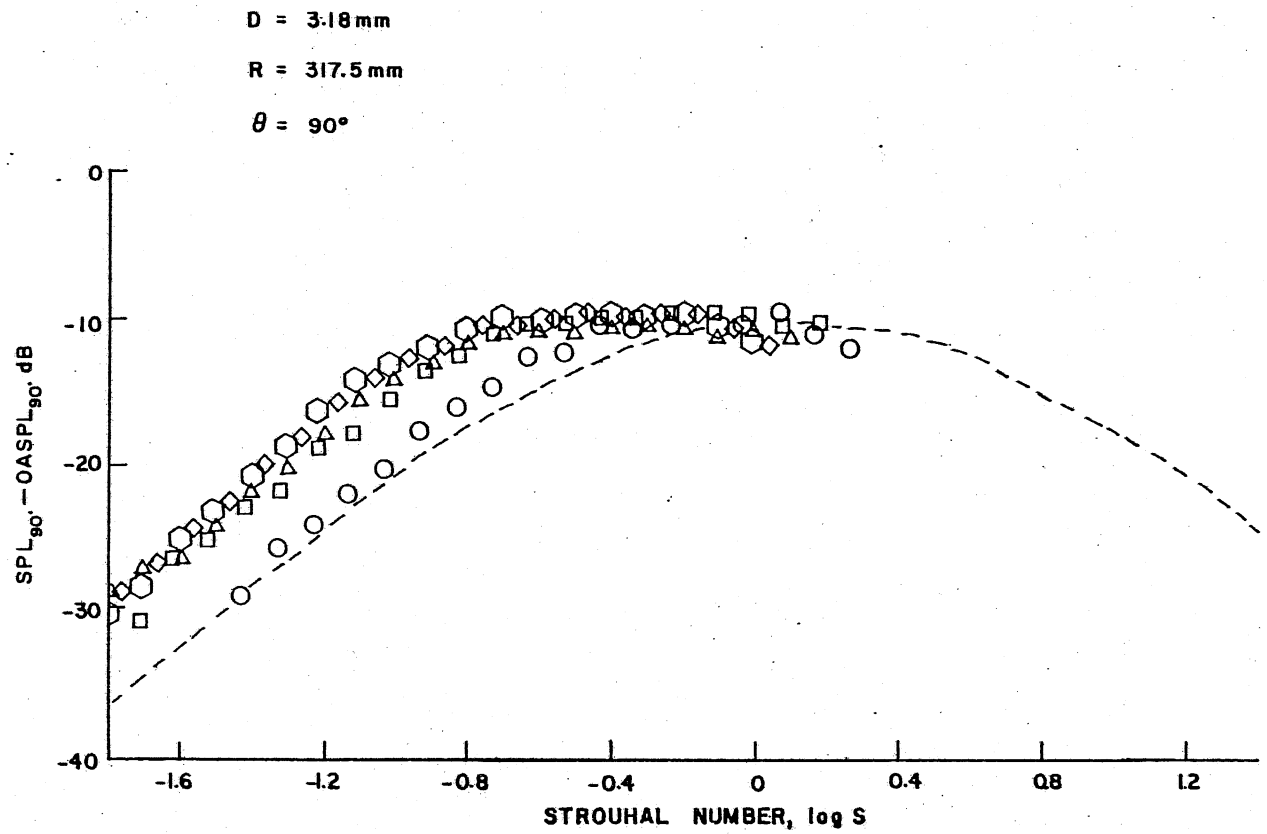

Figure 57: Sound Pressure Level Spectra of the 3.18 mm Jet at $\hat{\theta}$ = 90° for Various Jet Velocities (See Figure 55 for Symbols

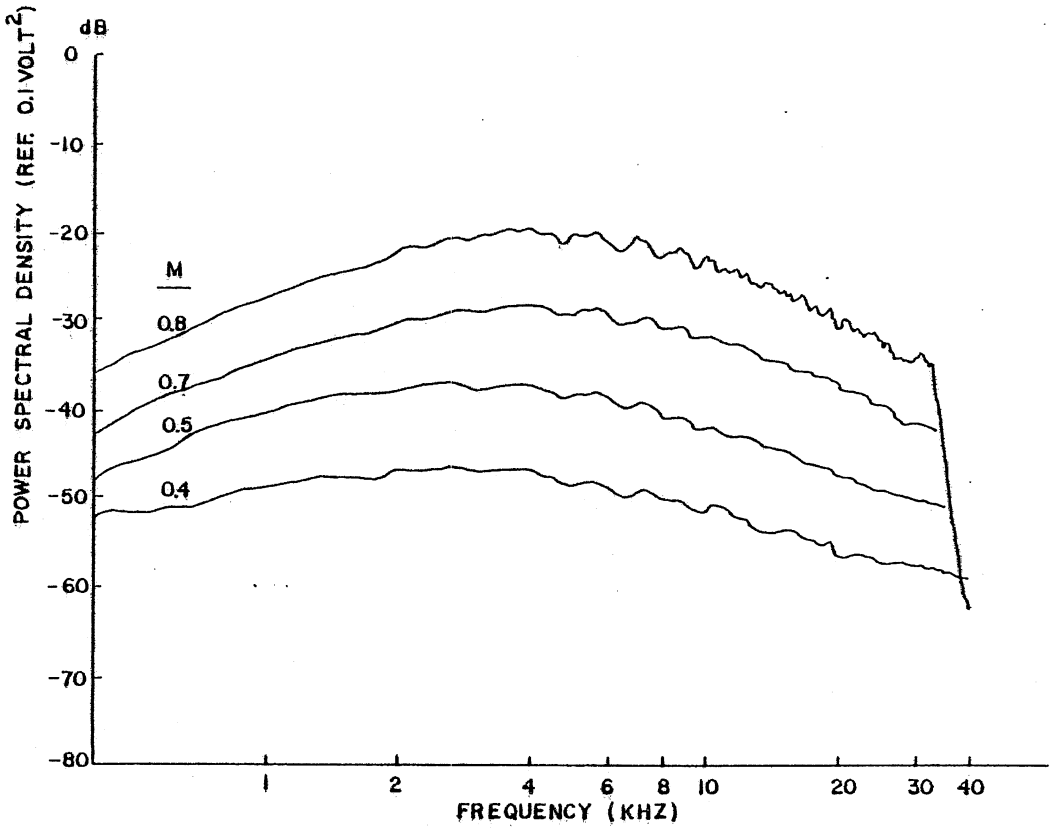

Figure 58: Power Spectral Density of the Noise from the 12.7 mm Jet at $\hat{\theta}$ = 30° for Various Jet Velocities

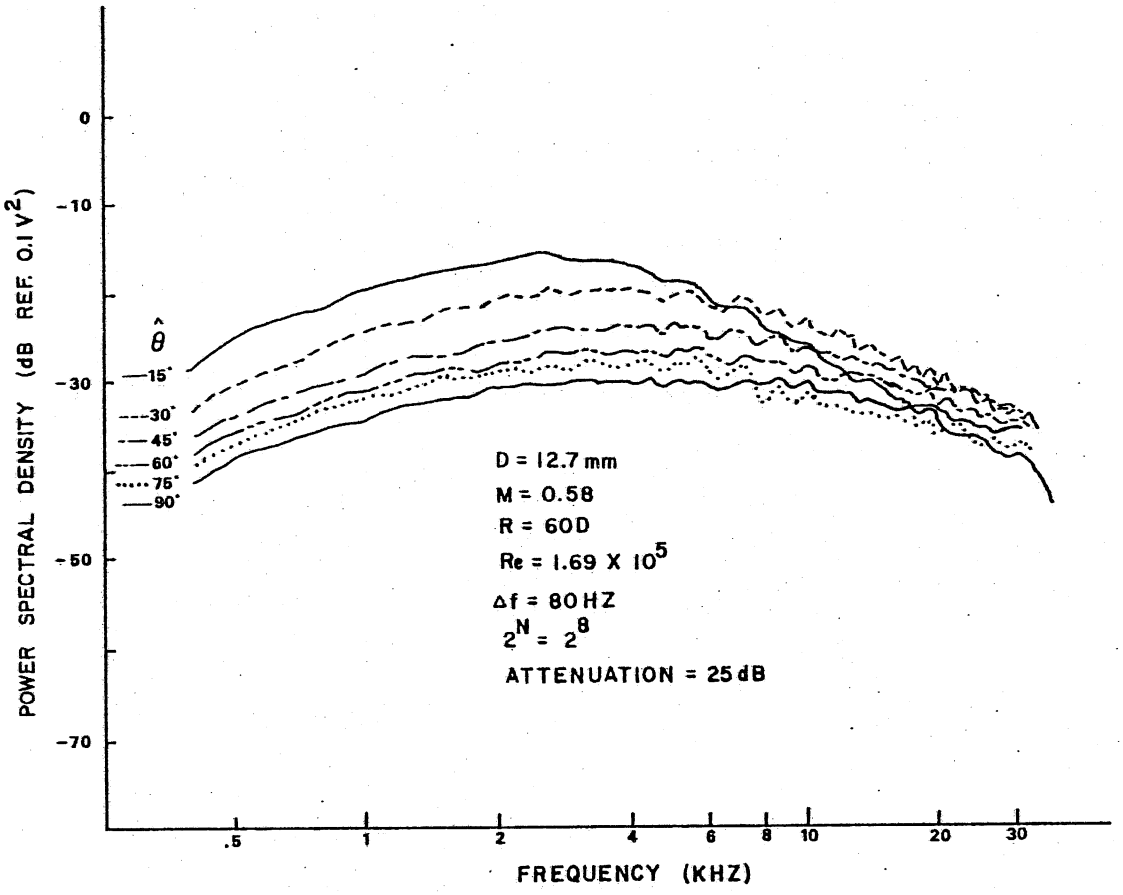

Figure 59: Power Spectral Density of the 12.7 mm Jet Noise at Various Radiation Angles

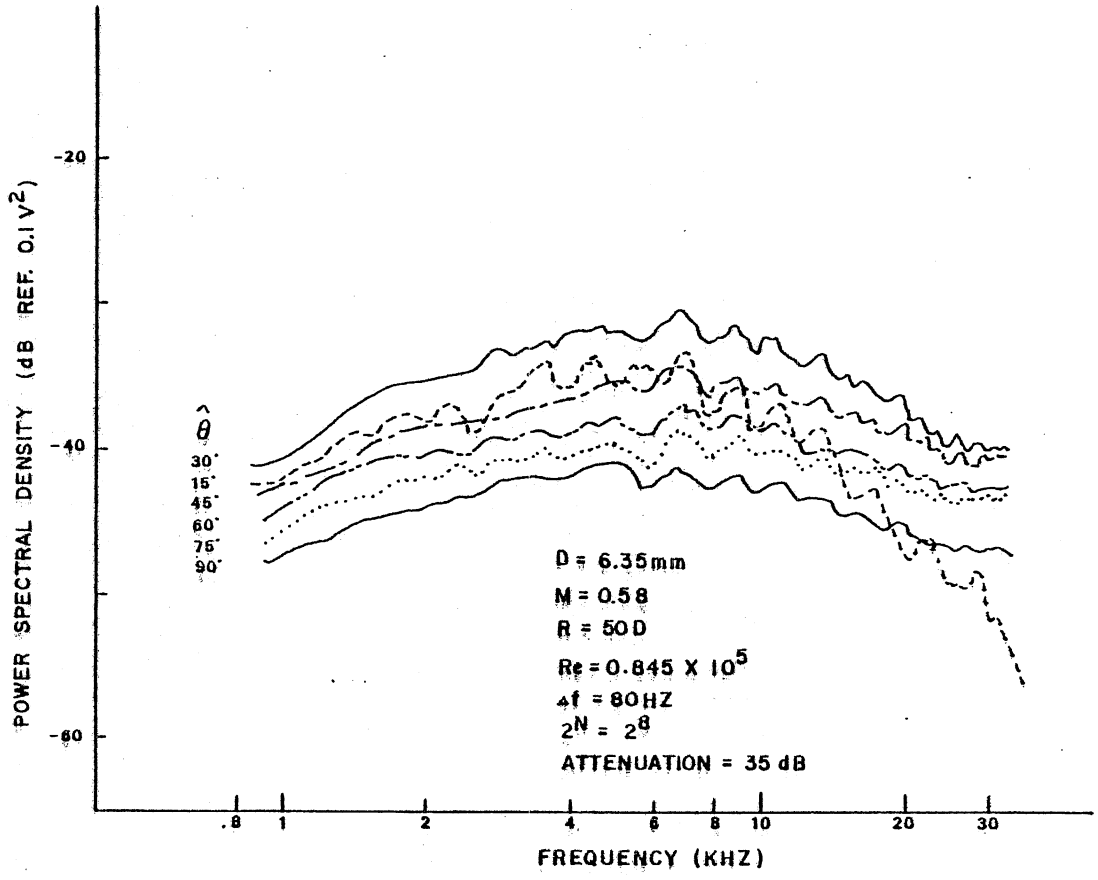

Figure 60: Power Spectral Density of the 6.35 mm Jet Noise at Various Radiation Angles

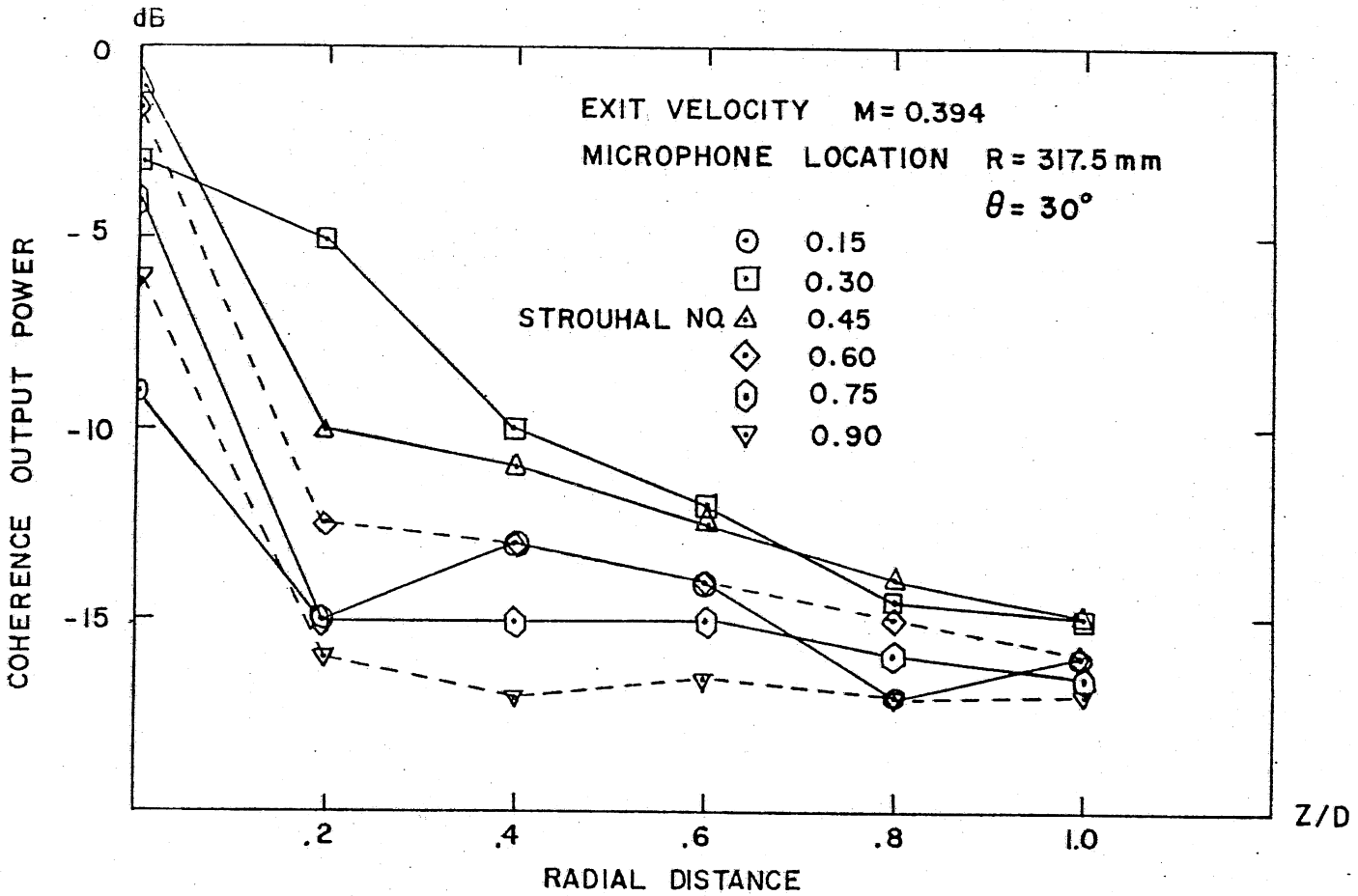

Figure 61: Coherent Output Power of the 6.35 mm Jet at Various Radial Locations at X/D = 4

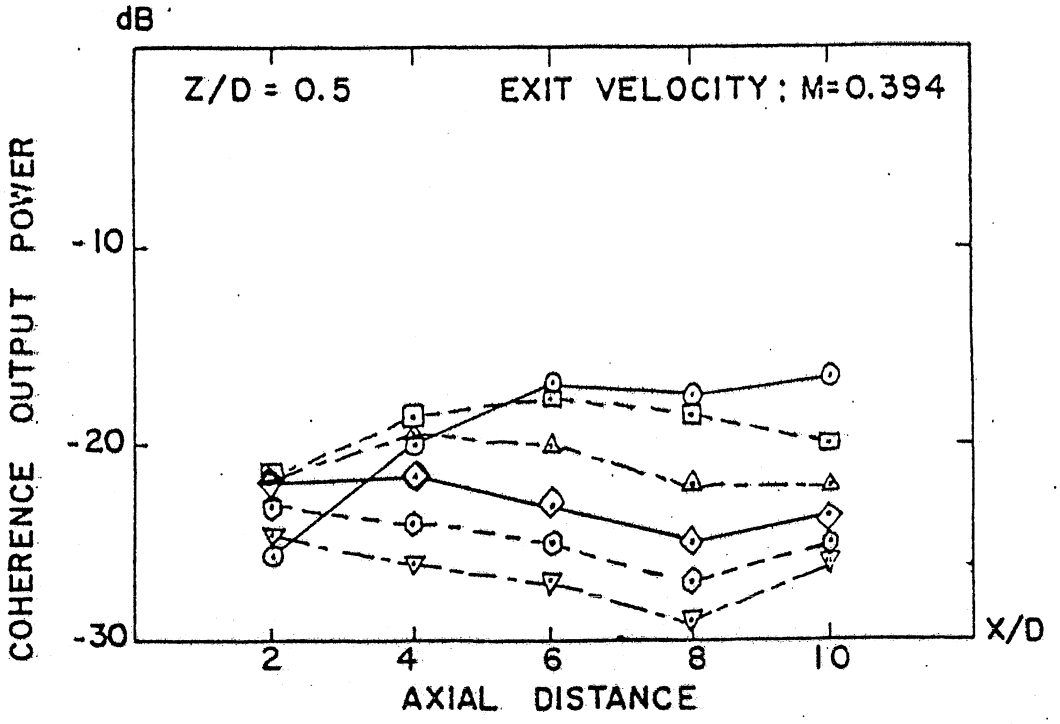

Figure 62a: Coherent Output Power of the 6.35 mm Jet at Z/D = 0.5

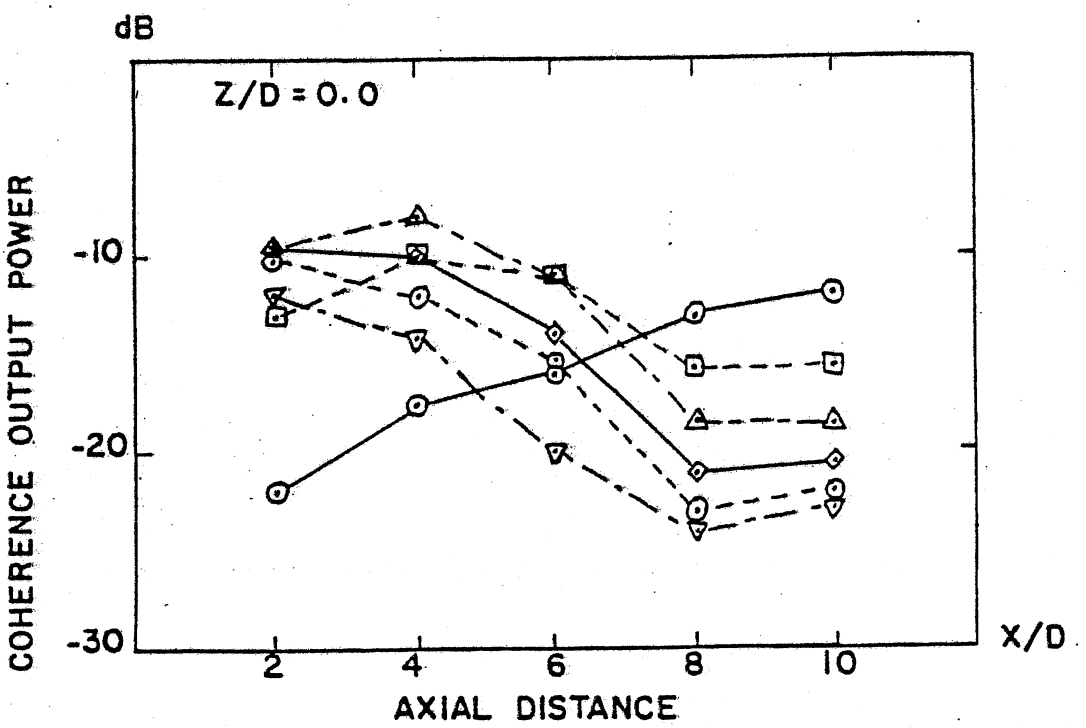

Figure 62b: Coherent Output Power of the 6.35 mm Jet at Z/D = 0 (see
M = 0.488, $\hat{\theta}$ = 30°

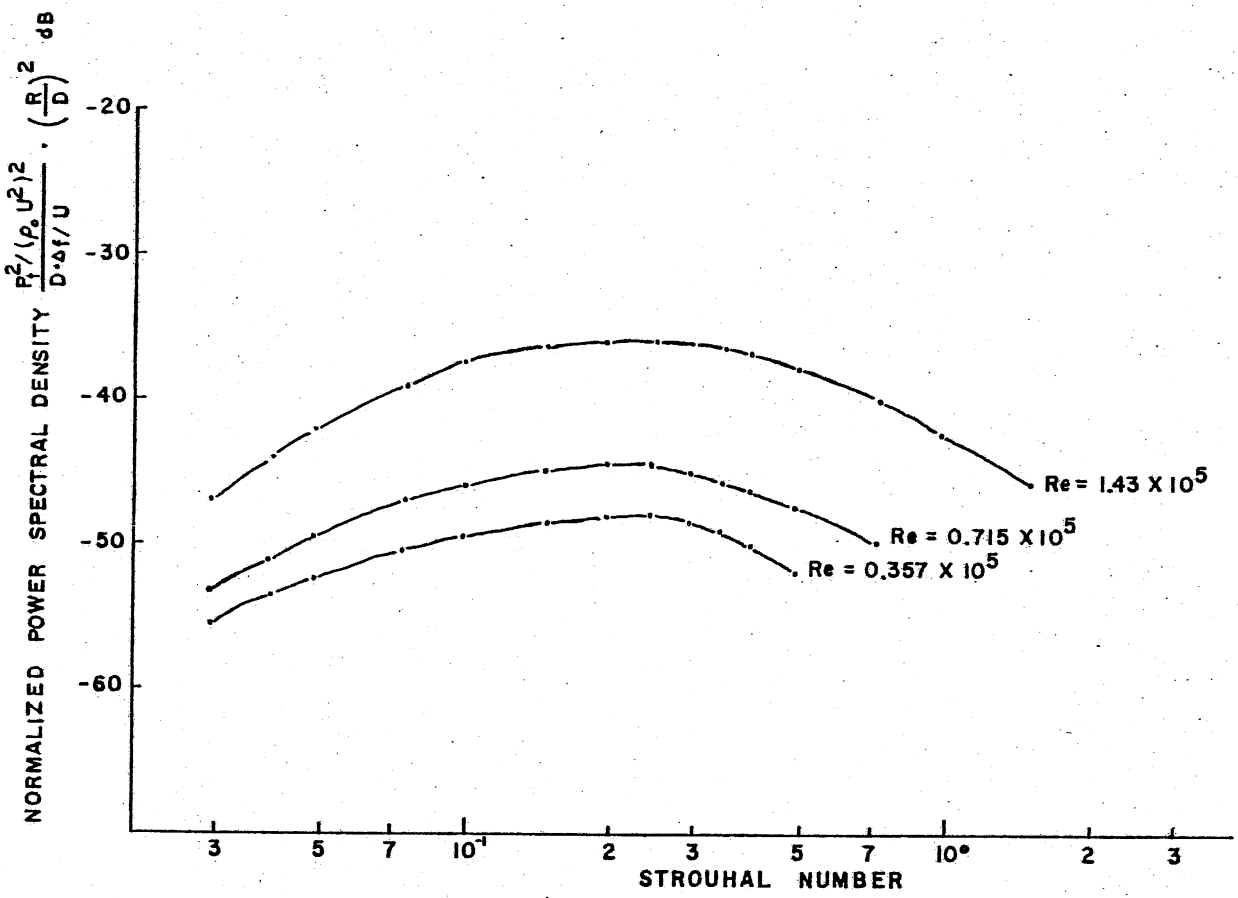

Figure 63: Power Spectral Density-Reynolds Number Relationship at M = 0.488, $\hat{\theta}$ = 30°

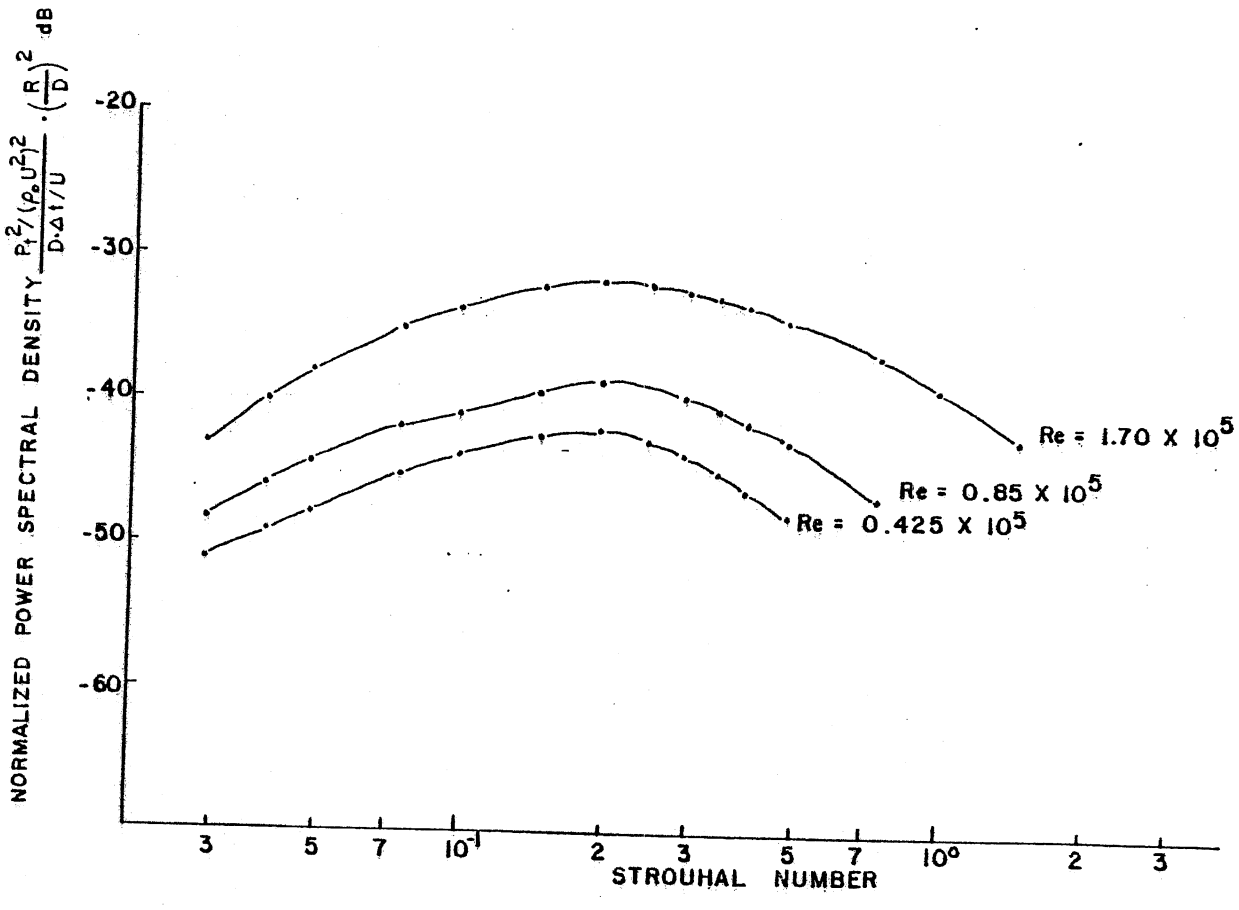

Figure 64: Power Spectral Density-Reynolds Number Relationship at M = 0.58, $\hat{\theta}$ = 30°

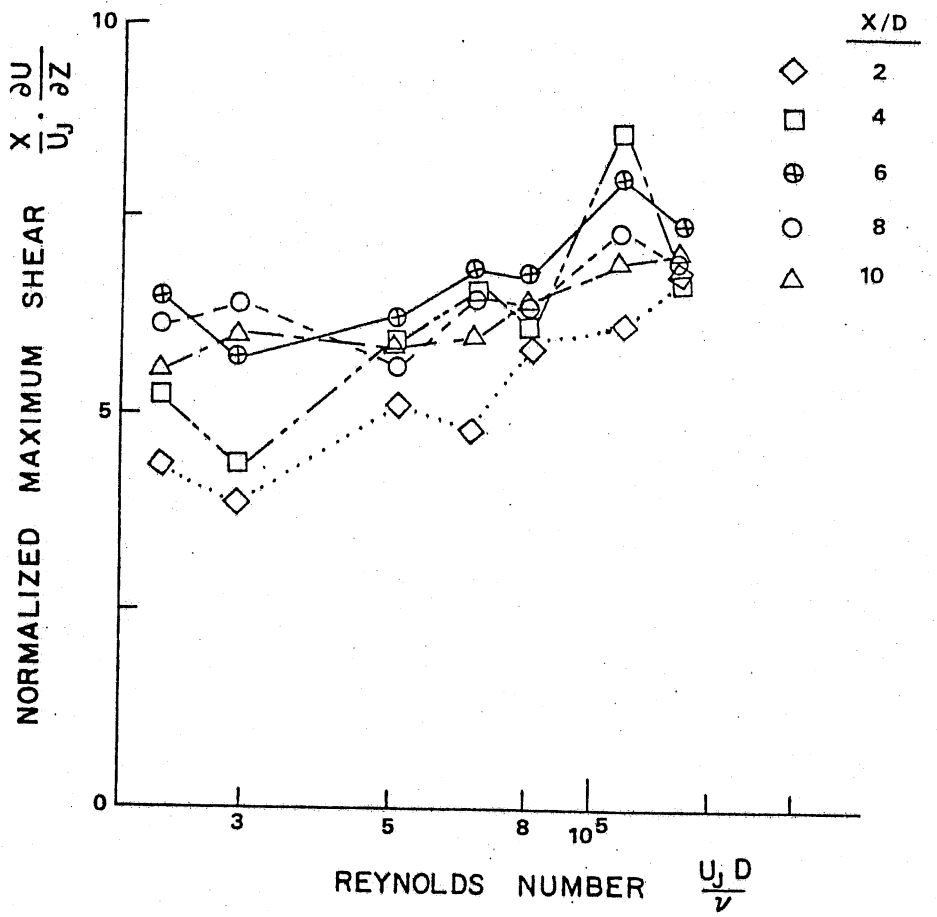

Figure 65: Normalized Maximum Shear as a Function of Reynolds Number

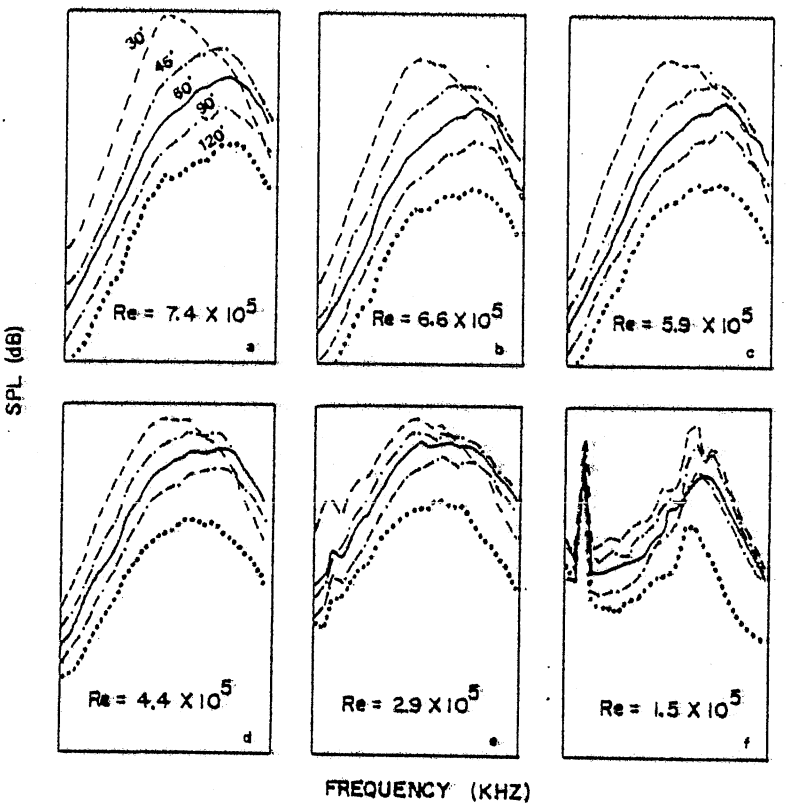

Figure 66: 1/3 Octave Spectra for Nozzle Diameter of 1.52 inch. Jet Velocity Values: (a) 1000 ft/s; (b) 900 ft/s; (c) 800 ft/s; (d) 600 ft/s; (e) 400 ft/s; (f) 200 ft/s. Values for θ are given in (a) (AHUJA et al., 1973)

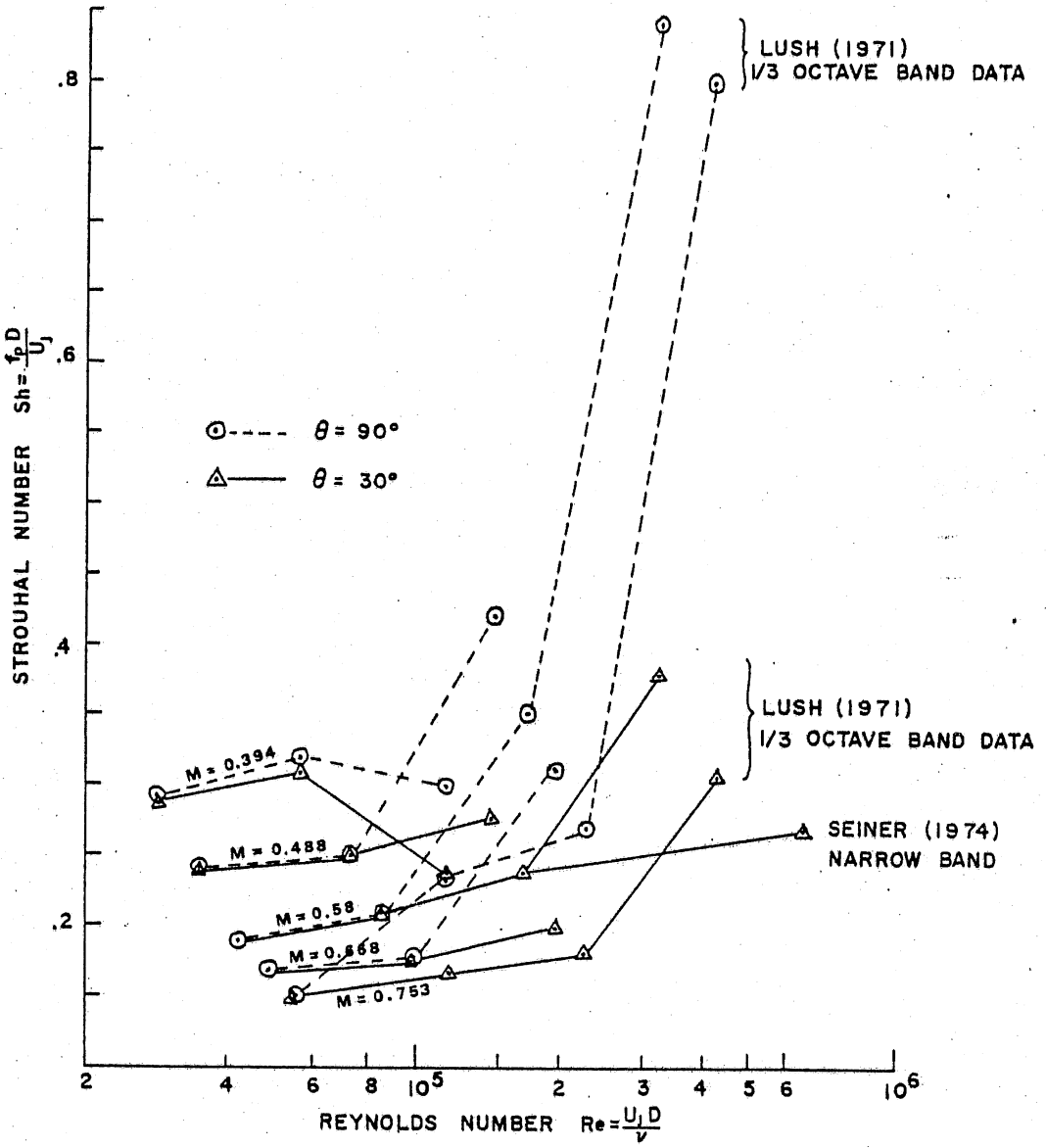

Figure 67: Narrow-Band Peak Frequency of Jet Noise as a Function of Reynolds Number at Various Mach Numbers

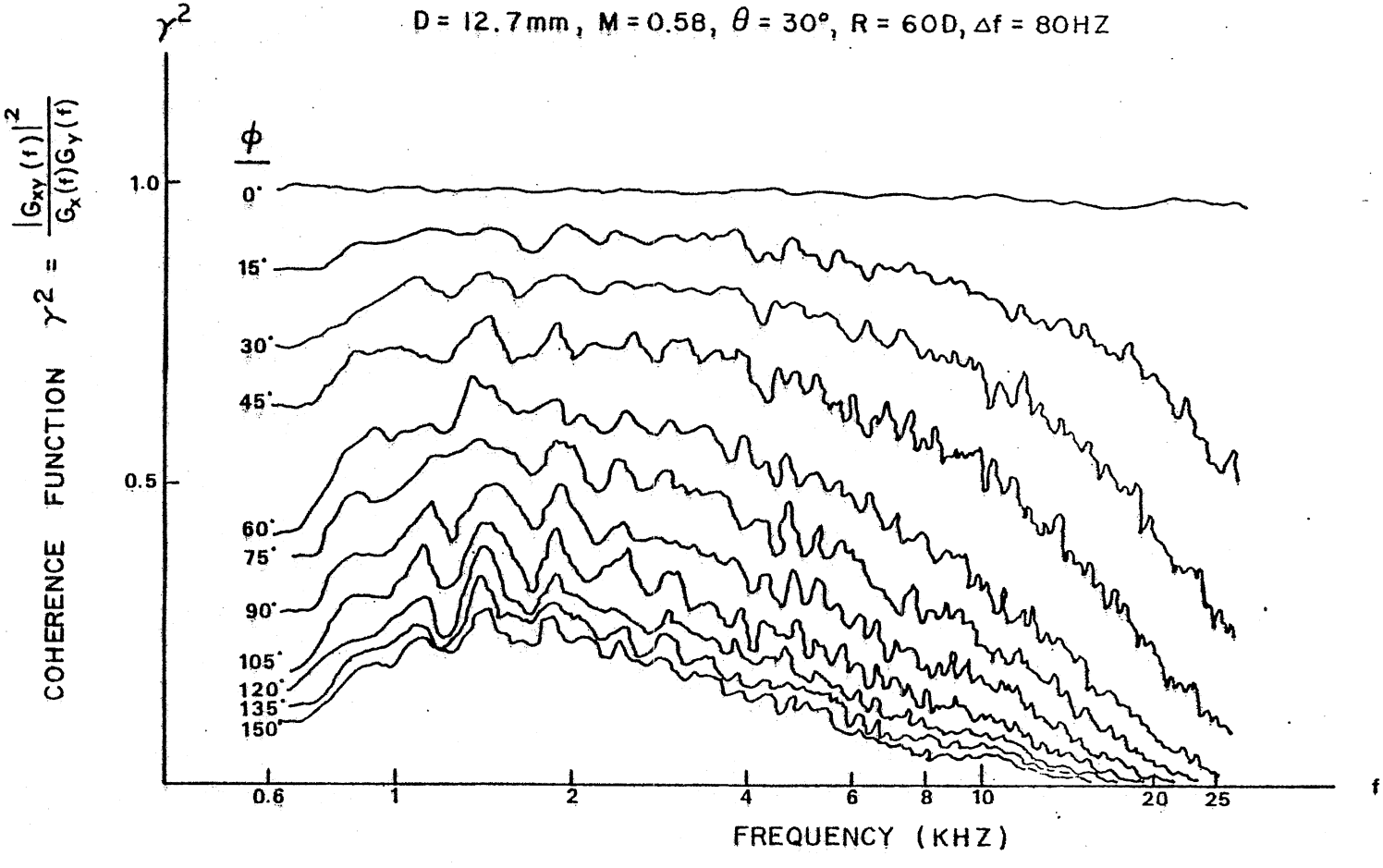

Figure 68: Coherence Function of Circumferentially Correlated Noise Signals Versus Frequency ($\hat{\theta}$ = 0° ~ 150°)

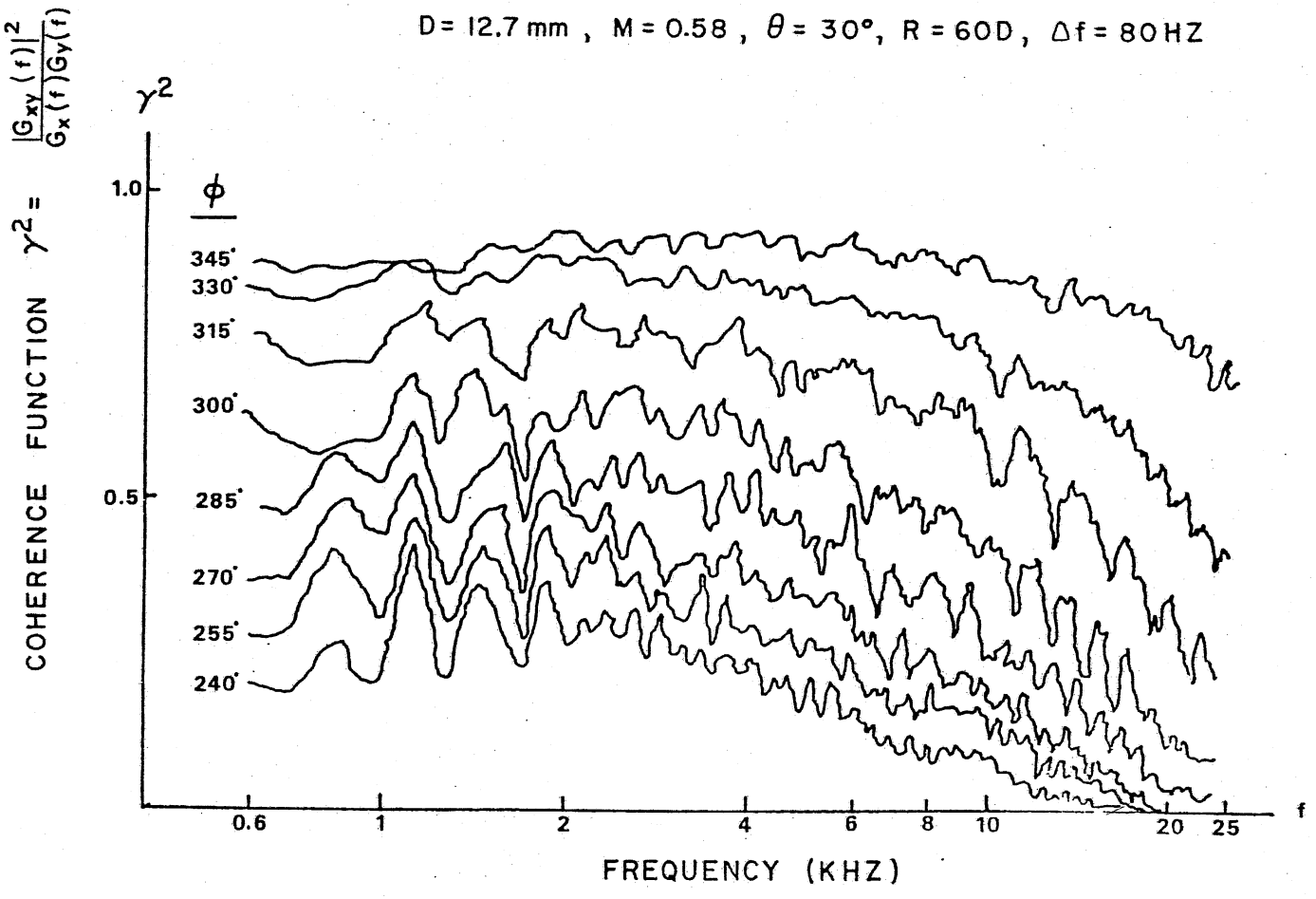

Figure 69: Coherence Functions of Circumferentially Correlated Noise Signals Versus Frequency ($\hat{\theta} = 240° \sim 345°$)

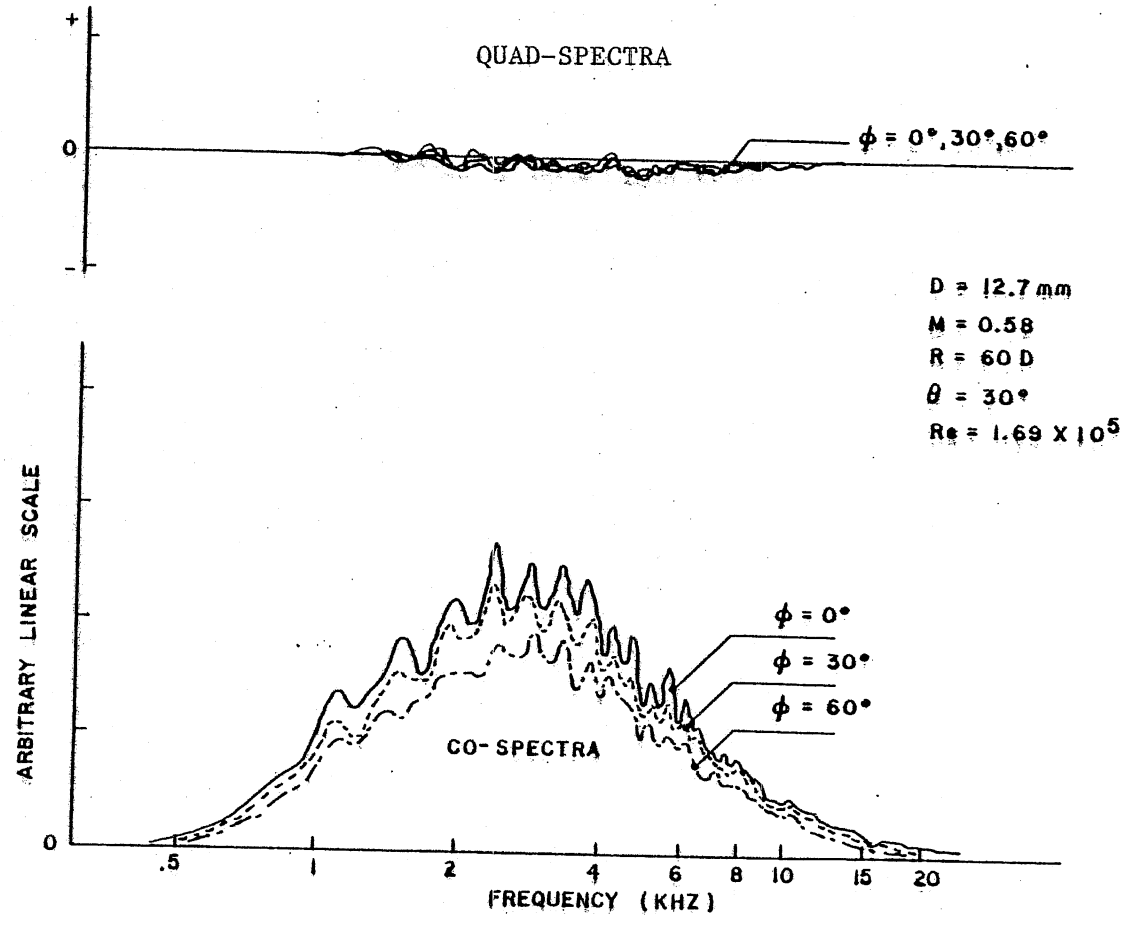

Figure 70: Cross Spectral Density of Jet Noise at Various Azimuthal Locations

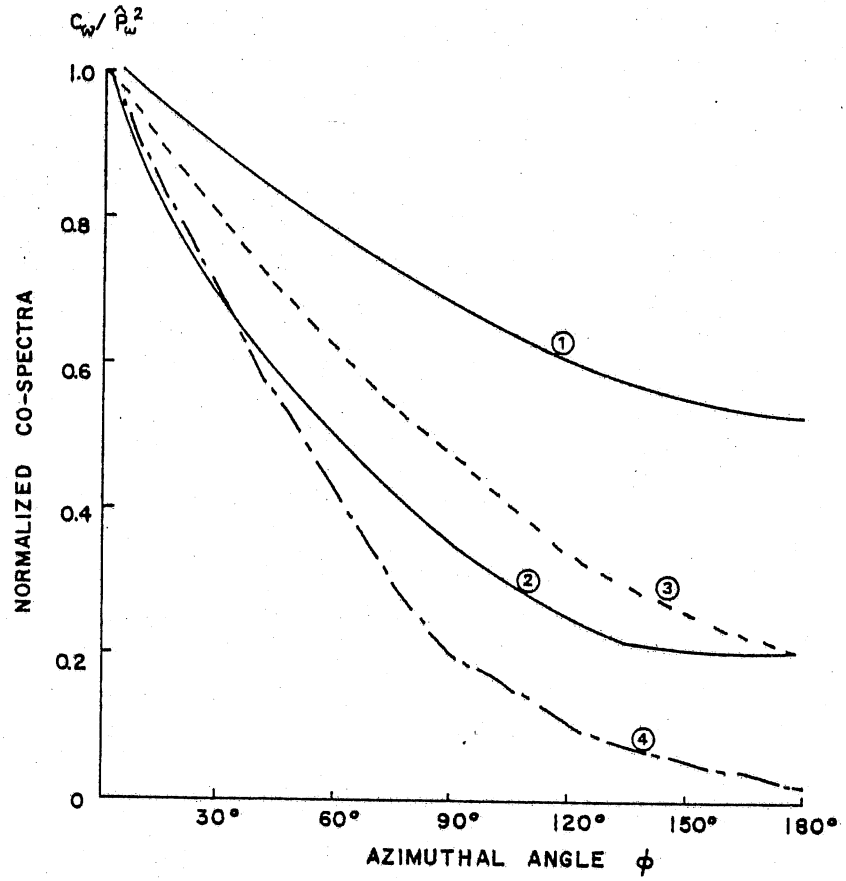

Figure 71: Normalized Azimuthal Correlation Coefficients of the 12.7 mm Jet for Various Strouhal Numbers Compared with Near Field Data: (1) Near Field X = 3D, Z = D/4, D = 100 mm, Sh = 0.45 (Fuchs); (2) Near Field X = 3D, Z = D/2, D = 100 mm, Sh = 0.45 (Fuchs); (3) Far Field R = 762 mm, $\hat{\theta}$ = 30°, D = 12.7 mm, M = 0.58, Sh = 0.1; (4) Far Field R = 762 mm, $\hat{\theta}$ = 30°, D = 12.7 mm, M = 0.58, Sh = 0.514

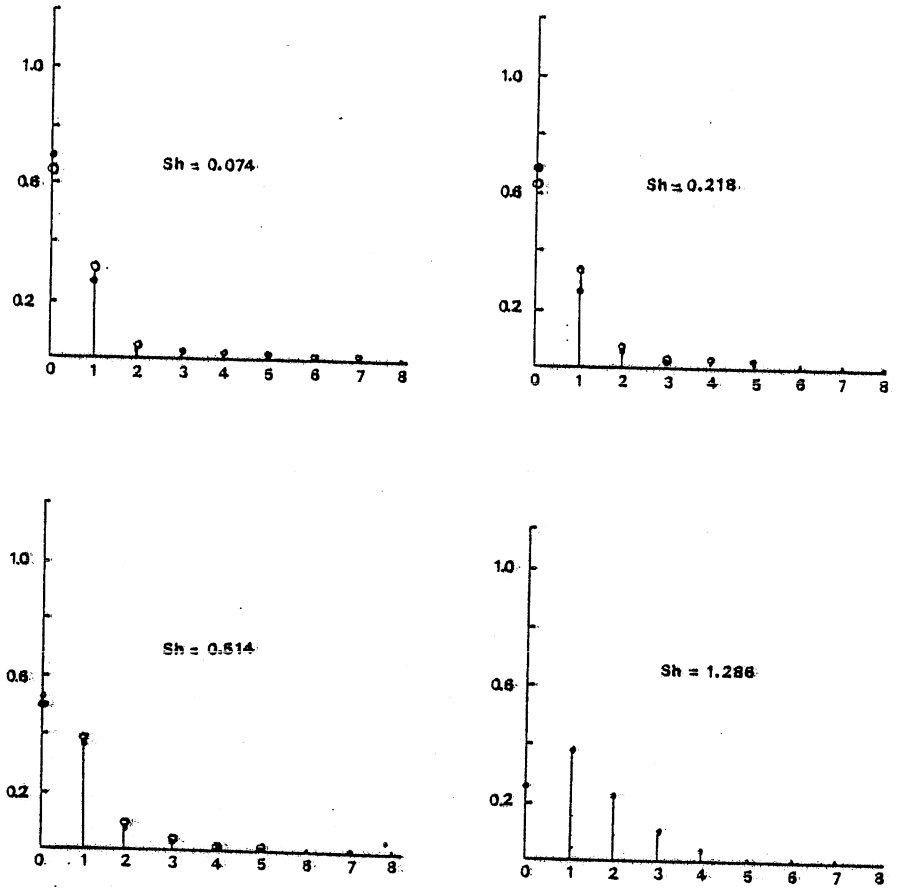

Figure 72: Fourier Coefficients of Decomposed Coherence Functions for the 12.7 mm Jet at M = 0.58 (Solid Circles) and the 6.35 mm Jet at M = 0.58 (Open Circles) for m = 0, 1, 2, ... 8

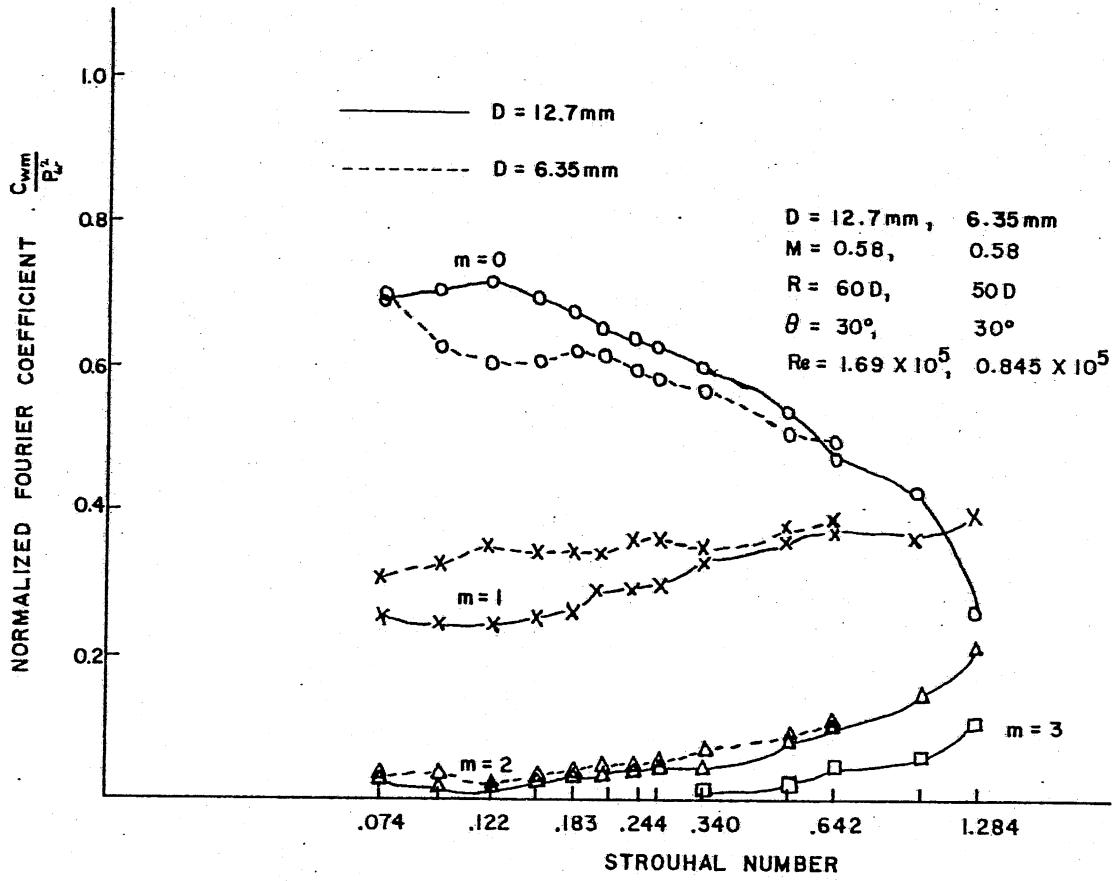

Figure 73: Fourier Decomposition of Coherence Function of Circumferentially Correlated Noise Signals

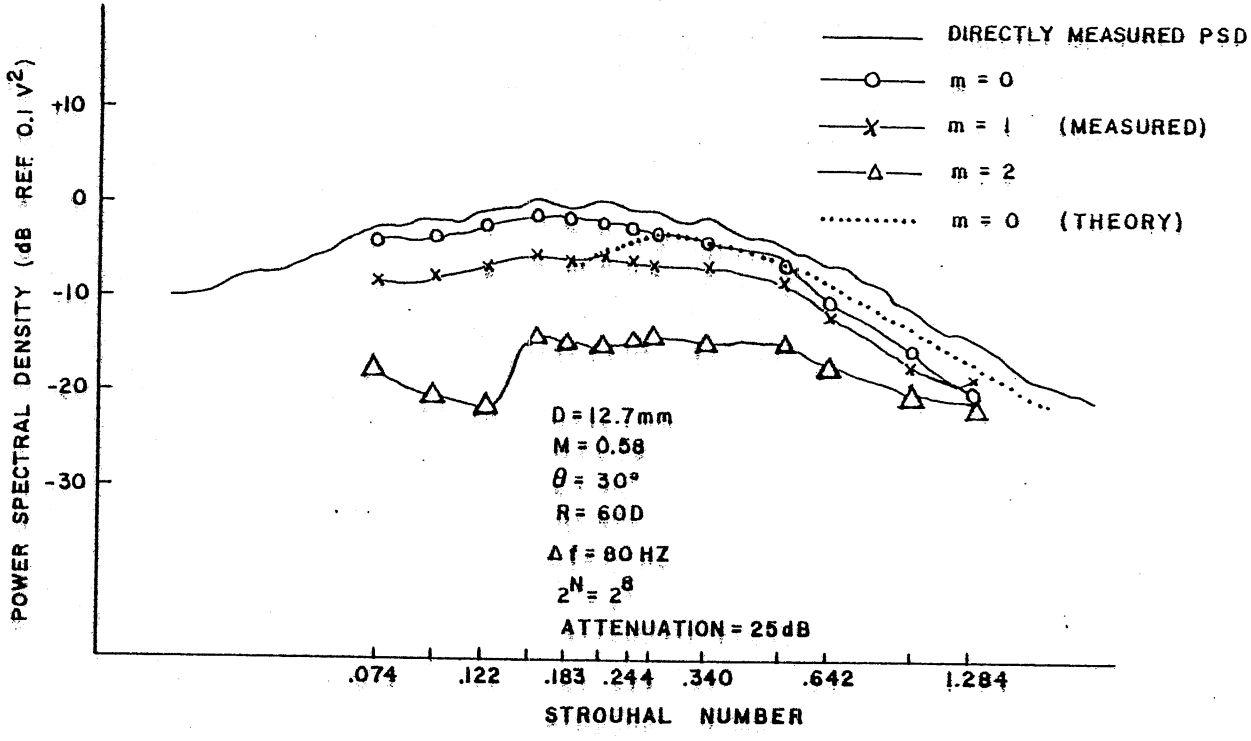

Figure 74: Fourier Decomposition of the Power Spectral Density of Jet Noise Compared with Theory

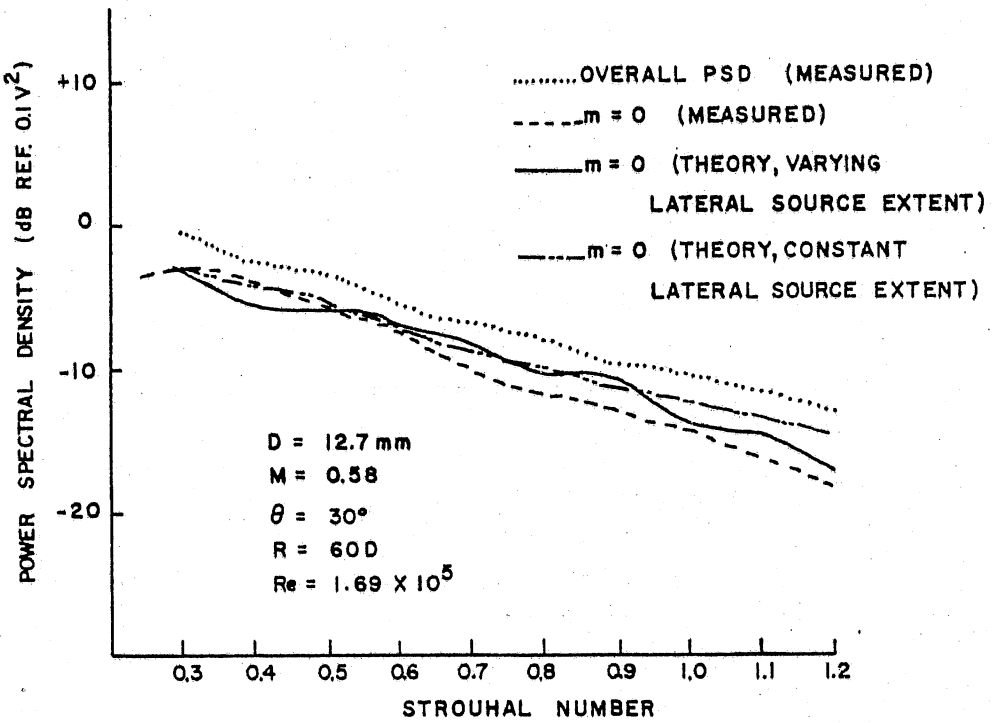

Figure 75: Power Spectral Density Compared with Theory

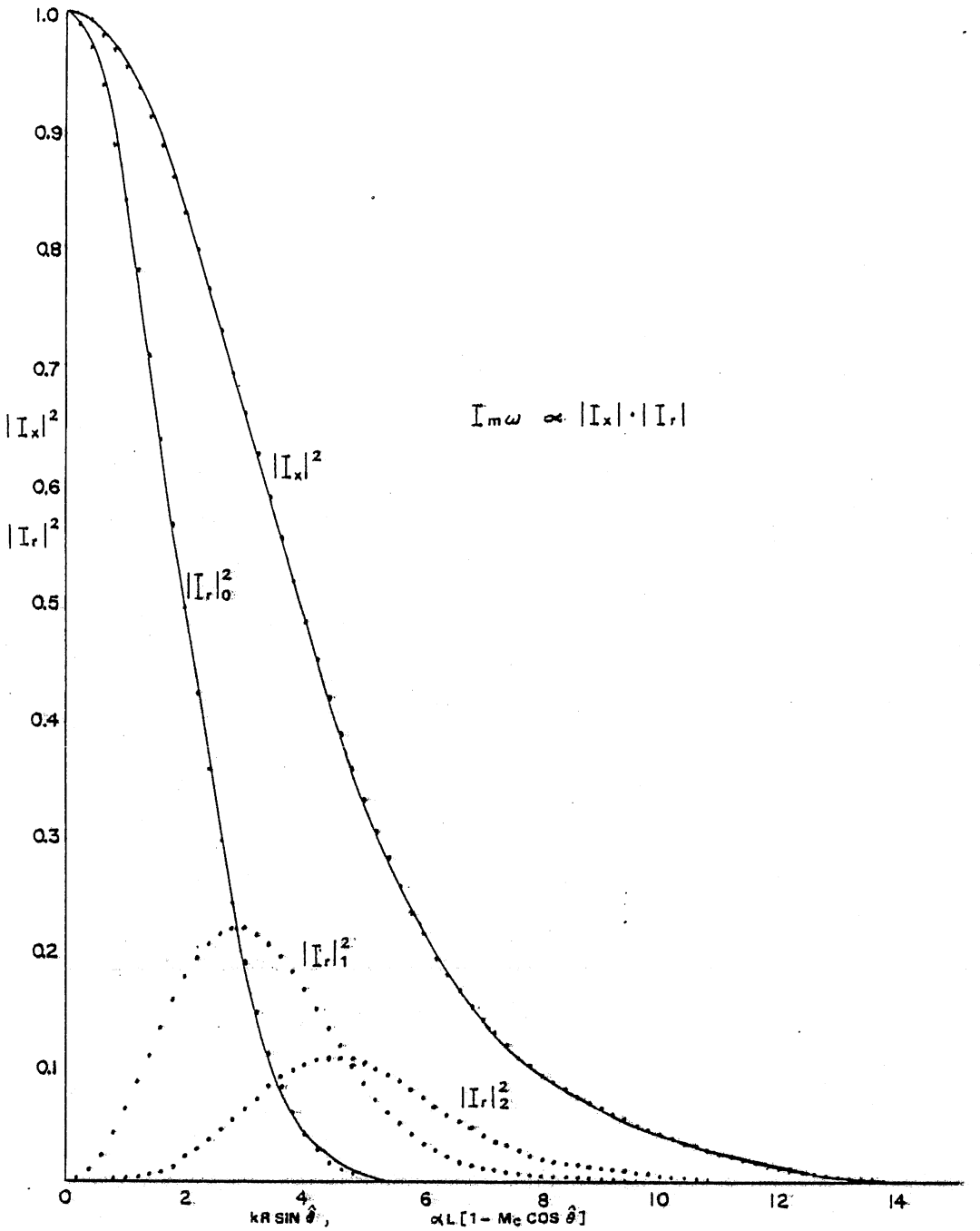

Figure 76: Longitudinal Source Integral I_x Versus $\alpha L[1 - M_c \cos\hat{\theta}]$ and Lateral Source Integral I_r Versus $k\hat{R} \sin\hat{\theta}$ (Calculated from Eq. (4), Chan, 1974)

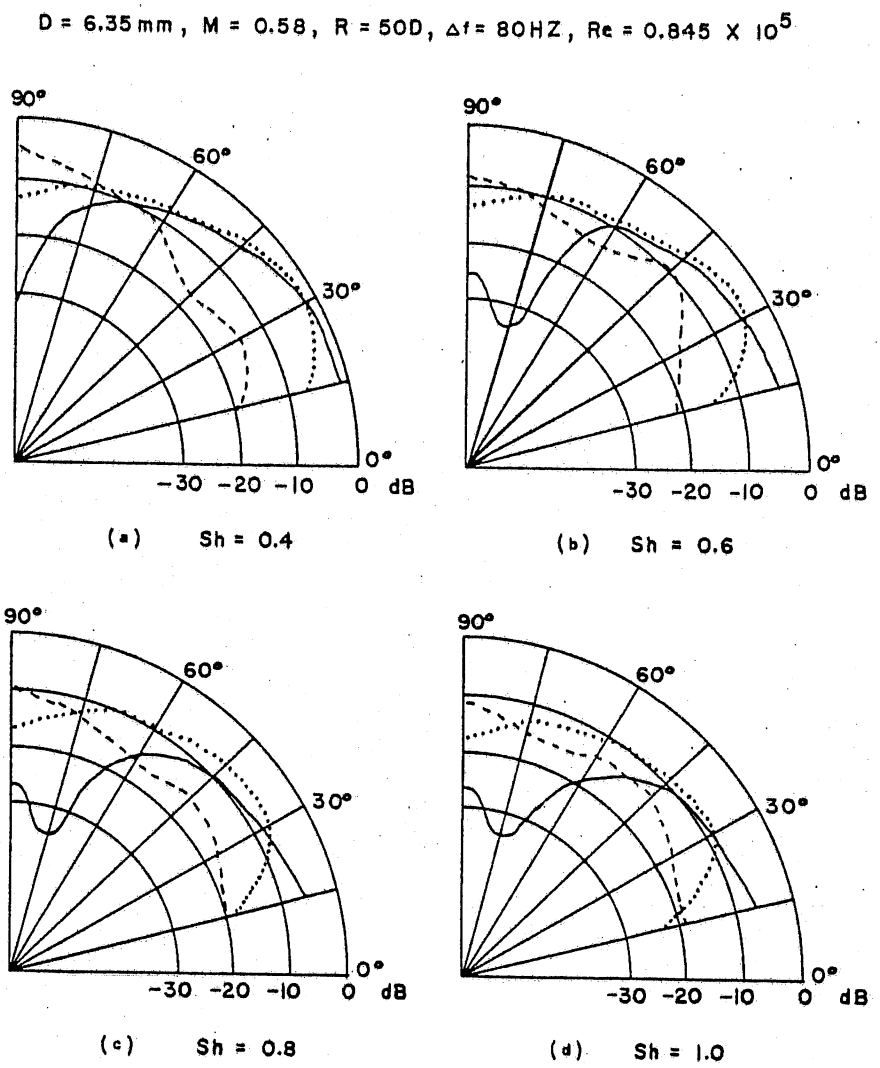

Figure 77: Directivity of the Narrow-Band Jet Noise Spectrum Compared with Theory (D = 12.7 mm) (.....: Measured Power Spectral Density; ———: Prediction for m = 0; -----: Prediction for m = 1)

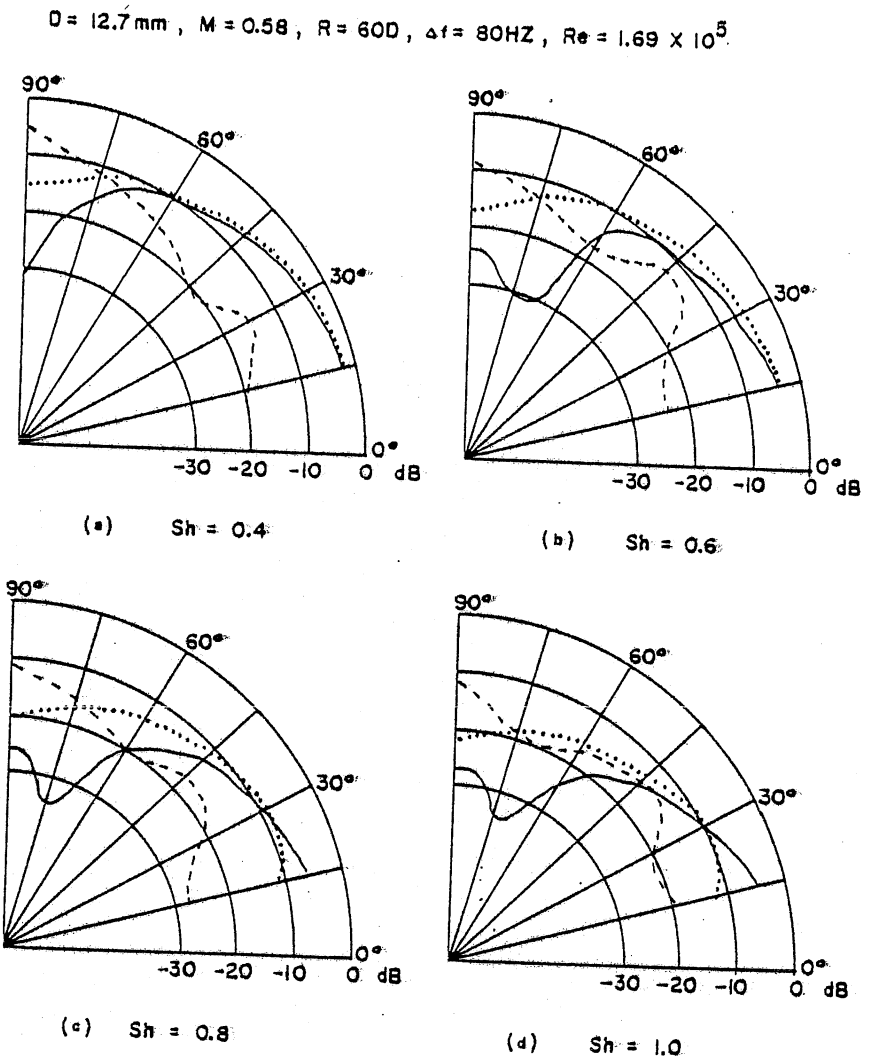

Figure 78: Directivity of the Narrow-Band Jet Noise Spectrum Compared with Theory (D = 6.35 mm) (See Figure 77 for Symbols)

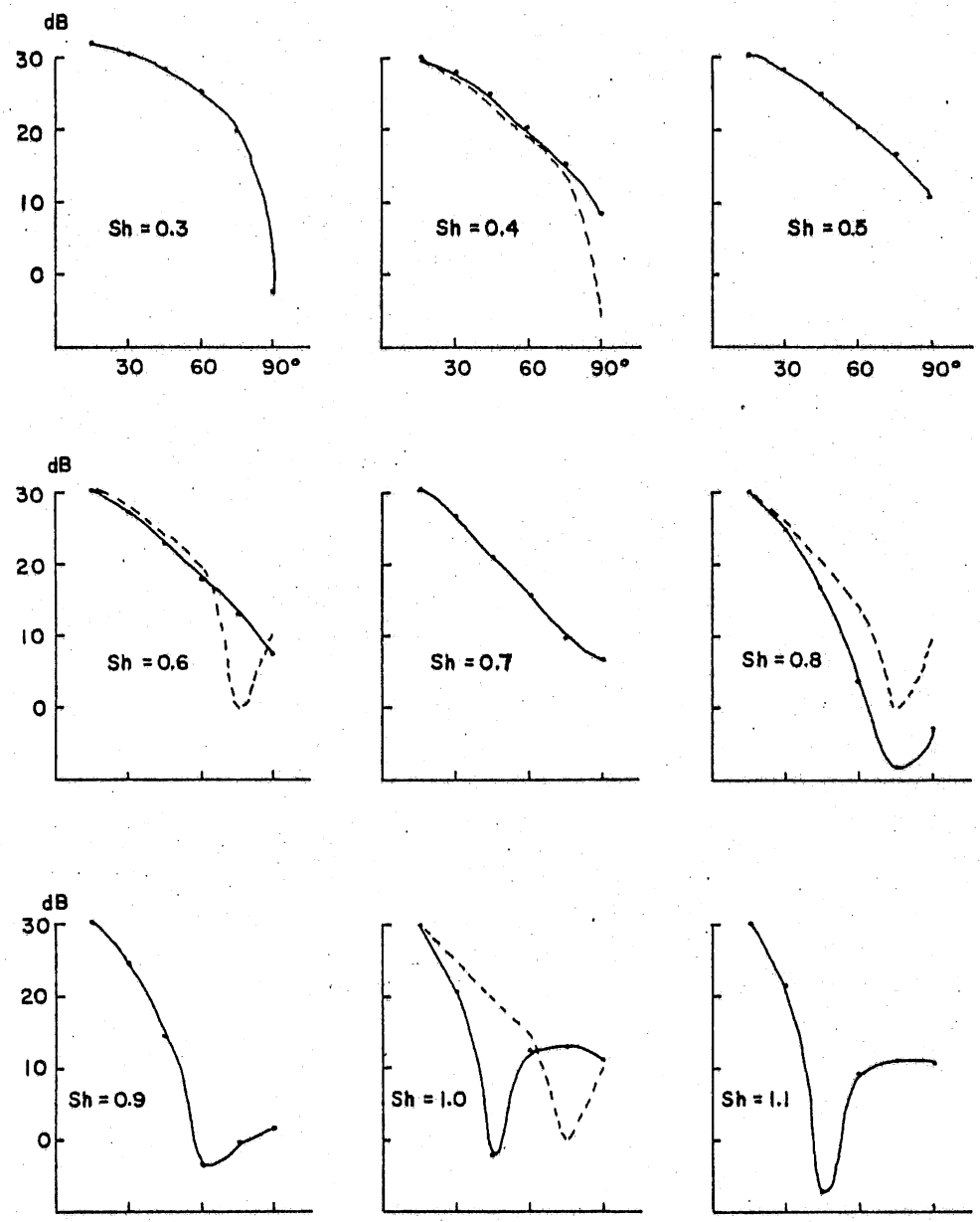

Figure 79: Calculated Directivity for the m = 0 Mode, D = 12.7 mm at M = 0.58 (The Solid Line Corresponds to $\hat{G}(\bar{r})$ Assumed Constant. The Dashed Line Corresponds to $\hat{G}(\bar{r})$ Assumed to be a Function of Strouhal Number.)

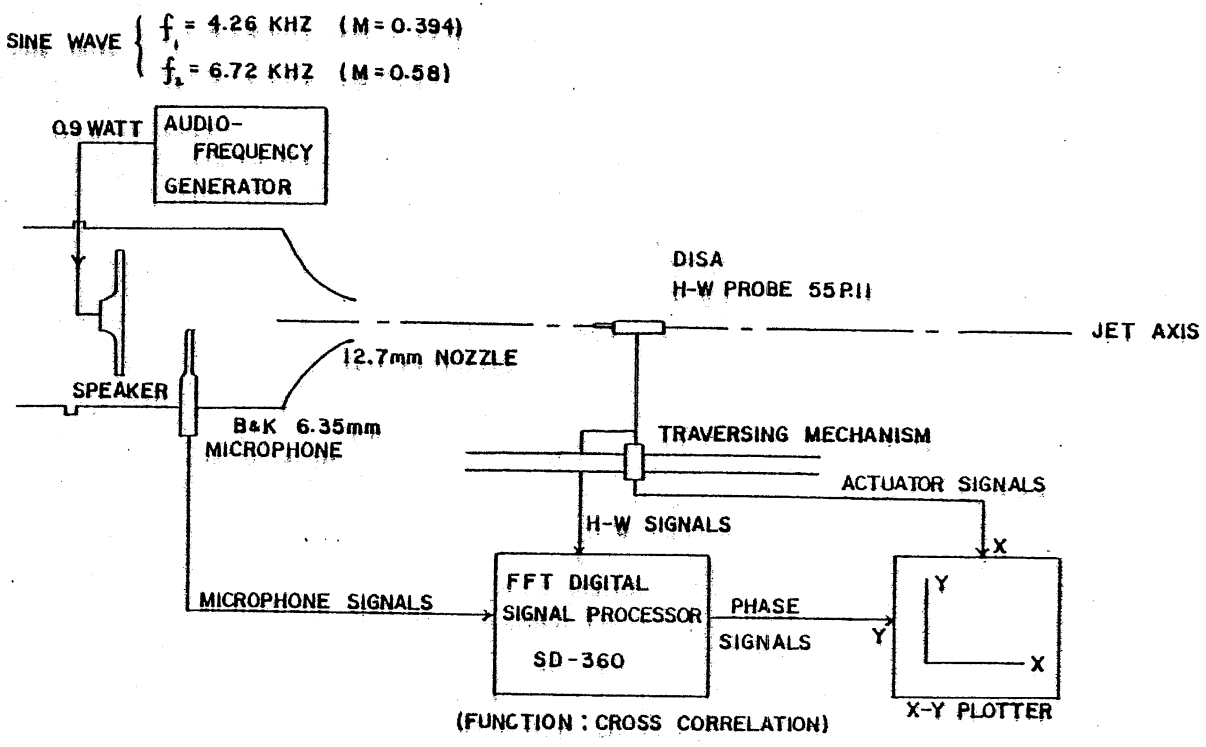

Figure 80: Schematic Diagram of the Phase Velocity Measurement System

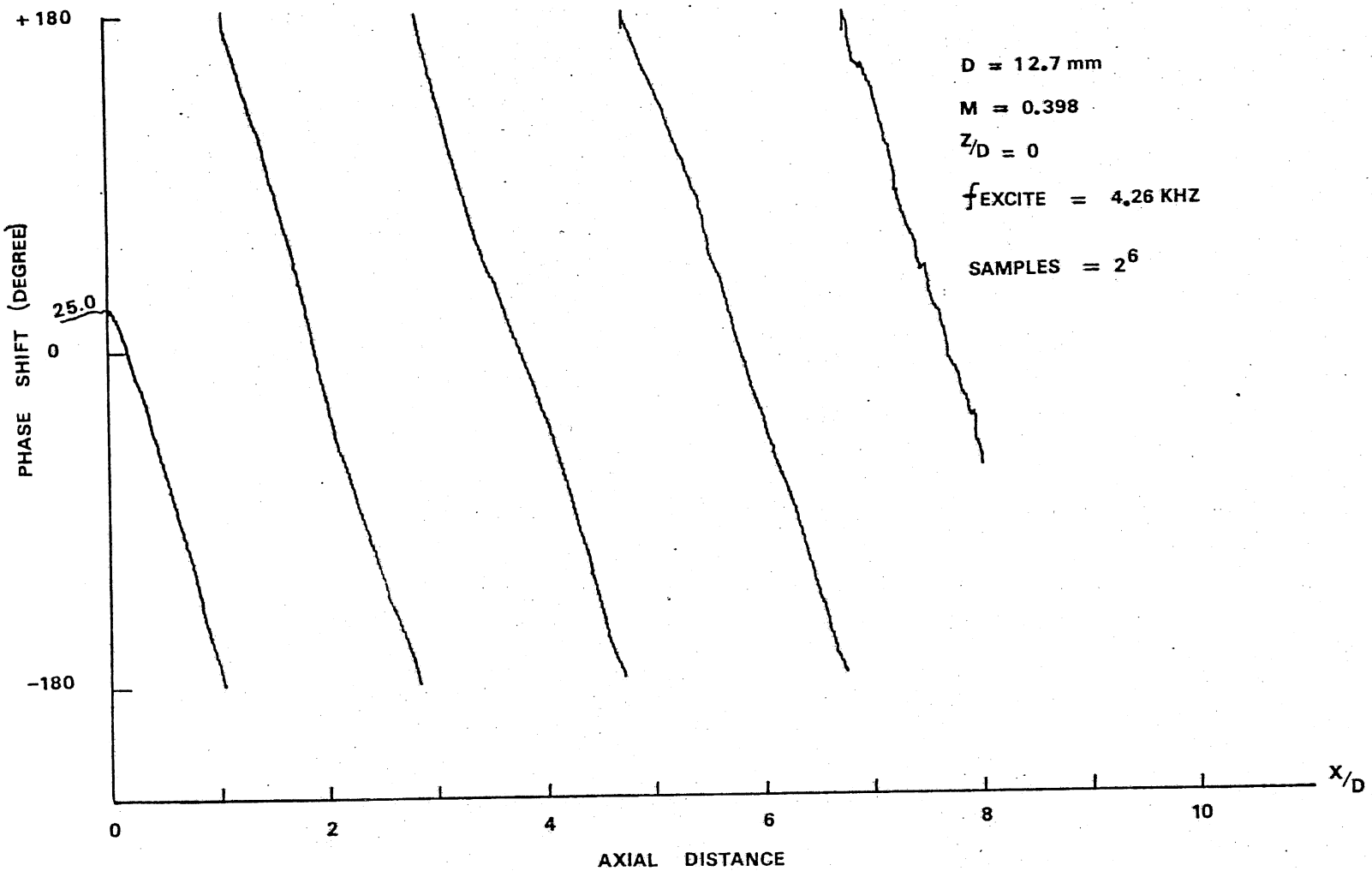

Figure 81: Phase Shift Between the Microphone Signal and the Hot-Wire Signal as a Function of Axial Distance

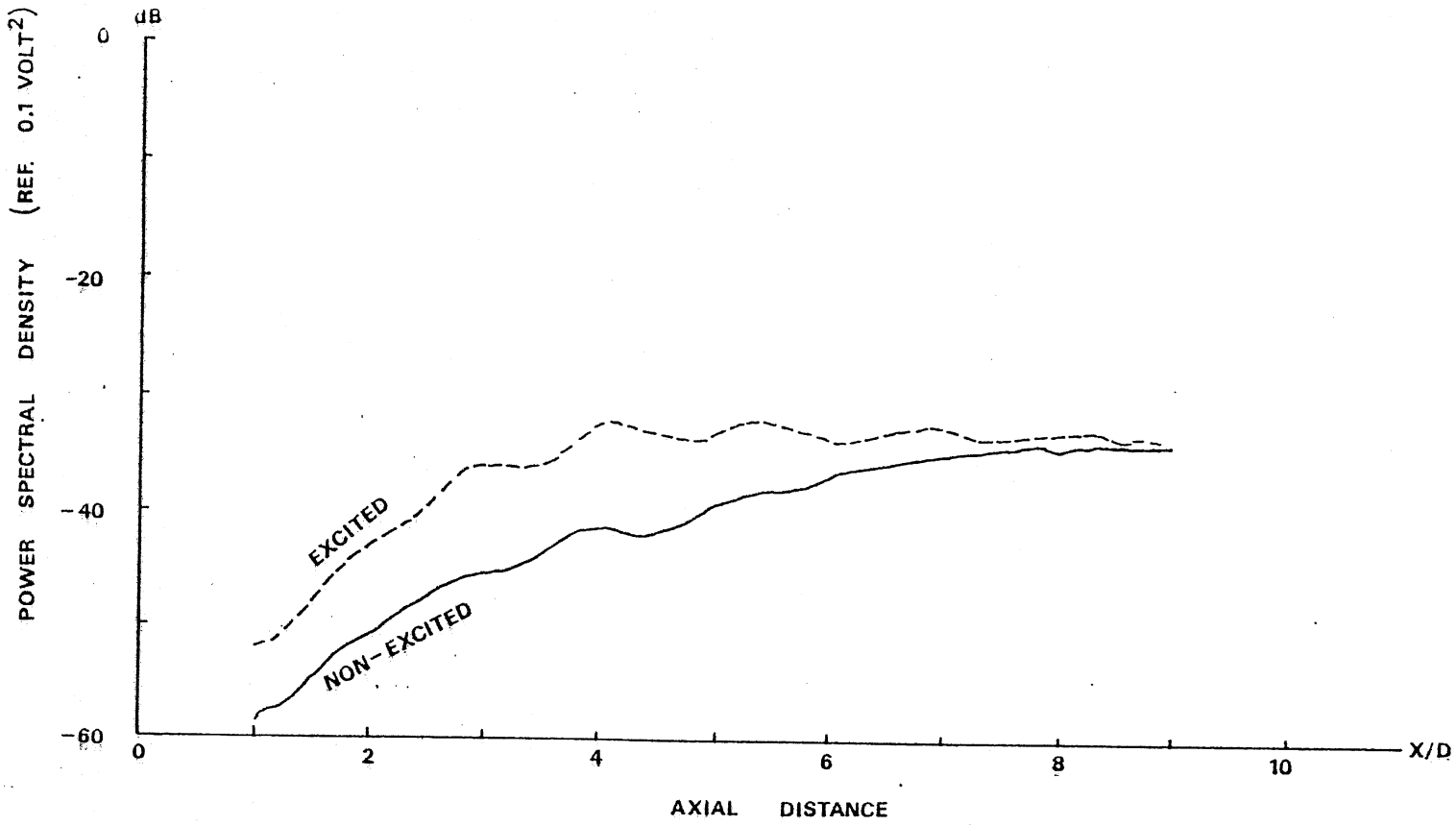

Figure 82: Peak Value of the Power Spectral Density of the Fluctuating Velocity (u-Component) on the Jet Axis Versus Axial Distance (D = 12.7 mm, M = 0.394, Exciting Frequency = 4.26 KHz, Averaging Time = 2^8)

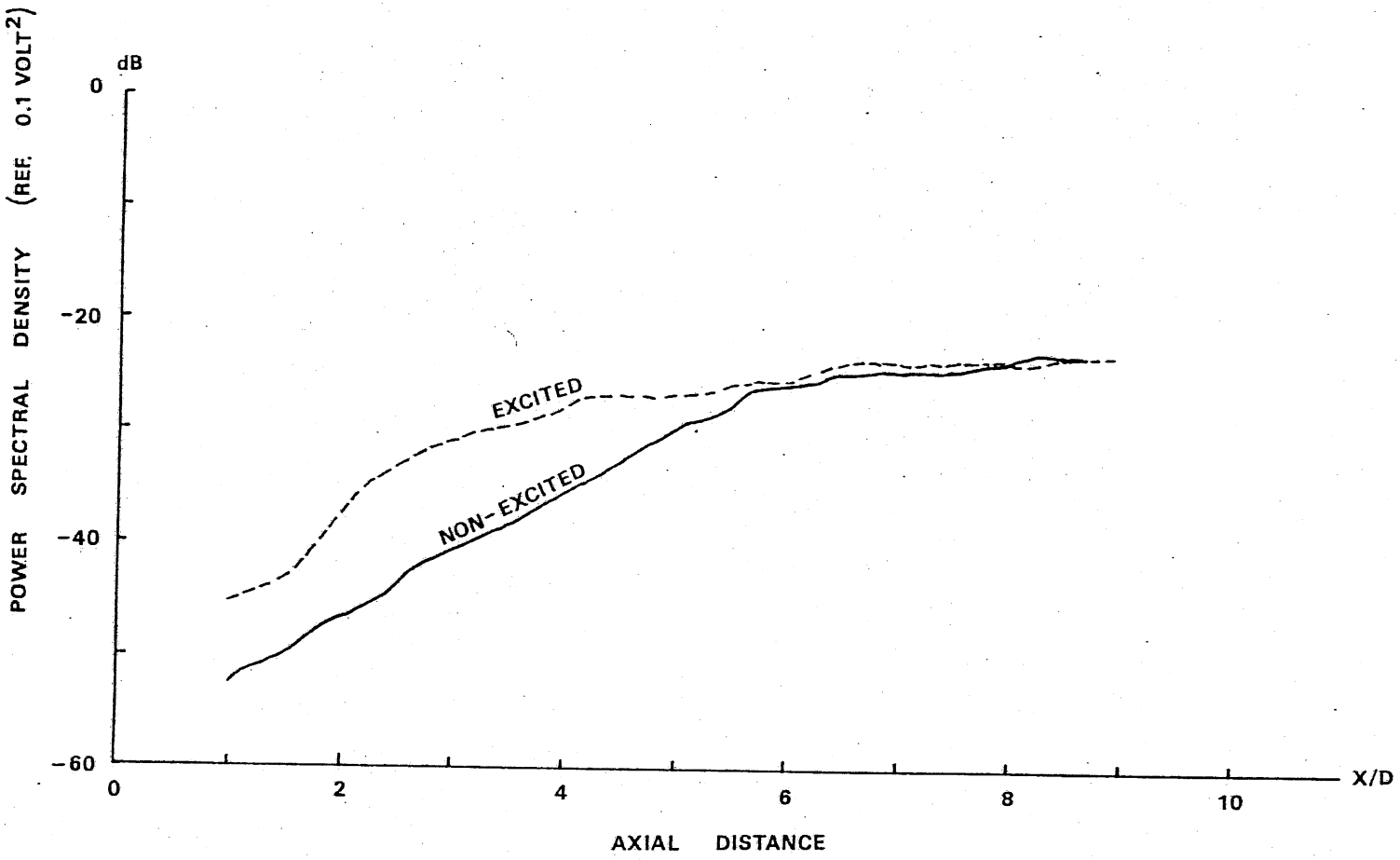

Figure 83: Peak Value of the Power Spectral Density of the Fluctuating Velocity (u-Component) on the Jet Axis Versus Axial Distance (D = 12.7 mm, M = 0.58, Exciting Frequency = 6.72 KHz, Averaging Time = 2^8)

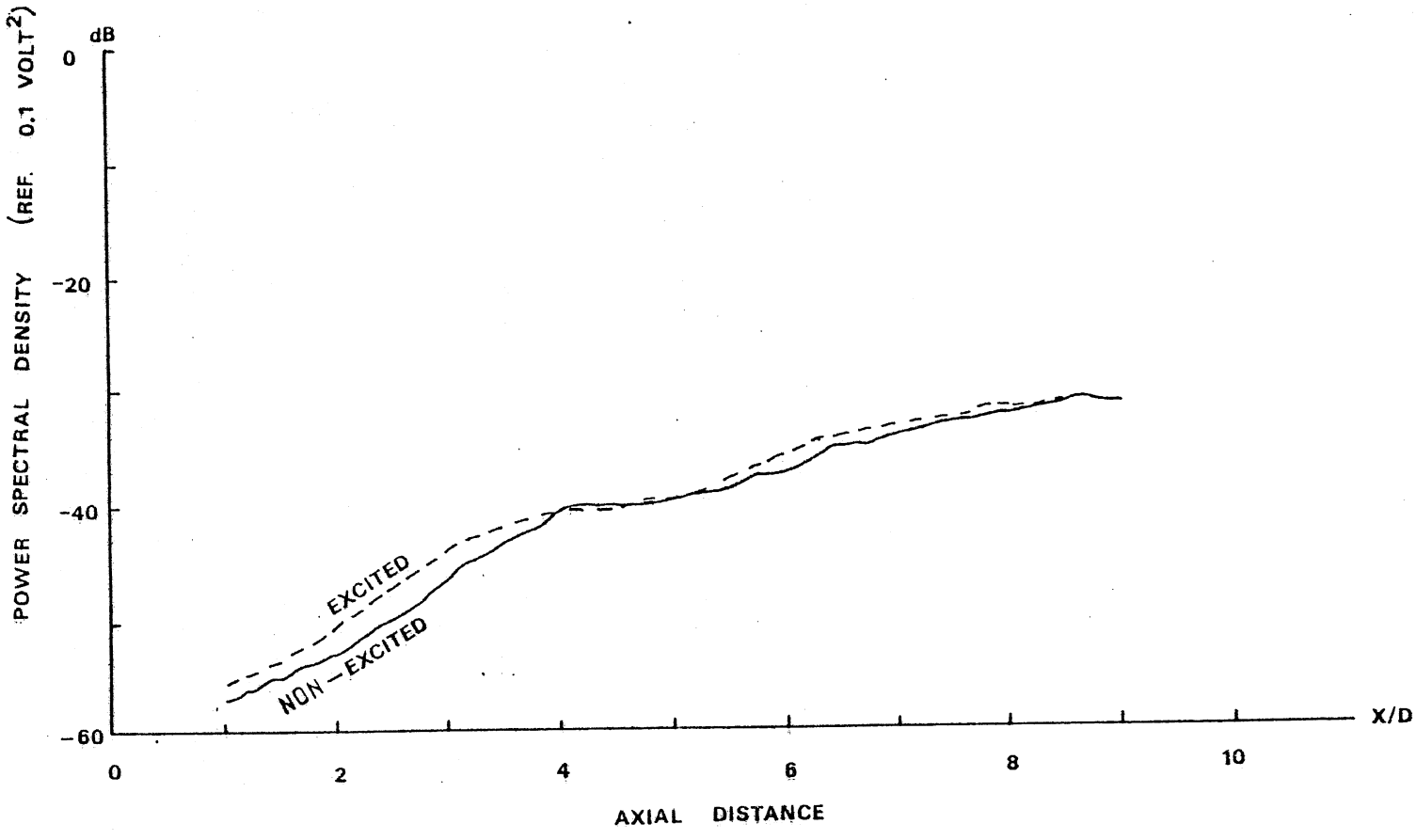

Figure 84: Peak Value of the Power Spectral Density of the Fluctuating Velocity (u-Component) on the Jet Axis Versus Axial Distance (D = 12.7 mm, M = 0.58, Exciting Frequency = 4.26 KHz, Averaging Time = 2^8)